Universidad
Carlos III de Madrid

TESIS DOCTORAL

Measurements and modelling of impurity flows in the TJ-II stellarator

Autor:
Juan Arévalo Gutiérrez

Directores:
Dr. Kieran Joseph McCarthy
Dr. Juan Arturo Alonso

Departamento de Física, Universidad Carlos III de Madrid

Leganés, Noviembre 2013

A mi madre

"Por decir lo que pienso,
sin pensar lo que digo,
más de un beso me dieron
y más de un bofetón."

J. Sabina en "Tan joven y tan viejo" (1998).

This work was partially funded by the FPI grant awarded by CIEMAT (BOE resolution n^{o} 171, 24/06/2008) and the Spanish Ministry of Science and Innovation under contract ENE2010-19676.

This thesis report was last revised on November 14, 2013 and has been compiled using pdfLaTeX. The offcial version is the printed version as registered for copyright.

Abstract

This thesis is concerned with the understanding of plasma velocity fields in three-dimensional toroidal magnetic confinement plasma devices such as the TJ-II stellarator –the magnetic confinement device subject of this thesis. Flow in these magnetic configurations is predominantly tangential to a set of nested toroidal surfaces known as magnetic or flux surfaces. The way in which the main plasma species (generally hydrogen or deuterium in fusion-oriented experiments) moves along these flux surfaces can have important effects on the confinement and stability properties of these devices. As an example, the improved confinement regime, known as H-mode, is associated with a strong variation of the $\mathbf{E}\times\mathbf{B}$ flow component across neighbouring flux surfaces.

The main experimental technique used in this work is Charge eXchange Recombination Spectroscopy (CXRS) of fully ionized carbon, C^{6+}. Velocity and temperature measurements are obtained from Doppler shift and broadening of a C^{5+} spectral emission line, respectively, after C^{6+} ions undergo a charge exchange reaction with a neutral atom. The sightline arrangement of the TJ-II CXRS system, together with a compact neutral beam injector to stimulate C^{5+} line emission, allows local perpendicular and parallel velocity components to be obtained at different positions within a set of magnetic surfaces.

CXRS velocity measurements are compared with theoretical expectations of flow spatial variation and of flow component size in strongly magnetized plasmas. The flow component perpendicular to the magnetic field direction consist of $\mathbf{E}\times\mathbf{B}$ and diamagnetic flows. In toroidal systems such flows are compressible, i.e. they have a non-zero divergence. To conserve the number of particles, the parallel flow component is constrained to vary so that the total (perpendicular plus parallel) flow is incompressible. In this framework, the full incompressible velocity field within a flux surface is determined by two constant factors that multiply different flow components. These constants are directly related to the radial electric field, E_r, and the so-called *bootstrap* factor, both of which are obtained from standard neoclassical theory in non-axisymmetric configurations. The understanding of the mechanisms that determine these quantities is important. For instance, the radial electric field profile has profound consequences on the confinement of particles, as mentioned before. On the other hand, the differences between the bootstrap components of ions and electrons give rise to the bootstrap current, which can modify some properties of the magnetic structure and affect the stability of the plasma.

The results of this comparison are twofold.

In low pressure-gradient plasmas of TJ-II good agreement is obtained, both in the incompressible variation of the flow (which CXRS allows to verify) and between the measured and computed values of E_r and bootstrap factor at several magnetic surfaces. A careful treatment of the complicated magnetic geometry has been fundamental to obtain this agreement, that provides confidence in the capability of the neoclassical theory to determine such factors.

In medium pressure-gradient plasmas, parallel flow measurements in TJ-II show notable and systematic deviations from an incompressible flow pattern. To interpret this observation it should be recalled that (1) incompressibility of the flow field of a given species relies on its number density being approximately constant on magnetic surfaces and that (2) CXRS measures the flow of C^{6+} ions. Because of their high charge number, carbon impurities can be in a collisional

regime that is prone to develop density inhomogeneities on flux surfaces. The resulting impurity parallel pressure gradient drives a return flow that departs from incompressibility.

The calculation of the impurity density inhomogeneity and parallel return flow requires solving the particle continuity equation and parallel momentum balance consistently. This is done numerically with the aid of magnetic libraries. The results of these calculations for the higher pressure gradient plasma cast an impurity return flow of a size comparable to the measured incompressible flow deviations. However, at the location of the measurements the model generally predicts a small deviation with opposite sign to the observations. This remains true when additional terms like parallel electric fields or inertia are included in the model. To conclude it should be noted that an explanation for such flow deviations is of considerable importance as it can modify the ion-impurity friction driven radial impurity transport.

Outline. This thesis report is divided into three parts: a theoretical introduction, a description of the diagnostic and analysis technique, experimental findings plus conclusions and outlook for future developments. In the first part, some basic concepts of magnetic confinement fusion are introduced, together with a brief description of the TJ-II stellarator. Next, the fundamentals of plasma rotation are reviewed in chapter 2. In a fluid description of the plasma, see section 2.1, the structure of an incompressible flow is derived, see section 2.2. The moments approach to the neoclassical theory is followed in section 2.3 in order to understand how such flows are damped through neoclassical viscosity. Finally, the breakdown of flow incompressibility when considering impurities is revisited in section 2.4, where the equations for a friction-driven impurity density redistribution within a magnetic surface are made explicit.

Next, a description of the CXRS technique is given in chapter 3 –which constitutes the second part of the report. This chapter includes a description of the experimental set-up used to measure the velocity, temperature and relative density profiles of fully-ionized carbon ions across the plasma minor radius, together with a review of all the instrumental and atomic processes than can contribute to uncertainties in such measurements. Finally, the data analysis procedures developed are outlined; examples of fully ionized carbon temperature and relative density profiles are presented and discussed.

In the final part of the thesis the results on the validation of a total incompressible flow tangent to the surface are presented. Measurements performed in low-density plasmas, $\bar{n}_e \leq 1.2 \times 10^{19}$ m^{-3}, are presented in chapter 4 where flow incompressibility is experimentally demonstrated and a comparison with neoclassical predictions is established. Afterwards, the observations of impurity rotation in medium-density plasmas, i.e. $\bar{n}_e \in (1.2 - 2.4) \times 10^{19}$ m^{-3}, are presented in chapter 5. There, measured impurity velocities which deviate from an incompressible pattern are reported and compared with the parallel return flow calculated from a modelled impurity density redistribution within a surface.

Finally, three appendices are included in the report. In appendix A, the coordinates used within this report are explained. Appendix B shows calculations of hydrogen-like fine structure levels and populations used for data analysis. In addition, the numerical implementation of the second-order partial differential equation that appears in the impurity density inhomogeneity model is presented in appendix C.

CONTENTS

Theoretical background

CHAPTER 1

INTRODUCTION

In this chapter, a brief introduction to the energy problem, fusion power and magnetic confinement fusion devices is addressed. No attempt is made here to cover such a vast area of research, see e.g. [1–3], but give a context for this research work and revisit some basic concepts required for the understanding of this report. In addition, a concise description of the TJ-II stellarator, in which this thesis has been carried out, is provided in section 1.3.

1.1 The energy problem and fusion power

In the last decades, much effort has been expended to answer the problem of rising energy demand with reliable, affordable and environmentally respectful energy sources [4]. The major sources of energy consumed on the planet are, nowadays, fossil fuels [5]. Paradoxically, these are the least abundant natural resources. Furthermore, the ability of major fossil fuels producers to withhold supplies hihglights the importance of geographically distributed energy sources. Examples of that are the temporary boycott of the world market by OPEC in the early '70s, or the gas-disputes between Russia and Ukraine which resulted in several days cut to European supplies[1]. In addition, the global warming that results from the use of burning fossil fuels and the subsequent greenhouse effect has become unmistakably important. Besides the aforementioned issues, namely growing demand/abundance of natural resources, political stability and environmental care, a fourth concern to be considered in the energy problem is safety: let us remember the nuclear catastrophes in Chernobyl or Fukushima, oil spills (the explosion of the Deepwater Horizon oil platform in 2010, the Prestige spill in 2002, and so on) or the contention of long-term radioactive fission waste.

Renewable energies are a promising solution from the point of view of safety, abundance, political stability and environmental care. Indeed, the European Union aims to obtain 20% of its energy from renewable sources by 2020[2]. However, the efficiency of commercial electric power

[1] See, e.g. http://en.wikipedia.org/wiki/1973_oil_crisis and https://en.wikipedia.org/wiki/Russia-Ukraine_gas_disputes.

[2] See http://ec.europa.eu/energy/renewables/targets_en.htm

from renewable source for industrial purposes is limited. In addition, they are subjected to climate conditions, and thus, reliable and efficient ways to store the produced energy are necessary. The development of on-demand and economically viable sources of energy is therefore mandatory. As we shall see next, fusion power can meet most of the renewable energy benefits, with the additional advantage of on-demand supply and the efficiency of a conventional electric generator. Hence, it is a good candidate to supply a large fraction of the world energy consumption.

Fusion power is understood as the potential commercial production of net usable power from a fusion source. There are many different fusion processes, but in all of them several light nuclei combine together into heavier and more stable nuclei. The difference in mass between the reactants and the products is converted to energy according to Einstein's formula ($\Delta E = (\Delta m)c^2$, with c the speed of light). The kinetic energy imparted to the products can be used both to sustain a stable system of fusion reactions and to produce electricity.

For a single fusion reaction to occur as a result of random collisions between two nuclei, they must be made highly energetic, as the initial nuclei must be close enough ($\sim 10^{-15}$ m) so that the attractive nuclear force can overcome the repulsive long-range Coulomb force[3]. Typically, temperatures as high as $10-100$ keV are required. Note: in Plasma Physics it is customary to express the temperature in energy units, e.g. $1\,\mathrm{eV} \equiv 1.16 \times 10^4$ K, due to the equivalence $E \equiv k_\mathrm{B}T$, with k_B the Boltzmann constant. Under such conditions atoms are ionized –completely, for light particles– forming a globally neutral gas consisting of positively charged nuclei and electrons, which is called a (thermonuclear) plasma [7, 8]. Since no conceivable material could confine a thermonuclear plasma, confinement other than by walls is necessary. Current fusion research is based on two main approaches: inertial and magnetic confinement. The former consists of compressing with focused lasers a small pellet of fuel to high densities ($\sim 10^{27}$ particles per cubic meter) in short time scales ($\sim 10 - 100$ ns), in which inertial implosion occurs, see e.g. [9]. In the latter, magnetic fields are used to confine the charged particles through the Lorentz force, see e.g. [10]. In the following, we restrict ourselves to magnetically confined fusion plasmas.

In a magnetically confined fusion reactor, the heating of the plasma by the products of fusion reactions must be sufficient to maintain the high plasma temperature –required to fuse further nuclei– against all losses and without external power input. Such a self-sustained thermonuclear fusion process is known as a burning fusion plasma. In order to achieve it, a sufficient number of fusion encounters must occur so the total energy produced, W, matches at least the rate at which the system looses energy to its environment, P_loss. Therefore, besides the high temperatures required to produce a single fusion reaction, a certain density of reactants is needed to produce the energy W, which must be confined during a time $\tau_E = W/P_\mathrm{loss}$ so the system is not cooled down. The minimum of the triple product of density, temperature and energy confinement time required to start a burning plasma is known as the Lawson criterion [11], and depends on each particular reaction. According to this criterion, the most suited reaction is the one between deuterium (D) and tritium (T) hydrogen isotopes (see e.g. chapter 9 in [3]), i.e.

$$\mathrm{D} + \mathrm{T} \rightarrow {}^4\mathrm{He}(3.5\ \mathrm{MeV}) + \mathrm{n}(14.1\ \mathrm{MeV}), \tag{1.1}$$

[3] Another approach is the so-called muon-catalysed fusion, in which the muon replaces an electron in a hydrogen isotope molecule. Since muons are about 207 times heavier than electrons, the nuclei are drawn consequently 207 times closer, see e.g. reference [6] or visit `http://en.wikipedia.org/wiki/Muon-catalyzed_fusion`.

with a neutron (n) and helium nuclei (^{4}He) as fusion products. The kinetic energy of the alpha particle –helium– is deposited in the surrounding fuel plasma and thus heats it. Once thermalized, the helium ash must be exhausted from the plasma to avoid diluting the fuel, see e.g. [12]. On the other hand, as neutrons do not suffer the Coulomb force they can escape the plasma. In order to thermalize these neutrons, a radiation shield and blanket with a thickness of $\sim$ 1 m is necessary [13]. The heat produced in the blanket can be converted to electricity with conventional methods (e.g. with a refrigerating circuit that conducts the heat to a steam turbine which, in turn, drives electrical generators).

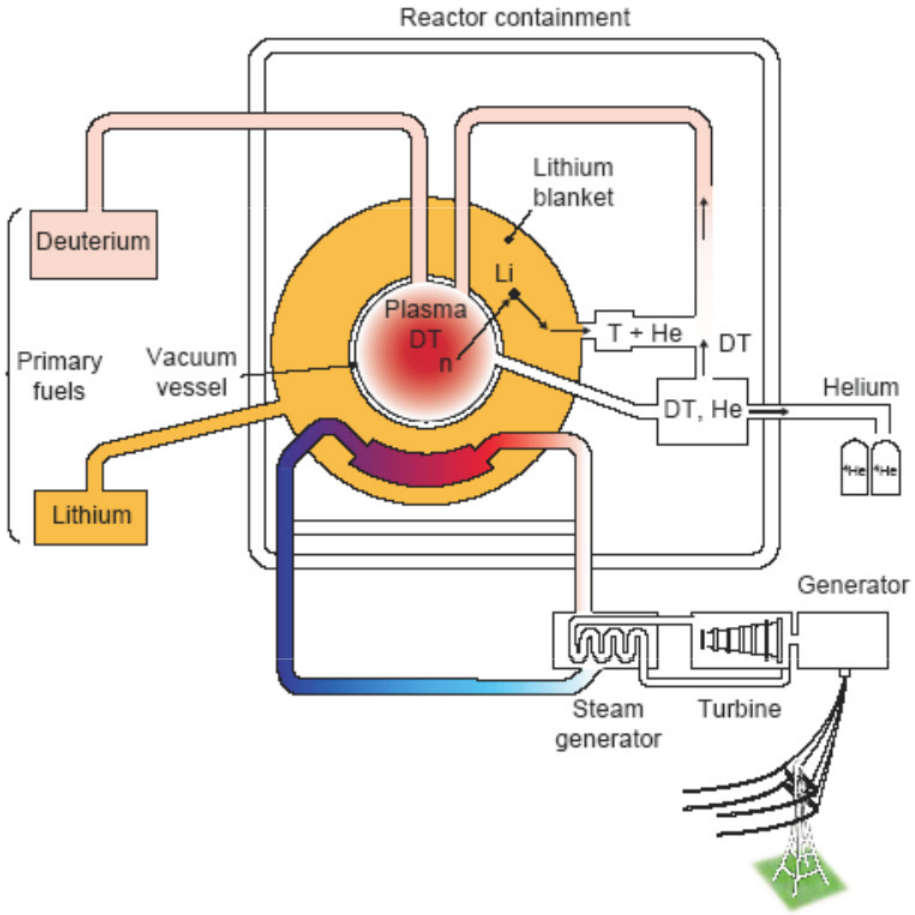

Figure 1.1. Sketch of a D-T fuel cycle and heat extraction in a magnetic confinement fusion reactor, from [14]. Tritium is produced in the lithium blankets after capturing a neutron that results from a D-T reaction. A refrigerating circuit cools down the blanket and operates a steam turbine.

Most of the advantages and difficulties of fusion power can be derived from the above simplified view. Deuterium is an stable isotope of hydrogen naturally present in sea water, with an abundance close to 1 in 6000 of that of hydrogen. On the other hand, tritium is unstable due to β-decay with a half-life of 12.5 years, but can be produced with the capture by a lithium nucleus of the neutron that results from the D-T reaction (1.1). Therefore, if the aforementioned blankets –originally meant to thermilize the neutrons and shield radiation– contain lithium, the necessary amount of tritium could be produced, see e.g. [15]. A schematic diagram of a self-sustained D-T fuel cycle for a magnetically confined fusion reactor plasma is presented in figure

1.1. The D-T gas is contained in a vacuum vessel, fed directly with deuterium and the tritium recycled from the blankets. As also shown in the figure, the heat deposited by neutron thermalization in the blanket is conducted to a steam turbine, which in turn drives an electric generator. Thus, a fusion reactor would have the efficiency of a conventional electric generator, being at the same time environmentally respectful as it does not emit carbon dioxide. However, the large flux of high-energy neutrons produced in fusion reactions will activate the materials containing the reactor. As most of these are structural components, the utilized materials can be selected specifically to have low activation, see e.g. [16, 17]. A final important feature of fusion reactors is that they are intrinsically safe, in the sense that a chain reaction -like in a nuclear bomb- cannot occur.

The next step in magnetic confinement fusion research towards commercial fusion power is the international collaboration ITER [18] (*International Thermonuclear Experimental Reactor*), currently under construction in Cadarache, France. First plasmas are expected in 2020, and its primary goal will be the production of a burning plasma, delivering 10 times the power it consumes. During its operational lifetime, ITER will test key technologies necessary for a commercial fusion reactor, the demonstration fusion power plant (DEMO).

In parallel, research institutes keep on extending the scientific knowledge required for the energy production from fusion. In the following, the attention is focused on the physics of magnetically confined plasmas, rather than on specific issues relevant for a fusion reactor. Several concepts have been developed over the years, among which the tokamak and stellarator have attained the best performance. Here, some of the features shared by both devices are summarized and the advantages and disadvantages of each machine are briefly discussed.

1.2 Magnetic confinement devices: the stellarator

As a plasma is locally charged, the Lorentz force produced by the magnetic field $\mathbf{B}$ in a magnetically confined plasma device makes charged particles travel a circle about the magnetic field lines in the so-called Larmor gyromotion; these particles are nonetheless free to move along the field lines, see e.g. [7, 8]. Thus, if the magnetic field lines are closed over themselves, the charged particles in the plasma are confined by the magnetic field. Nevertheless, plasma confinement implies a gradient in the plasma pressure (i.e. the product of the density and temperature $p = nT$) as charged particles will eventually touch some material, e.g. the vacuum vessel, and thus become neutral. The gradient in the pressure, ∇p, is balanced at lowest order by the electromagnetic force produced by the cross product of the current density in the plasma, $\mathbf{j}$, and the magnetic field [19],

$$\nabla p = \mathbf{j} \times \mathbf{B}. \tag{1.2}$$

From this ideal equilibrium (1.2) a magnetic-field line $\mathbf{B}$ must lie on a surface of constant pressure through its entire length, i.e. $\mathbf{B} \cdot \nabla p = 0$. As a consequence, the plasma is constrained to have the topological form of a torus [10], where the surfaces of constant plasma pressure are nested tori. The $\mathbf{B}$-lines cover such surfaces, either closing after a number of turns or wrapping the surface densely. The surfaces of constant pressure are usually called 'magnetic' surfaces; 'flux'

surfaces is also utilized, as the flux of particles flows mainly along magnetic field lines. It is noted here that nested magnetic surfaces can also be created without a plasma, as in the stellarator devices explained next. In such a case, the existence of nested magnetic surfaces is not always guaranteed, see e.g. chapter 2 in [3], but is assumed in the following, see e.g. [20].

The nested toroidal magnetic surfaces are labelled by a radial coordinate, here ρ, connected to a quantity that is constant on the magnetic surface, e.g. the plasma pressure, the geometrical volume V or the toroidal magnetic flux Ψ_t contained by the surface. A magnetic surface $\rho =$constant is defined by the condition $\mathbf{B}\cdot\nabla\rho = 0$, so that the magnetic field vector is tangential to the surface ρ. Throughout this document a dimensionless radial coordinate

$$\rho = \sqrt{\frac{V}{V_\mathrm{LCFS}}}, \tag{1.3}$$

is used to identify a surface in the representation of experimental and numerical data. Here, V is the volume contained by the surface of interest, and V_LCFS is the total plasma volume (LCFS is the last closed flux surface or the last closed magnetic surface). The choice of this radial coordinate is motivated by the library used for the calculation of the magnetic field [21]. However, some other magnetic surface labels will be utilized in chapter 2 to ease the algebra, so ρ is left as a general radial coordinate without loss of generality. To avoid confusion, when ρ is given by equation (1.3) it will be named *normalised radius* of the plasma. Indeed, a radius $r \equiv \sqrt{V/(\pi L_\mathrm{ax})}$ can be defined for a toroidal length L_ax (e.g. the length of the axis of the tours, called the magnetic axis, or the circumference of the major radius, R_0). Then, $\rho \equiv r/a$ stands effectively for a normalised radius with $a \equiv \sqrt{V_\mathrm{LCFS}/(\pi L_\mathrm{ax})}$ the minor radius of the plasma.

Charged particles are tied to magnetic field lines, thus making the particle stream flow tangent to the magnetic surface in first approximation. However the magnetic field curvature, intrinsic to a toroidal confinement device, makes particles drift away from the original magnetic surface until they are lost through the LCFS, see e.g. chapter 6 in [22]. In order to diminish such a drift the magnetic field lines must be twisted to create what is called a rotational transform [23], $\iota = 1/q$ (here, q is the safety factor). The rotational transform is defined as the averaged number of poloidal turns given by a magnetic field line after one toroidal loop. Equivalently, it can be written in terms of poloidal and toroidal magnetic fluxes, $\Psi_i = \int \mathbf{B}\cdot\mathrm{d}\mathbf{S}_i$ ($i =$ p, t), as

$$\iota \equiv \frac{\mathrm{d}\Psi_\mathrm{p}}{\mathrm{d}\Psi_\mathrm{t}}. \tag{1.4}$$

The rotational transform can be induced in several ways [24], for instance by (a) driving a toroidal current, by (b) elongating the flux surfaces and making them rotate poloidally in the toroidal direction or by (c) making the magnetic axis non-planar.

The way in which the rotational transform is produced defines the two main lines of research in magnetically confined plasmas: the tokamak and stellarator concepts. In the former, part of the magnetic field (its poloidal component) is generated by inducing a toroidal current in the plasma by transformer action. The toroidal magnetic field is created by external field coils and so these machines are toroidally invariant. However, the discreteness of the toroidal coils and the use of magnetic field perturbations to mitigate edge localized modes [25] has renewed the interest of the tokamak community in 3 dimensional magnetic topologies. In the stellarator

case the magnetic field is completely determined by external coils and takes advantage of the methods (b) and (c) to make $\iota \neq 0$, although a small parallel current can exist. There are several kinds of stellarator [3]. For instance, Heliotrons/torsatrons (LHD, W7-A) use a planar magnetic axis with a toroidal winding of elongated flux surfaces, i.e. surfaces with a non-circular-shaped minor cross section. On the other hand, heliac and helias configurations take advantage of both flux elongation and helical winding of the magnetic axis. The helias (helical advanced stellarator, e.g. W7-AS [26]) is designed to reduce the Shafranov shift, i.e. the outward shift of the centre of flux surfaces induced by plasma pressure, by reducing the Pfirsch-Schlüter current, see e.g. [27]. The heliac is characterized by a bean-shaped minor cross section with favourable stability properties in the infinite aspect-ratio, helical-axis straight stellarator limits [28]. Such stability might, nonetheless, be spoilt in actual toroidal configurations as the presence of low-order rational surfaces (i.e. surfaces in which $\iota = m/n$ for $m, n \in \mathrm{Z}$ and small) may destroy the existence of nested toroidal surfaces as the pressure increases, see e.g. [29]. The use of helical coils [30] provides flexibility and control in the ι profile and its shear, and thus in the location of low-order rational surfaces, see e.g. [31]. This thesis has been performed in a flexible heliac device, the TJ-II stellarator. The description of the machine and its characteristics is left to section 1.3.

As a consequence of its magnetic field generation the tokamak is -ideally- invariant under toroidal transformations, whilst the stellarator is a completely three-dimensional device. This difference has a deep impact on the physics of tokamak and stellarator devices, see e.g. [24]. Since the latter does not require a toroidal plasma current it can be operated in steady-state, is less affected by magneto-hydrodynamic (MHD) instabilities and avoids current disruptions or density limits [32], etc. However, the complicated magnetic field topology makes them technically complex to build (see, e.g., the sketch of the W7-X stellarator magnetic field coils in figure 1.2). The strength of such a magnetic field is generally decomposed into poloidal θ and toroidal ϕ angles as

$$\frac{B}{B_0} = 1 + \sum_{m,n} \left[\varepsilon_{\mathrm{t}}^{(m,n=0)}(\rho)\cos(m\theta) + \varepsilon_{\mathrm{h}}^{(m,n)}(\rho)\cos(m\theta - n\phi) \right]. \tag{1.5}$$

The first term in the summation corresponds to toroidal components, which are also present in a tokamak configuration; the second term is characteristic of a helical variation of the magnetic field strength. As a result of this helical ripple, ε_{h}, there are generally unconfined particles in the helical traps, thus increasing the neoclassical transport well to above the tokamak level (here the term 'neoclassical' refers to transport processes produced by Coulomb encounters in the presence of a toroidal magnetic field, see chapter 2). Indeed, new regimes of collisionality appear in stellarators [3], e.g. the so-called $1/\nu$ and $\sqrt{\nu}$ regimes, which are absent in tokamaks. The resultant neoclassical radial diffusion coefficients depend on the mass and charge of the species and thus, for equal temperatures, the fluxes of particles are different for each species. As a consequence the total flux of charge on a surface is not zero, thereby violating ambipolarity. The radial electric field, E_r, is adjusted to reduce the ion (electron) particle transport to the electron (ion) level. This condition on E_r, together with parallel momentum conservation, sets the rotation in stellarators, in the absence of external input of momentum. Furthermore, the lack of toroidal symmetry impedes the development of the large toroidal flows [33] (close to sonic)

frequently observed in tokamaks.

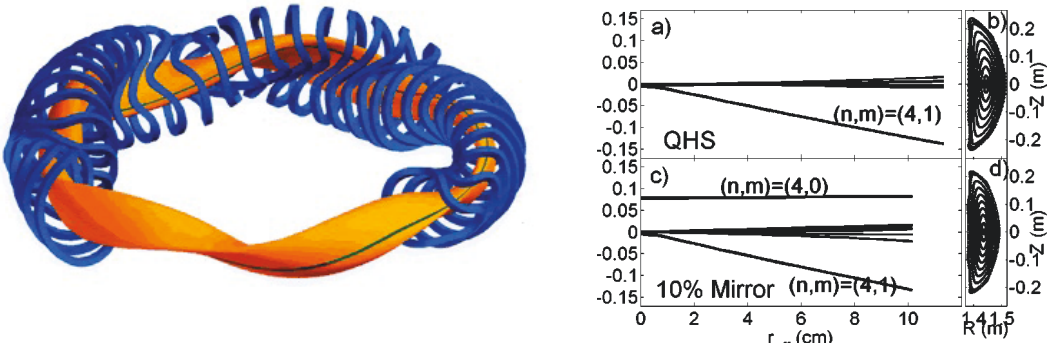

Figure 1.2. (Left) Schematic of Wendelstein 7-X superconducting modular coils (in blue) and plasma (orange), from `http://www.ipp.mpg.de/ippcms/eng/pr/forschung/w7x`. (Right) Magnetic field spectrum of the Helically Symmetric eXperiment (HSX) in Hamada coordinates, from reference [34]. (a) Quasi-Helically Symmetric (QHS) and (c) mirror configurations of HSX. The magnetic surfaces in a vertical cut at the elliptical symmetry plane are also shown for (b) the QHS and (d) the mirror configurations.

All these detrimental neoclassical effects may be greatly reduced when the stellarator is omnigenous, meaning that the time-averaged radial guiding centre drift vanishes for the trapped population, and thus, trapped orbits are confined as in a tokamak (see e.g. reference [35] for an introduction to the subject). The omnigenety condition implies that the maximum and minimum of the magnetic field strength B form closed curves on a magnetic surface, rather than isolated points as in a classical stellarator. Two main approaches are considered then: quasi-symmetry and quasi-isodynamicy. In the latter, contours of B close poloidally and the bootstrap current is minimized. The W7-X helias, currently under construction, is the first attempt to build a nearly quasi-isodynamic device, see the left column of figure 1.2. On the other hand, quasi-symmetry is achieved if the magnetic field strength (1.5) has a single component[4], $M\theta - N\phi$, see e.g. [37]. Then, the contours of B in the (θ, ϕ) plane are straight lines, see figure 1.3 in [35] and figure 3 in [38]. In contrast, in iso-dynamic stellarators the contours of B are not straight lines. There are three general classes of quasi-symmetry: poloidal ($M = 0$), toroidal ($N = 0$) and helical (both N and M nonzero). The National Compact Stellarator Experiment (NCSX), which was partially built in Princeton [39] but not finished, is a quasi-toroidal stellarator and is almost axisymmetric, thus closely related to a tokamak. The Helically Symmetric Experiment (HSX), currently in operation at the University of Wisconsin-Madison [40], is a quasi-helical stellarator with a dominant ($N = 4, M = 1$) component, see the right column of figure 1.2. Quasi-symmetric devices are designed to reduce the neoclassical viscosity in the direction of symmetry and thus to increase the flow in that direction [38]. Such a reduction of the neoclassical damping in the direction of symmetry has been confirmed by experiment [34]. The concept of neoclassical viscosity and its effect on rotation is explained in chapter 2.

[4] More precisely, if it has a single helical component in Boozer or Hamada coordinates, see e.g. [36]. The Hamada coordinates are introduced in sections 2.3 and A.3.

The following section is concentrated on the TJ-II flexible Heliac stellarator, in which this thesis has been carried out. First, a brief description of the machine is provided, namely the set of coils, the magnetic configurations, heating systems and diagnostics equipment. Finally, some of the most salient and recent results are highlighted, e.g. wall conditioning, improved confinement regimes and flow dynamic.

1.3 The TJ-II stellarator

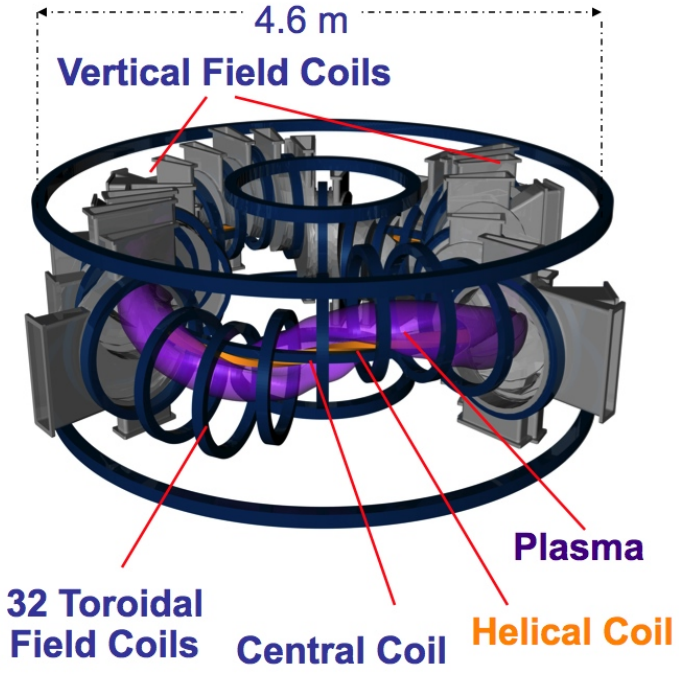

Figure 1.3. Schematic diagram of TJ-II coils and part of the vacuum chamber.

TJ-II (Torus JEN II) is a 4-period stellarator of the heliac type, located at the National Fusion Laboratory at CIEMAT (Madrid, Spain), in operation since 1997 [41]. It has a major radius $R_0 = 1.5$ m and average minor radius $a = 0.2$ m. The magnetic field of about 1 T is generated by a system of poloidal, toroidal and vertical field coils, including two helical coils, see figure 1.3. The vertical excursion of the toroidal fields in a helical axis provides the required torsion of the magnetic axis to make $\iota \neq 0$. The central conductors, which generate the poloidal magnetic field, consist of a circular coil and two helical coils which are wrapped around the central conductor. These coils provide a high flexibility in the rotational transform, which can be varied over a wide range, see e.g. figure 3 of reference [42]. The vacuum chamber is composed by 32 stainless-steel sectors with a total of 92 ports. At present, one graphite limiter and one liquid lithium limiter, positioned in equivalent sectors of the machine, can be used to limit the extent of the plasma [43]. Hydrogen, deuterium or helium plasmas are created and heated by 2 gyrotrons operated at 53.2 GHz (2^{nd} harmonic, X-mode polarization, $\text{P}_{\text{ECRH}} \leq 600$ kW). During this heating phase central electron densities, $\text{n}_e(0)$, and temperatures, $\text{T}_e(0)$, up to 1.7×10^{19}

m^{-3} and 1 keV, respectively, are achieved. In addition, plasmas can be maintained by two tangential Neutral Beam Injectors (NBI), each providing $\leq$500 kW. As a result, plasmas with $n_e(0) \leq 5 \times 10^{19}$ m^{-3} and $T_e(0) \leq$400 eV are attained.

The magnetic configurations in TJ-II are labelled with the currents in the central, helical and vertical field coils, i.e. $I_{cc}\_I_{hc}\_I_{vc}$. The resultant magnetic surfaces have bean-shaped cross sections, see figure 1.4. The hard-core, i.e. the region of the vacuum chamber that wraps around the central conductors, acts as a helical limiter, and no natural ergodic zones appear outside the last closed magnetic surface. In this thesis two main magnetic configurations have been utilized: 100_44_64 and 100_40_63. The vacuum rotational transform, ι, covers the ranges $1.55 \leq \iota \leq 1.65$ and $1.509 \leq \iota \leq 1.608$, and the volumes are 1.098 and 1.043 m^3, respectively. These two configurations have been studied in references [44] and [45] from the neoclassical point of view. For similar plasma profiles and momentum input, no qualitative differences are predicted in the flows within the surface.

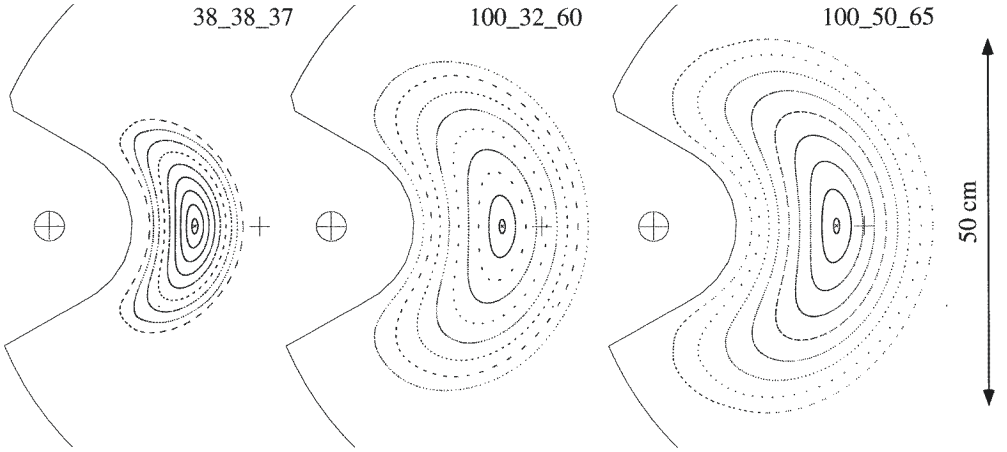

Figure 1.4. Poloidal cuts of TJ-II vacuum magnetic surfaces, from reference [41]. The volume and plasma indentation can be varied over a wide range.

TJ-II is equipped with a large variety of diagnostics, see figure 1.5. The one used in this thesis is the Charge-Exchange Recombination Spectroscopy (CXRS) diagnostic [46], which makes use of a Diagnostic Neutral Beam Injector (DNBI) [47] to excite spectral lines via electron capture by fully ionised impurity ions and measure profiles of density, temperature and velocity of such impurities [48]. The CXRS diagnostic is explained separately in chapter 3. Other diagnostics utilized in this work are briefly listed next (see e.g. the book *Principles of Plasma Diagnostics* [49], or visit the web page of TJ-II [50] for specific details):

- Microwave and infrared interferometry (see e.g. [51]) provide the line-averaged electron density. Electron density and temperature profiles are measured by Thomson Scattering [52] and Helium beam [53] diagnostics in the core (with normalised radius $\rho \leq 0.6$) and edge regions, respectively. Edge electron density profiles are also obtained from an amplitude modulated reflectometer [54]. These diagnostics are combined with a Bayesian technique

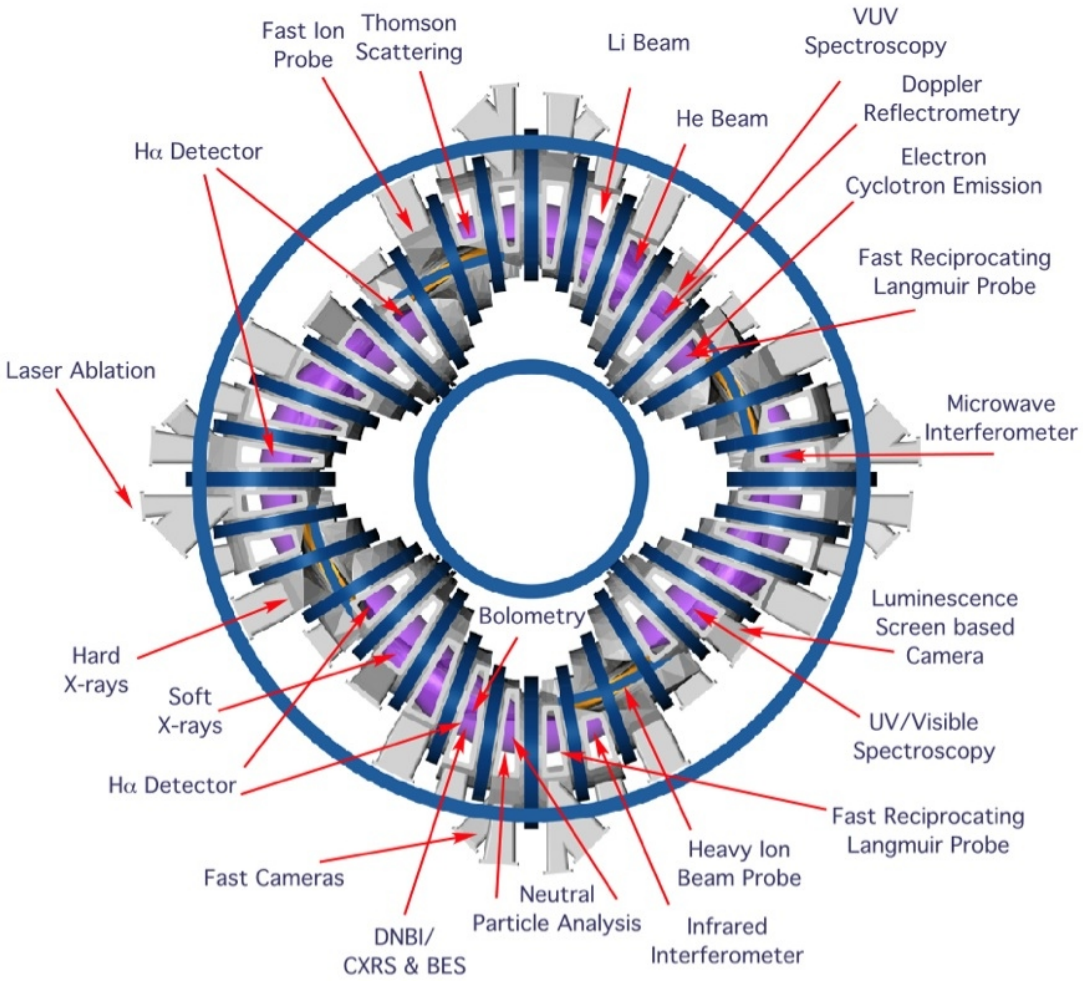

Figure 1.5. Bird's eye view of TJ-II diagnostics.

[55] to provide smoothed and reliable electron density and temperature profiles at selected times along a discharge. In addition the time evolution of the central electron temperature is estimated [56] from the soft X-ray emission using the foil absorption technique, see e.g. [57].

- Line integrated ion temperatures are routinely measured by Neutral Particle Analysers (NPA) [58], while the CXRS technique gives local values of the C^{6+} temperature profile [59].
- The plasma current and diamagnetic energy are measured with Rogowski coils and diamagnetic loops [60], respectively.
- The temporal evolution of impurity content and radiation is followed using bolometers [61], a vacuum ultra-violet spectrometer [62] and a C^{4+} line emission monitor. In addition, H_α line emission is monitored by photodiodes installed in different toroidal locations [63].
- Finally, a number of rotation diagnostics are utilized for comparison with the impurity velocity profiles obtained in this thesis: passive spectroscopy provides non-localized values of poloidal [64] and toroidal [65] impurity rotation. Profiles of the plasma electrostatic

potential –and thus of the radial electric field– are measured by the Heavy Ion Beam Probe (HIBP) [66]. In addition, the perpendicular rotation of the turbulence, dominated by the $\mathbf{E} \times \mathbf{B}$ rotation, is measured with Doppler Reflectometry [67].

TJ-II has been operated under several first wall conditions [68, 69], with the aim of improving and controlling the plasma-wall interaction (PWI). Since 2008 the boronization and lithiumization of the first wall has permitted considerable improvements in density control and plasma confinement [70–72]. In particular, the lithium coating has allowed central electron densities of $n_e \leq 0.8 \times 10^{20}$ m^{-3} and line-averaged densities of $\bar{n}_e \leq 5 \times 10^{19}$ m^{-3} [73, 74] to be achieved. Under these wall conditions 'bell' type profiles with strong pressure gradients and enhanced central confinement appear, accompanied by central impurity accumulation [75, 76]. Alternatively, a broader 'dome' like emissivity profile characterized by a lower central Z_{eff} can develop under certain circumstances. However, the larger ratio of edge to core emissivity found in the dome profiles make them prone to radiative collapse [77]. Transitions between both emissivity profiles develop spontaneously or are triggered by external gas puffing. These two profiles will be used in chapter 5 to scan different main ion collisionalities and parallel ion-impurity friction forces.

In addition to such PWI studies and their impact on transport and confinement, another important line of research in TJ-II is the dynamics of flows [74] and their relation with improved confinement regimes [71, 78]. A confinement transition in low density, ECRH plasmas (see, e.g. reference [79], and references therein) is observed to be associated with the development of a sheared radial electric field at the edge of TJ-II plasmas [80, 81]. On the other hand, a spontaneous transition from low- to high-confinement mode is observed in higher density, NBI-heated plasmas [71], concomitant with the formation of a E_r shear layer [72]. In both low and high density transitions, turbulent phenomena arise [82–84], showing a close relation with the temporal evolution of the flow [85] and the plasma gradients [86]. It has been recently shown [87] that the emergent turbulence-related features at the low density transition can be understood as a consequence of a reduction in the neoclassical poloidal viscosity, when the E_r-root is changed. However, the mechanisms responsible for the L-H transition and the formation of a E_r shear layer are still unknown.

This thesis contributes to the above rotation studies and their relation to transport with an experimental and theoretical analysis of the impurity equilibrium flow in both parallel and perpendicular directions.

CHAPTER 2

PLASMA ROTATION

As introduced in the summary, plasma rotation has become one of the key ingredients of fusion plasma performance after the discovery of a reduction of turbulence and transport [88] through a sheared $E \times B$ rotation. With regard to stability, large toroidal rotations can stabilize resistive wall modes and neoclassical tearing modes. For these reasons, the physics of toroidal momentum transport, and the so-called intrinsic rotation, have become a very active area of research, mainly for their importance in the operation of a reactor plasma, for which the external torque will be negligible [89]. On the other hand, parallel flows give rise to currents that are a fundamental part of the stellarator MHD equilibrium in high-beta reactor-relevant plasmas, see e.g. ref. [27]. Firstly, the Pfirsch-Schlüter current can cause a radial (Shafranov) shift of magnetic surfaces as the pressure gradient increases (see e.g. chapter 3 of ref. [3]). Secondly, the bootstrap current carries a net toroidal current and can potentially change the iota profile. Therefore, experimental validation of plasma flows and currents models is of considerable importance.

In this chapter the rotation pattern of different particle species is derived following a fluid description, see e.g. [90]. Perpendicular flows are set by the $E \times B$ flow and the different diamagnetic velocities of each species. Simultaneously, the total flow must be tangent to flux surfaces. Next, the velocity field is shown to be incompressible, i.e. divergence-free. The incompressibility condition results from particle number conservation with constant density on flux surfaces. Then, parallel flows can be split into Pfirsch-Schlüter and parallel mass (carrying a net toroidal current) flows. The former arises in response to the compressibility of the perpendicular flow and carries no net toroidal current. With this scheme the incompressible velocity field, $\mathbf{u} = E\mathbf{e}_\vartheta + \Lambda\mathbf{B}$,[1] consists of perpendicular, Pfirsch-Schlüter and parallel mass flow components and is fully determined by two flux functions, $E(\rho)$ and $\Lambda(\rho)$, related with the radial electric field and the bootstrap current. Note that flow incompressibility follows from the usual neoclassical (and gyrokinetic) ordering schemes but it neither assumes nor implies flows to be of *neoclassical origin*.

The determination of the flux constants E and Λ is the task of any transport theory. These

[1] This expression for an incompressible velocity field will be derived latter on sections 2.2 and 2.3, and is included here to ease the reading. It is noted that the Hamada poloidal vector, $\mathbf{e}_\vartheta$, encapsulates the geometrical part of the perpendicular and Pfirsch-Schlüter flows.

two constants are obtained from the poloidal and parallel momentum balances of the different species after requiring charge and momentum conservation, respectively. In non quasi-symmetric stellarators the fluxes of charge of the different species are not intrinsically ambipolar, i.e. they are not equal for an arbitrary value of the radial electric field. Thus, the radial electric field self adjusts so as to conserve the total flux of charge through each magnetic surface, see e.g. [3, 33]. Consequently, the inclusion of the lowest ordered forces –such as collisions or mirror forces– is sufficient to predict the flow of mass along flux surfaces in stellarators[2]. This framework is known as the neoclassical (NC) transport theory, which extends classical Coulomb scatterings to include the toroidal geometry of magnetic confinement devices; the latter give rise to new particles drifts, mirror effects and trapping in magnetic wells, see e.g. references [22, 92]. In contrast, the toroidal symmetry of tokamak devices causes the poloidal and parallel balances be degenerated at lowest order, so that only the poloidal component of the flow is neoclassically damped [22]. Therefore, second order forces -such as micro instabilities, finite orbit effects, etc.– must be accounted for when predicting the toroidal velocity –or equivalently the radial electric field. The adequate framework to describe plasma rotation in tokamaks is then the gyrokinetic theory, which includes self-consistent electromagnetic fluctuations. Such processes will not be considered in this work, so we restrict ourselves to the NC framework.

In the so-called moments equation approach (or moments method) to NC theory [92] a linear relation between fluxes and thermodynamic forces and flows is established through viscosity coefficients, see e.g. [93]. The viscous coefficients are obtained as projections of the pressure anisotropy tensor, which is computed after solving the Drift Kinetic Equation (DKE) [94]. The complicated magnetic field topology in stellarators impedes general analytical solutions of the DKE and so numerical codes such as the Drift Kinetic Equation Solver (DKES) [95] are required. In this chapter, the viscosity coefficients calculated with DKES [93, 96] are compared with semi-analytic expressions that are valid only for certain plasma parameter ranges [97–99].

Once the viscosity coefficients are obtained, the flow of mass along flux-surfaces is completely determined -i.e., the flux constants E and Λ. However, the above view relies on the incompressibility of flows, which follows from a particle density constant on flux-surfaces. Such an assumption holds for electron and ions at lowest order, but may fail when considering medium to high Z impurities, see e.g. [100]. In this case a return impurity flow must appear to account for the impurity density compression, causing the parallel mass flow of impurities to differ from the that of bulk ions. Since plasma rotation is typically monitored through impurity rotation [48, 101], an understanding of impurity flows and their deviations from incompressibility is desirable. Furthermore, the fact that impurity density inhomogeneities can alter the radial transport of impurities [100, 102] makes the understanding of these inhomogeneities particularly relevant.

In this chapter, we first revisit the kinetic and fluid descriptions of a strongly magnetized plasma in order to lay down the basis for the so called momentum equation approach to the neoclassical theory. Next, the structure of an incompressible flow is addressed in section 2.2, with some examples of the Pfirsch-Schlüter flow in the TJ-II stellarator. After that, attention is

[2]The agreement with the experiments is fine at least in the core region, $r/a < 2/3$, where turbulence is not dominant, see e.g. [91].

focused on the viscous and friction forces, which in the fluid picture, are responsible for particle transport and damping of flows. In addition, friction with neutrals is considered as a sink of momentum. Numerical calculations for the viscosity coefficients, damping times and friction with neutrals using analytical expressions, and its comparison with DKES, are presented in section 2.3. Finally, the possibility of an impurity density variation within a surface, and thus of a compressible impurity flow, is briefly introduced in section 2.4.

2.1 From kinetic to fluid description

[In this subsection we mostly follow chapter 2 of reference [22].] Let $f_s(\mathbf{x}, \mathbf{v}, t)$ be the distribution function of particle species s, defined as the number of particles of that species per unit of volume in the phase space (in the volume element $\mathrm{d}\mathcal{V} = \mathrm{d}^3\mathbf{x}\mathrm{d}^3\mathbf{v}$) near the point $\mathbf{z} = (\mathbf{x}, \mathbf{v})$ at the time t. Since the distribution function is the number density of particles in the phase space, it obeys the conservation equation

$$\frac{\partial f_s}{\partial t} + \frac{\partial}{\partial \mathbf{z}} \left(\dot{\mathbf{z}} f_s \right) = 0. \tag{2.1}$$

Here, upper-dot stands for total time derivative, i.e. $\dot{\mathbf{z}} = (\dot{\mathbf{x}}, \dot{\mathbf{v}}) = (\mathbf{v}, \mathbf{a})$, with $\mathbf{v}$ and $\mathbf{a}$ the particle velocity and acceleration, respectively. In a magnetized plasma the acceleration is given by the Lorentz force,

$$\dot{\mathbf{v}} = \frac{e_s}{m_s} \left(\mathbf{E} + \mathbf{v} \times \mathbf{B} \right), \tag{2.2}$$

with m_s and e_s the mass and charge of the species s, and $\mathbf{E}$ and $\mathbf{B}$ the large-scale –compared to the Debye length– electric and magnetic fields. With (2.2), the continuity equation (2.1) is known as the Vlasov equation. The effect of short-range electromagnetic fluctuations (collisions) on the distribution function are introduced by a collision operator,

$$\left. \frac{\partial f_s}{\partial t} \right|_{\text{collisions}} \equiv C_s(f_s) = \sum_r C_{sr}(f_s, f_r), \tag{2.3}$$

which is the sum of contributions from collisions with each particle species, including self-collisions (see, e.g., chapter 3 in reference [22]). With the term (2.3) the kinetic equation (2.1) has the form of a Fokker-Planck equation, i.e.

$$\frac{\partial f_s}{\partial t} + \mathbf{v} \cdot \nabla f_s + \frac{e_s}{m_s} \left(\mathbf{E} + \mathbf{v} \times \mathbf{B} \right) \cdot \frac{\partial f_s}{\partial \mathbf{v}} = C_s(f_s). \tag{2.4}$$

Here, we have used the divergence-free of the phase-space flow of a Hamiltonian system, $\nabla \cdot \dot{\mathbf{z}} = 0$ (Liouville's theorem).

In the derivation of a transport theory for a strongly magnetized plasma [90] it is assumed that the fastest movement of a particle is the gyration around the magnetic field line, i.e. the gyromotion. Thus, the gyro-frequency of a charged particle

$$\Omega_s = \frac{e_s B}{m_s}, \tag{2.5}$$

is much larger than any other frequency characterizing the plasma, e.g. the transit frequency, $\omega_{Ts} = v_s/L$, or the typical collision frequency, ν_s, i.e.

$$\omega_{Ts} \ll \Omega_s, \quad \nu_s \ll \Omega_s. \tag{2.6}$$

Here, $v_s = (2T_s/m_s)^{1/2}$ is the thermal velocity of species s, T_s is its temperature and L is the characteristic length of plasma parameters variation. The latter is usually taken as the connection length, $L \equiv L_\parallel = R_0/\iota$, or the plasma minor radius, $L \equiv L_\perp \sim a$. Note that the orderings given by (2.6) do not specify the ratio of collision and transit frequencies,

$$\hat{\nu}_s = \frac{\nu_s}{\omega_{Ts}}, \tag{2.7}$$

where $\hat{\nu}_s$ is the normalized collision frequency or collisionality and depends on plasma parameters. For $\hat{\nu}_s \gg 1$ particle species s are in the collisional or Pfrisch-Schlüter regime, which is typical for the main ions at the edge of fusion plasmas or for heavy impurity ions ($Z \gg 1$) all across the plasma. When the collisionality is such that $\varepsilon_t^{3/2} \ll \hat{\nu}_s \ll 1$[3] [98], transport is dominated by circulating particles, which are in the so-called plateau regime. Finally, for small values of the collisionality, $\hat{\nu}_s \ll 1$, particles become collisionless and thus mirror forces dominate. Particles are trapped in magnetic mirrors and describe banana orbits, hence the name banana regime. In this regime, a $1/\hat{\nu}_s$ dependence of transport coefficients appears in stellarators [3] thus greatly enhancing the level of NC transport.

With the ordering (2.6) the Larmor radius

$$\rho_s = \frac{v_s}{\Omega_s}, \tag{2.8}$$

must be smaller than the plasma scale length L –normally $L \equiv L_\perp \leq L_\parallel$. Therefore,

$$\delta_s = \frac{\omega_{Ts}}{\Omega_s} = \frac{\rho_s}{L_\perp} \ll 1 \tag{2.9}$$

follows, and the spatial dependence of the distribution function f_s can be expanded in powers of the small parameter δ_s,

$$f_s = f_{s0} + f_{s1} + \mathcal{O}(\delta_s^2), \tag{2.10}$$

where $f_{s1} \sim \delta_s f_{s0}$ represents a small deviation from local thermodynamic equilibrium, which is characterized by a Maxwellian distribution function, i.e.

$$f_{s0} = \frac{n_{s0}}{\pi^{3/2} v_s^3} \exp\left(-\frac{\epsilon_s}{T_{s0}}\right) = f_{s\mathrm{M}} \exp\left(-\frac{e_s \Phi_0}{T_{s0}}\right), \tag{2.11}$$

with $\epsilon_s = m_s v^2/2 + e_s \Phi_0$ the total particle energy. Additionally, all plasma parameters can be expanded in terms of δ_s, e.g. the density of particle species s, $n_s(\mathbf{x}) = n_{s0}(\rho) + n_{s1} + \mathcal{O}(\delta_s^2)$, the electrostatic potential $\Phi(\mathbf{x}) = \Phi_0(\rho) + \Phi_1 + \mathcal{O}(\delta_s^2)$,[4] and so on. Here, the sub-index 0 indicates the flux-surface averaged of these quantities, e.g. $\Phi_0 = \langle \Phi \rangle$.

Throughout this chapter, the so called 'moment' or 'fluid' approach is considered, see e.g. section 3 of reference [92]. It consists of taking moments of the kinetic equation (2.4), which establish relations among macroscopic quantities such as the density, temperature, pressure,

[3] Here, ε_t is the toroidal ripple of the magnetic field strength, see equation (1.5).

[4] The electric field is usually composed of electrostatic and inductive terms,

$$\mathbf{E} = -\nabla\Phi - \frac{\partial \mathbf{A}}{\partial t}, \tag{2.12}$$

with $\mathbf{A}$ the vector potential and Φ the electric potential. The second term, important in the inductive phase of a tokamak, can be neglected in a stellarator with stationary magnetic fields and so $\mathbf{E} = -\nabla\Phi$.

etc. Here, the 'moment' is defined as the integral over velocity space of a certain quantity (or equation) multiplied by different functions of the particle velocity $\mathbf{v}$. For instance, the particle density, flow velocity and pressure of the species s, are obtained from the zero, first and second moments of the distribution function f_s, as

$$n_s = \int f_s \mathrm{d}^3\mathbf{v}, \tag{2.13a}$$

$$n_s\mathbf{u}_s = \int \mathbf{v} f_s \mathrm{d}^3\mathbf{v}, \tag{2.13b}$$

$$p_s = \frac{1}{3} m_s \int |\mathbf{w}_s|^2 f_s \mathrm{d}^3\mathbf{v}. \tag{2.13c}$$

Here, we have introduced the relative velocity of a particle respect to the species mean value as $\mathbf{w}_s = \mathbf{v} - \mathbf{u}_s$. Moments of the collision operator are identified as momentum and heat exchange terms -friction forces-, i.e.

$$\mathbf{F}_s = m_s \int \mathbf{v} C_s(f_s) \mathrm{d}^3\mathbf{v}, \tag{2.14a}$$

$$Q_s = \frac{1}{2} m_s \int |\mathbf{w}_s|^2 C_s(f_s) \mathrm{d}^3\mathbf{v}. \tag{2.14b}$$

The continuity equation is obtained from the zero*th* velocity moment of the kinetic equation (2.4),

$$\frac{\partial n_s}{\partial t} + \nabla \cdot (n_s \mathbf{u}_s) = 0. \tag{2.15}$$

Similarly, the first velocity moment of the Fokker-Planck equation yields the conservation of momentum,

$$m_s n_s \frac{\partial \mathbf{u}_s}{\partial t} + m_s n_s \mathbf{u}_s \cdot \nabla \mathbf{u}_s = n_s e_s \left(\mathbf{E} + \mathbf{u}_s \times \mathbf{B}\right) + \mathbf{F}_s - \nabla p_s - \nabla \cdot \overleftrightarrow{\pi}_s. \tag{2.16}$$

Note that no external sources of particle and momentum are considered in equations (2.15) and (2.16). The viscosity tensor in (2.16) is defined as

$$\overleftrightarrow{\pi}_s = m_s \int \left(\mathbf{w}_s \mathbf{w}_s - \frac{1}{3} w_s^2 \overleftrightarrow{I} \right) f_s \mathrm{d}^3\mathbf{v}, \tag{2.17}$$

where $\overleftrightarrow{I}$ is the unity tensor. The second term in (2.17) is just the scalar pressure. The total pressure tensor is therefore: $\overleftrightarrow{P}_s = \overleftrightarrow{\pi}_s + p_s \overleftrightarrow{I}$. Since momentum is conserved in Coulomb collisions the friction forces satisfy

$$\sum_s \mathbf{F}_s = 0. \tag{2.18}$$

In the expansion of the distribution function in powers of δ_s, equation (2.10), the zero*th* order contribution f_{s0} does not carry a net flow. Hence, besides the ordering (2.9), small flows are considered through this document, i.e.

$$\mathbf{u}_s = \mathbf{u}_{s1} + \mathcal{O}(\delta_s^2) \sim \delta_s v_s, \tag{2.19}$$

which follows from equations (2.13b), (2.10) and (2.11). This is known as the drift ordering, and implies that the flow velocity is of the order of the diamagnetic velocity,

$$\mathbf{u}_{s,\mathrm{diam}} = \frac{1}{n_{s0} e_s} \frac{\mathbf{B} \times \nabla p_{s0}}{B^2} \sim \frac{m_s}{\Omega_s} \frac{T_{s0}}{L_\perp} \sim \delta_s v_s. \tag{2.20}$$

In particular, the radial derivative of the zero*th*-order electric potential is assumed to be comparable with the electron temperature gradient, i.e. $e\Phi_0' \sim T_{e0}'$, where the prime denotes radial derivative ($'\equiv \mathrm{d}/\mathrm{d}\rho$). The ordering (2.19) has been extensively confirmed in TJ-II, see e.g. references [66, 72, 103–105].

Then, the steady-state continuity equation (2.15) is, to leading order,

$$0 = \nabla\cdot(n_s\mathbf{u}_s) = \nabla\cdot(n_{s0}\mathbf{u}_{s1}) + \mathcal{O}(\delta_s^2), \tag{2.21}$$

Thus, particle flow is incompressible $\nabla\cdot\mathbf{u}_s = 0$. A similar relation can be derived for the heat flow $\mathbf{q}_s$ if inter-species heat exchange is neglected [22]. With the drift ordering (2.19) the inertial term in equation (2.16) results

$$m_s n_s \frac{\partial \mathbf{u}_s}{\partial t} \sim m_s n_s \Omega_s v_s \delta_s^2, \tag{2.22a}$$

$$m_s n_s \mathbf{u}_s\cdot\nabla\mathbf{u}_s \sim n_s \frac{\delta_s^2 T_s}{L}. \tag{2.22b}$$

The contribution of the stress tensor $\nabla\cdot\overleftrightarrow{\pi}_s$[5] and friction force $\mathbf{F}_s$ can be roughly estimated as

$$\nabla\cdot\overleftrightarrow{\pi}_s \sim p_s\tau_{ss}\frac{\mathbf{u}_s}{L^2} \sim \frac{n_s T_s}{L}\frac{\delta_s}{\hat{\nu}_{ss}}, \tag{2.23a}$$

$$\mathbf{F}_s \sim m_s n_s \nu_s \mathbf{u}_s \sim \frac{n_s T_s}{L}\hat{\nu}_s\delta_s, \tag{2.23b}$$

where equation (2.7) has been used. Here the double sub-index indicates self-collisions, e.g. τ_{ss} is the self-collision time of particle species s. In contrast a single sub-index stands for the total collisionality that includes collisions with several particle species. Expressions for the viscosity and friction will be provided throughout this chapter.

According to the above estimations, equations (2.19) to (2.23), the flow patterns of the different species present in the plasma (main ions, electrons and impurity ions) deviate from the $E\times B$ flow and from each other through their different diamagnetic velocity components and parallel momentum balances to order $\sim\mathcal{O}(\delta_s)$, as will be shown in the following sections. In section 2.2, after determining the perpendicular velocity component, the incompressibility condition (2.21) is utilized to split parallel flows into Pfirsch-Schlüter (PS) and parallel mass flows (i.e. those carrying a net toroidal current). The former arises in response to the compression of the perpendicular flow, while the latter is determined by parallel forces. As shown in section 2.3, the parallel momentum balance is dominated by the viscosity stress in low collisionality regimes, $\hat{\nu}_s \ll 1$. The viscous damping of the flows –i.e. the determination of equilibrium flows through viscosity– is analysed in asymptotic limits of collisionality which are semi-analytically tractable, and are compared with numerical results from the Drift Kinetic Equation Solver (DKES). Finally, deviations from flow incompressibility are studied in section 2.4. It is noted that the strong collisional coupling between main-ions and impurities, $\hat{\nu}_{zi} \gg 1$, makes parallel viscous forces on the impurities negligible when compared with parallel friction, which may result in the development of a zero*th*-order variation of the impurity density within the surface [100], i.e. $n_{z0} = n_{z0}(\rho,\theta,\phi)$. As a consequence, a return flow appear to compensate for the impurity density compression.

[5] Here we are using the collisional result for the pressure anisotropy, see equation (2.54).

2.2 Structure of first-order flows

The component of the fluid velocity perpendicular to the magnetic field direction $\mathbf{b} \equiv \mathbf{B}/B$, $\mathbf{u}_{s\perp} = \mathbf{b} \times (\mathbf{u}_s \times \mathbf{b})$, is obtained from the cross product of the magnetic field and the momentum balance equation, $\mathbf{B}\times$(2.16), to yield [90]

$$\begin{aligned} \mathbf{u}_{s\perp} &= \frac{\mathbf{E}\times\mathbf{B}}{B^2} + \frac{1}{n_{s0}e_s}\frac{\mathbf{B}\times\nabla p_{s0}}{B^2} \\ &\quad + \frac{\mathbf{b}}{\Omega_s}\times\left(\frac{\partial \mathbf{u}_s}{\partial t} + \mathbf{u}_s\cdot\nabla\mathbf{u}_s + \frac{\nabla\cdot\overleftrightarrow{\pi}_s - \mathbf{F}_s}{m_s n_{s0}}\right). \end{aligned} \tag{2.24}$$

From equations (2.22) and (2.23), the terms in parenthesis appear as a small correction to the dominant $\mathbf{E}\times\mathbf{B}$ and diamagnetic terms,

$$\frac{\mathbf{b}}{\Omega_s}\times\left(\frac{\partial \mathbf{u}_s}{\partial t} + \mathbf{u}_s\cdot\nabla\mathbf{u}_s + \frac{\nabla\cdot\overleftrightarrow{\pi}_s - \mathbf{F}_s}{m_s n_{s0}}.\right) \sim v_s\delta_s^2\left(1+\delta_s+\hat{\nu}_{ss}^{-1}+\hat{\nu}_s\right),$$

and thus will be neglected henceforth. Then the first order perpendicular velocity is tangential to flux-surfaces and is recast as

$$\mathbf{u}_{s\perp} = E_s\frac{\mathbf{B}\times\nabla\rho}{B^2} + \mathcal{O}(\delta_s^2), \tag{2.25}$$

with the flux-surface constant $E_s(\rho)$ given by

$$E_s(\rho) = \frac{\mathrm{d}\langle\Phi\rangle}{\mathrm{d}\rho} + \frac{1}{\langle n_s\rangle e_s}\frac{\mathrm{d}\langle p_s\rangle}{\mathrm{d}\rho}. \tag{2.26}$$

In addition, a flux-surface averaged radial electric field is defined as[6]

$$E_r = -\frac{\mathrm{d}\langle\Phi\rangle}{\mathrm{d}\rho}\langle|\nabla\rho|\rangle. \tag{2.27}$$

The form of the parallel flow is obtained from the steady-state particle density conservation (2.15) with the perpendicular flow given by (2.25),

$$\mathbf{B}\cdot\nabla\left(\frac{n_{s0}u_{s\|}}{B}\right) = -E_s(\rho)\mathbf{B}\times\nabla\rho\cdot\nabla\left(\frac{n_{s0}}{B^2}\right). \tag{2.28}$$

If the density is constant on flux surfaces, flows become incompressible, $\nabla\cdot\mathbf{u_s} = 0$, and a local parallel flow (Pfirsch-Schlüter) must compensate for the compression of the perpendicular flows. The general expression of the parallel flow that preserves the incompressibility condition is then

$$\mathbf{u}_{s\|} = (E_s h + \Lambda_s)\,\mathbf{B}, \tag{2.29}$$

with the function $h(\rho,\theta,\phi)$ satisfying equations 2.28 and 2.29 for a constant density, i.e.[7]

$$\mathbf{B}\cdot\nabla h = -\mathbf{B}\times\nabla\rho\cdot\nabla\left(\frac{1}{B^2}\right) = \frac{2}{B^2}\mathbf{B}\times\nabla\rho\cdot\nabla\left(\ln B\right), \tag{2.30}$$

[6] Another possible definition is $E_r \equiv -(\mathrm{d}\langle\Phi\rangle/\mathrm{d}\rho)/a$, with a the minor radius. These two definitions differ in a factor of ~ 1.2 for the 100_44_64 standard magnetic configuration in TJ-II.

[7] This function h equals the function u defined in references [33,106], or the function $-(\tilde{U}/B)$ utilised in [38,93].

The flux-constant $\Lambda_s(\rho)$ and the function h are chosen so that

$$\Lambda_s(\rho) \equiv \frac{\langle \mathbf{u}_s \cdot \mathbf{B} \rangle}{\langle B^2 \rangle}, \quad \langle hB^2 \rangle = 0. \tag{2.31}$$

In such a case, $\mathbf{u}_{\rm PS} = E_s(\rho) h \mathbf{B}$, is the well-known Pfirsch-Schlüter flow. The magnetic equation (2.30) is solved in magnetic coordinates and re-sampled in the machine ones (see the appendix A).

It is useful to define a dimensionless quantity,

$$f_{\rm PS} = -\frac{\langle B \rangle}{\langle |\nabla \rho| \rangle} hB, \tag{2.32}$$

which stores the variation of the PS flow in a magnetic surface. This dimensionless PS factor will be used to determine experimentally the flux constants $E_s(\rho)$ and $\Lambda_s(\rho)$ (see chapters 4 and 5) and is depicted in figure 2.1 for several poloidal cuts of TJ-II closed magnetic surfaces. The PS parallel flow is then obtained after multiplying such a PS factor, $f_{\rm PS}$, by the flux-surface averaged perpendicular flow. Therefore, if the diamagnetic flow is neglected against the $\mathbf{E} \times \mathbf{B}$ rotation (a valid approximation for medium to high Z-impurities), the PS flow is simply

$$u_{\rm PS} \approx \frac{E_r}{\langle B \rangle} f_{\rm PS}.$$

Values of $E_r \sim \pm 5$ kV m^{-1} are predicted [45, 107, 108] and measured [66, 72, 104, 105, 109] in TJ-II L-mode plasmas. Therefore, Pfirsch-Schlüter flows of $u_{\rm PS} \leq \pm 20$ km s^{-1} are expected in TJ-II, see figure 2.1. Note that in H-mode plasmas the radial electric field can reach $E_r \sim -15$ kV m^{-1} [72] and thus $u_{\rm PS} \sim \pm 50$ km s^{-1}.

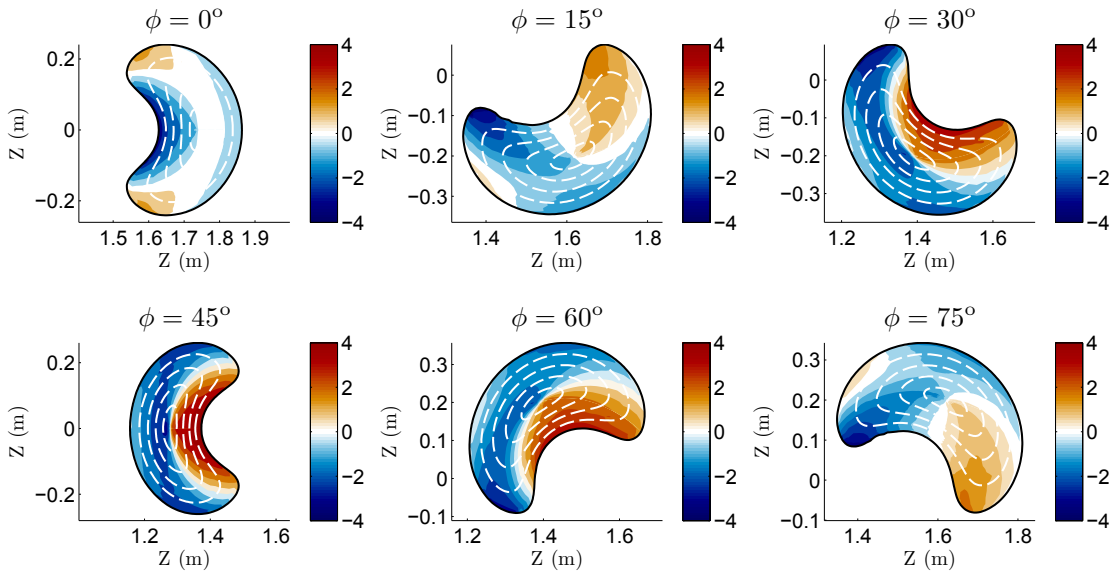

Figure 2.1. Dimensionless PS factor, $f_{\rm PS}$, for several poloidal cuts of TJ-II. Positive values will result in a parallel flow in the $\mathbf{B}$ direction for $E_s > 0$. Poloidal cuts of the magnetic surfaces $\rho = 0.2$, 0.4, 0.6 and 0.8 are shown (white dash lines). The poloidal cut of the last-closed magnetic surface is plotted in black.

The final expression for the incompressible velocity field is

$$\mathbf{u}_s = \mathbf{u}_{s\perp} + \mathbf{u}_{s\parallel} = E_s \frac{\mathbf{B}\times\nabla\rho}{B^2} + (\Lambda_s + E_s h)\,\mathbf{B} = E_s\left(\frac{\mathbf{B}\times\nabla\rho}{B^2} + h\mathbf{B}\right) + \Lambda_s\mathbf{B}, \tag{2.33}$$

which gives the variation of an incompressible flow within the surface for any values of the flux-surface constants $E_s(\rho)$ and $\Lambda_s(\rho)$ –which, nonetheless, depend on the regime of collisionality. Recall that (2.33) just relies on the orderings given in equation (2.6) and (2.19). However, as is discussed in section 2.4 and chapter 5, when medium to high Z-impurities are considered the incompressibility condition might be modified and thus new contributions to the impurity parallel flow may appear.

Before proceeding with the study of the two flux constants E_s and Λ_s, let us connect the above general equation (2.33) for an incompressible flow with the more familiar tokamak expression, as it will be required in section 2.4.

2.2.1 Flow structure in a tokamak

The magnetic field vector can be expressed in flux coordinates $(\chi, \theta_\mathrm{f}, \phi_\mathrm{f})$ (i.e. those in which magnetic field lines are straight, see section A.2 in the appendix A) as

$$\mathbf{B} = \nabla\chi\times\nabla(q\theta_\mathrm{f} - \phi_\mathrm{f}). \tag{2.34}$$

Here, $q = 1/\iota$ is the safety factor and the poloidal flux $\chi = \Psi_p/(2\pi)$ is used as the radial coordinate. The Jacobian is therefore $\sqrt{g_\mathrm{f}} = (\mathbf{B}\cdot\nabla\theta_\mathrm{f})^{-1}$.

Since a tokamak is symmetric with respect to the toroidal cylindrical angle, ϕ, all physical quantities are independent of ϕ, i.e. $\partial/\partial\phi = 0$. Therefore, if $\phi_\mathrm{f} = \phi$ is taken, the relations $\nabla\chi\cdot\nabla\phi = 0$ and $\nabla\theta\cdot\nabla\phi = 0$ follow and so $\mathbf{e}_\phi = \sqrt{g_\mathrm{f}}\nabla\chi\times\nabla\theta_\mathrm{f} \propto \nabla\phi$, see e.g. [36]. The magnetic field is then expressed in the well-known form [22]

$$\mathbf{B} = I(\chi)\nabla\phi + \nabla\phi\times\nabla\chi. \tag{2.35}$$

Here, $I = qR^2/\sqrt{g_\mathrm{f}}$ is the total poloidal current, R is the distance from the major axis to a point in the plasma and $\nabla\phi = R^{-1}\hat{\phi}$, with $\hat{\phi}$ a unitary toroidal vector. The perpendicular component of the flow, equation (2.25), is recast as

$$\mathbf{u}_{s\perp} = E_s(\chi)\frac{\mathbf{B}\times\nabla\chi}{B^2} = \omega_s(\chi)\left(R\hat{\phi} - \frac{I}{B}\mathbf{b}\right), \tag{2.36}$$

where $\omega_s(\chi) = -E_s(\chi) = -(\mathrm{d}\Phi/\mathrm{d}\chi) - (n_s e_s)^{-1}(\mathrm{d}p_s/\mathrm{d}\chi)$. To derive equation (2.36), the relation $R^2B^2 = I^2 + |\nabla\chi|^2$ is used and so

$$\mathbf{B}\times\nabla\chi = I\nabla\phi\times\nabla\chi - |\nabla\chi|^2\nabla\phi = I\mathbf{B} - \nabla\phi(I^2 + |\nabla\chi|^2).$$

The form of the parallel flow is obtained as before from particle conservation, i.e. $\nabla\cdot(n_s\mathbf{u}_{s\parallel}) = -\nabla\cdot(n_s\mathbf{u}_{s\perp})$. Since $\sqrt{g_\mathrm{f}} = (\mathbf{B}\cdot\nabla\theta_\mathrm{f})^{-1}$ and $\partial/\partial\phi = 0$, the divergence of the perpendicular particle flux is

$$\nabla\cdot(n_s\mathbf{u}_{s\perp}) = \frac{1}{\sqrt{g_\mathrm{f}}}\frac{\partial}{\partial\theta_\mathrm{f}}\left(\frac{n_s\mathbf{u}_{s\perp}\cdot\nabla\theta_\mathrm{f}}{\mathbf{B}\cdot\nabla\theta_\mathrm{f}}\right) = -\frac{1}{\sqrt{g_\mathrm{f}}}\frac{\partial}{\partial\theta_\mathrm{f}}\left(\frac{n_s\omega_s I}{B^2}\right),$$

and that of the parallel flow is

$$\nabla \cdot (n_s \mathbf{u}_{s\parallel}) = \frac{1}{\sqrt{g_{\rm f}}} \frac{\partial}{\partial \theta_{\rm f}} \left(\frac{n_s u_{s\parallel}}{B} \right),$$

so the general expression of the parallel flow in a tokamak is

$$u_{s\parallel} = \frac{I(\chi)\omega_s(\chi)}{B} + \frac{K_s(\chi)}{n_s} B. \tag{2.37}$$

The Pfirsch-Schlüter flow is obtained by relating the constant K_s to the flux-surface average $\langle \mathbf{u}_{s\parallel} \cdot \mathbf{B} \rangle$, i.e.

$$\mathbf{u}_{s\parallel} = \Lambda_s(\chi)\mathbf{B} + I(\chi)\omega_s(\chi)\mathbf{B} \left(\frac{1}{B^2} - \frac{1}{\langle B^2 \rangle} \right),$$

where $n_s = n_s(\chi)$ is been taken and Λ_s is given by equation (2.31). Note, however, that the expression (2.37) is derived without imposing $n_s = n_s(\chi)$, in contrast to the expression (2.29), which is valid for general geometries but assumes a flux-constant particle density.

The total flow (2.33) is, from equations (2.36) and (2.37),

$$\mathbf{u}_s = \omega_s(\chi) R\hat{\phi} + \frac{K_s(\chi)}{n_s}\mathbf{B}. \tag{2.38}$$

Finally the poloidal flow, $\mathbf{u}_s \cdot \nabla\theta_{\rm f}$, is related to the flux-constant K_s as

$$u_{s,{\rm p}} = \frac{K_s(\chi)}{n_s} B_{\rm p}, \tag{2.39}$$

and thus, it does not depend on the radial electric field in a tokamak (or, equivalently, the flux-constant ω_s). This reflects the equivalence of the toroidal rotation and the radial electric field in a tokamak, which are neoclassically un-damped in the absence of a toroidal ripple.

2.3 Viscous damping and equilibrium ion flows

In this section, the two flux-surface constants E_s and Λ_s are studied for the bulk ion in terms of the parallel viscosity. Here it is shown that the ambipolarity of viscous fluxes determine the averaged radial electric field [33] and hence the constant E_s –if the pressure gradient is known, see equation (2.26). In addition, the parallel mass flow $\Lambda_s\mathbf{B}$ is damped by the parallel viscosity, thus determining the equilibrium flow (2.33).

Throughout this section Hamada coordinates [110] (ψ, ϑ, ζ) are used, with $\psi = (2\pi)^{-1} \int \mathbf{B} \cdot {\rm d}\mathbf{S}_t$ the toroidal magnetic flux divided by 2π, and ϑ and ζ the poloidal and toroidal angles, respectively. The Jacobian in these coordinates is a flux-function [36], $\sqrt{g} = (4\pi^2)^{-1} {\rm d}V/{\rm d}\psi$, with V the volume enclosed by a magnetic surface. More details are given in appendix A.3. The magnetic field is expressed as

$$\mathbf{B} = \mathbf{B}_{\rm t} + \mathbf{B}_{\rm p} = \nabla\psi \times \nabla(\vartheta - \iota\zeta), \tag{2.40}$$

where $\iota = {\rm d}\chi/{\rm d}\psi$ is the rotational transform and $2\pi\chi$ is the poloidal magnetic flux. The contravariant $\mathbf{B}$-components are flux constants in the Hamada basis, i.e. $B^\zeta = \mathbf{B} \cdot \nabla\zeta = (\sqrt{g})^{-1}$

and $B^\vartheta = \mathbf{B}\cdot\nabla\vartheta = (\sqrt{g})^{-1}\iota$. The co-variant toroidal and poloidal $\mathbf{B}$-components are $\mathbf{B}_\mathrm{t} = \nabla\psi\times\nabla\vartheta = (\sqrt{g})^{-1}\mathbf{e}_\zeta$ and $\mathbf{B}_\mathrm{p} = \iota\nabla\zeta\times\nabla\psi = \iota(\sqrt{g})^{-1}\mathbf{e}_\vartheta$, respectively.

As the Jacobian is a flux-function, the Hamada basis vectors $\mathbf{e}_\vartheta$ and $\mathbf{e}_\zeta$ have a zero divergence, e.g. $\nabla\cdot\mathbf{e}_\vartheta = (\sqrt{g})^{-1}\partial_{x^i}(\sqrt{g}\mathbf{e}_\vartheta\cdot\nabla x^i) = \partial_\vartheta(\mathbf{e}_\vartheta\cdot\nabla\vartheta) = 0$. Then, the flux-surface average of $\mathbf{e}_i\cdot\nabla g$ ($i\equiv\vartheta,\zeta$) vanishes for any single-valued function g (see e.g. subsection 4.9.3 in reference [36]), i.e.

$$\langle\mathbf{e}_\vartheta\cdot\nabla g\rangle = \langle\mathbf{e}_\zeta\cdot\nabla g\rangle = 0, \tag{2.41}$$

This property is the main motivation to use the Hamada representation in this section, as most of the calculations involve flux-surface averages. Note that the flux-surface average also annihilates the operator $\mathbf{B}\cdot\nabla$, i.e. $\langle\mathbf{B}\cdot\nabla g\rangle = 0$.

The equilibrium ion flow (2.33) is written in the Hamada basis as [20, 84]

$$\mathbf{u}_\mathrm{i} = E_i(\psi)\mathbf{e}_\vartheta + \Lambda_i(\psi)\mathbf{B}, \tag{2.42}$$

where the constant $E_i(\psi)$ is given by equation (2.26) with $\rho\equiv\psi$ as flux label. The Hamada poloidal vector encapsulates the perpendicular and Pfirsch-Schlüter flow components, since the relations $\mathbf{e}_{\vartheta\perp} = \mathbf{B}\times\nabla\psi/B^2$ and $\mathbf{e}_\vartheta\cdot\mathbf{b} = hB(\mathrm{d}\psi/\mathrm{d}\rho)$ follow from equations (2.40) and (2.30), see subsection A.3.1.

In the case of a pure electron-ion plasma the time evolution of the ion flow is obtained from the surface-average of the parallel force balance (2.16) summed over species and projected over $\mathbf{B}$ and $\mathbf{e}_\vartheta$,

$$m_i n_i \frac{\partial}{\partial t}\langle\mathbf{e}_\vartheta\cdot\mathbf{u}_i\rangle = -\langle\mathbf{j}\cdot\nabla\psi\rangle - \sum_{s=(e,i)}\langle\mathbf{e}_\vartheta\cdot\nabla\cdot\overleftrightarrow{\pi}_s\rangle, \tag{2.43a}$$

$$m_i n_i \frac{\partial}{\partial t}\langle\mathbf{B}\cdot\mathbf{u}_i\rangle = -\sum_{s=(e,i)}\langle\mathbf{B}\cdot\nabla\cdot\overleftrightarrow{\pi}_s\rangle. \tag{2.43b}$$

Here, electron's inertia is dropped against ion's inertia given their much smaller mass, $m_e \ll m_i$. In addition, the inertial force $m_i n_i\mathbf{u}_i\cdot\nabla\mathbf{u}_i$ vanishes when projected upon either $\mathbf{B}$ and $\mathbf{e}_\vartheta$ for a velocity field like (2.42)[8]. Finally, the term including the total current [111] is obtained from the Lorentz force and pressure gradient terms summed over species[9] and is zero from quasi-neutrality, i.e. $\nabla\cdot\mathbf{j} = 0$, in the absence of an external biasing [34, 111]. Equation (2.43a) can be seen as the damping of the radial electric field to its stationary value, see e.g. [87]. If the

[8] For instance, the projection of ion inertia over $\mathbf{B}$ results after surface averaging, see e.g. [20],

$$\langle\mathbf{B}\cdot(\mathbf{u}_i\cdot\nabla)\,\mathbf{u}_i\rangle = \left\langle\mathbf{B}\cdot\nabla\left(\frac{u_i^2}{2}\right)\right\rangle - \langle\mathbf{B}\cdot\mathbf{u}_i\times\nabla\times\mathbf{u}_i\rangle = -\langle\mathbf{B}\times\mathbf{u}_i\cdot\nabla\times\mathbf{u}_i\rangle = E_i(\psi)\,\langle\nabla\psi\cdot\nabla\times\mathbf{u}_i\rangle = 0,$$

as $\langle\mathbf{B}\cdot\nabla g\rangle = 0$ for any single-valued g and $\mathbf{B}\times\mathbf{u}_i = E_i(\psi)B^\zeta\mathbf{e}_\zeta\times\mathbf{e}_\vartheta = -E_i(\psi)\nabla\psi$. The same result is obtained after projecting the inertial term over $\mathbf{e}_\vartheta$.

[9] Indeed, the term $\mathbf{j}\times\mathbf{B}-\nabla p$ is obtained from the Lorentz force and pressure gradient terms in the fluid equation (2.16), after summing over species. Here, $p = p_e + p_i$ is the total pressure. Its projection on the poloidal direction yields after averaging on a surface,

$$\langle\mathbf{e}_\vartheta\cdot(\mathbf{j}\times\mathbf{B}-\nabla p)\rangle = \langle\mathbf{e}_\vartheta\cdot\mathbf{j}\times\mathbf{B}\rangle = -\psi'\langle\mathbf{j}\cdot\nabla\psi\rangle,$$

whit $\mathbf{B}$ given by equation (2.40). Note that $\langle\mathbf{e}_\vartheta\cdot\nabla p\rangle = 0$ in the Hamada basis, see eq. (2.41).

velocity field (2.42) is inserted in equation (2.43a), the time evolution of the radial electric field is obtained as

$$\frac{\partial E_i}{\partial t} = \frac{1}{m_i n_i \langle \mathbf{e}_\vartheta \cdot \mathbf{e}_\vartheta \rangle} \left\{ \sum_s e_s \Gamma_s^{\mathrm{na}}(E_r) - \langle \mathbf{j} \cdot \nabla \psi \rangle \right\}, \tag{2.44}$$

where the nonaxisymmetric particle flux Γ_s^{na} is given by

$$\Gamma_s^{\mathrm{na}} = -\frac{1}{e_s} \left\langle \mathbf{e}_\vartheta \cdot \nabla \cdot \overleftrightarrow{\pi}_s \right\rangle, \tag{2.45}$$

see e.g. the particle flux decomposition in section 7.4 of ref. [3]. As we shall see in subsection 2.3.1, Γ_s^{na} depends on the mass and charge of each species s in a stellarator. Thus, in order to conserve the total flux of charge through a magnetic surface –i.e. $\sum_s e_s \Gamma_s = 0$– the radial electric field is adjusted to make

$$\sum_s e_s \Gamma_s^{\mathrm{na}}(E_r) = 0, \tag{2.46}$$

which is known as the ambipolar condition. Therefore, equation (2.43a), or equivalently equation (2.44), represents the damping of the radial electric field to its stationary value, which in a stellarator is fixed after requiring ambipolarity, see equation (2.46). Note that in tokamak geometry the ambipolar condition (2.46) is recast as

$$\sum_s e_s \Gamma_s^{\mathrm{na}} = -\frac{\sqrt{g}}{\iota} \sum_s \left\langle (\mathbf{B} - \mathbf{B}_{\mathrm{t}}) \cdot \nabla \cdot \overleftrightarrow{\pi}_s \right\rangle = \frac{\sqrt{g}}{\iota} \sum_s \left\langle \mathbf{B} \cdot \nabla \cdot \overleftrightarrow{\pi}_s \right\rangle,$$

as the toroidal symmetry in a tokamak implies $\langle \mathbf{e}_\zeta \cdot \nabla \cdot \overleftrightarrow{\pi}_s \rangle = 0$. Thus, the two equations in (2.43) are degenerated in a tokamak and so only a relationship between E_i and Λ_i can be established from NC theory.

An expression for the viscosity tensor is needed to obtain the time evolution and equilibrium value of the ion flow. In the Chew-Goldberger-Low form, the off-diagonal terms of the viscous tensor –in a filed-aligned orthogonal coordinate system– are small since the velocity distribution function depends weakly on the gyro-phase, see e.g. chapter 12 in [22]. In other words, only the gyro-averaged part of the distribution function is considered [112] and so the gyroviscosity is neglected [33]. Hence, for any regime of collisionality, the viscosity tensor is given by

$$\overleftrightarrow{\pi}_s = \pi_{\parallel s} (\mathbf{bb} - \frac{1}{3} \overleftrightarrow{I}) + \mathcal{O}(\delta_i^2 p_i), \tag{2.47}$$

where $\pi_{\parallel s} = p_{\parallel s} - p_{\perp s}$ is the pressure anisotropy and the parallel and perpendicular pressures are defined as

$$\begin{pmatrix} p_{\parallel s} \\ p_{\perp s} \end{pmatrix} = m_s \int \begin{pmatrix} v_\parallel^2 \\ \frac{1}{2} v_\perp^2 \end{pmatrix} f_{s1} \mathrm{d}^3 \mathbf{v}. \tag{2.48}$$

Note that the standard pressure is the weighted mean of these pressures, $p_s = (2p_{\perp s} + p_{\parallel s})/3$. The projection of the viscous force $\nabla \cdot \overleftrightarrow{\pi}_s$ into parallel and poloidal directions required in equations (2.43) can be generally written as [98]

$$\langle \mathbf{A} \cdot \nabla \cdot \overleftrightarrow{\pi}_s \rangle = -\langle \pi_{\parallel s} \mathbf{A} \cdot \nabla \ln B \rangle, \tag{2.49}$$

for any vector $\mathbf{A}$ such that $\mathbf{A}\cdot\nabla\psi = 0$ and $\nabla\cdot\mathbf{A} = 0$[10]. In particular the relation (2.49) holds for the Hamada covariant vectors and the magnetic field, i.e. $\mathbf{A}\equiv\mathbf{e}_\vartheta, \mathbf{B}$.

Next, the pressure anisotropy $\pi_{\|s}$ is calculated after solving the Drift Kinetic Equation for f_{s1}. More specifically, only the $l=2$ Legendre component of f_{s1} is necessary since, from equations (2.47) to (2.49), the stress tensor is written as [93]

$$\left\langle \mathbf{A}\cdot\nabla\cdot\overset{\leftrightarrow}{\pi}_s \right\rangle = -2T_{s0}\left\langle \mathbf{A}\cdot\nabla\ln B\int \mathrm{d}^3\mathbf{v} K P_2(\xi) f_{s1}\right\rangle, \tag{2.50}$$

where $K\equiv x_s^2 = m_s v^2/2T_{s0}$ is the normalised kinetic energy, $\xi = v_\|/v$ is the pitch-angle and $P_2(\xi) = 3\xi^2/2 - 1/2$ the $l=2$ Legendre polynomial. This allows the use of numerical codes such as DKES [95] to estimate the above integral (2.50) since the $l=2$ Legendre component of f_{s1} is not affected by the use of simplified forms of the collision operator [93] –in particular those which do not conserve momentum.

The flux-surface averaged viscous force in (2.50) can be expressed as linear combinations of the first order particle and heat fluxes [92, 93, 97, 99], where the proportionality constants are named viscosity coefficients (see e.g. transport matrices defined in equations (35) and (38) of reference [93]). For the sake of simplicity the effect of heat fluxes and temperature gradients is neglected in the following, as in [113–115]. In this context, it is convenient to define a poloidal μ_p, parallel μ_t and bootstrap μ_b viscosity coefficients such that [20]

$$\langle \mathbf{B}\cdot\nabla\cdot\overset{\leftrightarrow}{\pi}_s\rangle = \mu_{\mathrm{b,s}}E_s + \mu_{\mathrm{t,s}}\Lambda_s, \tag{2.51a}$$

$$\langle \mathbf{e}_\vartheta\cdot\nabla\cdot\overset{\leftrightarrow}{\pi}_s\rangle = \mu_{\mathrm{p,s}}E_s + \mu_{\mathrm{b,s}}\Lambda_s. \tag{2.51b}$$

For similar species temperatures $T_\mathrm{e}\sim T_\mathrm{i}$, the electron viscosity is taken to be an order $\sim\sqrt{m_\mathrm{e}/m_\mathrm{i}}$ smaller than that of the ions[11] and thus

$$\langle \mathbf{B}\cdot\nabla\cdot\overset{\leftrightarrow}{\pi}_e\rangle \ll \langle \mathbf{B}\cdot\nabla\cdot\overset{\leftrightarrow}{\pi}_i\rangle, \quad \langle \mathbf{e}_\vartheta\cdot\nabla\cdot\overset{\leftrightarrow}{\pi}_e\rangle \ll \langle \mathbf{e}_\vartheta\cdot\nabla\cdot\overset{\leftrightarrow}{\pi}_i\rangle. \tag{2.53}$$

[10] Let $\mathbf{A}$ be such that $\mathbf{A}\cdot\nabla\psi = 0$ and $\nabla\cdot\mathbf{A} = 0$, and consider the projection of the viscous stress on such a vector, i.e. $\mathbf{A}\cdot\nabla\cdot\overset{\leftrightarrow}{\pi}_s = \mathbf{A}\cdot\nabla\cdot\left(\pi_{\|s}\mathbf{bb}\right) - \mathbf{A}\cdot\nabla\pi_{\|s}/3$. The second term vanishes after averaging on a surface. On the other hand, the first term is massaged as

$$\mathbf{A}\cdot\nabla\cdot\left(\pi_{\|s}\mathbf{bb}\right) = \mathbf{A}\cdot\mathbf{b}\nabla\cdot\left(\pi_{\|s}\mathbf{b}\right) + \pi_{\|s}\mathbf{A}\cdot\boldsymbol{\kappa} = \mathbf{B}\cdot\nabla\left(\pi_{\|s}\frac{\mathbf{A}\cdot\mathbf{B}}{B^2}\right) - \pi_{\|s}\mathbf{b}\cdot\nabla\left(\frac{\mathbf{A}\cdot\mathbf{B}}{B}\right) + \pi_{\|s}\mathbf{A}\cdot\boldsymbol{\kappa},$$

with $\boldsymbol{\kappa} = \nabla_\|\mathbf{b} = -\mathbf{b}\times(\nabla\times\mathbf{b})$ the curvature vector. The first term vanishes after the surface-average and the other two are recast as

$$-\nabla_\|(\mathbf{A}\cdot\mathbf{b}) + \mathbf{A}\cdot\nabla_\|\mathbf{b} = -\frac{1}{B^2}\mathbf{B}\cdot(\mathbf{B}\cdot\nabla)\mathbf{A} = -\mathbf{A}\cdot\nabla\ln B.$$

Here the orthogonality of the curvature and magnetic field vectors have been used. In addition, since $\mathbf{A}$ and $\mathbf{B}$ are tangent to the surface the cross product $\mathbf{A}\times\mathbf{B} = f(\psi)\nabla\psi$ has zero rotational, and so the relation $\mathbf{B}\cdot(\mathbf{B}\cdot\nabla)\mathbf{A} = \mathbf{B}\cdot(\mathbf{A}\cdot\nabla)\mathbf{B} = B(\mathbf{A}\cdot\nabla)B$ holds. To sum up,

$$\left\langle \mathbf{A}\cdot\nabla\cdot\overset{\leftrightarrow}{\pi}_s\right\rangle = \left\langle \mathbf{A}\cdot\nabla\cdot\left(\pi_{\|s}\mathbf{bb}\right)\right\rangle = -\left\langle \pi_{\|s}\mathbf{b}\cdot(\mathbf{b}\cdot\nabla)\mathbf{A}\right\rangle = -\left\langle \pi_{\|s}\mathbf{A}\cdot\nabla\ln B\right\rangle.$$

[11] From the pressure anisotropy definition in equation (2.48), the ratio of electron and ion viscosities can be estimated as

$$\frac{\pi_{\|\mathrm{e}}}{\pi_{\|\mathrm{i}}} \sim \frac{T_{\mathrm{e}0}\delta_\mathrm{e}\int f_{\mathrm{e}0}\mathrm{d}^3\mathbf{v}}{T_{\mathrm{i}0}\delta_\mathrm{i}\int f_{\mathrm{i}0}\mathrm{d}^3\mathbf{v}} = \frac{T_{\mathrm{e}0}n_{\mathrm{e}0}}{T_{\mathrm{i}0}n_{\mathrm{i}0}}\frac{\delta_\mathrm{e}}{\delta_\mathrm{i}} \sim \left(\frac{T_{\mathrm{e}0}}{T_{\mathrm{i}0}}\right)^{3/2}\left(\frac{m_\mathrm{e}}{m_\mathrm{i}}\right)^{1/2}. \tag{2.52}$$

Here, the orderings $f_{s1}\sim\delta_s f_{s0}$ and $m_s v_{\|,\perp}^2\sim T_{s0}$ have been used.

While this approximation may be correct in ion-root –i.e., $E_r < 0$– plasmas of TJ-II, the electron viscosity must be kept to model TJ-II low density electron-root –i.e., $E_r > 0$– plasmas since $T_e \gg T_i$ [84]. In this parameter region, the ion and electron neoclassical fluxes display a similar strong E_r dependence around its equilibrium value [45] and therefore both contribute to the return to the neoclassical ambipolarity [116]. In the next subsections electron viscosity is neglected, so we restrict our treatment to plasmas with $T_\mathrm{e} \sim T_\mathrm{i}$.

2.3.1 Viscosity coefficients

In this subsection semi-analytic expressions for the ion neoclassical viscosity coefficients in the Pfirsch-Schlüter (PS) and plateau regimes of collisionality are applied to the TJ-II stellarator geometry. Here, we follow the pioneering work in stellarators of Shaing and Callen [97] in the PS –collisional– regime, and that of Coronado and Wobig [98] and Shaing [99] for the plateau regime. Next, a comparison of the DKES outputs with these semi-analytic results is addressed following the so-called Sugama-Nishimura method [93, 117], which extends the moments approach to NC theory so to relate the NC viscosity coefficients to the DKES [95] monoenergetic coefficients. In the asymptotic limits of collisionality considered here –PS and plateau– the effect of the $\mathbf{E}\times\mathbf{B}$ drift on f_{i1} can be neglected against the collisionless operator acting on f_{i1}[12]. Therefore the comparison will be established for $E_r = 0$.

2.3.1.1 Pfirsch-Schlüter regime

In the Pfirsch-Schlüter regime Coulomb collisions are so frequent that a subsidiary expansion of f_{i1} in the inverse of the collisionality, $\hat{\nu}_{ii}^{-1} \ll 1$, can be made (see e.g. section 4.3.1 in the review paper of Hirshman and Sigmar [92]). The ion pressure anisotropy is determined in this scheme by the second order piece of f_{i1}[13] and is written as [97]

$$\pi_{i\|} = -3p_i\tau_i\left(\mu_{i1}\mathbf{u}_i + \mu_{i2}\frac{2}{5}\frac{\mathbf{q}_i}{p_{i0}}\right)\cdot\nabla\ln B, \tag{2.54}$$

with τ_i the self collision time

$$\tau_i = \sqrt{2}\tau_{ii} = \frac{12\pi^{3/2}\varepsilon_0^2 m_i^{1/2}T_i^{3/2}}{n_i e^4\ln\Lambda}. \tag{2.55}$$

The dimensionless factors μ_{ij} are calculated in reference [92] for the full linearised collision operator. In case of a pure plasma the resulting coefficients are $\mu_{i1} = 1.365$ and $\mu_{i2} = 2.31$ [97].

[12] The collisionless operator consists of parallel streaming and mirror forces, i.e.

$$V_\| \equiv v\xi\nabla_\| - \frac{1}{2}v(1-\xi^2)\nabla_\|\ln B\frac{\partial}{\partial\xi},$$

see e.g. [117]. Thus, it is ordered as $\mathcal{O}(v_s)$, whilst the operator associated with the $\mathbf{E}\times\mathbf{B}$ drift,

$$V_E \equiv -\frac{\partial\Phi}{\partial\rho}\frac{\nabla\rho\times\mathbf{B}\cdot\nabla}{\langle B^2\rangle},$$

is ordered as $\mathcal{O}(v_s\delta_s)$. Here, the compressional part of the $\mathbf{E}\times\mathbf{B}$ drift is removed, as in DKES [95]. It is noted that at very high collisionalities, $\hat{\nu}_s > 10^2$, the effect of the $\mathbf{E}\times\mathbf{B}$ drift on f_{i1} must be account for in the TJ-II, see e.g. figure 1 in ref. [45].

[13] In the expansion of f_{i1} in powers of $\hat{\nu}_{ii}^{-1}$, i.e. $f_{i1} = \sum_k f_{i1}^{(k)}$, the first three terms are proportional to $\hat{\nu}_{ii}$, $\hat{\nu}_{ii}^0$ and $\hat{\nu}_{ii}^{-1}$, respectively, so that the zero order term is ordered as $f_{i1}^{(-1)} = \mathcal{O}\left(\hat{\nu}_{ii}\delta_i f_{i0}\right) \sim \mathcal{O}\left(f_{i0}\right)$, the first order piece is $f_{i1}^{(0)} = \mathcal{O}(\delta_i f_{i0})$ and the second order piece is $f_{i1}^{(1)} = \mathcal{O}\left(\delta_i/\hat{\nu}_{ii} f_{i0}\right)$.

Note that the expression (2.54) has the same form as the Braginskii result in the fluid closure (see, e.g., chapter 4 in [22]). The ion viscosity coefficients (2.51) are then [20, 97]

$$\mu_{\rm p} = C_{\rm PS}\langle(\mathrm{e}_\vartheta\cdot\nabla\ln B)^2\rangle, \tag{2.56a}$$

$$\mu_{\rm t} = C_{\rm PS}\langle(\mathrm{B}\cdot\nabla\ln B)^2\rangle, \tag{2.56b}$$

$$\mu_{\rm b} = C_{\rm PS}\langle(\mathrm{e}_\vartheta\cdot\nabla\ln B)(\mathrm{B}\cdot\nabla\ln B)\rangle. \tag{2.56c}$$

Here, $C_{\rm PS}\equiv 3p_i\tau_i\mu_{i1}$. The natural way to calculate the ion viscosity coefficients in the PS regime, equations (2.56), would be in Hamada coordinates,

$$\mathrm{e}_\vartheta\cdot\nabla\ln B = \frac{\partial\ln B}{\partial\vartheta}. \tag{2.57}$$

However, it requires the sampling of $\ln B$ in these coordinates. Since the Hamada poloidal angle ϑ is a known function of general flux coordinates (θ_f,ϕ_f) (i.e., those in which the magnetic field lines are straight lines, see section A.3 in the appendix A)

$$\vartheta = \theta_f + \iota G(\psi,\theta_f,\phi_f),$$

the derivative respect to the Hamada poloidal vector in (2.57) is recast as

$$\frac{\partial\ln B}{\partial\vartheta} = \frac{\sqrt{g}}{\sqrt{g_f}}\left\{\left(1+\frac{\partial G}{\partial\phi_f}\right)\frac{\partial}{\partial\theta_f} - \frac{\partial G}{\partial\theta_f}\frac{\partial}{\partial\phi_f}\right\}\ln B.$$

Details on the calculation of the flux coordinates (θ_f,ϕ_f) and the generating function $G(\theta_f,\phi_f)$ are given sections A.2 and A.3 of the appendix A.

The dependence of the coefficients (2.56) on plasma parameters comes from the $p_s\tau_s$ prefactor, with the ion self-collision time, $\tau_i\propto T_i^{3/2}n_i^{-1}$, defined in equation (2.55). Therefore, $\mu_i^{\rm PS}\propto T_i^{5/2}$. For instance, typical values of the poloidal viscosity would be $\mu_{\rm p}^{\rm PS}\sim 10^{-2}-10^{-3}$ kg m^{-1} s^{-1} for $T_i\sim 100$ eV.

2.3.1.2 Plateau regime

In the plateau regime of collisionality the orbits of circulating particles are completed before being scattered by Coulomb collisions, and so, short mean-free-path cannot be assumed. On the other hand, trapped particles in magnetic wells are constantly interrupted by collisions so that particle transport is dominated by passing particles [98]. The diffusion process is determined by the particles whose pitch-angle $\xi = v_\parallel/v$ is sufficiently large to avoid trapping, but small enough to suffer Coulomb scattering, i.e.

$$\left(\frac{\omega_{s\rm b}}{\omega_{Ts}}\right)^{1/3} \ll \xi \sim \left(\frac{\nu_d^s}{\omega_{Ts}}\right)^{1/3} \ll 1. \tag{2.58}$$

Here, $\omega_{s\rm b}\sim\varepsilon_t^{3/2}\omega_{Ts}$ is the typical toroidal-trapping frequency, ε_t the toroidal ripple, ω_{Ts} the transit frequency, and ν_d^s the collision frequency representing the pitch-angle deflection rate for particle species s. Note that the plateau regime only exists in large aspect-ratio devices [3, 22], i.e. $\varepsilon_t^{3/2}\ll\hat{\nu}_{ss}\ll 1$.

To calculate the viscosities [98], the magnetic field strength is Fourier-decomposed in the Hamada angles as

$$B = \langle B \rangle \sum_{m,n} b_{mn}(\psi) \cos(m\vartheta - n\zeta), \tag{2.59}$$

where the strength of each (m, n) mode is

$$\langle B \rangle b_{mn}(\psi) = \frac{1}{4\pi^2} \int d\vartheta \int d\zeta B e^{-i(m\vartheta - n\zeta)} = \langle B \cos(m\vartheta - n\zeta) \rangle \,. \tag{2.60}$$

In the last step, the stellarator symmetry $B(\vartheta, \zeta) = B(-\vartheta, -\zeta)$ has been used. As in the collisional case, we do not re-sample any function directly in Hamada coordinates. In the present case, the expansion (2.59) is performed in Hamada angles, which are known functions of the magnetic flux coordinates, see section A.3 in the appendix A. Thus, the magnetic field strength is finally expressed in flux coordinates, $(\theta_\mathrm{f}, \phi_\mathrm{f})$, even though the modes correspond to the Hamada expansion. The relative error $(B_\mathrm{H} - B_\mathrm{f})/B_\mathrm{f}$ (in percentage) introduced by this decomposition is shown in the left column of figure 2.2. Although it can be up to 2.5 % at some points, the mean of its absolute value is $\leq 0.3\,\%$. The relative strength of each mode b_{mn}, with respect to the maximum value is shown in the same figure (the $(0, 0)$ mode is not included). Note that the toroidal and helical modes (b_{10} and b_{14}, respectively) dominate the spectrum.

Next, the viscosity coefficients (2.51) in the plateau regime [99] are given by[14]

$$\mu_\mathrm{p} = \frac{\kappa_i}{B^\zeta} \sum_{(m,n)\neq(0,0)} \frac{m^2 b_{mn}^2}{|n - \iota m|}, \tag{2.61a}$$

$$\mu_\mathrm{b} = -\kappa_i \sum_{(m,n)\neq(0,0)} m b_{mn}^2 \frac{n - \iota m}{|n - \iota m|}, \tag{2.61b}$$

$$\mu_\mathrm{t} = \kappa_i B^\zeta \sum_{(m,n)\neq(0,0)} b_{mn}^2 |n - \iota m|, \tag{2.61c}$$

with $\kappa_i = \pi^{1/2} p_i \langle B \rangle / v_{Ti}$. In the above expressions, the approximation $(\ln B)_{mn} \approx b_{mn}$ is made, as follows from the decomposition (2.59) and the large aspect-ratio of TJ-II, which makes $b_{mn} \leq 0.2$. The poloidal viscosity in (2.61a) presents a singularity on rational surfaces, i.e. $\mu_\mathrm{p} \to \infty$ when $|n - \iota m| \to 0$. Such a divergent behaviour has been extensively studied in both tokamaks and stellarators [113,119–121]. The singularity disappears when the effects of collisions and the $\mathbf{E} \times \mathbf{B}$ drift on particle orbits are included. A local maximum in μ_p as a function of the poloidal Mach number, $M_\mathrm{p} = E_r/(B_p v_i)$, is obtained for M_p close to unity. Such a non-linear behaviour of $\mu_p = \mu_p(M_p)$ gives rise to a bifurcation phenomena [122–124], i.e. different poloidal

[14] In references [98,99] the parallel and poloidal projections of the stress tensor in equations (2.51) are expressed as linear combinations of poloidal and toroidal velocities ($u_i^\vartheta = \mathbf{u}_i \cdot \nabla\vartheta = E_i + B^\vartheta \Lambda_i$ and $u_i^\zeta = \mathbf{u}_i \cdot \nabla\zeta = B^\zeta \Lambda_i$, respectively),

$$\langle \mathbf{B} \cdot \nabla \cdot \overleftrightarrow{\pi}_i \rangle = \mu_\vartheta u_i^\vartheta + \mu_\zeta u_i^\zeta,$$
$$\langle \mathbf{e}_\vartheta \cdot \nabla \cdot \overleftrightarrow{\pi}_i \rangle = \mu_\vartheta^P u_i^\vartheta + \mu_\zeta^P u_i^\zeta,$$

rather than in terms of the flux-constants E_i and Λ_i. Then, it is straightforward to show that $\mu_\mathrm{p} = \mu_\vartheta^P$, $\mu_\mathrm{b} = \mu_\vartheta$ and $\mu_\mathrm{t} = \mu_\vartheta B^\vartheta + \mu_\zeta B^\zeta$. The viscosity coefficients in the from (2.61) are also consistent with those defined in [114]. However, the poloidal and parallel viscosity coefficients given in references [93, 118] are 2 times larger than those in (2.61).

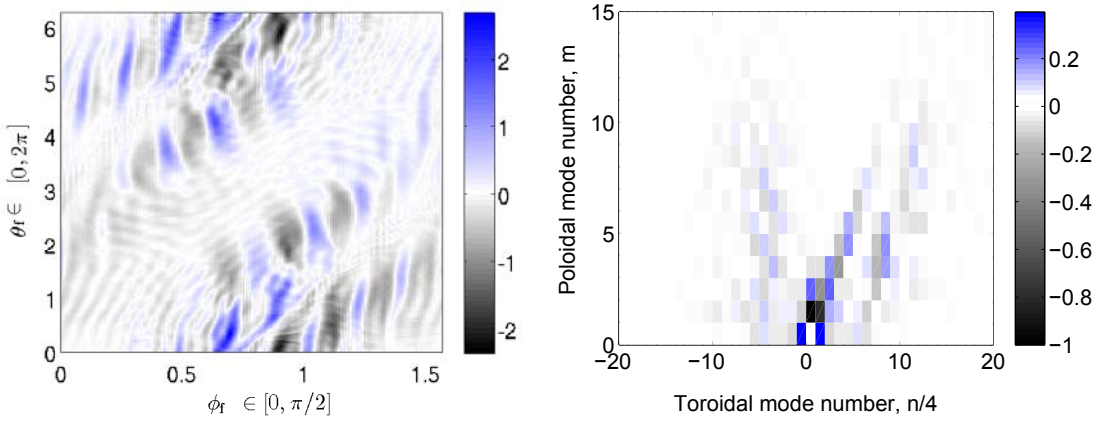

Figure 2.2. Fourier decomposition of B at the surface $\rho = 0.9$ using Hamada angles. (Left) Relative error introduced by the decomposition (in percentage); (Right) Relative strength of each mode, $b_{mn}/\max(|b_{mn}|)$, without considering the $(0,0)$ mode. The toroidal and helical modes, b_{10}, b_{14}, dominate the spectrum.

rotation states appear for the same viscous damping. The study of this non-linearity is out of the scope of this work, and thus the Hamada spectrum (2.59) is not calculated exactly at the rational surface, but in a close irrational surface [114].

For representation purposes, it is convenient to convert the viscosity coefficients to frequencies as

$$\nu_{\rm p} \equiv \frac{\mu_{\rm p}}{m_i n_i \langle \mathbf{e}_\vartheta \cdot \mathbf{e}_\vartheta \rangle}, \quad \nu_{\rm t} \equiv \frac{\mu_{\rm t}}{m_i n_i \langle B^2 \rangle}, \quad \nu_{\rm b} \equiv \frac{\mu_{\rm b}}{m_i n_i \langle \mathbf{e}_\vartheta \mathbf{e}_\vartheta \rangle^{1/2} \langle B^2 \rangle^{1/2}}. \tag{2.62}$$

These viscous frequencies will be useful to understand the damping of the ionic flow in subsection 2.3.2 and are presented in figure 2.3 as a function of the normalised radius ρ for the Pfirsch-Schlüter and plateau regimes, see equations (2.56) and (2.61). The ion temperature and density have been set to $T_{\rm i} = 100$ eV and $n_{\rm i} = 10^{19}$ m^{-3}, respectively, so that $\hat{\nu}_{ii} \approx 6 \times 10^{-2}$. This places the ions in the plateau regime of collisionality, which is characteristic of TJ-II plasmas, see e.g. [45]. Thus, the collisional result does not apply for the plasma parameters used in figure 2.3. Note: it is straightforward to estimate the viscous frequencies for another set $(n_{\rm i}, T_{\rm i})$ from the numerical results shown in figure 2.3, as their dependence on plasma parameters is $\nu_{\rm p}^{\rm PS} \propto T_i^{5/2}/n_i$ and $\nu_{\rm p}^{\rm plat} \propto T_i^{1/2}$.

Some general comments can be made in light of the numerical results shown in figure 2.3. For the plasma parameters chosen (with $\hat{\nu}_{ii} \ll 1$) the plateau frequencies are smaller than those obtained in the Pfrisch-Schlüter regime. However, for collisional plasmas (with $\hat{\nu}_{ii} > 10$) the PS viscosities greatly reduces due to the $T_i^{5/2}$ dependence; indeed, for $\hat{\nu}_{ii} \to \infty$ ($\tau_{ii} \to 0$) the pressure anisotropy goes to zero, see equation (2.54). The viscous frequencies increase when moving towards the edge. This increment can be understood as the enlargement of the radial diffusion coefficient, produced by the increment of the effective ripple, see e.g. [45, 96].

The poloidal damping frequency $\nu_{\rm p}$ dominates the entire plasma minor radius, with frequencies ranging several tens of kHz. Thus, low frequency radial electric field fluctuations –such as zonal flows– are neoclassically damped, see e.g. [87]. This justifies the neoclassical treatment

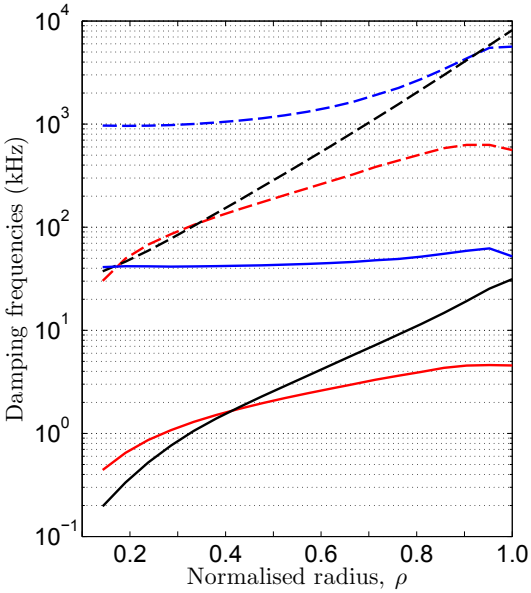

Figure 2.3. Neoclassical ion viscous frequencies $\nu_{\rm p}$ (in blue), $\nu_{\rm t}$ (in black) and $-\nu_{\rm b}$ (in red) for the Pfirsch-Schlüter (dashed lines) and plateau (solid lines) regimes of collisionality as a function of the normalised radius. The ion temperature and density are set to $T_{\rm i} = 100$ eV and $n_{\rm i} = 10^{19}$ m^{-3}, respectively.

of ionic flows considered in here. On the other hand, a finite parallel mass (bootstrap) flow is expected at the core due to the finite value of the quotient $\mu_{\rm b}/\mu_{\rm t}$, see section 2.3.2. In the plateau regime such a ratio is up to 2 times higher than that in the PS case, reflecting the higher efficiency in the transference of momentum from the trapped population to the circulating particles by collisions (see, e.g. the discussion in section 11.4 of ref. [22]). The sign of the bootstrap flow (current) can change in a helical system (respect to the usual tokamak result, where it always has the same direction of the Ohmic current) due to the presence of non toroidal modes [3, 99], $b_{(m,n\neq 0)}$, that may change the sign of the bootstrap viscosity coefficient $\mu_{\rm b}$, see equation (2.61b).

In the following, the semi-analytical viscosity coefficients (2.56) and (2.61) are compared with those calculated with DKES [96,115] by using the so-called Sugama-Nishimura method [93,117].

2.3.1.3 Comparison with DKES in the asymptotic limits of collisionality

The poloidal $\mu_{\rm p}$ and parallel $\mu_{\rm t}$ ion viscosity coefficients defined in (2.51) can be written in the form of the energy integral [93, 115]

$$[\mu_{\rm t}, \mu_{\rm p}] = \frac{4p_i}{v_i \pi^{1/2}} \int_0^\infty dK K^2 {\rm e}^{-K} \times [M^*(K), \left(\frac{{\rm d}\psi}{{\rm d}V}\right)^2 L^*(K)]. \tag{2.63}$$

Here $M^*(K)$ and $L^*(K)$ represent contributions of mono-energetic particles with energy $K \equiv x_i^2$ to the parallel and poloidal viscosities, respectively, and are calculated with DKES [95]. The dependence of these mono-energetic viscosity coefficients on the radial electric field is labelled by the parameter $\Omega \equiv E_r/(v\langle B\rangle)$, see e.g. [45]. Note that $\Omega = 0$ is taken in the asymptotic limits of collisionality considered in this work. The values of M^* and L^* coefficients in the asymptotic limits of collisionality are obtained from equation (2.63) and the semi-analytical results for $\mu_{\rm t}$ and $\mu_{\rm p}$ in equations (2.56) and (2.61), using that M^* and L^* are independent on the collisionality in the plateau regime and vary as $(\nu^*)^{-1}$ in the collisional case, see e.g. [93, 118]. Note: as the M^* and L^* dependence on the collisionality is the same for any species, the symbol ν^* is used in the following to label a normalised collisionality.

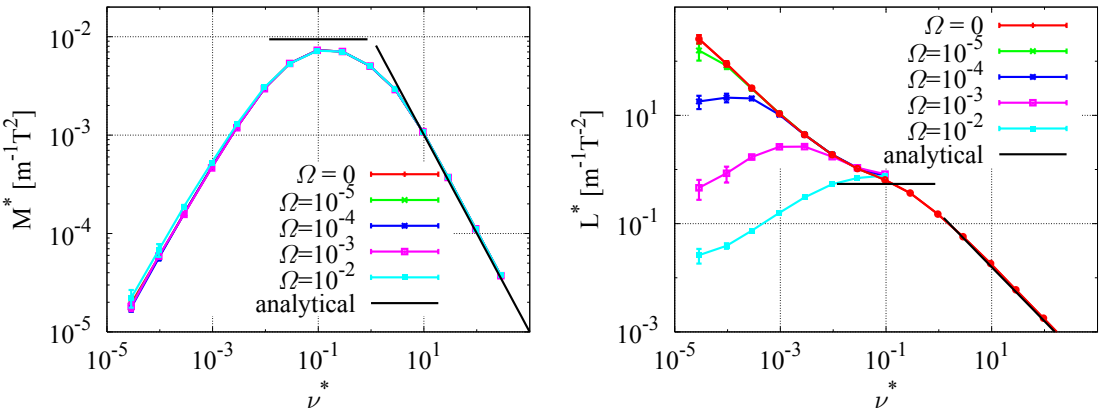

Figure 2.4. Comparison of the normalized monoenergetic contribution to the parallel (left) and poloidal (right) viscous coefficients calculated by DKES (coloured lines) and the collisional and plateau semi-analytical limits (black lines). The dependence of the viscosity coefficients on the radial electric field is indicated by the parameter $\Omega \equiv E_r/(v\langle B\rangle)$.

The normalized monoenergetic contributions, M^* and L^*, to the parallel and poloidal viscosities (μ_t and μ_p respectively) are presented in figure 2.4. The coefficients are nearly independent of collisionality in the plateau regime –hence the name "plateau"– and decrease linearly with the collisionality in the Pfirsch-Schlüter regime [93]. Good quantitative agreement is observed at high collisionalities, and within 20% in the plateau limit of collisionality. The dependence of the coefficients on the radial electric field –stored in the parameter Ω– is small except for the poloidal viscosity (equivalently L^*) in the banana-plateau regimes, thus justifying the approach considered previously in 2.3.1.1 and 2.3.1.2.

The bootstrap μ_b viscosity coefficient can also be expressed in terms of the energy integral [93]

$$\mu_\mathrm{b} = \frac{1}{\langle B^2\rangle}\frac{\mathrm{d}\psi}{\mathrm{d}V}\frac{4p_i}{v_i\pi^{1/2}}\int_0^\infty dK K^2 \mathrm{e}^{-K} M^*(K) G_\mathrm{b}(K), \tag{2.64}$$

with the geometric factor G_b given by [97]

$$G_\mathrm{b} = \frac{\mathrm{d}V}{\mathrm{d}\psi}\frac{\mu_\mathrm{b}}{\mu_\mathrm{t}}. \tag{2.65}$$

Here, G_b is a flux-surface function representing a geometrical factor associated with the bootstrap current that relates the parallel flows to the thermodynamic forces. This flux-function is shown in figure 2.5 as a function of normalized collisionality. As observed, the calculations in the asymptotic limits of collisionality correctly reproduce the DKES outputs. In the long mean-free-path the bootstrap geometrical factor depends strongly on the radial electric field and can reverse its sign, depending on the value of Ω.

In summary, good quantitative agreement is obtained when comparing the viscosity coefficients calculated in the Pfirsch-Sclüter and plateau asymptotic limits of collisionality [97, 98] and those obtained with DKES [96, 115] following the Sugama-Nishimura method [93, 117]. The asymptotic limits are demonstrated to be useful in determining the bootstrap geometric factor[15],

[15] Which determines the bootstrap parallel flow for a given radial electric field, as shown in the next subsection.

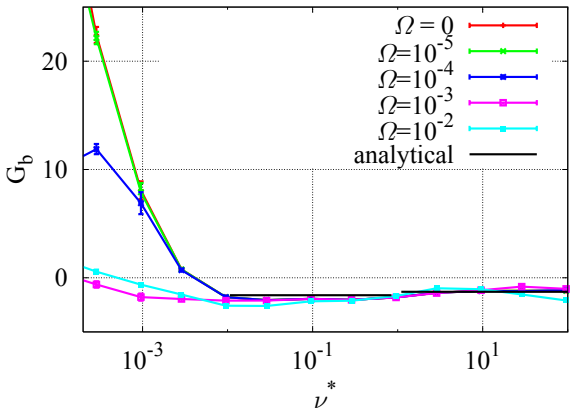

Figure 2.5. Comparison of the bootstrap geometrical factor calculated by DKES (coloured lines) and the collisional and plateau semi-analytical limits (black lines). The legend is the same as in figure 2.4.

even though the effect of the radial electric field on particle orbits has been neglected. In the two following sections, the effect of the viscosity in transient and equilibrium ionic flows is studied, as well as the drag force produced by cold neutrals.

2.3.2 Damping times and equilibrium flows

Once the expressions for the viscosity coefficients are known in some asymptotic limits of collisionality, the time evolution of ionic mass flows can be studied through the time evolution and steady-sate values of the two flux constants $E_i(\psi)$ and $\Lambda_s(\psi)$ (see equations (2.26), (2.31) and (2.42)). Recall that the effect of heat fluxes and temperature gradients has been neglected, equations (2.51), and that the electron viscous stress has been neglected, see (2.53). Then, the transient phase of the first order ionic mass flow, equations (2.43), is written as [20, 115]

$$mn \begin{pmatrix} \langle \mathbf{e}_\vartheta \cdot \mathbf{e}_\vartheta \rangle & I_{\mathrm{T}} \\ I_{\mathrm{T}} & \langle B^2 \rangle \end{pmatrix} \frac{\partial}{\partial t} \begin{pmatrix} E \\ \Lambda \end{pmatrix} = \begin{pmatrix} R \\ 0 \end{pmatrix} - \begin{pmatrix} \mu_{\mathrm{p}} & \mu_{\mathrm{b}} \\ \mu_{\mathrm{b}} & \mu_{\mathrm{t}} \end{pmatrix} \begin{pmatrix} E \\ \Lambda \end{pmatrix}. \tag{2.66}$$

Here species sub-index has been dropped and ion flows have been expressed in Hamada coordinates, see equation (2.42). In addition, R stands for a possible driving term [34,84]. The effect of a time-dependent viscosity [125, 126] is neglected. Finally, the non-diagonal terms in the inertia matrix, $\langle \mathbf{e}_\vartheta \cdot \mathbf{B} \rangle = I_{\mathrm{T}}$, are zero for a currentless stellarator.

The set of equations (2.66) can be solved by inverting the inertia matrix L [$L_{12} = L_{21} = 0$, $L_{11} = mn\langle \mathbf{e}_\vartheta \cdot \mathbf{e}_\vartheta \rangle$, $L_{22} = mn\langle B^2 \rangle$] and considering the equivalent system [127]

$$\dot{\mathbf{u}} = \mathbf{r} - M\mathbf{u}, \tag{2.67}$$

where $\mathbf{u} = [E, \Lambda]^T$, $\mathbf{r} = L^{-1} \times [R, 0]^T$ and $M = L^{-1} \times V$. The matrix V contains the ion viscosity coefficients [$V_{12} = V_{21} = \mu_{\mathrm{b}}$, $V_{11} = \mu_{\mathrm{p}}$, $V_{22} = \mu_{\mathrm{t}}$], so that

$$M = \begin{pmatrix} \nu_{\mathrm{p}} & \tilde{l}\nu_{\mathrm{b}} \\ \nu_{\mathrm{b}}/\tilde{l} & \nu_{\mathrm{t}} \end{pmatrix} \begin{pmatrix} E \\ \Lambda \end{pmatrix}, \tag{2.68}$$

with ν_i the damping frequencies defined in (2.62) and $\tilde{l} \equiv \sqrt{\langle B^2 \rangle / \langle \mathbf{e}_\vartheta \cdot \mathbf{e}_\vartheta \rangle}$ a geometrical factor (with units $[\tilde{l}]$ =T m^{-1}). For a constant source term [84], or if the external current is abruptly

terminated [34], the flows will decay exponentially with two different damping rates in the eigendirections of the matrix M, i.e.

$$\nu_{\mathrm{f/s}} = \frac{\nu_{\mathrm{p}} + \nu_{\mathrm{t}}}{2} \pm \sqrt{\left(\frac{\nu_{\mathrm{p}} - \nu_{\mathrm{t}}}{2}\right)^2 + \nu_{\mathrm{b}}^2}. \tag{2.69}$$

Here, $\nu_{\mathrm{f/s}}$ correspond to fast/slow damping rates [114]. As the poloidal viscous frequency dominates over the entire plasma minor radius, see figure 2.3, the damping rates are approximately $\nu_{\mathrm{f}} \approx \nu_{\mathrm{p}}$ and $\nu_{\mathrm{s}} \approx \nu_{\mathrm{t}}$ [115]. The corresponding damping times $\tau_i = 1/\nu_i$ are presented in figure 2.6 as a function of the normalised radius ρ for the plateau asymptotic limit of collisionality characteristic of TJ-II. The ion temperature and density have been set to $T_{\mathrm{i}} = 100$ eV and $n_{\mathrm{i}} = 10^{19}$ m^{-3}, respectively, as in figure 2.3. Values of $\tau_{\mathrm{t}} \sim 0.1 - 1$ ms and $\tau_{\mathrm{p}} \sim 20$ μs are obtained in this calculation. Note that $\tau^{\mathrm{plat}} \propto T_i^{-1/2}$. Thus, for a more realistic value of the ion temperature at the plasma edge, $T_i \sim 20$ eV, the theoretical poloidal decay time is $\tau_{\mathrm{p}} \sim 50$ μs [115], in reasonable agreement with the experimental results obtained at the edge of TJ-II, $\tau_{\mathrm{p}}^{\mathrm{exp}} \sim 25$ μs, in relaxation biasing experiments [128].

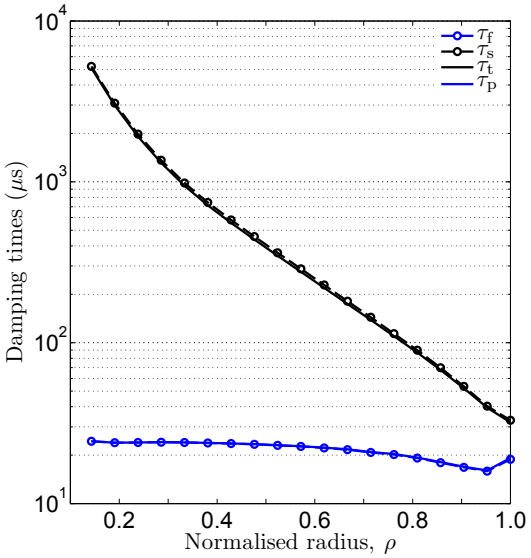

Figure 2.6. Neoclassical ion damping times in the plateau regime as a function of the normalised radius. The ion temperature and density are set to $T_{\mathrm{i}} = 100$ eV and $n_{\mathrm{i}} = 10^{19}$ m^{-3}, respectively. Here, the fast and slow decay times are presented together with the parallel and poloidal damping times.

It is noted here that the numerical results presented in figures 2.3 and 2.6 are based on the calculation of the Hamada poloidal inertia, $\langle \mathbf{e}_\vartheta \cdot \mathbf{e}_\vartheta \rangle$. In a large aspect-ratio, circular cross-section tokamak the poloidal inertia is approximated by $\langle \mathbf{e}_\vartheta \cdot \mathbf{e}_\vartheta \rangle \equiv \langle \mathbf{e}_\vartheta \cdot \mathbf{e}_\vartheta \rangle \approx r^2(1 + 2q^2)$ (see, e.g., the comparison made in the HSX stellarator [129]. Here, r is the effective minor radius and $q = 1/\iota$ the safety factor). An alternative way to examine the goodness of the $\langle \mathbf{e}_\vartheta \cdot \mathbf{e}_\vartheta \rangle$ calculation has been pointed out by Spong [38]. In the limit of high collisionality (and zero radial electric field) the radial transport coefficient incorporates the cross-field transport produced by friction forces acting on the Pfirsch-Schlüter flow [93]. As a result, the parallel contribution to the poloidal inertia can be evaluated in terms of the normalised DKES radial diffusion mono-energetic coefficient [45, 95] as

$$\langle (\mathbf{e}_\vartheta \cdot \mathbf{B})^2 \rangle = \lim_{\nu^* \to \infty} \frac{3}{2} \frac{D_{11}^*}{\nu^*}, \tag{2.70}$$

with $D_{11}^* \equiv D_{11}(K)/[\frac{1}{2} v_s (m_s v_s / e_s)^2 K^{3/2}]$ [93]. In the figure 2.7, a comparison of the parallel contribution to the poloidal inertia is presented, as obtained in the tokamak limit, from DKES through equation (2.70), and from the solution of equations (2.30) in magnetic coordinates. In TJ-II, the large aspect-ratio, circular cross-section tokamak approximation is only valid within

a factor of three. Quantitative agreement is observed between the other two methods in most of the plasma minor radius, $\rho \leq 0.8$. This reinforces the reliability on the calculation of damping times presented in here, as well as those obtained by DKES [84, 87].

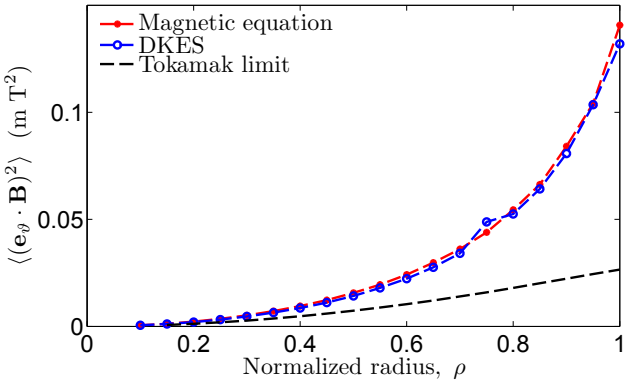

Figure 2.7. Contribution of the parallel component of the Hamada poloidal vector to the poloidal inertia, $\langle(\mathbf{e}_\vartheta \cdot \mathbf{B})^2\rangle$, as obtained from the direct estimation of $\mathbf{e}_\vartheta \cdot \mathbf{B}$ in magnetic coordinates (red), from DKES radial coefficient in (2.70) (blue) and from the tokamak approximation $\langle(\mathbf{e}_\vartheta \cdot \mathbf{B})^2\rangle \approx 2r^2q^2\langle B\rangle^2$ (black).

Finally, the equilibrium ion flow is specified. From equations (2.67) and (2.68) the time evolution of the parallel mass flow is given by

$$\frac{\partial \Lambda_i}{\partial t} = \frac{\nu_\mathrm{b}}{\tilde{l}} E_i + \nu_\mathrm{t} \Lambda_i. \tag{2.71}$$

Therefore, for steady state conditions $\Lambda_i = -E_i \nu_\mathrm{b}/(\tilde{l}\nu_\mathrm{t}) = -E_i \mu_\mathrm{b}/\mu_\mathrm{t}$. The equilibrium ion flow, equations (2.33) or (2.42), results

$$\mathbf{u}_i = E_i(\psi)\left(\mathbf{e}_\vartheta - \frac{\mu_b}{\mu_t}\mathbf{B}\right) = E_i(\rho)\left(\frac{\mathbf{B}\times\nabla\rho}{B^2} + h\mathbf{B} - \frac{\mathrm{d}\psi}{\mathrm{d}\rho}G_\mathrm{b}\mathbf{B}\right). \tag{2.72}$$

In the last step, the Pfirsch-Schlüter flow $E_i h\mathbf{B}$ encapsulated in the parallel component of the Hamada poloidal vector is made explicit. In addition, the geometrical bootstrap factor (G_b form equation (2.65)) has been utilized. Note that since $G_\mathrm{b} < 0$ for the ion collisionality regimes accessible in TJ-II plasmas, figure 2.5, the parallel (bootstrap) mass flow $\Lambda_i\mathbf{B}$ has the same sign of E_i in the absence of external input of momentum. Then, for regimes in which $E_i \approx \mathrm{d}\Phi/\mathrm{d}\rho \propto -E_r$ (e.g., in ECRH plasmas where the radial electric field is mainly determined by the electron temperature gradient [45] and the electron density and ion temperature gradients are small) the bootstrap flow has the opposite direction of the magnetic field, in agreement with the experimental measurements [105].

2.3.2.1 Neutral damping

In the above discussion, the friction with neutral particles has been neglected. However, since neutral mass is similar to that of the ions, the damping produced by neutrals can modify the poloidal and parallel momentum balances [20,34,111,130], equations (2.51) and (2.43). The drag force caused by neutrals is modelled as [92, 111]:

$$\mathbf{F}_n = -m_i n_i \nu_n (\mathbf{u}_i - \mathbf{u}_n) \approx -m_i n_i \nu_n \mathbf{u}_i. \tag{2.73}$$

Here ν_n represents the momentum damping rate, expected to be dominated by charge-exchange momentum losses [131]. The CX collision frequency between ions and neutrals can be approxi-

mated by

$$\nu_n = n_n \langle \sigma_{\rm cx} |\mathbf{v}_i - \mathbf{v}_n| \rangle \approx n_n \sigma_{\rm cx} v_{Ti}, \tag{2.74}$$

with $\sigma_{\rm cx}(E)$ the CX cross section and

$$\begin{aligned} \langle \sigma_{\rm cx} |\mathbf{v}_i - \mathbf{v}_n| \rangle &= \frac{1}{n_n n_i} \int \mathrm{d}^3\mathbf{v} \mathrm{d}^3\mathbf{v}' f_i(\mathbf{x}, \mathbf{v}') f_n(\mathbf{x}, \mathbf{v}) \sigma_{\rm cx} \left(|\mathbf{v}' - \mathbf{v}| \right) |\mathbf{v}' - \mathbf{v}| \\ &\approx \frac{1}{n_i} \int \mathrm{d}^3\mathbf{v}' f_i(\mathbf{x}, \mathbf{v}') \sigma_{\rm cx} \left(|v'| \right) |v'| \equiv \sigma_{\rm cx}(T_i) v_{Ti}, \end{aligned} \tag{2.75}$$

the CX rate coefficient. Equation (2.75) defines, indeed, the CX cross section as a function of the ion temperature. The numerical data has been obtained from the IAEA recommended atomic data [132], and is displayed in fig. 2.8. For TJ-II plasmas, where the ion temperature profile is rather flat [133] and $T_i \leq 200$ eV, the CX cross section is almost constant, $\sigma_{\rm cx} \sim 2-3\times10^{-19}$ m^2. The surface average neutral density profile is estimated with the 3-dimensional code EIRENE [134], which provides typical values of $n_n \sim 10^{15} - 10^{16}$ m^{-3}. Hence, for thermal velocities in the range $100 - 200$ km s^{-1}, the CX collision frequency is typically of the order of hundreds of Hz ($\tau_{\rm cx} \geq 1$ ms, see e.g. [135]).

If friction with neutrals is added to the NC viscosity in the steady state parallel momentum balance (2.16), the viscosity relations (2.51) are modified as

$$\langle \mathbf{B} \cdot \nabla \cdot \overleftrightarrow{\pi}_i \rangle - m_i n_i \nu_n \langle B^2 \rangle \Lambda_i = \mu_{\rm b} E_i + \mu_{\rm t} \Lambda_i, \tag{2.76a}$$

$$\langle \mathbf{e}_\vartheta \cdot \nabla \cdot \overleftrightarrow{\pi}_i \rangle - m_i n_i \nu_n \langle \mathbf{e}_\vartheta \cdot \mathbf{e}_\vartheta \rangle E_i = \mu_{\rm p} E_i + \mu_{\rm b} \Lambda_i. \tag{2.76b}$$

Here, we have used the fact that $\langle \mathbf{e}_\vartheta \cdot \mathbf{B} \rangle = I_T = 0$ for a currentless stellarator. Therefore, the viscosity relationships (2.51) are still valid, with an effective poloidal and parallel viscosity given by

$$\mu_{pn} \equiv \mu_p + m_i n_i \nu_n \langle \mathbf{e}_\vartheta \cdot \mathbf{e}_\vartheta \rangle \tag{2.77a}$$

$$\mu_{tn} \equiv \mu_t + m_i n_i \nu_n \langle B^2 \rangle. \tag{2.77b}$$

These modifications would also affect the calculated damping rates through equations (2.69). In addition, the equilibrium flows (2.72) are also modified to

$$\mathbf{u}_i = \frac{1}{\psi'} E_i \mathbf{e}_\vartheta + \Lambda_i \mathbf{B} = \frac{1}{\psi'} E_i \left(\mathbf{e}_\vartheta - \frac{\mu_b}{\mu_t + m_i n_i \nu_n \langle B^2 \rangle} \mathbf{B} \right). \tag{2.78}$$

The magnitude of the viscosity induced by neutrals is $m_i n_i \nu_n \sim 10^{-6} - 10^{-5}$ kg s^{-1} m^{-3}, which is smaller than the calculated neoclassical poloidal and parallel viscosities, see figure 2.3. Such a simple estimation is confirmed by the numerical calculations presented in the right column of figure 2.8, in which the viscosity generated by friction with neutral particles is added to the neoclassical viscosity calculated in the plateau regime. Nonetheless the damping caused by neutrals should be considered in regions close to a limiter, where the neutral particle densities increase considerably, $n_H \leq 10^{17}$ m^{-3} and $n_{H_2} \leq 10^{18}$ m^{-3} [136].

2.4 Compressible impurity flow in a stellarator

As put forward in section 2.2, the perpendicular flow is determined by the $\mathbf{E} \times \mathbf{B}$ and diamagnetic flows at order $\mathcal{O}(v_s \delta_s)$. This result holds at the same level that having a total flow

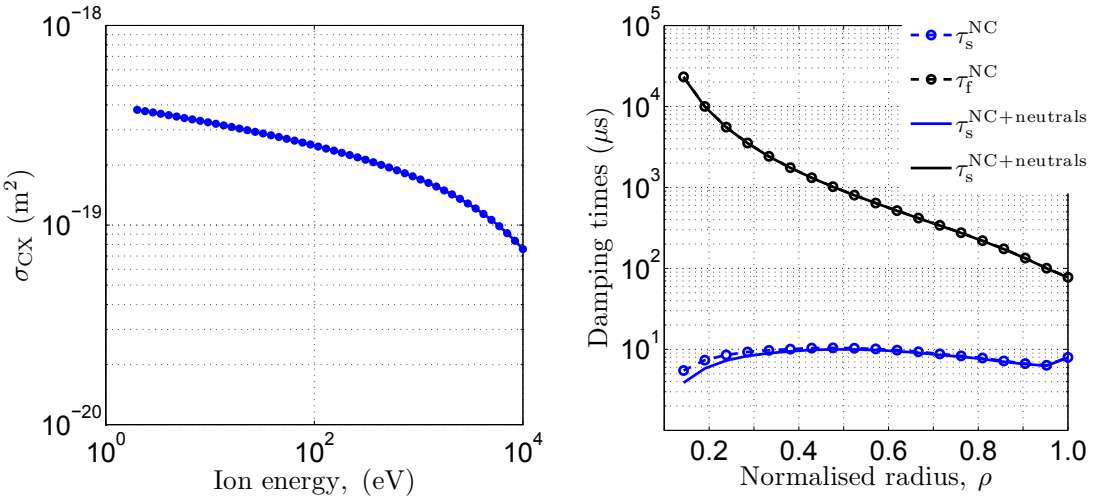

Figure 2.8. (Left) Charge-Exchange cross section between cold hydrogen neutrals and protons. (Right) Effect of the neutral drag on the calculated neoclassical damping times in the plateau regime.

tangential to the surface, i.e. $\mathbf{u}_s \cdot \nabla r = \mathcal{O}(v_s \delta_s^2)$. Next, the structure of the equilibrium parallel flows is determined from the steady-state particle number conservation, equation (2.28). In the axisymmetric case particle number conservation yields an algebraic relation between the parallel flow and the density, see equation (2.37). However, in general toroidal systems such as TJ-II the parallel flow structure (2.29) is obtained from the incompressibility condition, that follows from a particle density that is constant on flux surfaces.

The inhomogeneity of the main ion density, although existing [137, 138], is small in the ordering schemes of kinetic theory, i.e. $n_i = \langle n_i \rangle + \mathcal{O}(\delta_i \langle n_i \rangle)$. Therefore, the lowest order bulk-ion flow is incompressible and thus the form of the parallel flow in (2.29) holds. The situation for impurity ions may be different. For the plateau ions characteristic of TJ-II, medium to high Z impurities are in the Pfirsch-Schlüter collisional regime. As noted in, e.g., reference [100] this collisional character can cause the impurity density variations within a surface to be comparable to their mean value on the surface. This ratio scales like $n_z/\langle n_z \rangle \sim \delta_i \hat{\nu}_{ii} Z^2$. The relative variations of the impurity density within a surface can be of order unity, $n_z/\langle n_z \rangle \sim \mathcal{O}(1)$, even with $\delta_i \ll 1$ still a valid expansion parameter. Indeed, poloidal density variations of high-Z impurities have been observed in several tokamak devices (see reference [139] and references therein). These in-surface density variations cause the parallel impurity flow to deviate from the ion parallel flow as the parallel pressure gradients drive a return flow. Furthermore, the return flows need not preserve an incompressible pattern as particle conservation $\nabla \cdot (n_z \mathbf{u}_z) = 0$ does not reduce to flow incompressibility $\nabla \cdot \mathbf{u}_z = 0$ for a non-constant impurity density n_z. Recent experiments on light impurities (B^{5+} and C^{6+}) using the CXRS technique have reported a poloidal asymmetry of the impurity parallel flow at the pedestal region of the Alcator C-Mod [140] and ASDEX-Upgrade [141] tokamaks, thus indicating a substantial poloidal density variation of light-Z impurities from particle conservation. This impurity density inhomogeneity was later confirmed through direct measurements of the density asymmetry [142–144]. In stellarators, a poloidal variation of the C^{6+} density and poloidal velocity was observed in the core region of

outward shifted plasmas in CHS [145].

The in-surface density variations cause the impurity flows to be compressible, i.e. the function Λ_z in equation (2.29) is not a flux function any more. In a tokamak, since the expression (2.37) is still valid, the inboard/outboard variation of the impurity poloidal flow can be utilized to derive the density asymmetry [140]

$$\frac{n_z^{\rm in}}{n_z^{\rm out}} = \frac{B_{\rm p}^{\rm in}}{B_{\rm p}^{\rm out}} \cdot \frac{u_{z,{\rm p}}^{\rm out}}{u_{z,{\rm p}}^{\rm in}}, \tag{2.79}$$

see equation (2.39). In general stellarator geometry no such closed form can be found. Now, as Λ_z is no longer a flux function, it is convenient to define an impurity parallel return flow as

$$\Lambda(\rho,\theta,\phi) = \Lambda_z(\rho,\theta,\phi) - \Lambda_i(\rho), \tag{2.80}$$

which is associated with parallel gradients of the impurity density. With this particular choice impurity flows are written as the sum of an incompressible flow,

$$\mathbf{u}_{z0} = E_z \frac{\mathbf{B}\times\nabla\rho}{B^2} + (\Lambda_i + E_z h)\,\mathbf{B}, \tag{2.81}$$

plus the return flow (2.80) which compensates for the impurity density redistribution, i.e.

$$\mathbf{u}_z = \mathbf{u}_{z0} + \Lambda(\rho,\theta,\phi)\mathbf{B}. \tag{2.82}$$

Note that this velocity field is the same as that given by equations (2.25) and (2.29), but with $\Lambda_z(\rho,\theta,\phi)$ given by (2.80). Finally, with the impurity flow expression (2.82) the continuity equation (2.28) reads

$$\mathbf{B}\cdot\nabla(n_z\Lambda) = -\mathbf{u}_{z0}\cdot\nabla n_z, \tag{2.83}$$

since $\nabla\cdot\mathbf{u}_{z0} = 0$.

In the next subsection the parallel momentum balance (2.16) is specified for collisional impurities under steady-state conditions [100]. It is shown that the differences in the parallel mass flow between main-ions and impurities generate a friction force which may drive a parallel gradient on the impurity density. Next, from particle conservation a return flow appears, see equation (2.83). Therefore, the impurity parallel momentum balance is solved consistently [102] with impurity continuity equation (2.83). The experimental observation of a compressible impurity flow in ion-root, medium density plasmas of TJ-II is presented in chapter 5. There, we characterize and study the parallel flow $\Lambda_z\mathbf{B}$ in terms of a friction-driven impurity density redistribution. Such a friction model is derived next, although the results of the numerical simulations are left to chapter 5.

2.4.1 Impurity parallel momentum balance

The impurity parallel momentum equation is taken to be

$$T_z\nabla_\parallel n_z + n_z Ze\nabla_\parallel\Phi = R_{z\parallel}, \tag{2.84}$$

where $R_{z\parallel}$ is the parallel friction on the impurities and Φ the electrostatic potential. As demonstrated in reference [100] the impurity temperature is equilibrated with the bulk ion temperature

and is therefore constant on the flux surface. As it is also shown in [100], impurity parallel inertia and viscosity can be neglected in (2.84) if $\delta_i/(Z\hat{\nu}_{ii}) \ll 1$. For the medium density ion-root plasmas to be considered in chapter 5 ($n_\mathrm{i} \in (0.5-3)\times 10^{19}$ m^{-3}, $T_\mathrm{i} \in 100-200$ eV) typical values of the normalised ion gyro-radius and collisionality are $\delta_i \sim 10^{-2}$ and $\hat{\nu}_{ii} \sim 10^{-1}$, respectively. Then, for fully-ionised carbon impurity ions ($Z=6$), $\delta_i/(Z\hat{\nu}_{ii}) \sim 10^{-2}$. Hence, the assumptions made in reference [100] to derive equation (2.84) are applicable here.

In the trace impurity limit, $\sum n_z Z^2 \ll n_i$, the parallel friction on the impurities may be approximated by [146]

$$R_{z\parallel} \approx R_{zi\parallel} = -R_{iz\parallel} = -\int \mathrm{d}^3 v m_i v_\parallel C_{iz}\{f_{i1}\}, \tag{2.85}$$

with f_{i1} the first order departure of the bulk ion distribution function from a Maxwellian. The ion-impurity collision operator can be modelled with a Lorentz operator in a large mass ratio approximation, i.e. $m_z/m_i \gg 1$, plus a term guaranteeing parallel momentum conservation [22]

$$C_{iz}\{f_{i1}\} = \nu_{iz}\mathcal{L}\{f_{i1}\} + \nu_{iz}\frac{m_i v_\parallel u_{z\parallel}}{T_i} f_{i\mathrm{M}}, \tag{2.86}$$

$$\mathcal{L} = \frac{1}{2}\frac{\partial}{\partial\xi}\left[(1-\xi^2)\frac{\partial}{\partial\xi}\right]. \tag{2.87}$$

Here, $\nu_{iz} = 3\pi^{1/2}/(4\tau_{iz}x_i^3)$, $\tau_{iz} = \tau_{ii}n_i/(n_z Z^2)$ is the ion-impurity collision time (with τ_{ii} given by (2.55)), $x_i = v/v_i$, $v_i = \sqrt{2T_i/m_i}$ the ion thermal speed, $\xi = v_\parallel/v$ the pitch-angle and $f_{i\mathrm{M}} = n_{i0}/(\pi^{3/2}v_i^3)\exp\left(-x_i^2\right)$ is a flux-function Maxwellian. Since the collision operator is self-adjoint and $\mathcal{L}\{v_\parallel\} = -v_\parallel$, the term in the parallel friction force arising from the Lorentz operator is written as

$$-\int \mathrm{d}^3 v m_i v_\parallel \nu_{iz}\mathcal{L}\{f_{i1}\} = \frac{3\pi^{1/2}}{4\tau_{iz}} m_i v_i \int \mathrm{d}^3 v \frac{\xi}{x_i^2} f_{i1}. \tag{2.88}$$

Let us consider now the expansion of $f_{i1}(\mathbf{x}, v, \xi)$ in Legendre polynomials $P_l(\xi)$, i.e. $P_0 = 1$, $P_1 = \xi$, etc. [93]. Due to the orthogonality properties of the P_l polynomials in $\xi \in [-1,1]$ only the $l=1$ component of f_{i1} contributes to equation (2.88). Such a component is associated with the parallel particle and heat flows ($u_{i\parallel}$ and $q_{i\parallel}$, respectively) and is expanded by Laguerre (Sonine) polynomials $L_j^{(3/2)}(x_i^2)$[16] as [22, 93]

$$f_{i1}^{(l=1)} = \frac{2}{v_i}\xi x_i\left\{u_{i\parallel} - L_1^{(3/2)}(x_i^2)\frac{2}{5}\frac{q_{i\parallel}}{p_i}\right\} f_{i\mathrm{M}} + f_{i1}^{(l=1,j\geq 2)}. \tag{2.89}$$

Here, $f_{i1}^{(l=1,j\geq 2)}$ denotes the sum of the jth Laguerre polynomial components with $j \geq 2$. The inclusion of $j > 1$ terms [147] is out the scope of this report and thus $f_{i1}^{(l=1)} \approx f_{i1}^{(l=1,j\leq 1)}$ is taken in equation (2.89), as is customary in the moments approach to neoclassical transport [22] (the so-called 13 M approximation). See the comments in section 5.4 regarding the effect of this truncation. With this assumption the parallel friction on the impurities becomes

$$R_{z\parallel} \approx \frac{m_i n_{i0}}{\tau_{iz}}\left(u_{i\parallel} - \frac{3}{5}\frac{q_{i\parallel}}{p_i} - u_{z\parallel}\right), \tag{2.90}$$

[16] The first Sonine polynomials $L_j^{(3/2)}(x_i^2)$ are $L_0^{(3/2)} = 1$, $L_1^{(3/2)} = -x_i^2 + 5/2$, $L_1^{(3/2)} = x_i^4/2 - 7x_i^2/2 + 15/8$, etc.

with $u_{z\|}$ the impurity ion parallel flow[17]. Note that if the exact result for the main-ion distribution function in the Pfirsch-Schlüter regime is used [102]

$$f_{i1}^{(l=1)} = \frac{2}{v_i}\xi x_i \left\{ u_{i\|} - \left(L_1^{(3/2)}(x_i^2) - \frac{4}{15} L_2^{(3/2)}(x_i^2) \right) \frac{2}{5} \frac{q_{i\|}}{p_i} \right\} f_{i\mathrm{M}},$$

the pre-factor $-3/5$ accompanying the parallel heat flow in (2.90) must be replaced by $-2/5$. For simplicity energy exchange is neglected, thus making heat flows incompressible for each particle species, $\nabla \cdot \mathbf{q}_\alpha \approx 0$. Then the bulk ion parallel heat flow is

$$q_{i\|} = \frac{5p_i}{2e}\frac{\partial T_i}{\partial \rho} hB + \langle \mathbf{q}_{i\|} \cdot \mathbf{B} \rangle \frac{B}{\langle B^2 \rangle}, \tag{2.92}$$

with the function h defined in section 2.2. Using the general expression for a compressible impurity flow, equation (2.82), and equation (2.92), the parallel friction on the impurities is finally recast as

$$\begin{aligned} R_{z\|} &= \frac{m_i n_{i0}}{\tau_{iz}} B \left(\left[E_i - E_z - \frac{3p_i}{2e}\frac{\partial T_i}{\partial \rho} \right] h - \Lambda - \frac{3}{5} \frac{\langle \mathbf{q}_{i\|} \cdot \mathbf{B} \rangle}{p_i \langle B^2 \rangle} \right) \\ &\approx p_z \gamma_f B \left(A_i h + B_i - \Lambda \right), \end{aligned} \tag{2.93}$$

with the flux constants $\gamma_f(\rho)$, $A_i(\rho)$ and $B_i(\rho)$ given by

$$\gamma_\mathrm{f} \equiv \frac{m_i Z^2}{T_\mathrm{i} \tau_{ii}}, \tag{2.94a}$$

$$A_\mathrm{i} \equiv \frac{T_\mathrm{i}}{e}\frac{\mathrm{d}\ln n_\mathrm{i}}{\mathrm{d}\rho} - \frac{1}{2e}\frac{\mathrm{d}T_\mathrm{i}}{\mathrm{d}\rho}, \tag{2.94b}$$

$$B_\mathrm{i} \equiv -\frac{3}{5}\frac{\langle \mathbf{q}_\mathrm{i} \cdot \mathbf{B} \rangle}{p_\mathrm{i} \langle B^2 \rangle}, \tag{2.94c}$$

with τ_{ii} the ion self-collision time, see equation (2.55), and $\mathbf{q}_i$ the ion heat flow. In the last step, the impurity diamagnetic term has been neglected against the main ion one. With these assumptions (i.e. trace impurities, $\sum n_z Z^2 \ll n_i$, and 13 M approximation, $f_{i1}^{(l=1)} \approx f_{i1}^{(l=1,j\leq 1)}$) the impurity parallel momentum balance (2.84) results

$$\mathbf{B} \cdot \nabla n_z = \gamma_\mathrm{f} n_z B^2 \left(A_i h + B_i - \Lambda \right) - n_z \frac{eZ}{T_z} \mathbf{B} \cdot \nabla \Phi, \tag{2.95}$$

In stellarator geometry, equation (2.95) and the continuity equation (2.83) form a coupled system [102] of partial differential equations (PDEs). This set of equations can be expressed as a parabolic PDE in the variable $n = n_z / \langle n_z \rangle$

$$\mathbf{B} \cdot \nabla \left(\mathbf{B} \cdot \nabla n \right) - g \mathbf{B} \cdot \nabla n - \gamma_\mathrm{f} B^2 \mathbf{u}_{z\perp} \cdot \nabla n - f n = 0, \tag{2.96}$$

[17] In order to derive equation (2.90), the integral (2.88) is given by

$$\frac{3\pi^{1/2}}{4\tau_{iz}} m_i v_i \int \mathrm{d}^3 v \frac{\xi}{x_i^2} f_{i1} = \frac{m_i n_{i0}}{\tau_{iz}} \sum_{j=0}^{\infty} u_{i\|,j} \int_0^\infty dt e^{-t} L_j^{(3/2)}(t) = \frac{m_i n_{i0}}{\tau_{iz}} \sum_j \frac{(2j+1)!!}{j! 2^j} u_{i\|,j},$$

where $u_{i\|,j}$ (with $j = 0, 1, ...$) are coefficients in the expansion $f_{i1}^{(l=1)} = 2/v_i \xi x_i f_{i\mathrm{M}} \sum_j u_{i\|,j} L_j^{(3/2)}$. From equation (2.89), the first two coefficients are $u_{i\|,0} = u_{i\|}$ and $u_{i\|,1} = -2q_{i\|}/(5p_i)$, so that the parallel friction in its form (2.85) is

$$R_{z\|} = \frac{m_i n_{i0}}{\tau_{iz}} \left(u_{i\|} - \frac{3}{5}\frac{q_{i\|}}{p_i} - u_{z\|} + \sum_{j\geq 2} \frac{(2j+1)!!}{j! 2^j} u_{i\|,j} \right), \tag{2.91}$$

thus recovering equation (2.90) when $j \geq 2$ terms are neglected.

where

$$g(\rho,\theta,\phi) = \mathbf{B}\cdot\nabla\ln B^2 - \frac{eZ}{T_z}\mathbf{B}\cdot\nabla\Phi + \gamma_{\mathbf{f}}B^2\left\{(A_i+E_z)h + B_i + \Lambda_i\right\}, \tag{2.97}$$

$$f(\rho,\theta,\phi) = \gamma_{\mathrm{f}}A_i\mathbf{B}\times\nabla\rho\cdot\nabla\ln B^2 + \frac{eZ}{T_z}\left(\mathbf{B}\cdot\nabla\ln B^2 - \mathbf{B}\cdot\nabla\right)\mathbf{B}\cdot\nabla\Phi. \tag{2.98}$$

Equation (2.96) is converted to an algebraic system of equations by applying finite differences to the variable n, see the appendix C. The angular periodicity of the TJ-II ($T_\theta = 2\pi$ and $T_\phi = \pi/2$) and the condition $\langle n\rangle = 1$ are imposed. The parallel return flow ΛB is obtained from equation (2.83). The system of PDEs has also been solved by Fourier expanding the variables in Boozer coordinates, showing consistency with the finite differences scheme.

Finally, it is noted that the impurity radial transport is written for collisional impurities as [102]

$$\langle\Gamma_z\cdot\nabla\rho\rangle = \frac{1}{e_z}\langle hBR_{z\|}\rangle = \frac{T_z\gamma_{\mathrm{f}}}{e_z}\left[A_i\langle n_z(hB)^2\rangle + B_i\langle n_z hB^2\rangle - \langle n_z hB^2\Lambda\rangle\right]. \tag{2.99}$$

In the last step, the result (2.93) has been used. In addition, the classical flux associated with perpendicular friction is not included in (2.99). Note that in the absence of impurity redistribution, i.e. $n_z = n_z(\rho)$ and $\Lambda = 0$, the last two terms disappear in (2.99) and the usual result, see e.g. ref. [148], is recovered.

Experimental technique

CHAPTER 3

CHARGE EXCHANGE RECOMBINATION SPECTROSCOPY

The study of spectral lines emitted from laboratory and astrophysical plasmas has been used historically to measure numerous plasma characteristics such as concentration and transport of light impurities, or impurity rotation and temperature, these latter being extracted from the Doppler broadening and shift of such lines. However, as plasma temperatures increase in magnetically confined devices [149], the low-Z elements become completely ionized in the interior of these plasmas and no longer emit spectral lines; on the other hand, the detection of high-Z emission lines is restricted to wavelengths shorter than visible wavelengths, typically < 100 nm, where vacuum techniques are required and impurity line shifts might not be resolved.

In the late 70's, R. C. Isler reported [150] on the observation of emission lines from O VIII[1] after the injection of a fast neutral beam in the Oak Ridge Tokamak. The use of such beam-induced line emissions from fully-ionized light impurities became a very active are of research in the 80's [151–153], and was consolidated as a technique for diagnosing hot fusion plasmas in the 90's [48]. Nowadays it is known as Charge-Exchange Spectroscopy (CES) or, more commonly, Charge-eXchange Recombination Spectroscopy (CXRS, also called CXS or CHERS). The European Fusion Development Agreement (EFDA) organisation explains the CXRS technique as follows [154]:

> Neutral atoms in the plasma (from, for example, a neutral beam) donate electrons to fully ionised impurity ions, producing hydrogen-like ions. As the electrons decay from excited states they emit photons from which the impurity temperature, rotation and density can be measured using conventional spectroscopy.

From the analysis point of view, CXRS spectra are convolved with contributions from several atomic effects such as Doppler or Zeeman broadening, as well as from uncertainties in the unresolved emission wavelength transitions from fine-structure levels, which are perturbed by the collisional plasma environment. Furthermore, CXRS requires the use of high-throughput optics plus a high-dispersion optical spectrometer to obtain measurements of impurity temperature and velocity with high accuracy and precision. Therefore, the spectral response of the optical device must be analysed and taken into account.

[1] In spectroscopic notation, O VIII stands for O^{7+}, C VI for C^{5+} and so on.

On the other hand, as an active technique (i.e. a perturbative method) CXRS takes advantage of the localised emission produced by an external source of neutral atoms; usually, a beam of fast neutral particles. The intersection of such a beam and the optical line of sight determines the volume of measurement. However, even though the use of beams permits spatially resolved measurements, the finite de-excitation time of the accepting ion [155] in conjunction with the large velocity of the neutral beam particles [156] cause the daughter distribution function to depart from the original one [157] (which is the one under to study). In particular, the effect on the measured velocity can be considerable.

In this chapter, the above issues are reviewed while highlighting those aspects which are more relevant for CXRS measurements in TJ-II. This chapter is organised as follows: in section 3.1, general concepts such as the charge-exchange process plus active and passive emission are introduced. Next, the collection optics and its alignment are detailed. In section 3.3 the Diagnostic Neutral Beam Injector (DNBI) utilised to excite the spectral line emission is described, together with a method to obtain the beam/line-of-sight interaction volume. In the following section, the mechanisms that affect the recorded line emission are explained and corrected when required. These are, Doppler and Zeeman broadening (section 3.4.1), instrumental response (section 3.4.2), fine-structure effects (section 3.4.3) and the beam-induced line emission during the finite lifetime of the excited impurity ion (section 3.4.4). In section 3.5 all the aforementioned aspects are combined in the data analysis procedure. In addition, examples of measured C^{6+} temperature and density profiles are given. Finally, conclusions are drawn in section 3.6.

3.1 Introduction to Charge-Exchange spectroscopy

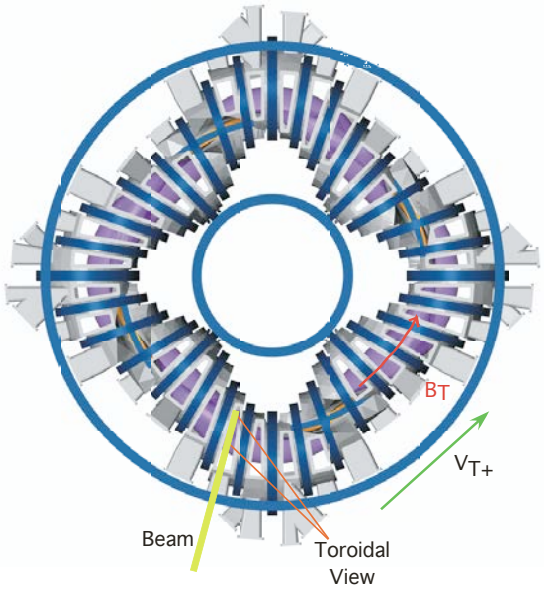

Figure 3.1. Bird's eye view of the TJ-II Stellarator, showing the locations of CXRS diagnostics: the dedicated Diagnostic Neutral Beam Injector (DNBI) and toroidal sightline. Also shown are the direction of the toroidal magnetic field, B_{T}, for the experiments undertaken here and the positive toroidal flow of ions, $V_{\mathrm{T}+}$.

The CXRS technique is based on the transference of charge between a neutral particle and a fully ionised atom. The donor is usually an energetic particle coming from an externally injected beam [48, 158]. Among the charge-exchange (CX) processes between neutral beam particles,

H_b^0, and hot plasma impurities, A^Z, there are several reactions which result in well isolated line emissions, e.g., those involving O^{8+}, C^{6+} or He^{2+}. In the TJ-II CXRS diagnostic the process

$$C^{6+} + H_b^0(nl) \rightarrow C^{5+}(n = 8, l^*) + H_b^+ \rightarrow C^{5+}(n = 7, l) + H_b^+ + h\nu(8 \rightarrow 7), \tag{3.1}$$

was chosen (see section 3.2 in reference [159]). The emitted line is in the visible range, $\lambda_0 = 529.07$ nm, which simplifies the spectroscopic techniques used. Hence, such emissions can be collected by commercial camera lenses, optical fibres and a spectrograph, which permits the C^{6+} impurity poloidal density, temperature and velocity to be measured [46, 105]. For the latter parameters, the ion temperature can be determined from the Doppler broadening of the collected emission line. Besides, the impurity rotation is obtained from the shift in wavelength with respect to the rest wavelength of the emission line of interest.

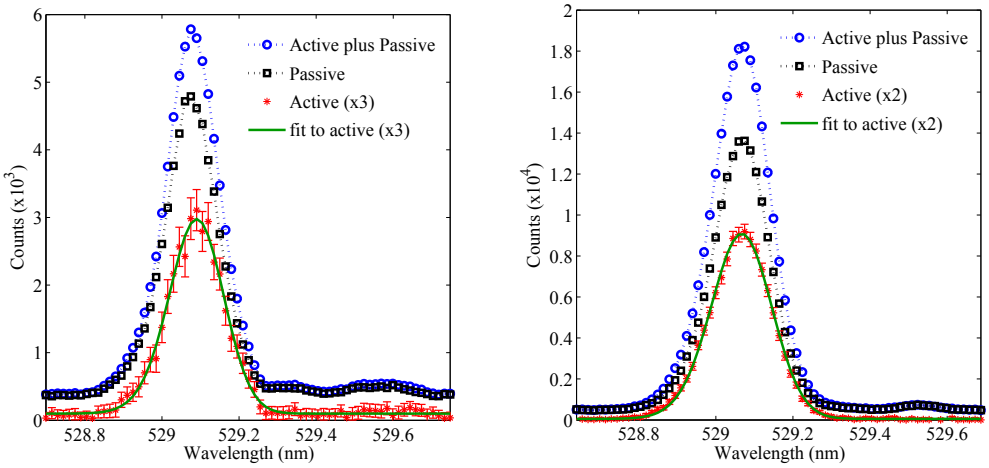

Figure 3.2. DNBI-excited raw C-VI spectral line data (Active plus Passive) and background C-VI line emission (Passive). Note: in spectroscopic notation spectral lines from C^{5+} ions are termed C VI. On the left, two reproducible ECRH plasmas are depicted (A+P: shot#25801; P: shot#25799), whilst the right column corresponds to the NBI heated phase (A+P: shot#32577,; P: shot#32576 on the right, respectively). The active signal is obtained from the difference of the two discharges. Multi-Gaussian fits to the latter are presented.

Before proceeding further, it should be noted that the line emission resulting from (3.1) already exists in the plasma, mostly due to electron excitation [152, 153] and is not a spatially localised emission. Such emission is termed passive. A volume-localized excitation of fully stripped carbon is achieved by injecting a neutral beam into the plasma; Heating NBIs are normally used, see e.g. [160–162], although dedicated Diagnostic Neutral Beams (DNBI) are also frequently employed, as in [46, 163–165]. The advantage of the former is that the beam-excited emission is significantly stronger than the passive contribution, with the drawback of a partial loss of the spatial resolution [166]. On the other hand a DNBI provides the possibility of making measurements in plasmas heated only by waves, as well as obtaining relatively high spatial resolution[2]. In TJ-II, such a system has been installed, see figure 3.1 (from reference [47]). It provides a 5 ms long pulse of neutral hydrogen accelerated to 30 keV (the ratio of its full,

[2] It is noted here that the increasing interest on the impurity density inhomogeneities and flow compression

half and third energy components is 90 : 8 : 2) [46]. Its $1/e$-radius at focus is 21 mm; thus, well localised measurements can be made along the beam path.

As aforementioned, in order to obtain neutral beam induced spectral line data –and hence spatially localized information along sightlines– it is necessary to remove background (passive) C^{5+} light from spectra. This is done by alternatively injecting and not injecting the DNBI into reproducible plasmas (shot-to-shot technique [46]). Then, by subtracting a background spectrum from the stimulated plus background (active plus passive) spectrum the CXRS data are obtained. For ECRH plasmas, the active emission is a factor of ∼5 smaller than the passive one, while in NBI heated plasmas, this ratio is reduced to a factor of 3, see figure 3.2. A multi-Gaussian fit to the active signal is also shown in the figure, and will be explained in section 3.5.

3.2 Collection Optics and Spectrograph

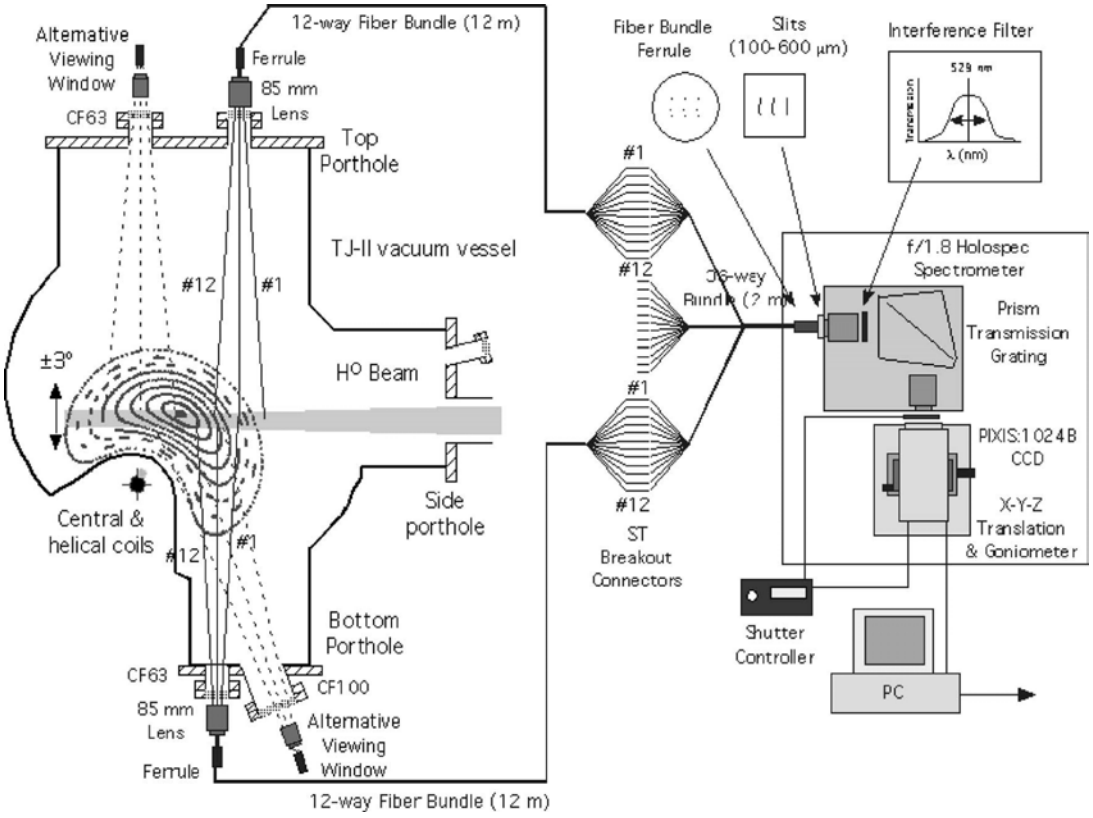

Figure 3.3. Schematic of the multi-channel spectroscopic system for CXRS measurements [46].

For light collection, a tri-directional optical system (two poloidal views plus one toroidal line of sight array) is installed to measure Doppler shifts and widths of this C VI line. It consists of three optical paths which are composed of a 63 mm diameter fused quartz vacuum window/internal

described in section 2.4 has led recently to the development of CXRS rotation measurements which are not based on the use of beams, see e.g. [140, 165, 167, 168]. To this end, cold neutral gas is puffed on the high-field side of a tokamak, where the beams are attenuated before reaching that region of the plasma and cannot be directly injected.

shutter assembly, a commercial camera lenses (85 mm-$f/1.2$ for the poloidal bottom porthole, and 50 mm-$f/1.4$ for toroidal and poloidal top views) and a 12-way fibre optic bundle located at the lens focus. The light is transmitted to the spectrograph equipped with three curved input slits, a bandpass filter (2.0 $\pm$ 0.5 nm), a holographic transmission grating sandwiched between two BK7 prisms, a fast mechanical shutter and a back-illuminated CCD camera (1024x1024 pixel with 13x13 μm^2 sized pixels). Such an optical system is described schematically in figure 3.3, taken from reference [46]. Here, only the poloidal sightlines are shown. The poloidal top fibres are used to correct for uncertainties in the C^{5+} rest emission wavelength, and thus, do not provide additional information about the parent C^{6+} distribution function (further details are given in subsection 3.4.3.1).

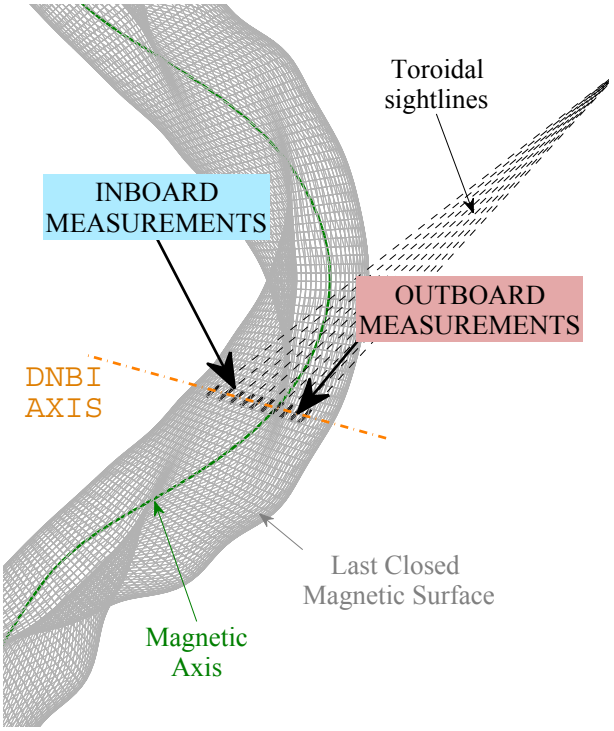

Figure 3.4. A bird's eye view showing the CXRS toroidal lines-of-sight plus the DNBI axis. Also shown is the last-closed magnetic surface for the standard magnetic configuration 100_44_64, plus the magnetic axis. The inboard and outboard toroidal sightlines are highlighted.

The toroidal sightlines were installed during this thesis. It views the DNBI beam from the tangential porthole highlighted in figure 3.1. The toroidal system shares the porthole with a tangential Neutral Particle Analyser, see e.g. [135]. Therefore, a retractable in-vacuum mirror located in the mouth of the access port is needed to redirect light to the lens. This, together with the intricate TJ-II geometry and the lack of access to the vacuum vessel, complicates the alignment of the sightlines and the DNBI, see subsection 3.2.1. In figure 3.4 a top view of TJ-II last-closed magnetic surface and toroidal sightlines is sketched. Note that this system views both sides of the magnetic axis (inboard and outboard toroidal measurements in the figure).

The light focussed by the lenses onto the fibre bundle ferrule is transmitted through 600 μm core superguide G silica fibres to a Holospec Spectrograph, by Kaiser Optical Systems. The 36 fibres are joined together in a single bundle which terminates in a ferrule, fixed to the spectrometer input. As explained in references [46, 169] the entrance slits must be curved to avert the strong curvature produced by the short focal length of the spectrograph. The impact of this

effect on velocity and temperature measurements is studied in section 3.4.2.

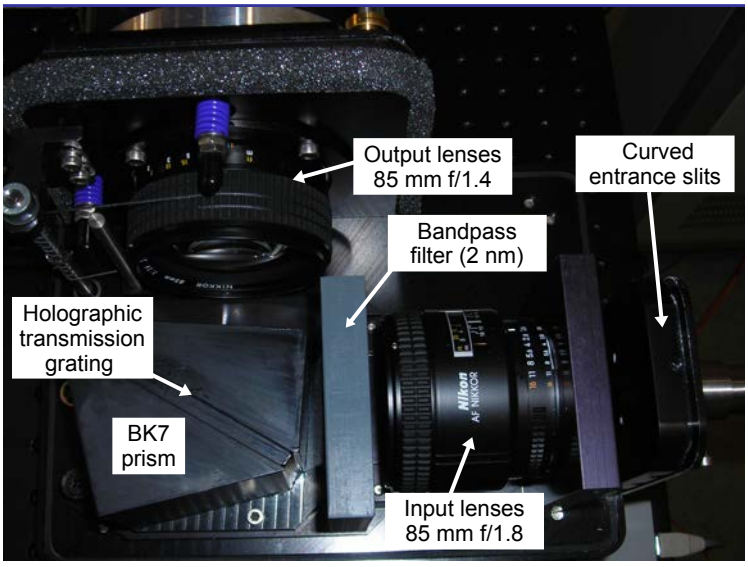

Figure 3.5. Photo of the interior of the Holospec Spectrograph. The main parts are indicated. The bandpass filter was positioned between the input lens and grating.

The Holospec spectrograph is a transmission grating spectrometer, widely employed in CXRS diagnostics, see e.g. [166,170,171]. For the TJ-II, the system consists of an 85 mm $f/1.8$ input lens to provide parallel light, a transmission grating (centred at 5291 Å) that is sandwiched between two right angle BK7 prisms in order to increase the wavelength dispersion at the output focal plane, and an output 85 mm $f/1.4$ lens that focuses the dispersed lighted onto the image plane (see figure 3.5). Finally, a 1024×1024 pixel back illuminated CCD detector (by Roper Scientific, Model Pixis 1024B) is positioned at this image plane. The pixel size is 13×13 μm, resulting in an active area of 13.3×13.3 mm and a linear dispersion at the focal plane of 0.1495 Å/pixel. Further details can be found in reference [159]. A mechanical shutter was installed between the spectrograph and the CCD camera to minimize background light and smearing during the CCD reading time. It allows exposure times of 5 ms to be achieved (the DNBI beam pulse length), with reduced opening and closing times.

3.2.1 Optical alignment and measurement positions

Alignment of the poloidal sightlines is performed by illuminating each fibre bundle with an intense light source and observing, through a nearby view-port, the orientation and location of the resultant bright spots with respect to markings on the inside of the opposing vacuum flange, see the left column of figure 3.6. From these, the sightline paths through the neutral beam are determined using a poloidal cross-section drawing of the machine in the DNBI sector.

On the other hand, alignment of the tangential viewing sightlines involves aligning the in-vacuum mirror as well as orienting the fibre bundle ferrule. For this, a preliminary alignment is made by illuminating the fibres with the intense light source and observing, through a view-port located in a sector downstream of the neutral beam sector, the location of bright spots on the inside of the vacuum chamber as the mirror is rotated. Once the mirror is set so that the lines-

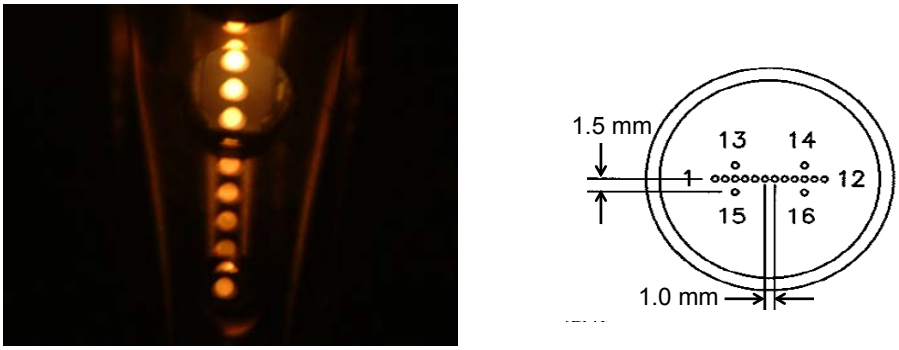

Figure 3.6. (Left) A photo taken through a lower viewport, showing illuminated spots created on the upper vacuum flange of sector A7 when aligning the bottom sightlines: The orientation and location of these bright spots with respect to markings on the inside of the opposing vacuum flange, allow the DNBI-sightline intersections to be determined. (Right) Layout of toroidal fibre bundle ferrule. The fibres numbered 13 to 16 are used to check for line-of-sight symmetry about the beam centre (see text).

of-sight pass through the beam, the light source is removed. Then, the fibre ends that attach to the spectrograph input fibre bundle, are connected to Avalanche Photodiodes (APD) whose bias voltages were previously adjusted to a common gain. Then, by repeatedly injecting the DNBI into the TJ-II chamber, the mirror and fibre bundle are adjusted in-turn until all APD signals are maximized. Moreover, as an additional check, light from the sightlines that straddle the 12 principal sightlines are checked for symmetry about the beam centre, see the right column of figure 3.6. Finally, by repeating the fibre illumination procedure described before for the toroidal fibres, the location of bright spots on the vessel inboard wall are noted and cross-checked. Then, using a 3 dimensional computer aided design (CAD) software with the geometrical coordinates of the vacuum chamber, neutral beam and sightlines as inputs, the beam/sightline crossing points are found for the magnetic configuration of interest. This is schematically represented in figure 3.7.

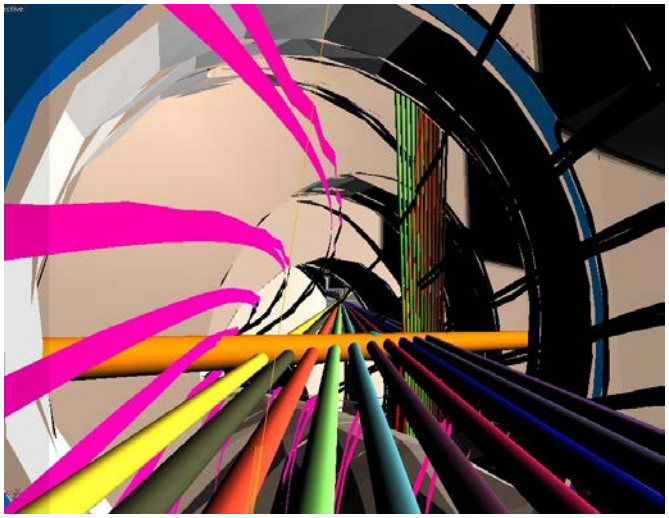

Figure 3.7. Computer Aided Design sketch for the calculation of the DNBI and toroidal sightlines crossing points. The geometrical coordinates of the vacuum chamber, neutral beam (orange cylinder) and sightlines (coloured cylinders) are input to the program. The poloidal sightlines appear as thin vertical cylinders, whilst the toroidal views extend towards the observer. The pink streamers delimit the last-closed magnetic surface (LCMS).

Finally, having determined the poloidal and toroidal measurement positions, their coordinates

are interpolated with the aid of magnetic configuration maps [21] to obtain the corresponding flux surface labels, see equation (1.3). The location of the flux surfaces is known accurately from the vacuum field. Note that the helical axis of TJ-II makes the Shafranov shift is negligible (≤ 3 mm $\beta \leq 1\%$, see e.g. [172]), smaller than the spot size of the fibres. Consequently, the inboard and outboard measurements are directly mapped to flux coordinates using the known magnetic field geometry, and in contrast to the tokamak experiments [140, 141], no additional relative shift between the inboard and outboard measurements is needed for aligning.

An additional check to confirm the goodness of the toroidal ρ mapping is made. For this, the spectrograph grating (set at 529 nm [46]) was exchanged for one centred at 656.2 nm. Then, by injecting the DNBI beam into the vacuum chamber with no magnetic fields, spectra with Doppler-shifted H_α line emission from the beam were collected and analysed. Hence, by determining the Doppler shift of the beam-H_α for each sight line, the corresponding beam velocity was calculated without correcting for the beam to sight line angle. Knowing the beam energy, the beam to sight line angles were determined and the beam/sight line intersection points could be determined. These intersection points were compared with the values obtained using the illumination method described above, thereby confirming the uncertainties in the alignment of toroidal fibres, i.e. $\sim \pm 3$ mm. Note: the separation between toroidal sightlines, ≥ 3 cm, is fixed by the fibre bundle and focusing lens.

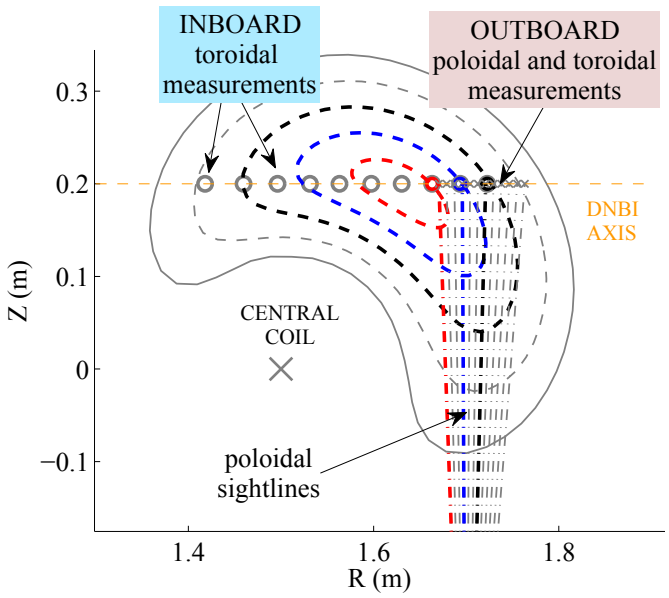

Figure 3.8. A schematic diagram of CXRS diagnostic sightlines with a poloidal cut that shows several magnetic surfaces for the standard magnetic configuration of TJ-II. Toroidal views go into the page, see figure 3.4. The inboard and outboard posiitons of measurement are highlighted. The magnetic surfaces in which poloidal and toroidal outboard measurements coincide, $\rho \sim 0.2, 0.4$ and 0.6, are coloured red, blue and black, respectively. For simplicity, the poloidal top fibres, which are symmetrically opposite to the poloidal bottom ones, are not shown.

A schematic layout of the diagnostic measurement positions is depicted in figure 3.8 (see also figure 3.4). As observed, poloidal cuts of TJ-II magnetic surfaces are bean shaped and exhibit large flux compressions within a surface. The plasma minor radius region spanned by nearly symmetric poloidal views is $\rho \in (0.25, 0.85)$ in the 100_44_64 standard magnetic configuration. As explained in section 3.4.3.1, poloidal top fibres are used to correct for uncertainties in the C^{5+} rest emission wavelength, and thus, do not provide additional information about the C^{6+} distribution function.

On the other hand, the toroidal fibres cover both sides of the magnetic axis, from $\rho = -0.75$

to $\rho = 0.6$ at 10 locations (2 of the 12 sightlines are obstructed by the vacuum chamber). The region in which both poloidal and toroidal measurements are taken is labelled as outboard, in analogy with tokamaks; while the zone where only toroidal measurements are made is labelled as inboard. The nomenclature $\rho \geq 0$ and $\rho \leq 0$ is also utilized to define these regions. In the outboard region, poloidal and toroidal fibres view the same surfaces at $\rho \sim 0.2, 0.4$ and 0.6 (in figure 3.8 these surfaces are coloured red, blue and black respectively). Therefore, the 2D-flow velocity is completely determined at these locations. The redundant inboard-toroidal measurements will be used in chapters 4 and 5 to verify whether the flow incompressibility condition explained in section 2.2 holds or not.

3.3 Diagnostic beam and volume averaged measurements

The measurement volume for a given line of sight, $\mathcal{V}_{\rm los}$, results from the intersection of the DNBI path and the volume observed by each fibre. Therefore, the measured density, temperature and velocity of C^{6+} ions are the result of averaging in that volume. When CXRS is performed with a heating NBI, inversion techniques are needed to recover the local values [166]. In TJ-II, the use of a compact DNBI with a small footprint in the plasma (its 1/e-radius at focus is 21 mm [46]) allows for measuring local quantities. However, since these are averaged measurements, any geometrical quantity $X(\mathbf{r})$ used during data processing (e.g. magnetic field strength, sight-line cosines or Pfirsch-Schlüter dimensionless factor (2.32), among others) has to be averaged in the measurement volume $\mathcal{V}_{\rm los}$. This is done by considering the weighted integral

$$\langle X \rangle_{\mathcal{V}_{\rm los}} := \frac{\int_{\mathcal{V}_{\rm los}} d^3\mathbf{r} \varepsilon X}{\int_{\mathcal{V}_{\rm los}} d^3\mathbf{r} \varepsilon}, \tag{3.2}$$

with $\varepsilon = \langle \sigma v \rangle_{\rm cx} n_{\rm b} n_{\rm C}$ the local C^{5+} brightness, $n_{\rm b}$ the density of fast neutral particles and $n_{\rm C}$ the density of C^{6+} ions. Thus, local beam and carbon impurity densities are required to solve this integral.

3.3.1 Diagnostic neutral beam injector profile

The work presented in this subsection is based on reference [159]. The intention here is not to characterize the beam in detail (see, e.g., the detailed work in reference [163]), but rather to provide an estimate of its radial extent, and consequently, of the measurement volume. To this end, beam attenuation is estimated by considering a simple pencil-like attenuation model [49, 159],

$$n_{\rm b} \approx n_{\rm b,vac} \exp\left(- \int_{\substack{\rm beam \\ \rm path}} \alpha(l) {\rm d}l \right), \tag{3.3}$$

with $\alpha(l)$ the local attenuation factor along the beam path [135],

$$\alpha(l) \approx n_{\rm e}(l) \left(\sigma_{\rm p} + \sigma_{\rm cx} + \frac{\langle \sigma_e v_e \rangle_0}{v_b} \right), \tag{3.4}$$

where the charge exchange ($\sigma_{\rm cx}$), and ionization by proton impact ($\sigma_{\rm p}$) and by electron impact ($\langle \sigma_e v_e \rangle_0 / v_{\rm b}$) cross sections [132, 173] are expressed in terms of the beam energy in the top of

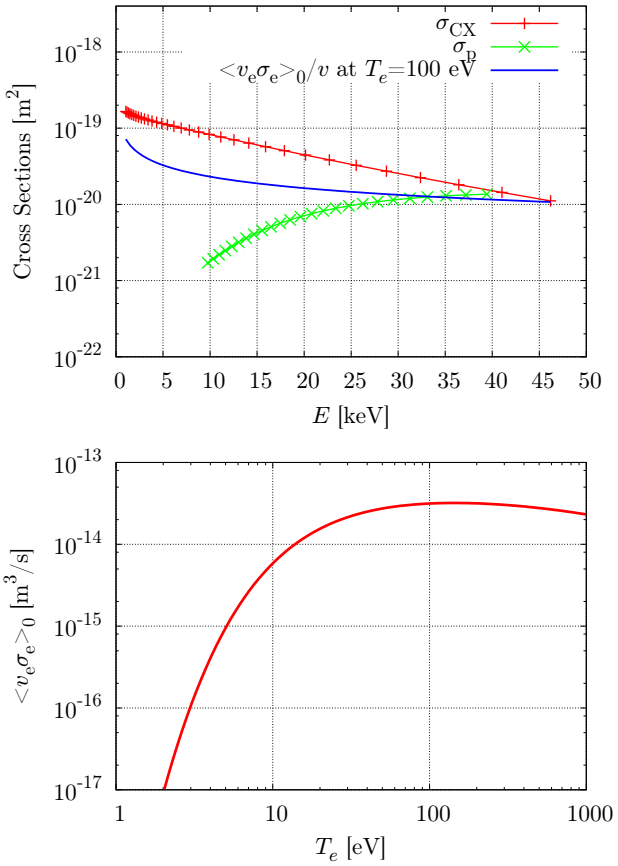

Figure 3.9. Cross sections for the relevant atomic processes in DNBI attenuation [132]: charge exchange (σ_{cx}), ionization by proton impact (σ_p) and ionization by electron impact (σ_e) as a function of the neutral energy. Note that the ionization by electron impact rate, $\langle\sigma_e v_e\rangle_0$, depends also on the background electron temperature, T_e, as shown at the bottom.

figure 3.9. The ionization by electron impact rate ($\langle\sigma_e v_e\rangle_0$) depends also on the background electron temperature T_e, as shown at the bottom of the figure.

In equation (3.3) $n_{b,vac}$ stands for the beam particle density profile in vacuum, which is proportional to the current density in vacuum [159],

$$n_{b,vac} \propto j_v(0) \exp\left(-\frac{\pi}{I_b} j_v(0) r^2\right), \tag{3.5}$$

with I_b the total beam intensity, r the radial distance to the beam axis and $j_v(0)$ the beam current in vacuum at the beam axis,

$$j_v(z,0) = \frac{I_b}{\pi r_0^2}\frac{z_*^2}{z^2}\left\{1 - \exp\left(-\frac{\alpha_0 r_0^2}{z_*^2}\right)\right\}. \tag{3.6}$$

Here, $\alpha_0 \approx 5^o$ is the beam divergence, $r_0 = 4$ cm the acceleration grid radius, z the axial distance along the beam path, $z_* = (1/z - 1/z_f)^{-1}$, and $z_f = 170$ cm the focal distance [159]. Such formula (3.5) has been benchmarked with the equations derived in references [163, 174], showing quantitative agreement. Profiles of the DNBI, equations (3.3) and (3.5), can be found in reference [159] for several plasma conditions.

3.3.2 Volume averaged measurements

In order to perform averaging over a measurement volume, equation (3.2) requires the carbon impurity density as input. As an approximation, the carbon density can be substituted by the electron density in equation(3.2), which is thus simplified to

$$\langle X \rangle_{\mathcal{V}_{\rm los}} \approx \frac{\int_{\mathcal{V}_{\rm los}} d^3\mathbf{r} n_{\rm b} n_{\rm e} X}{\int_{\mathcal{V}_{\rm los}} d^3\mathbf{r} n_{\rm b} n_{\rm e}}. \tag{3.7}$$

The integral (3.7) requires the use of three different grids to interpolate the magnitudes: a cylindrical grid for the beam, 36 cylindrical grids for the sightlines, and the curvilinear grid developed by J. Guasp [21] for plasma magnitudes. Numerical routines to quickly interpolate in a grid a certain quantity defined in another grid have been developed.

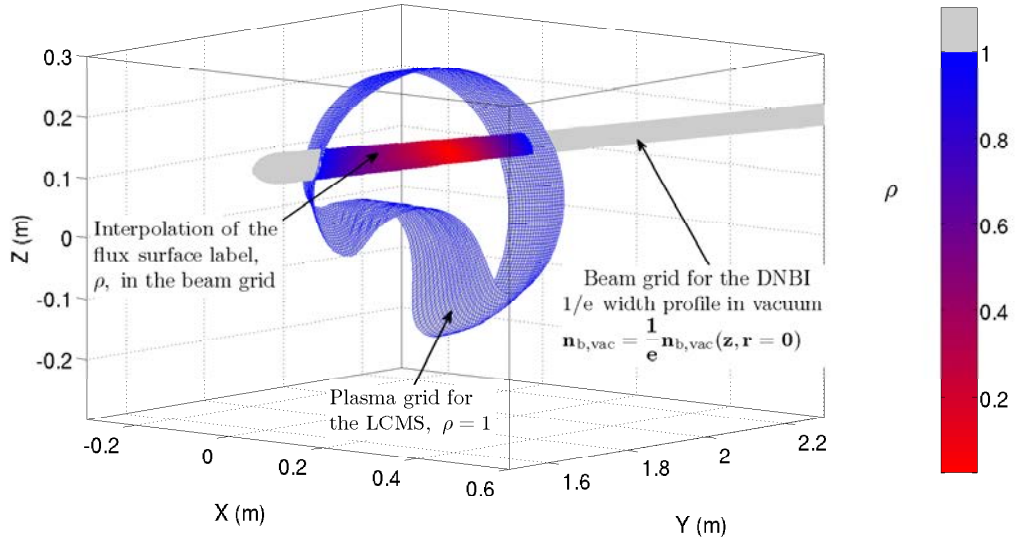

Figure 3.10. DNBI profile at its $1/e$-width, with the magnetic surfaces crossed by the DNBI. The last closed magnetic surface ($\rho = 1$) is shown as well. The DNBI enters the plasma at constant toroidal angle, $\phi = 75.5$ °, and vertical position, $Z = 0.2$ cm. Note that the beam axis does pass through the magnetic axis.

As an example of such a calculation, the DNBI vacuum profile at its $1/e$-width is represented in figure 3.10. The vacuum profile is calculated with equation (3.5); from it, the positions at which the beam particle density has been reduced by a factor $\sim 1/e$ of its value at the beam axis are obtained. The colour label in figure 3.10 represents the magnetic surface crossed along the beam path at these positions. Here, the magnetic surface label ρ has been obtained in the plasma grid (from the known vacuum magnetic field [21]) and interpolated in the beam grid. These kind of interpolations are useful for rapid data processing. For instance, they allow estimating the beam attenuation, equation (3.3), since the electron density and temperature in the attenuation coefficient, equation (3.4), are flux-functions.

The errors associated with the average of the geometrical factors, equation (3.7), are given by the standard deviation in the measurement volume,

$$\delta_X = \left\{ \langle X^2 \rangle_{\mathcal{V}_{\rm los}} - \left(\langle X \rangle_{\mathcal{V}_{\rm los}} \right)^2 \right\}^{1/2}, \tag{3.8}$$

and are propagated through the code. Therefore, the errors in the final results will consist of statistical ones, plus standard deviations of geometrical factors in the measurement volume.

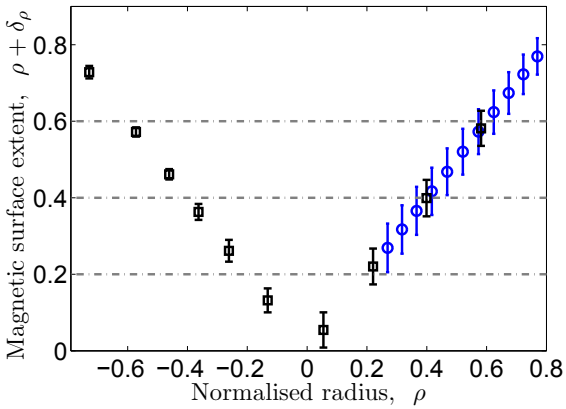

Figure 3.11. Magnetic surface extent (vertical axis) observed by poloidal (blue) and toroidal (black) CXRS sightlines for the 100_44_64 magnetic configuration, as calculated from equations (3.7) and (3.8). For clarity, poloidal top measuring positions are not shown. Horizontal dashed lines at $\rho = 0.2, 0.4$ and 0.6 are plotted, to indicate the magnetic surfaces in which three independent measurements are made (toroidal inboard and outboard, and poloidal outboard).

In figure 3.11, the magnetic surface extent $\rho \pm \delta_\rho$ seen by the poloidal bottom and toroidal sightlines in the standard magnetic configuration is presented in blue and black, respectively, as calculated from equations (3.7) and (3.8). It is observed that in the outboard region, the poloidal and toroidal fibres view the same radial locations at $\rho \sim 0.2, 0.4$ and 0.6. Although not shown in this figure, the poloidal top and bottom measurements coincide over the region $\rho \in (0.25, 0.85)$ (see section 3.2.1). The magnetic surfaces spanned by a poloidal sightline increase as moving towards the magnetic axis, due to the vertical inclination of these sightlines. In contrast, the number of surfaces observed by a toroidal sightline is smaller, due to the alignment of these with the magnetic field.

3.4 Mechanisms affecting line emission

As a spectroscopic technique, CXRS requires knowledge of the atomic processes involved in the spectral line broadening and shifting (e.g., Doppler, Zeeman, Stark effects etc. or fine structure broadening), as well as instrumental effects. In addition, other contributions arising from the use of neutral beams, e.g., gyro-orbit motion, plume effect, energy cross-section dependence, etc. must be taken into account. Here, such effects are highlighted and discussed with respect to their effect on carbon temperature and rotation measurements for TJ-II specific conditions (i.e., $B \leq 1$T; $\mathrm{T_i}$,$\mathrm{T_C} \leq 200$ eV; $u_\mathrm{t}, u_\mathrm{p} \leq 30$ km s^{-1} $\ll v_{Ti}$ and $\bar{n}_\mathrm{e} \leq 5 \times 10^{19}$ m^{-3}).

3.4.1 Classical line-broadening: Doppler and Zeeman broadenings.

3.4.1.1 Doppler effect

A photon emitted by a fast particle appears shifted in frequency when observed in a laboratory frame. This is known as Doppler effect, and can be explain heuristically as follows: let us consider an excited particle emitting with a frequency ν_0 when at rest. If this particle is moving with a velocity v, it continues emitting at the same frequency in the rest frame. However, in the laboratory frame, the time between two wave-fronts has changed, due to the relative movement of both systems. As frequency, ν, and wavelength, λ, are related through the speed of light as

$c = \nu\lambda$, a change in frequency produces a change in wavelength: $\delta\lambda/\lambda = -\delta\nu/\nu$. Therefore, for small variations, $\Delta\lambda/\lambda_0 = -\Delta\nu/\nu_0$. Mathematically, this can be expressed in a compact form as

$$\lambda_v = \lambda_0 \sqrt{\frac{1 + \mathbf{v}\cdot\mathbf{l}/c}{1 - \mathbf{v}\cdot\mathbf{l}/c}} \sim \lambda_0 (1 + \frac{\mathbf{v}\cdot\mathbf{l}}{c}) \tag{3.9}$$

Here, $\mathbf{v}$ is the relative velocity between the particle and the observer and $\mathbf{l}$ is a unitary vector in the direction of observation. If the particle is moving away from the observer the frequency measured by the observer decreases and the wavelength increases, i.e. there is a red-shift in wavelength, $\Delta\lambda = \lambda_v - \lambda_0 > 0$, towards longer wavelengths (in the visible range, towards the infrared region). On the other hand, if the particle is moving towards the observer, there will be a blue-shift towards shorter wavelengths (in the visible range, towards the ultra-violet region).

When a population of excited atoms is emitting, each one produces a different displacement in wavelength, thereby broadening the otherwise delta function-like emission. If the particles of species s have a Maxwellian distribution of velocities, then, as each moving particle produces a different wavelength shift in the laboratory frame, equation (3.9), the spectral line acquires a Gaussian shape,

$$I_s(\lambda)d\lambda = I_{\mathrm{sp}} f_{s\mathrm{M}}(v) d^3v \propto \exp\left(-4\ln 2 \left(\frac{\lambda_v - \lambda_{u_s}}{\sigma_s}\right)^2\right) d\lambda. \tag{3.10}$$

Here, I_{sp} is the light emitted by a single particle of the species s, $f_{s\mathrm{M}}$ is a Maxwellian distribution function (see equation (2.11)), σ_s is the Full-Width at Half-Maximum (FWHM) of the spectral line, λ_v is the shift produced by each velocity $\mathbf{v}$ and λ_{u_s} is the wavelength displacement due to the mean velocity $\mathbf{u}_s$. From this, the temperature of the emitting population, i.e. the standard deviation of the velocities, can be determined as

$$T_s = \frac{m_s c^2}{8e\ln 2}\left(\frac{\sigma_s}{\lambda_0}\right)^2 = 1.68\times 10^8 m_s(\mathrm{u})\left(\frac{\sigma_s}{\lambda_0}\right)^2 \ (\mathrm{eV}) \tag{3.11}$$

Here, λ_0 is the unshifted wavelength of the spectral line. The mass m_s of the particle species s is in atomic mass units (u), and λ_0 and σ_s must be in length units. For the typical ion temperatures observed in TJ-II, $T_{\mathrm{i}} \leq 200$ eV, Doppler widths of about $\sigma_{\mathrm{C}} \leq 1.7$ Å are expected for the C VI $n{=}8 \rightarrow n{=}7$ line at 5290.7 Å. This is now compared with other broadening terms.

3.4.1.2 Zeeman effect

In the presence of a magnetic field the ion energy levels are split in accordance with the interchange energy term: $W = \mu_B g \vec{J}\cdot\vec{B}$ (here, μ_B is the Bohr magneton and g the Lande factor). For typical TJ-II magnetic fields of $B \sim 1$ T, the Russel-Sanders approximation can be used [175–177].

According to reference [48], the ratio between the Zeeman and Doppler broadening is:

$$\frac{\sigma_{\mathrm{Zeem}}}{\sigma_{\mathrm{Dopp}}} = 6.06\times 10^{-5}\left(\frac{m_s(\mathrm{u})}{T_s(\mathrm{eV})}\right)^{1/2} B(T)\cdot\lambda(\mathrm{Å}) \tag{3.12}$$

For the C VI emission at 5290.7 Å, $T_C = 100$ eV and B= 1 T, this ratio is ~ 0.11. This signifies that the shape of the line is not distorted by the Zeeman splitting, rather it is broadened. Thus a correction factor can be applied when estimating the temperature from the width of the measured spectral emission line [178, 179] rather than considering all Zeeman components when making a fit to the spectral line [180]. Such a derating factor is presented in figure 3.12 as a function of the measured impurity temperature. For the relative intensities of the π ($\Delta M_J = 0$) and σ ($\Delta M_J = \pm 1$) Zeeman components, the angle α between the magnetic field and the viewing chord must be known. In the figure, $\alpha = 60^0$ has been used, although the actual magnetic filed to each sightline angle is utilized in the data anlysis.

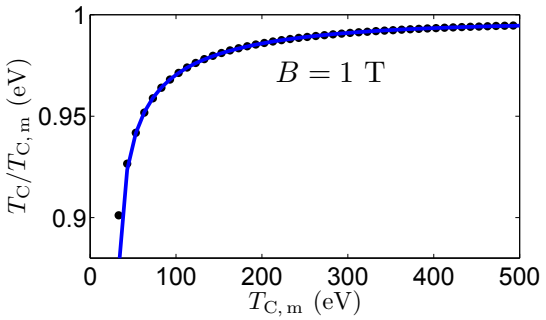

Figure 3.12. Derating factor for Zeeman temperature broadening. Here, $T_{C,m}$ is the C^{6+} temperature measured when making a Gaussian fit to the spectral line. The magnetic field is set to $B = 1$ T in this correction.

3.4.2 Instrumental effects

Correctly performed instrument calibration is essential if experimental uncertainties are to be minimized. Indeed, this should be done regularly during machine operation as thermal stresses in the spectrograph can be significant and can result in small but notable shifts of the CCD with respect to the focal plane centre [181], e.g. 4 μm K^{-1} at the focal plane –this being equivalent to an offset of $\sim$2.5 km s^{-1} K^{-1} for velocity measurements. For wavelength calibration, spectral lines [182] at 5274.0393, 5280.0853, 5298.1891 and 5304.758 Å from a neon pencil type lamp are used to establish the wavelength dispersion at each fibre location on the focal plane, this being $\sim$11.5 Å/mm at its centre. An in-house mounting structure was developed to facilitate this calibration procedure, see figure 3.13. In addition, all spectrographs suffer from broadening of the spectral emission line. As a result a numerical deconvolution of the instrument function and the measured spectral line must be carried out to determine the Doppler broadening of the said line, and hence the temperature. Here, the instrumental FWHMs, σ_{if}, are determined from the weighted means of the FWHMs of the Ne I lines at 5280.0853 and 5298.1891 Å.

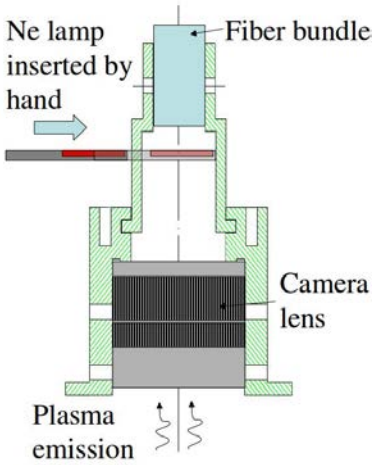

Figure 3.13. Scketch of the calibration mounting structure. The neon lamp is inserted manually between the light collections lens and the fibre bundle, which are located outside the vacuum chamber.

In the following subsections these effects (i.e. numerical deconvolution of the instrumental function, wavelength calibration and thermal drifts) are described and their influence on measurements are discussed.

3.4.2.1 Instrumental broadening

Spectrometers are not perfect and produce a spectral line with a finite width at the output. This broadening is called the instrumental function (IF). Generally, as well as a broadening of a spectral line there can also be loss of intensity and, in some cases, a deformation of the original shape. Therefore, the effect of the detection system must be removed from the measured emission before analysing the data.

This procedure is expressed mathematically as a deconvolution [183],

$$I_{\mathrm{m}}(x) = \int dx' I(x - x')\mathrm{IF}(x'). \tag{3.13}$$

Here, I_{m} and I are the light intensities at the spectrograph output and input, respectively, and x is the pixel number in the CCD horizontal direction. It is a common practice to approximate the IF by a Gaussian profile. Since the main broadening mechanism in hot fusion plasmas is Doppler broadening (which produces a Gaussian shape of the spectral lines as shown in section 3.4.1), the well known equation for the convolution of two Gaussian functions is generally employed,

$$\sigma_{\mathrm{m}}^2 = \sigma_{\mathrm{if}}^2 + \sigma^2. \tag{3.14}$$

Here, σ_{m}, σ_{if} and σ are the FWHM of the measured line, the instrumental function and the original line emission of the impurity ion.

Nonetheless, equation (3.14) is only applicable when the IF is Gaussian. For the transmission grating spectrometer used here, stigmatic imaging of the entrance slit results in a deviation of the instrumental function from a Gaussian shape, i.e., it becomes more trapezoidal as the entrance slit width is increased. Hence, for fitting, a Gaussian function modified by an exponent s is required,

$$\mathrm{IF}(x) \propto \exp\left(-\ln 2\left(\frac{4x^2}{\sigma^2}\right)^s\right). \tag{3.15}$$

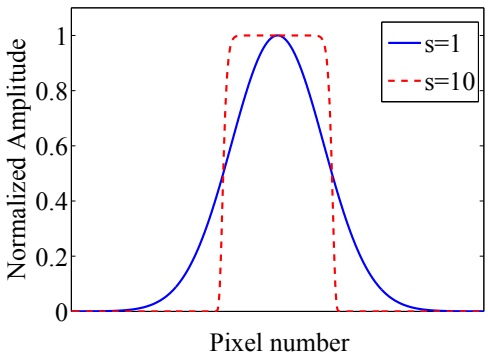

Figure 3.14. Effect of the s-exponent on the Instrumental function: when $s = 10$, the profile becomes rectangular, whilst for $s = 1$ a Gaussian is obtained.

The exponent s provides the IF with a *trapezoidal* shape [170]. Similar IFs have been measured in other devices which use the same spectrograph [171, 184]. Furthermore, this effect was also observed in the HSX, where two Czerny-Turner spectrographs with relatively wide input slits of ~ 200 μm are used. The effect of such an exponent on the IF is shown in figure 3.14. For high values of the s-exponent, $s \sim 10$, the profile acquires a rectangular shape; when s=1, a Gaussian curve is recovered.

The source of the trapezoidal IF can be found in the stigmatic imaging produced by the entrance slit [170]. Due to the finite size of the entrance slit, incoming light will produce a finite spot at the diffraction device -a grating-. There, wavelengths are separated spatially, so each one arrives at a different location at the focal plane (i.e., the CCD detector). Therefore, each wavelength will produce a different spot at the image plane. Hence, overlapping of individual wavelength images at the CCD detector is obtained. The coupling of the wavelengths depends on the input slit width, the dispersion power of the grating, etc. For instance, different entrance slit widths produce different IFs for the same optical system, as is demonstrated by comparing the instrumental response of two similar CXRS systems, in TFTR [170] and TJ-II [59]. In the former case, where a 250 μm-slit was used during a glow discharge calibration, the IF was almost rectangular. In contrast, a 100 μm-wide slit is utilized in TJ-II, and an IF with an exponent $s = 1.3$ is observed.

The influence of the IF on the 5298.189 Å Ne I line used for calibration is presented in figure 3.15. On the left column, a fit with the trapezoidal profile given by equation 3.15 is performed. The resultant FWHM is $\sigma_{\mathrm{if,trapez}}$=7.68 pixels =1.15 Å, and s=1.31. A second fit is plotted on the right (red solid line). In this case, a small broadened ($\sigma_{\mathrm{if,wing}}$=1.47 Å) Gaussian function is superimposed on the trapezoidal curve, in order to reproduce the wing-like features that appear at the edges of the Ne I line. The inclusion of these wings causes an increase in the exponent s. Note: the centroids, λ_0, of both curves are left free. The wavelength difference in the best fit line centroids obtained by fitting with or without the broad Gaussian would result in a velocity uncertainty smaller than statistical errors. However, as will be shown, the deconvolution process can give rise to different impurity temperatures when the wings are considered in the fit.

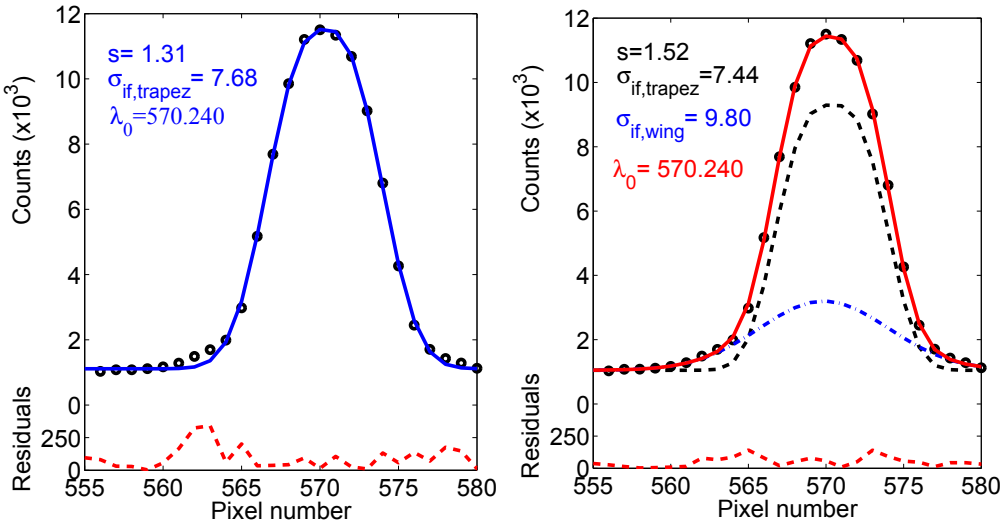

Figure 3.15. Trapezoidal Instrument Function for the 5298.189 Å Ne I line. Instrumental FWHM, σ_{if}, and centroid wavelength, λ_0, are given in pixels. The dispersion at this region is 0.15 Å/pixel. (Left) Trapezoidal profile, with s=1.31. (Right) Trapezoidal plus a broadened Gaussian (labelled "wings"). Residuals are plotted at the bottom.

The effect of wavelength overlapping is dependent on the original spectra line width [59]: for emission lines from calibration lamps, it is been shown that the otherwise Gaussian shape

is distorted towards a trapezoidal curve. In contrast, when the Doppler temperature broadened C VI emission line is considered, even though the coupling is the same (it depends only on slit width), it is not sufficient to modify the shape of the curve for the experimental conditions considered here. This is shown in figure 3.16, where fits with s=1 (blue dashed line) and s=1.31 (red dash-dot line) have been applied to the experimental C VI data (black open circles) from a NBI heated plasma in the final steps of the discharge. The one with s=1 provides the best fit to the C VI experimental data as demonstrated by lower residuals across the full wavelength range (fine structure effects are also considered in the fit models [153]). The carbon temperatures obtained after applying a Gaussian deconvolution, equation (3.14), are $T_{\rm C}(s{=}1) = 77.2$ eV and $T_{\rm C}(s{=}1.31) = 104.3$ eV. Thus, the use of the calibration exponent to fit the C VI data leads to an overestimated temperature [185].

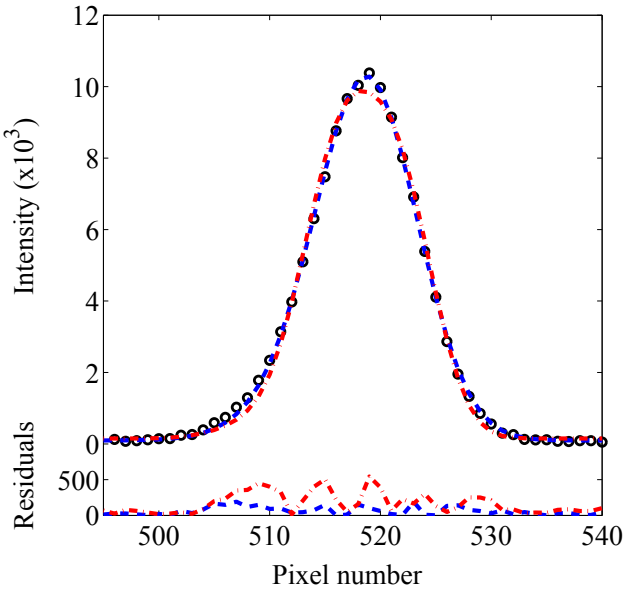

Figure 3.16. A measured C VI line at 529.055 nm (black circles), fitted with a Gaussian profile (s=1, dashed blue line) and the exponent $s = 1.31$ obtained from calibration (dash-dot red line). Residuals are presented at the bottom.

However, as commented before, equation (3.14) is only valid when two Gaussian functions are considered. In the present case, the previous convolution must be considered, see equation (3.13). It implies the division of two polynomials, which in general is inexact. Instead, a numerical convolution is performed for a range of test Maxwellian emissions, $\mathrm{I_{test}}$,

$$I_{\rm m}(x) = \int dx' I_{\rm test}(x) \mathrm{IF}(x - x'). \tag{3.16}$$

As the integration, and so the convolution, is a linear process fine structure components of the C VI emission are not considered during $\mathrm{I_{test}}$ construction. So, once the measured $\sigma_{\rm if}$ and $\sigma_{\rm m}$ have been input, test functions with different Doppler broadening are convolved until the FWHM of the resultant function matches the measured one. This process demonstrates that the detected light is not distorted by the optical system, i.e., its shape remains Gaussian, rather it is just broadened. For the experimental data shown in figure 3.16 this procedure yields $T_{\rm C} = 95.43$ eV.

The differences in estimated impurity temperature when using equations 3.14 and 3.16 are displayed in figure 3.17 as a function of the actual carbon temperature. When Doppler broadening is large compared to the instrumental width the convolution process approaches the classical

one, and the correction factor tends to one. In contrast, for impurity temperatures close to the instrumental temperature –T_{if}, obtained by inserting σ_{if} in equation (3.11)–, the difference becomes significant. For the experimental conditions outlined here, this is ∼15%.

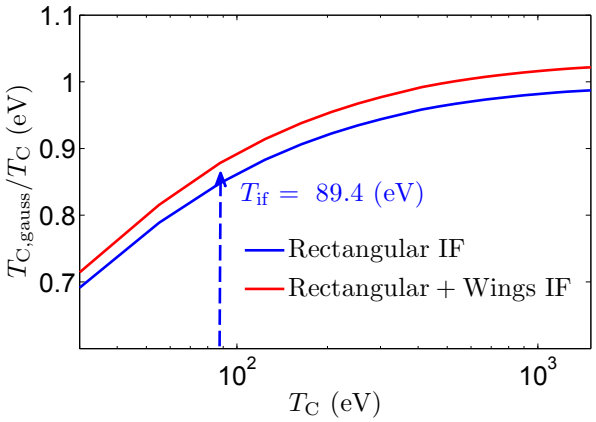

Figure 3.17. Correction factors for impurity temperature obtained through Gaussian and direct deconvolution, using a trapezoidal IF and a trapezoidal plus wings model for the IF. Here, T_{if} is the equivalent temperature obtained by inserting the measured instrumental width, σ_{if}, in equation (3.11).

In addition, as seen in figure 3.15, the best fit profile obtained with equation (3.15) does not completely reproduce the instrumental shape at the edges where "wings" exist, these possibly being due to the diffraction pattern introduced by the slit and the grating. These "wing" features can be modelled by imposing a small but broad Gaussian function when fitting with equation (3.15), with the centroids of both curves set as free parameters. The result of such a fit is shown in figure 3.15. The wavelength difference in the best fit line centroids, λ_0, obtained by fitting with or without the broad Gaussian, yields a velocity uncertainty that is less than the statistical errors. As observed in figure 3.17, both methods (with/without wings) give values that are in good agreement for the range of ion impurity temperatures expected in the core of TJ-II plasmas, $100 \leq T_C \leq 200$ eV. However, this multi-curve fit is less stable when the instrumental function differs greatly from the expected trapezoidal shape. Therefore the more stable fit model without wings is used in the data analysis.

In summary, careful handling of the instrumental function deconvolution is necessary, when this differs from a Gaussian shape, in order to avoid a systematic underestimation of impurity ion temperature in plasmas. In the case of the TJ-II such an underestimation can be up to 20% when the impurity temperature approaches the instrumental temperature (∼90 eV for 100μm slits). Whilst the choice of fitting function is critical when determining impurity ion temperature, its influence on impurity flow is less that statistical errors.

3.4.2.2 Wavelength calibration

As commented in the previous section, a correct analysis of the instrumental function is essential for impurity temperature determination. Besides, the light dispersed by the spectrometer and recorded by the CCD camera does not have an absolute wavelength reference. Hence, the multi-channel spectroscopic system must be calibrated for each sightline so that wavelength and pixel number are related. From it, the linear dispersion of the instrument, $\Delta\lambda/\Delta x$ (Å/ pixel), can be deduced.

For this a calibration is performed for each of the three 12-way fibre arrays with a Neon

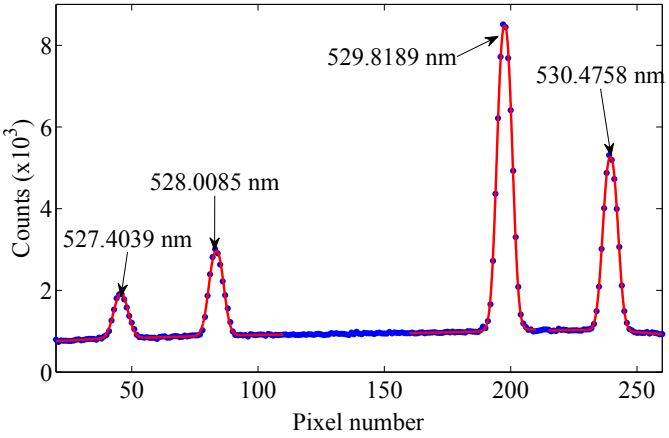

Figure 3.18. A spectrum of Ne I calibration lamp obtained for a poloidal top sightline plotted as a function of CCD pixel number. The emission line wavelengths [182] are shown. The dots represent counts in CCD pixels. The continuous red line is the best fit obtained by the fitting procedure developed.

pencil-type lamp (from Newport, California (USA), model 6032). The lamp is inserted between a 85 mm f/1.2 camera lens mounted on TJ-II and the fibre bundle [46], in such a way that the numerical aperture of each of the 12 fibres is filled. To this end, an in-house mounting structure was developed to facilitate this calibration procedure, see figure 3.13. Three or four Ne I lines close to the C VI 5290.55 Å emission are considered: 5274.0393, 5280.0853, 5298.1891, 5304.7580 Å [182]. A typical spectra is seen in figure 3.18.

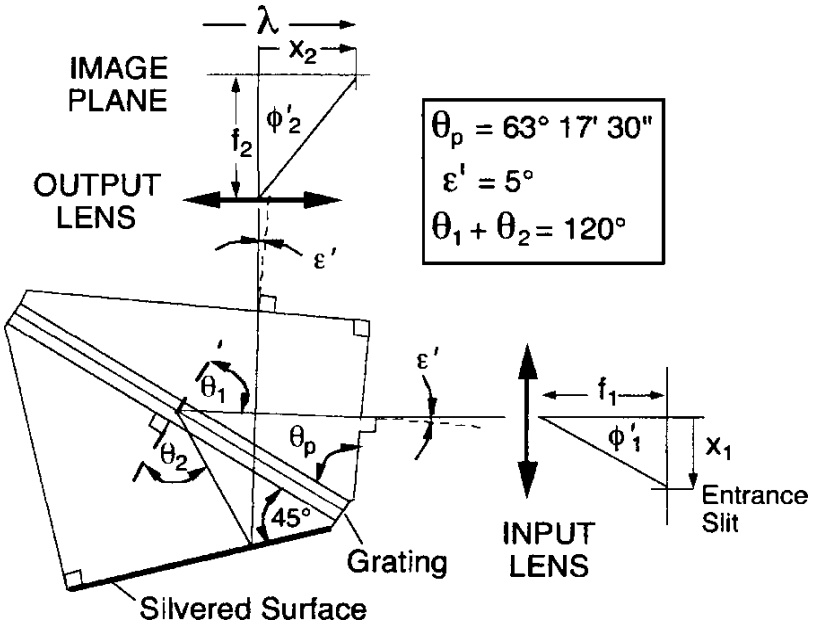

Figure 3.19. Schematic of the transmission grating Spectrograph. Image taken from reference [169].

Now, knowing the wavelengths of the calibration lines of interest, the calibration procedure can be started. However, a model for the relation $\lambda = \lambda(x)$ is needed. The theoretical grating equation for the Holospec spectrometer is:

$$\lambda\nu = \cos\gamma\,[\sin(\theta_1 + \phi_1) + \sin(\theta_2 + \phi_2)]\,, \tag{3.17}$$

where $\nu^{-1} = \lambda_0/(\sin\theta_1 + \sin\theta_2) \approx \lambda_0/\sqrt{3}$. Here, the nomenclature used by R. E. Bell in

reference [169] is followed, see figure 3.19. Then equation (3.17) can be recast as

$$\lambda = A + B(\sin\theta'_p \cos\alpha_2 - \cos\theta'_p \sin\alpha_2), \tag{3.18}$$

where $\theta'_p = \theta_p - (\theta_1 - \theta_2)$, $B = \cos\gamma/\nu$, $A = B\sin(\theta_1 + \phi_1)$ and

$$\sin\alpha_2 = \frac{\sin\epsilon' + \Delta(x + x_0)\cos\epsilon'}{N\sqrt{1 + \Delta^2(x + x_0)^2}}. \tag{3.19}$$

Here, $N \sim 1.5196$ is the BK7 refractive index, x is the pixel number and x_0 is the pixel number for optical axis with negative sign, $x_0 = -512$. In addition, the quantity Δ is the ratio between the pixel size and the focal length, $\Delta = 13\cdot10^{-6}/85\cdot10^{-3} = 1.5294\cdot10^{-3}$. The angle γ is related with fibre position (vertical displacement along the CCD) and the angle ϕ_1 reflects the array (top and bottom poloidal or toroidal) location at the entrance slit. The holographic grating is optimized for $\lambda_0 = 5291$ Å [159]. For the experimental arrangement, $\varepsilon' = 5^o$, $\theta_1 = 60.0037^o$, $\theta_2 = 59.9963^o$ and $\theta'_p = 63.284267^o$, and for the simple case of $\gamma = 0$ (no deflection in the vertical direction of the CCD) and $\phi'_1 = 0$ (bottom array), $B = 305.46465$ nm and $A = 264.55000$ nm.

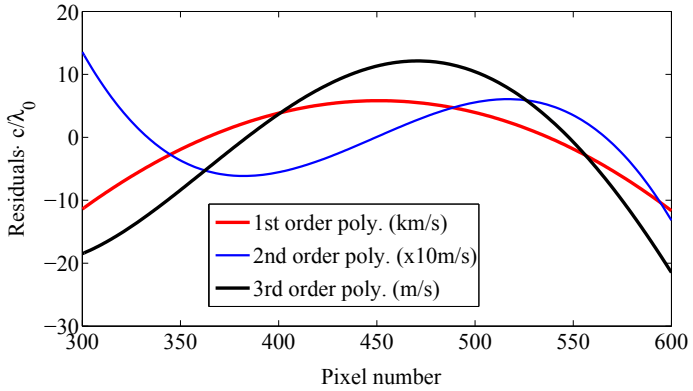

Figure 3.20. Residuals obtained after fitting the theoretical grating equation with different order polynomials: first (red, expressed in km s^{-1}), second (blue, in x10 m s^{-1}) and third order (black, in m s^{-1}).

Three polynomial fits have been applied to these theoretical data, equation (3.18). The residuals expressed in velocity units are plotted in figure 3.20. The error introduced by modelling the wavelength dispersion relation with a $2nd$ or $3rd$ order polynomial is less than 50 m s^{-1} in the region of interest (pixel numbers close to 500). This demonstrates that either a $2nd$ or $3rd$ order polynomial fit is good enough to reproduce the experimental data. Thus, the experimental method followed in the TJ-II CXRS system consists of recording several neon spectra, and fit the aforementioned four closest Ne I lines to the C VI emission with a second order polynomial fit.

Finally, another instrumental issue concerning the calibration in wavelength in TJ-II is the residual aberration which may arise from an incomplete correction for the short focal length of the spectrograph [46, 169]. Such an effect has been studied by changing the arrangement of the optical fibres at the entrance of the spectrograph 4 times at least over two years. Non systematic errors in wavelength determination have been observed, thus demonstrating that deviations from paraxial optics are unimportant here.

In conclusion, it is shown here that errors in impurity ion velocity measurements due to calibration of the instrument, ≤ 100 m s^{-1}, are significantly less than expected ion velocities in

the TJ-II, i.e. ≤ 10 km s^{-1}, and smaller than errors due to statistical uncertainties, ≥ 0.5 km s^{-1}.

3.4.2.3 Thermal Drifts

It was observed that the Holospec Spectrograph suffers from variations in the centroid and width of the spectral lines during TJ-II operation (~ 8 hours). In order to characterize this, 100 consecutive neon spectra were recorded during two days in intervals of 30 minutes. From each group of 100 spectra a single measurement is obtained with the errors given by the standard deviation of the fitted parameters. The total time of this single measurement is ~ 1 s (100 ms per spectra, plus 46.72 ms of CCD read out), not enough to allow any variation of the optical system, other than mechanical vibrations.

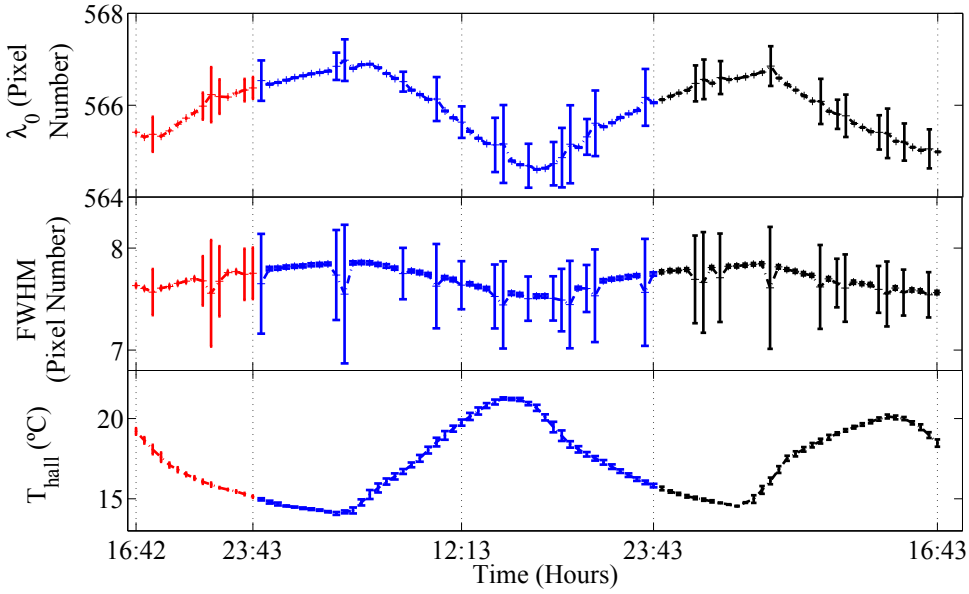

Figure 3.21. Time evolution of Ne I line 5298.189 Å centroid and FWHM in pixel number, and experimental hall temperature. Different colors represent different consecutive days.

In figure 3.21 the time evolution of the averaged fitted line centroid and FWHM of the Ne I line at 5298.189 Å is presented, together with the evolution of the experimental hall temperature, $T_{\rm hall}$. Error bars are also plotted; in general these are small (less than 0.03 pixel for λ_0, 0.05 pixel for FWHM and $\sim 0.5^o$C for T_{hall}), although in some cases the fit was poor, most likely due to a failure of the optical system, e.g., in the mechanical shutter or the CCD reading out, because of the long duration of the experiment.

These drifts are due to thermal stress and strain on the combined spectrograph and CCD camera instrumentation. Note that the CCD camera is not bolted onto the spectrograph in order to facilitate the positioning of the CCD image at the focal plane. Hence, the centroid and width of line vary with room temperature[3]. Rather than thermally insulating the detection system

[3] Note that, besides the thermal stress, the line centroid is affected by the changes in the refractive index of air produced by temperature variations, as shown in section 3.4.3. Nonetheless, these latter cannot explain the observed hysteresis, unless the aforesaid stress on the instrument exists.

in order to minimize such thermal drifts (this being both costly and complicated), frequently calibrations of the optical system are made during experiments with the disadvantage of opening and closing the experimental hall between shots.

3.4.3 Fine structure and local atmospheric effects

The CX process of interest in TJ-II, equation (3.1), involves the emission of a photon when the C^{5+} ion de-excites from the $n=8$ to the $n=7$ level. Such a transition must obey the well known selection rules for atomic transitions. In H-like ions, the J-transitions for these high levels are almost degenerate. Hence, the resultant photon wavelengths are much closer than can be resolved by the spectrometer used here, thus broadening the line [153]. Thus, it is essential to consider such broadening when analysing the C VI line emitted during the CX process (3.1). For this it is necessary to determine if the transition process is mixed by collisions for the plasma conditions under study.

For an isolated atom, it is straightforward to calculate the transition probabilities of each state and therefore determine the population of the different J levels. However, the plasma environment can mix the nearly degenerated states of hydrogen-like ions, by electric and magnetic fields, or collisional rearrangement [48]. For the TJ-II conditions, the most important mechanism is ion-ion collisions [186,187]. Collisional coupling depends, therefore, on plasma parameters such as density, temperature or impurity content. Sampson [188] has developed a criteria to estimate the critical electron density, n_e, at which collision rates from the $J = 1/2$ to all other sublevels J within the same n state equals the radiative rate from $(n, J = 1/2)$[4],

$$n_e \geq \frac{Z^{7.5}}{n^{8.5}} 1.18 \times 10^{21}\ \mathrm{m}^{-3}, \tag{3.20}$$

which for the C VI transition of interest (n=8, Z=6) gives $n_e \sim 1.7 \times 10^{19}\ \mathrm{m}^{-3}$. So, for plasmas with $n_e \geq 1.7 \times 10^{19}\ \mathrm{m}^{-3}$ even in the worst scenario (transitions from the furthest sublevel to all other J states) a statistical population of the J sublevels should be achieved.

Transition ($^{2S+1}L_J$)	$\delta\lambda_J = \lambda_0 - \lambda_J$ (Å)	Relative Intensity, I_J (a.u.)
$^2K_{15/2} \rightarrow ^2 I_{13/2}$	-0.217	0.605
$^2K_{13/2} \rightarrow ^2 I_{11/2}$ & $^2I_{13/2} \rightarrow ^2 H_{11/2}$	-0.143	1.000
$^2I_{11/2} \rightarrow ^2 H_{9/2}$ & $^2H_{11/2} \rightarrow ^2 G_{9/2}$	-0.036	0.644
$^2H_{9/2} \rightarrow ^2 G_{7/2}$ & $^2G_{9/2} \rightarrow ^2 F_{7/2}$	0.135	0.399
$^2G_{7/2} \rightarrow ^2 F_{5/2}$ & $^2F_{7/2} \rightarrow ^2 D_{5/2}$	0.443	0.233
$^2F_{5/2} \rightarrow ^2 D_{3/2}$ & $^2D_{5/2} \rightarrow ^2 P_{3/2}$	1.128	0.124

Table 3.1. Relative intensities of the fine structure components for the C VI transition $n = 8 \rightarrow n = 7$ in vacuum for statistically populated upper levels. Here, $\delta\lambda_J$ is the offset of the $\Delta J = 1$ wavelength transitions with respect to the unshifted wavelength λ_0.

In such a collisional-mixing case, the relative intensities of the fine structure components are the product of the Einstein coefficient and the statistical weight, $(2J + 1)/n^2$. The Einstein

[4]This is the most extreme case of collisional mixing, since the $J = 1/2$ is the least degenerate state.

coefficients are calculated here within the Pauli approximation [176] but without considering Lamb shifts or nuclear mass effects. In addition, the method developed by D. Hoang-Binh is used [189], which gives the value of the radial integral involved. See appendix B for details. Here only the $\Delta J = +1$ transitions are considered as they are the most intense [176]. Their relative intensities for emission in vacuum are presented in table 3.1. Transitions between $\mid \gamma, J = 3/2 >$ and $\mid \gamma, J = 1/2 >$ states are not considered within this model, since they have not been observed in the experimental data (for typical TJ-II impurity temperatures, they should appear isolated from the rest of the line emissions at lower wavelengths). This means that a complete statistical population of the J sublevels is not achieved, even when the critical density of equation (3.20) is exceeded in NBI heated plasmas of the TJ-II.

Next, the theoretical unshifted wavelength λ_0 is obtained after weighting the fine structure components,

$$\lambda_0 = \frac{\sum_i \lambda_i I_i}{\sum_i I_i} = \frac{5292.0426}{N} \text{ Å} \tag{3.21}$$

Here, N stands for the refractive index of air. It is calculated as in reference [190, 191], where local temperature, relative humidity and atmospheric pressure values are needed. For this a combined temperature and relative humidity sensor was installed in the TJ-II experimental hall. Typically, an atmospheric pressure of $p \approx 94$ kPa[5], a temperature of $T \sim 20$ °C and 20% of relative humidity are measured. The maximum change on N is caused by temperature variations, which results in a wavelength variation of $\delta\lambda_0 \sim 0.005$ Å K^{-1}. Usually, in the TJ-II experimental hall the temperature varies by about 5 ^{0}C during a day, see figure 3.21. In such conditions, the refractive index varies from $N(15\ ^\circ\text{C}) = 1.00025814$ to $N(20\ ^\circ\text{C}) = 1.00025373$, and hence, the rest wavelength in air is $\lambda_0 \sim 5290.677 - 5290.7$ Å. Similar values are reported in the literature [192, 193], where standard atmospheric conditions ($p = 101$ kPa and $T = 15$ °C) are used, and thus our calculated value is $\lambda_0 = 5290.58$ Å. Note: the inclusion of the atmospheric pressure in the analysis is critical as its non inclusion can give rise to an error of ~ 0.1 Å in the rest wavelength.

Finally, the C VI line emission excited by the DNBI is modelled by the sum of all these contributions, under the assumption of a Maxwellian equilibrium (see figure 3.22),

$$I(\lambda) = A \sum_J I_J \exp\left(-4 \ln 2 \left(\frac{\lambda_v - \lambda_u - \delta\lambda_J}{\sigma}\right)^2\right). \tag{3.22}$$

Here, the Doppler shift of each J-component, $(\lambda_v - \lambda_u)_J$, is been approximated by

$$(\lambda_v - \lambda_u)_J = \lambda_J \left(1 + \frac{\mathbf{w} \cdot \mathbf{l}}{c}\right) = (\lambda_0 - \delta\lambda_J)\left(1 + \frac{\mathbf{w} \cdot \mathbf{l}}{c}\right) \approx (\lambda_v - \lambda_u) - \delta\lambda_J,$$

where $\mathbf{w} = \mathbf{v} - \mathbf{u}$ is the relative particle velocity, see section 2.1, and $(\lambda_v - \lambda_u)$ is the Doppler shift of the central wavelength, λ_0. Hence, it is assumed that all the lines are shifted as a whole. Note that λ_v in (3.22) is a free parameter, whilst the velocity information is stored in the shift produced by the mean flow,

$$\lambda_u = \lambda_0 \left(1 + \frac{\mathbf{u} \cdot \mathbf{l}}{c}\right). \tag{3.23}$$

[5] Madrid is located at 600m and so the pressure is slightly lower than it nominal value of 101 kPa. Pressure data is obtained from http://www.ciemat.es/portal.do?IDM=266&NM=2

On the other hand, fine structure broadening is automatically included in the data analysis process through equation (3.22), without requiring additional correction factors to account for this effect in temperature measurements.

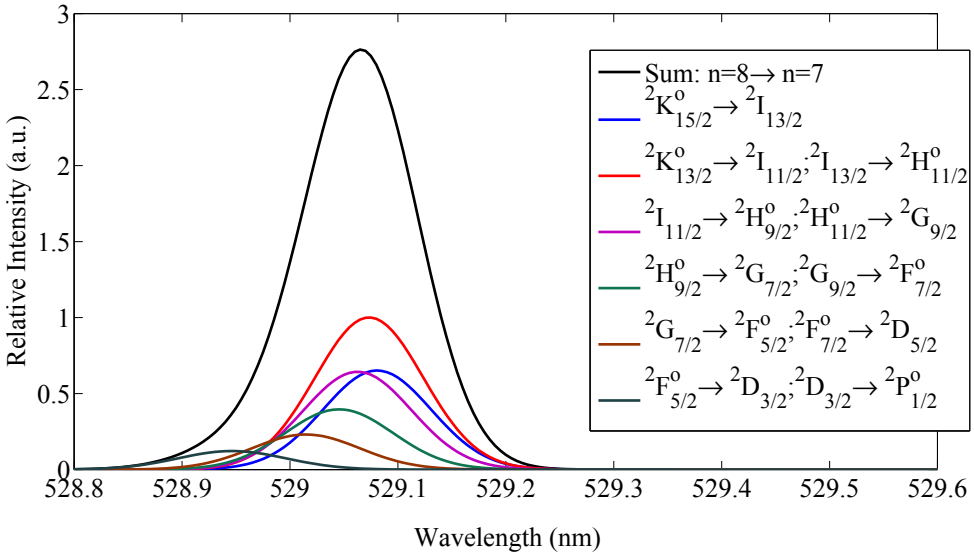

Figure 3.22. Modelled fine structure broadening of the C VI spectral line for a plasma in Maxwellian equilibrium with $T_C = 100$ eV. The resultant wavelength at rest is $\lambda_0 = 5290.7$ Å for $p = 94$ kPa and $T = 20$ °C.

3.4.3.1 Experimental determination of the C VI rest wavelength

From equations (3.22) and (3.23), it is clear that an incorrect estimate of the C VI line emission wavelength at rest, λ_0, produces incorrect values of the measured mean flow, $\mathbf{u}$. Therefore, precise knowledge of the relative population of the fine structure levels is needed, to avoid non-physical contributions to velocity measurements. As aforementioned, the population of the different J-levels is affected by the plasma, making its calculation highly complicated.

The procedure followed to overcome this difficulty is the use of opposing symmetric views (see e.g. references [155, 166, 194, 195]). Two sightlines that view the same plasma spot from opposing directions, $\mathbf{l}_+ = -\mathbf{l}_-$, can provide the value of the selected emission line wavelength at rest together with the projection of the velocity in these sightlines, $u_l = \mathbf{u} \cdot \mathbf{l} = u_{l_+} = -u_{l_-}$, i.e.

$$\lambda_0 = \frac{\lambda_{u_+} + \lambda_{u_-}}{2}, \quad u_l = \frac{\lambda_{u_+} - \lambda_{u_-}}{2} c. \tag{3.24}$$

Therefore it is necessary to resort to experimental techniques to overcome this drawback. For instance, in the HSX device, this is done by inverting the magnetic field and comparing the result with the velocities measured with the opposite magnetic field direction[6] [164]. However, not all the devices can meet these demands [160, 162, 171, 196, 197]; the impurity line emission at

[6] This method relies on the assumption that flow is reverted when reverting the magnetic filed (which is true if it is neoclassical).

rest is then calculated using complex codes [173] which rely on several plasma parameters such as impurity concentration, bulk ion and electron densities, temperatures, etc.

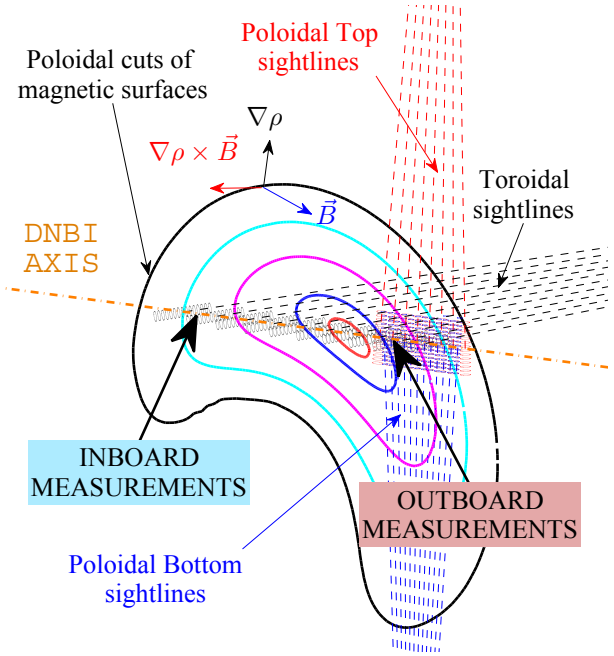

Figure 3.23. Schematic diagram of CXRS diagnostic sightlines for the 100_44_64 magnetic configuration. Only 8 Poloidal Top lines of sight are shown, as the outer most 4 do not provide useful data for this configuration. Inboard and outboard toroidal sightlines are highlighted. In addition, poloidal cuts of magnetic surfaces are presented, together with the directions of interest for velocity measurements: radial ($\nabla\rho$), parallel ($\mathbf{B}$) and $\nabla\rho \times \mathbf{B}$. Note that none of these vectors is contained in the poloidal plane. The magnetic field vector, $\mathbf{B}$, points into the page.

In TJ-II nearly opposing poloidal views are available to correct for this effect, see figure 3.23. The velocity along sightlines, u_l, is obtained from the line centroid shift, $\lambda_{\rm u}$, as [105]

$$\lambda_{\rm u} = (\lambda_0 + \lambda_{\rm cx})\left(1 + \frac{u_l}{c}\right) \approx \lambda_0\left(1 + \frac{u_l}{c}\right) + \lambda_{\rm cx}. \tag{3.25}$$

Here, $\lambda_{\rm cx}$ accounts for possible deviations in the populations of the fine structure level from a complete statistical mixing[7]. This is removed by adding measured wavelengths from top

[7] Expression (3.24) can be generalised to the case of opposing views which are not exactly symmetric. In such a case, since the direction of flow is unknown, three independent wavelength shifts are required at the same location,

$$\lambda_{\rm cx} = \frac{\nabla\rho \cdot \sum \delta\lambda_i \mathbf{e}_j \times \mathbf{e}_k}{\nabla\rho \cdot \sum \mathbf{e}_j \times \mathbf{e}_k}. \tag{3.26}$$

Here, $\delta\lambda_i = \lambda_i - \lambda_0$ is the wavelength shift (numbered i) with respect to the theoretical rest wavelength, and $\mathbf{e}_i$ the corresponding unitary vector in the direction of observation i. The summation in (3.26) must be cyclic, but the order in which the wavelength shifts (and the associated sightline unitary vectors) are summed is arbitrary, as long as such order is kept in the summation.

In the case of having poloidal opposing views, $\mathbf{e}_{p1} = -\mathbf{e}_{p2}$, the –typically– toroidal shift does not appear,

$$\lambda_{\rm cx} = \frac{\nabla\rho \cdot (\delta\lambda_1 \mathbf{e}_{p2} \times \mathbf{e}_t + \delta\lambda_2 \mathbf{e}_t \times \mathbf{e}_{p1})}{\nabla\rho \cdot \sum \mathbf{e}_j \times \mathbf{e}_k} = \frac{\delta\lambda_1 + \delta\lambda_2}{2} = -\lambda_0 + \frac{\lambda_1 + \lambda_2}{2},$$

thus recovering (3.24). Note that here the total rest wavelength is $(\lambda_0 + \lambda_{\rm cx})$. On the other hand, in tokamaks, the radial direction $\nabla\rho$ is orthogonal to the toroidal direction $\mathbf{e}_\phi \propto \hat{\phi}$ (see, e.g., the basis vectors obtained in reference [129] for a modelled tokamak), and so

$$\lambda_{\rm cx} = \frac{\nabla\theta \cdot (\delta\lambda_{p1} \mathbf{e}_{p2} - \delta\lambda_{p2} \mathbf{e}_{p1})}{\nabla\theta \cdot (\mathbf{e}_{p2} - \mathbf{e}_{p1})} = \frac{\delta\lambda_{p1}\cos\theta_2 - \delta\lambda_{p2}\cos\theta_1}{\cos\theta_2 - \cos\theta_1}, \tag{3.27}$$

even if the two poloidal sightlines are not opposing. Here, the relation $\nabla\rho \cdot \mathbf{e}_{p1} \times \mathbf{e}_{p2} \propto \nabla\rho \cdot \hat{\phi} = 0$, valid for tokamaks, has been invoked. An expression like (3.27) was utilized previously in TJ-II [159]. However, in nonaxisymmetric systems the gradient to a magnetic surface has a component in the toroidal direction, $\nabla\rho \cdot \hat{\phi} \neq 0$,

and bottom poloidal sightlines, equation (3.24), since they have almost the opposite direction. Besides, when correcting for this effect in the inboard toroidal velocity measurements, it is assumed that the rest wavelength ($\lambda_0 + \lambda_{cx}$) is a flux-function. Such an hypothesis relies on the collisional origin of λ_{cx} deviations, and on the assumption of flux constant ion density and temperature, i.e. $n_i \approx n_i(\rho)$ and $T_i \approx T_i(\rho)$.

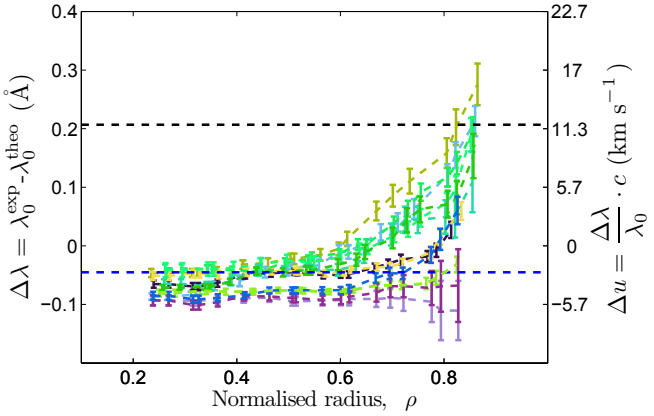

Figure 3.24. Radial profiles of the CVI rest wavelength deviations from collisional mixing for a set of NBI heated plasmas. The zero corresponds to the theoretical rest wavelength for standard atmospheric conditions, $\lambda_0 = 5290.58$ Å. The black dashed line indicates the long wavelength limit for the C VI line whilst the blue dashed line corresponds to the theoretical rest wavelength $\lambda_0 = 5290.53$ Å given in reference [192].

In figure 3.24 radial profiles of the experimental λ_{cx} with respect to the theoretical rest wavelength are presented. Here the zero in the y-axis corresponds to the calculated rest wavelength (for standard atmospheric conditions, $\lambda_0 = 5290.58$ Å). In addition, the black dashed line corresponds to the long wavelength limit for the C VI line (i.e., the wavelength of the $^2K_{15/2} \rightarrow ^2 I_{13/2}$ transition for this simulation, see table 3.1) whilst the blue dashed line corresponds to the theoretical rest wavelength $\lambda_0 = 5290.53$ Å given in reference [192]. The difference between the value in reference [192] and that calculated here could be due to transitions from lower l levels, that are not included here. From the figure it can be concluded that the statistical mixing among fine structure sublevels is reached in the core of TJ-II NBI heated plasmas. Hence, the criteria to achieve collisional mixing developed by Sampson [188] (and the calculations given in reference [187]) is fulfilled in the core of these plasmas, when $n_e \geq 1.5 \times 10^{19}$ m^{-3}. From the data shown in figure 3.24 a value of 5290.51 ± 0.02 Å is obtained at the core, in good agreement with that measured in DIII-D, 5290.52 ± 0.05 Å [193]. Note that variations in the local pressure or air humidity between the discharges used to create figure 3.24 are not considered, since they are expected to be small.

3.4.4 Line emission of charge-exchange excited states

As well as non-real velocities that arise when the fine structure is not correctly handled, the daughter distribution function may introduce some undesired velocities arising from the energy

and so the general expression (3.26) must be called. Calculations of the C VI line emission wavelength at rest with the general formula (3.26) and the simplified expression (3.24) show that the effect of the toroidal wavelength shift is negligible, as the poloidal sightlines are almost anti-parallel in TJ-II. Thus, the method considered in TJ-II is the simplified form of (3.24), with $\lambda_{cx} = \lambda_{cx}(\rho)$.

dependence of the CX cross-section [156] and the gyro-motion of the ions during the de-excitation process [155][8]. As a consequence, the daughter C^{5+} ions distribution function is distorted in the velocity space yielding a *real velocity* not associated with the parent C^{6+} distribution function, as discussed in refrence [181]. Such flows are usually called *pseudo-velocities*.

A first principle derivation from kinetic equation is provided in [157], and applied in [196,198]. For this, it is assumed that all plasma parameters are frozen in time scales of the order of the radiation decay time. Next, the continuity equation is expanded in the smallness of the impurity-Larmor radius, $\delta_z = \rho_z/L_\perp \ll 1$, and the smallness of the thermal impurity velocity compared to the beam velocity, $\varepsilon = v_z/v_b \ll 1$. Since typical ion temperatures observed in TJ-II are $T_i \leq 200$ eV, thermal carbon velocities $v_z \leq 60$ km s^{-1} are expected. Thus, $\delta_Z < 10^{-2}$. For hydrogen atoms accelerated to 30 keV in the DNBI their velocity is large $v_b \sim 2400$ km s^{-1}, hence $\varepsilon \ll 1$. Then, if a shifted (by the impurity mean flow $\mathbf{u}_z$) Maxwellian distribution function of the parent impurity ions is assumed, the light emitted in the direction of observation is recast as

$$I_{\rm obs} \propto \left(\frac{m_z}{2\pi T_z}\right)^{1/2} \tilde{n}_z \exp\left(-\frac{m_z}{2(T_z+\tilde{T}_z)}\,(w_l-\tilde{u}_z)^2\right), \tag{3.28}$$

where $w_l = (\mathbf{v}-\mathbf{u}_z)\cdot\mathbf{e}_l$ and $\mathbf{e}_l$ is a unitary vector in the viewing direction. In the following the sub-index z indicating impurity ions is dropped. The impurity density, $\tilde{n}$, temperature, $\tilde{T}$, and flow velocity, $\tilde{u}$, defined in (3.28) are

$$\tilde{n} \approx n\tau\nu_{\rm cx}\left(1-\frac{\tilde{\nu}_{\rm cx}}{v_b\nu_{\rm cx}}\mathbf{u}\cdot\mathbf{e}_l\right) \sim n\tau\nu_{\rm cx}, \tag{3.29a}$$

$$\tilde{T} = \frac{T}{\Omega} g\mathbf{e}_l\cdot\frac{\partial}{\partial\rho}\mathbf{u}_\parallel \sim \delta T, \tag{3.29b}$$

$$\tilde{u} = u_1 + u_2\frac{M(w_l')^2}{T} + u_3 + u_4. \tag{3.29c}$$

Here, $\tau \approx 1.1$ ns [155] is the lifetime of the excited state. In equation (3.29a) $\nu_{\rm cx}$ and $\tilde{\nu}_{\rm cx}$ are frequencies characterizing the neutral beam,

$$\nu_{\rm cx} \approx n_{\rm b}\langle\sigma_{\rm cx}v\rangle_{v_b} \tag{3.30a}$$

$$\frac{\tilde{\nu}_{\rm cx}}{v_b\nu_{\rm cx}} \approx \frac{1}{\langle\sigma_{\rm cx}v\rangle_{v_b}}\left.\frac{d\langle\sigma_{\rm cx}v\rangle}{dv}\right|_{v_b} \sim 2\times10^{-6}\ {\rm s\ m^{-1}}. \tag{3.30b}$$

In equation (3.30b) the results of [156] are used to give an order of magnitude. More details are given later. From this estimation, the approximation made in (3.29a) $\tilde{n} \sim n\tau\nu_{\rm cx}$ follows, so that $\tilde{n}$ can be interpreted as the number of impurity ions, n, that have emitted during a time τ after undertaking CX reactions with $n_{\rm b}$ neutral beam atoms. Note that the beam CX frequency $\nu_{\rm cx}$ causes the observed density, $\tilde{n}$, to vary strongly with position through the beam density, $n_{\rm b}$ (see sections 3.3 and 3.5).

The factor g in (3.29b) depends on the gyro-frequency of the parent, Ω, and daughter, $\omega = \Omega(Z-1)/Z$, impurity ions as

$$g = \frac{\tau(\omega-\Omega)\mathbf{e}_l\cdot\mathbf{e}_r + (1+\omega\Omega\tau^2)\mathbf{e}_l\cdot\mathbf{e}_\perp}{1+(\omega\tau)^2}|\nabla\rho| \sim \frac{1}{a}\mathbf{e}_l\cdot\mathbf{e}_\perp, \tag{3.31}$$

[8] These processes affect as well the density and temperature of the daughter distribution function, as shown below. However, the modifications are negligible for the experimental conditions outlined here.

with $\mathbf{e}_r$ a unitary vector in the radial direction, and $\mathbf{e}_\perp = \mathbf{b} \times \mathbf{e}_r$. A fully-ionised carbon in TJ-II has a typical cyclotron frequency of $\Omega \sim 50$ MHz. Thus, the product $\Omega\tau \sim 5 \times 10^{-2}$ is small and the approximation made in (3.31) follows, where $|\nabla\rho| \sim 1/a$ has been taken in order to give an estimation (here a is the plasma minor radius). From (3.31) the ordering $\tilde{T} \sim \delta T$ in equation (3.29b) is obtained, and thus the observed temperature equals the parent distribution temperature to the required order.

The corrections to the parent distribution velocity in (3.29c) are

$$u_1 = -g\frac{T}{m\Omega}\left(\frac{n'}{n} - \frac{T'}{2T}\right) \sim \delta v_z, \tag{3.32a}$$

$$u_2 = \frac{1}{2}g\frac{T'}{m\Omega} \sim u_1, \tag{3.32b}$$

$$\begin{aligned} u_3 &= -\frac{T}{m}\frac{\tau|\nabla\rho|}{1+(\omega\tau)^2}\left(\mathbf{e}_l\cdot\mathbf{e}_r - \omega\tau\mathbf{e}_l\cdot\mathbf{e}_\perp\right)\frac{\partial}{\partial\rho}\ln(\tau\nu_{\rm cx}) \\ &\sim -\frac{\tau}{a}\frac{T}{m}\frac{\partial}{\partial\rho}\ln(\tau n_{\rm b})\mathbf{e}_l\cdot\mathbf{e}_r \end{aligned} \tag{3.32c}$$

$$\begin{aligned} u_4 &= -\frac{T}{m}\frac{\tilde{\nu}_{\rm cx}}{v_b\nu_{\rm cx}}\Bigg(\mathbf{e}_b\cdot\mathbf{e}_\parallel\mathbf{e}_l\cdot\mathbf{e}_\parallel + \\ &\quad \frac{1}{1+(\omega\tau)^2}\left[\mathbf{e}_l\cdot\mathbf{e}_\perp(\mathbf{e}_b\cdot\mathbf{e}_\perp - \omega\tau\mathbf{e}_b\cdot\mathbf{e}_s) + \mathbf{e}_l\cdot\mathbf{e}_s(\mathbf{e}_b\cdot\mathbf{e}_s + \omega\tau\mathbf{e}_b\cdot\mathbf{e}_\perp)\right]\Bigg) \\ &\approx -\frac{T}{m}\frac{\tilde{\nu}_{\rm cx}}{v_b\nu_{\rm cx}}\left(\mathbf{e}_l\cdot\mathbf{e}_b + \frac{\omega\tau}{1+(\omega\tau)^2}\mathbf{e}_l\cdot(\mathbf{e}_b\times\mathbf{e}_\parallel)\right) \sim -\frac{T}{m}\frac{\tilde{\nu}_{\rm cx}}{v_b\nu_{\rm cx}}\mathbf{e}_l\cdot\mathbf{e}_b. \end{aligned} \tag{3.32d}$$

The first two contributions are diamagnetic velocities in the direction of observation and are negligible in TJ-II. On the other hand, u_3 is a radial diamagnetic velocity in the population of excited states and u_4 is the flow arising from the energy dependence of the CX reaction [156]. The latter appears even for a zero lifetime, and makes the largest contribution to the flow. For TJ-II conditions the estimation is $u_4 \leq -5\ \mathbf{e}_l\cdot\mathbf{e}_b$ km s^{-1}. A more detailed calculation will be addressed next. The term u_3 is ordered as $u_3 \sim -10\mathbf{e}_l\cdot\mathbf{e}_r\partial\ln(\tau n_b)/\partial\rho$. The radial variation in τ is related to that in the rest wavelength and is therefore expected to be unimportant, see figure 3.24. The radial derivative in the neutral density has contributions from the spatial variation of DNBI profile in vacuum and the attenuation of the beam [159],

$$\frac{\partial}{\partial\rho}\ln(\tau\nu_{\rm cx}) \approx \frac{\partial\ln n_{\rm b}}{\partial\rho} = \frac{\partial}{\partial\rho}\left(\ln j_v(0) - \frac{\pi}{I_{\rm b}}j_v(0)r^2\right) - \alpha(l_{\rm b})\frac{\partial l_{\rm b}}{\partial\rho} \tag{3.33}$$

Here, $j_v(0)$ is the beam current in vacuum at the beam axis, $I_{\rm b}$ the total beam intensity, r the radial distance to the beam axis and $\alpha(l_{\rm b})$ the attenuation coefficient of the beam particles [49, 135], with $l_{\rm b}$ the beam path length (see section 3.3.1). All the terms in (3.33) are $\mathcal{O}(1)$ or smaller, and thus the velocity u_3 is negligible in TJ-II (confirmed by numerical calculation). Note that for initial excited states with longer lifetimes, e.g. $He^+(n=4)$ or $H(n=3)$, the situation could be different [199].

In order to determine the flow arising from the energy dependence of the CX reaction, u_4, the emission rate $Q = \langle\sigma_{\rm cx}v\rangle$ is estimated with the analytic formula [156]

$$Q(E_{\rm col}) = Q_0\frac{X^p}{1+X^q}, \tag{3.34}$$

with $X = E_{\rm col}/E_{\rm m}$ a normalised energy and $E_{\rm col} \approx E_{\rm b}$ the colliding energy. In addition, $Q_0 = (23.7 \pm 0.5) \times 10^{-15}$ m^3 s^{-1}, $E_m = 49.2 \pm 1.7$ keV, $p = 3.05 \pm 0.18$ and $q = 4.76 \pm 0.12$

are fitting parameters obtained from a set of published atomic data for effective charge-exchange emission [156], which have been evaluated for the CXRS diagnostic in TJ-II. With (3.34), the quotient in equation (3.30b) results

$$\frac{\tilde{\nu}_{\rm cx}}{v_b \nu_{\rm cx}} \approx \frac{1}{Q}\frac{{\rm d}Q}{{\rm d}v}\bigg|_{v_{\rm b}} = \frac{2}{v_{\rm b}}\frac{p + X_{\rm b}^q (p-q)}{1 + X_{\rm b}^q} = 2.2 \times 10^{-6}\ {\rm s\ m^{-1}}, \tag{3.35}$$

a value in good agreement with the estimation made in equation (3.30b). The DNBI-driven flow u_4 in (3.32d) is then

$$u_4 = -1.76\ \mathbf{e}_{\rm b} \cdot \mathbf{e}_l \frac{T_{\rm C}({\rm eV})}{100}\ {\rm km\ s^{-1}}. \tag{3.36}$$

This velocity contribution is presented in figure 3.25 for a constant temperature of $T_{\rm C} = 100$ eV for the different sightlines used. As would be expected, when sightlines are nearly perpendicular to the injected beam direction such a flow is close to zero, as it is the case for the top and bottom poloidal lines-of-sight. However, the contribution to measurements of velocity for the toroidal view is not negligible, being of order $1-2$ km s^{-1} and dependant on the local value of the impurity temperature. Note this effect does not produce a large inboard/outboard asymmetry in the measured toroidal flow, as will be discussed in chapter 5. Finally, since this velocity is a real flow of the daughter C^{5+} distribution function, it is corrected in the analysis procedure after correcting for fine structure effects (see section 3.4.3.1 and equation 3.25). There are two additional effects

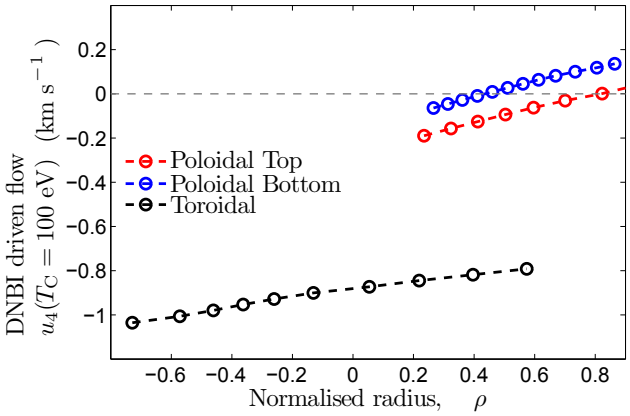

Figure 3.25. Pseudo-velocities due to energy dependence of the CX emission rate for the different sightlines. A constant temperature of 100 eV is been assumed across the plasma radius.

that have been omitted in deriving the pseudo-velocities (3.32), and can potentially affect the results shown in figure 3.25. First, it is necessary to consider the contribution to equations (3.30) of the relative populations of full (30 keV), half (15 keV) and third (10 keV) energy $H_{\rm b}^0$ particles in the injected beam. These were measured by injecting the beam into the chamber without magnetic fields and collecting the resultant spectrum emitted by cold hydrogen in the vacuum chamber and by the beam hydrogen, see figure 3.26. Following the method in [200] the $E : E/2 : E/3$ ratio is $94.5 : 4.25 : 1.25$. Thus, the approximation of a mono-energetic beam made in equations (3.30) is reasonable, and the impact of the half and third beam components, negligible. On the other hand, charge-exchange collisions between C^{6+} ions and accelerated $H_{\rm b}^0$ in excite states ($n = 2, 3$) can enhance the C^{5+} upper state population, since its rate coefficient is an order of magnitude larger than that of the ground state [173]. Therefore, even a small fraction

of excited beam neutrals can make considerable contributions. As discussed in reference [201] such an effect is important for energies below 20 keV. Since the DNBI in TJ-II is almost mono-energetic (with $E = 30$ keV) the effect of excited beam particles is expected to be negligible.

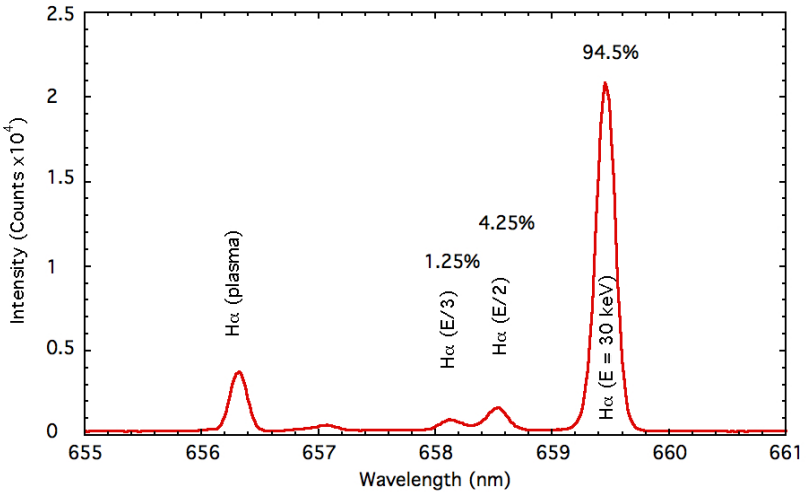

Figure 3.26. Measurements of the Doppler shifted Balmer H_α emission from the TJ-II DNBI beam. The full, half and third energy components are highlighted. Following the method in [200] the $E : E/2 : E/3$ ratio is $94.5 : 4.25 : 1.25$.

Through this subsection, a number of corrections to the measured density, temperature and flow velocity of the emitting C^{5+} ion have been described; these are necessary to recover the actual velocity moments of the C^{6+} distribution function. In the next section all the aspects affecting temperature, density, and velocity measurements of C^{6+} ions are combined in the data analysis procedure, with examples of C^{6+} temperature and density profiles measured in TJ-II.

3.5 Carbon impurity temperature, density and velocity measurements

A multi-Gaussian fit to an active signal is made using the expression [105],

$$I_C = I_0 \sum_j a_j \exp\left\{-\left(\frac{\lambda - \delta\lambda_j - \lambda_c}{\sigma}\right)^2\right\}, \tag{3.37}$$

where a_j is the relative amplitude of each of the fine structure components of the C VI spectral line when assuming a statistical population of the initial j-levels, and normalized to the sum, $\sum_j a_j = 1$. See section 3.4.3.1 for details. $\delta\lambda_j$ stands for the wavelength separation of the fine-structure components respect to the rest wavelength: $\lambda_0 = \sum_j a_j \lambda_j = 5292.04$ Å in vacuum [202]. In addition, λ_c measures the line centroid. Such a fit, equation (3.37), was applied to the data shown in figure 3.2 (green line).

3.5.1 Temperature profiles

Carbon temperatures are obtained from the parameter σ in equation (3.37), after considering Zeeman broadening and a numerical deconvolution of the instrumental function [59], see

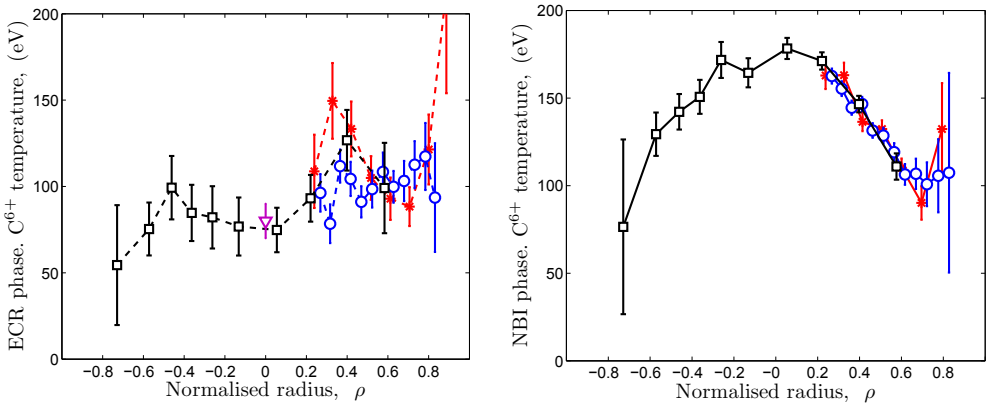

Figure 3.27. Fully-ionized carbon ion temperature profile for representative ECR-heated plasma (discharge #25801, with $n_e(0) \approx 0.5 \times 10^{19}$ m^{-3} and $T_e(0) \approx 0.8$ keV) and NBI-heated plasma (discharge #32577, with $n_e(0) \approx 2.0 \times 10^{19}$ m^{-3} and $T_e(0) \approx 0.3$ keV), as measured by poloidal bottom (blue circles), top (red asterisks) and toroidal sightlines (black squares). The central majority ion temperature measured by the NPA is shown for the ECRH plasma (purple triangle).

sections 3.4.1 and 3.4.2.1. Representative temperature profiles of ECR and NBI heated phases are displayed in figure 3.27. Note that the error bars are reduced in the higher density plasma (NBI phase, on the right of the figure) with respect to the low density case because of the improved photon statistics for the former situation. In general, it is found that CXRS temperature measurements are symmetric about magnetic axis within error bars. Indeed, the consistency of the temperature measurements from the three fibre arrays can be used as an additional check of the diagnostic optical alignment (section 3.2.1). It is noted, however, that outboard edge temperature measurements with $\rho > 0.7$ do not go to zero (this is a general result for both heating phases). This might be attributed to the low statistic counts recorded and poor S/N ratio. In addition, the presence of supra-thermal impurities [203] could broaden the C VI line. Such an effect has been numerically studied by considering a bi-Maxwellian emission with artificially added Poisson noise. In the simulation it is found that, for typical CXRS signals in ECRH plasmas, it is no possible to distinguish between thermal and suprathermal populations. As the present work is focused on core measurements with $|\rho| \leq 0.7$, this study is left for future work.

For completeness, the majority ion temperature measured by a central chord-view of a poloidal Neutral Particle Analyser (NPA) [58, 133], is shown for the ECRH case (left side of figure 3.27). This diagnostic detects hot neutral hydrogen particles that escape from the plasma after undergoing a CX reaction with cold neutrals that reach the plasma core via diffusion [204]. There is no comparison for the NBI plasma shown here –as the NPA diagnostic was being upgraded at the time CXRS measurements were performed in NBI plasmas– although values of $T_{NPA} \leq 120$ eV are routinely observed [58]. As pointed out in, e.g., reference [205], NPA provides a line-averaged temperature value[9]. Thus, lower temperatures are expected from this diagnos-

[9] In references [205, 206], it was claimed that the sharp variation of the NPA sightline with respect to the magnetic surface label, $\partial l_{NPA}/\partial\rho$, should be sufficient to localise the NPA measurement. Nevertheless, this was a bad interpretation, since this term will have an infinitesimal contribution, dρ, to the integral involved in the calculation of the NPA detected fluxes.

tic. Correction techniques have been implemented recently in the data analysis of the NPA diagnostic, yielding core bulk ion temperatures in the NBI phase of $T_\mathrm{i} \leq 140$ eV [207]. This, together with instrumental corrections to the carbon impurity temperature [59] (explained in section 3.4.2.1), have lead to improved agreement between these diagnostics [206].

Finally, TJ-II is also equipped with a toroidally viewing NPA that is set to observe the same plasma volume as the poloidal NPA. However, the former systematically observes a higher main ion temperature than the latter, as reported in [205]. These differences could be interpreted as a pressure anisotropy in the main ion distribution function, see section 2.3. Note that viscous forces are negligible for the more collisional impurities, see section 2.4. Thus, it can be expected that bulk ion temperatures differ when measuring in toroidal and poloidal directions, while the impurity temperatures do not. Nevertheless, the temperature difference observed by toroidal and poloidal NPAs is much larger (in the order of 100 eV) than the temperature anisotropy that could be expected from the neoclassical theory, i.e. $T_{i\parallel} - T_{i\perp} = \mathcal{O}(\delta_i T_i)$. The understanding of these observations is outside the framework of this thesis and is left for future work.

3.5.2 Density profiles

Carbon impurity density measurements are challenging with the experimental set-up used in TJ-II, since the beam density and the absolute throughput of the optical system need to be quantified, i.e.

$$n_\mathrm{C} = \eta \frac{\int d\lambda I_\mathrm{C}}{\tau n_\mathrm{b} \langle \sigma_\mathrm{cx} v \rangle_{v_b}}. \tag{3.38}$$

Here, η is the absolute efficiency of each sightline –that includes all the possible intensity losses– and $\int d\lambda I_\mathrm{C}$ is the integrated beam-excited C VI line emission at 5290.7 Å. In addition, the observed density –$\tilde{n}_\mathrm{C} = n_\mathrm{C} \tau \nu_\mathrm{cx}$ in equation (3.29a)– has been related to the C^{6+} density through the CX frequency $\nu_\mathrm{cx} = n_\mathrm{b} \langle \sigma_\mathrm{cx} v \rangle_{v_b}$, see equations (3.29a) and (3.30a).

The local beam density, n_b, was estimated in section 3.3.1 by considering a simple pencil-like beam attenuation model [49], together with an analytical expression to account for the beam profile in vacuum. On the other hand, the optical system is not absolutely calibrated so it is not possible to convert measured active counts in the CCD to C^{6+} ion densities in the plasma. However, an estimation of carbon density relative profiles can be made by assuming that the throughput of each fibre is proportional to the total intensity recorded during the instrument wavelength calibration procedure, i.e.

$$\langle n_\mathrm{C} \rangle_{\mathcal{V}_\mathrm{los}} \propto \frac{1}{\int_{\mathcal{V}_\mathrm{los}} d^3\mathbf{r} n_\mathrm{b}} \frac{\int d\lambda I_\mathrm{C}}{\int d\lambda I_\mathrm{Ne}}. \tag{3.39}$$

Here, the integral of the beam atoms is performed in the sightlines measurement volume, $\mathcal{V}_\mathrm{los}$, as explained in section 3.3. In addition, the total neon signal is obtained by integrating two Ne I lines that straddle the C VI line. Note that variations along the plasma minor radius of the lifetime τ and CX reaction rate $\langle \sigma_\mathrm{cx} v \rangle_{v_b}$ in equation (3.38), have been neglected in the approximation (3.39).

In figure 3.28, C^{6+} density profiles, as obtained using equation 3.39, are presented for two ECRH plasmas studied prior to and after December 2011 and January 2013. Profiles are nor-

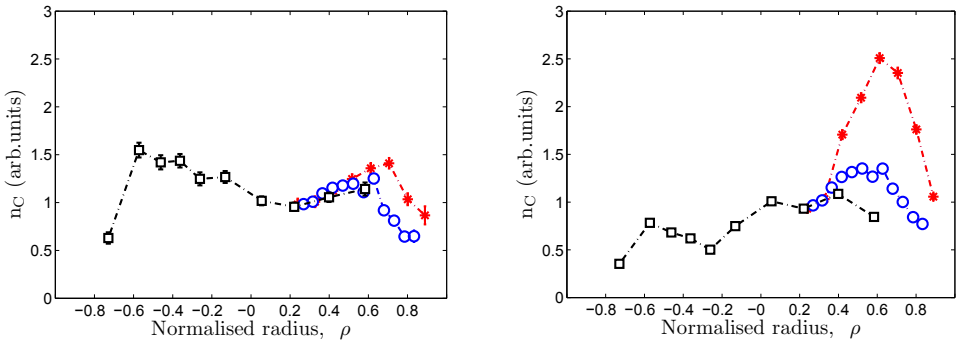

Figure 3.28. Fully-ionized carbon ion density profiles as measured by poloidal bottom (blue circles), top (red asterisks) and toroidal sightlines (black squares). Two ECRH discharges are shown. Left: shot#25801, with $n_e(0) \approx 0.5 \times 10^{19}$ m^{-3} and $T_e(0) \approx 0.8$ keV. Right: shot#32598, with $n_e(0) \approx 0.6 \times 10^{19}$ m^{-3} and $T_e(0) \approx 0.8$ keV. The disagreement among the three fibre arrays in the latter might be attributed to a lack of absolute calibration.

malised at $\rho \sim 0.3$, since they are not absolutely calibrated. The profile for shot#25801 (left) is flat and slightly hollow, as is the case of electron density profiles measured by Thomson Scattering [208] in the ECRH phase. As observed, measurements from the three fibre arrays coincide for this discharge within error bars, except in the region $\rho \geq 0.6$. The slight inboard/outboard asymmetry in the toroidal measurements might be due to uncertainties in the calculation of local beam neutral density, see section 3.3. Indeed, the beam profile varies sharply when crossing the plasma from the outboard side (where it enters the plasma) towards the inboard region. Thus, a more detailed characterization of the beam is required, prior to assessing possible asymmetries in the toroidal density measurements.

On the right column of figure 3.28 the carbon density profile measured by the poloidal top array develops a pronounced peak, which is not observable in the other arrays. Such a feature hass been observed in all measurements performed since 2011, but was not present in previous experiments (e.g., in the results reported in reference [105]). This points to a possible error in the estimation of the relative efficiency of each fibre, equation (3.39). Note that as the lamp used for spectrograph calibration is located between the light collections lens and fibre bundle, see figure 3.13, the influence of the internal mirror for the toroidal sightlines, the vacuum viewports or the focusing lenses are not included in the calibration, thereby introducing significant uncertainties into the carbon density profile measurements.

Therefore, carbon density profiles obtained since 2011 are considered unreliable. This complicates the interpretation of the results presented in chapter 5, where the possibility of an impurity compressible flow is studied, and so carbon density measurements are of great interest. In addition, these measurements are needed to calculate the impurity diamagnetic velocity and, hence, the radial electric field. Thus, the approximation $E_z \approx \mathrm{d}\langle\Phi\rangle/\mathrm{d}\rho$ in equation (2.26) is considered for the C^{6+} impurity ion under study.

3.5.3 Flow velocity

Finally, the velocity along sightlines, $v_l = \mathbf{v} \cdot \mathbf{e}_l$, is obtained from the line centroid shift, λ_c,

$$\lambda_c = (\lambda_0 + \lambda_{cx}) \left(1 + \frac{v_l}{c}\right) \approx \lambda_0 \left(1 + \frac{v_l}{c}\right) + \lambda_{cx}. \tag{3.40}$$

Here, λ_{cx} accounts for possible deviations in the populations of the fine structure level from a complete statistical mixing, that might cause unphysical contributions to the measured velocity. This is removed by adding the measured wavelengths from top and bottom poloidal sightlines (see section 3.4.3.1 for details), since they are almost symmetrically opposite. In addition, accurate and precise calibration in wavelength with frequent access to the experimental hall is required to correct for thermal drifts, as explained in sections 3.4.2.2 and 3.4.2.3.

As explained in section 3.4.4, the daughter distribution function of C^{5+} ions exhibits some apparent velocities, usually named *pseudo-velocities*, not related to the plasma flow. In TJ-II, due to the relatively small magnetic field strength and temperatures, the only significant contribution comes through the velocity arising from the energy dependence of the beam/carbon charge exchange cross-section, which is orientated in the DNBI direction. These effects are only significant for the toroidal view (since the poloidal sightlines view the beam almost perpendicularly), being $\leq 1 - 2$ km s^{-1} for the typical temperatures observed $T_C \leq 200$ eV, see figure 3.25.

The presentation of velocity profiles is left to the experimental results part, chapters 4 and 5, since further data analysis is required to extract the perpendicular and parallel flux-surface averaged flows.

3.6 Summary

A new toroidal viewing array has been installed during this thesis. In this chapter, specific methods have been developed to align the optical system, for both the poloidal and toroidal lines-of-sight. In addition, numerical routines to account for the uncertainties introduced by the average in volume intrinsic to CXRS measurements are provided.

Several instrumental, atomic and beam-related effects that can influence CXRS measurements reported in this thesis have been described and quantified: (a) atomic effects such as Doppler, Zeeman and fine-structure broadening; (b) instrumental issues such as the numerical deconvolution of the instrumental function, wavelength calibration and thermal drifts; and (c) velocity corrections coming from uncertainties in the C VI line emission rest wavelength, and pseudo-velocities arising from the energy dependence of the charge-exchange cross section. These correctinos have led to an improved agreement between main ion and carbon impurity temperatures in TJ-II plasmas [58, 59, 205], as well as accurate and precise rotation measurements [105, 209].

Finally, profiles of fully-ionized carbon density measurements have been presented. It is shown that relative C^{6+} density measurements obtained since 2011 are unreliable, as values from the three fibre arrays performed at the same location do not coincide. This is attributed to a lack of absolute calibration. Some solutions to this problem will be addressed at the end of this report as future work.

Experimental results

CHAPTER 4

INCOMPRESSIBILITY IN LOW-DENSITY PLASMAS AND COMPARISON WITH NEOCLASSICAL THEORY

In this chapter, the incompressibility of C^{6+} impurity flows is studied in low density plasmas of the TJ-II stellarator, i.e. for $\bar{n}_e \leq 1.2 \times 10^{19}$ m^{-3}. As explained in section 2.2, the incompressibility condition is a consequence of particle number conservation with a density constant on flux surfaces. Such an incompressible velocity field is fully determined by two flux functions, see equation (2.33), that ultimately relate to the radial electric field and bootstrap current. Next, the two flux-functions that determine the incompressible flow are studied in light of neoclassical (NC) theory. Note that the incompressibility of flows follows from the usual neoclassical (and gyrokinetic) ordering schemes but it neither assumes nor implies the flows to be of 'neoclassical origin'. Indeed, the spatial variation of an incompressible flow has been recently employed to estimate the poloidal velocity from inboard and outboard toroidal measurements in TCV and DIII-D [165, 168].

There is no clear picture concerning the NC nature of poloidal flows in tokamaks. Early measurements on TFTR with CXRS on fully-ionized carbon [210] indicated a large discrepancy with the NC theory. However, a deeper understanding of CXRS measurements [155] (see section 3.4.4 for a detailed explaination) led to better agreement between experimental poloidal flows and NC expectations on JT-60U [196], MAST [211] or NSTX [181], in H-Mode plasmas or even in the presence of an Internal Transport Barrier (ITB). Moreover, recent measurements on Alcator C-Mod [212] and ASDEX-Upgrade [213] tokamaks have been demonstrated to follow NC theory in the absence of impurity density asymmetries. Nevertheless, poloidal velocity measurements on JET within an ITB [214, 215], and on DIII-D during H-mode and quiescent H-mode [201], are still not fully understood.

On the other hand, toroidal flows in tokamaks are expected to be dominated by mechanisms other than neoclassical, since toroidal viscosity vanishes for axisymmetric systems. Nevertheless, the presence of a sizeable toroidal ripple and/or non-axisymmetric magnetic perturbations for ELM control in tokamak reactors could induce a non-negligible toroidal viscosity. For instance, the effect of an increasing toroidal ripple was study recently in Tore Supra [216], showing

consistency between measured flows and NC predictions.

In stellarator devices plasma cannot rotate freely [33] and the radial electric field is determined by the ambipolarity condition on the NC radial particle fluxes, see section 2.3. Detailed comparisons of the NC radial electric field with CXRS measurements have been performed on the W7-AS stellarator, showing reasonable agreement for most of the plasma scenarios studied [26]. In addition, in the LHD and CHS stellarators, qualitative agreement was found between radial electric field measurements and calculations with simplified NC theories [217, 218]. The effect of the magnetic field ripple on the toroidal flows was also investigated in CHS [219] and LHD [220], showing qualitative effects of helical and toroidal ripple on spontaneous toroidal flow. Finally, a recent work in HSX has shown a clear discrepancy between the experimental and NC radial electric fields [164]. The authors claim that the monoenergetic approximation used by DKES might be inadequate for radial electric fields close to the helical resonance [221]. Nonetheless, the parallel flow was well reproduced after including momentum-correction techniques and impurities in the calculations.

In the TJ-II stellarator the radial electric field has been studied by means of the Heavy Ion Beam Probe (HIBP) [66] and Doppler Reflectometry (DR) [72] diagnostics. Measurements from the former showed consistency with NC calculations in the electron root, within a factor a two [66]. However, the experimental values systematically exceed the NC predictions in ion-root operation [222]. In addition, passive spectroscopy has been utilized to measure poloidal and toroidal rotations of impurities [103, 104]. Qualitative agreement was reported between the experimental poloidal flow and NC values, mainly in the change of root as density increases [87]. In contrast, significant discrepancies were found in the toroidal flows for the different species studied and with NC calculations [103].

In this chapter we use CXRS to measure fully ionized carbon impurity flows in low density plasmas of the TJ-II stellarator and compare them with neoclassical calculations. First, we present in section 4.1 a general treatment of the sightlines and flow geometry, which allows the extraction of the two flux-surface averaged (FSA) flows from two velocity measurements. These flux constants define an incompressible flow within a flux surface and are related to the radial electric field and the ion bootstrap current. In section 4.3, the method is applied to two pairs from three measurements (poloidal, outboard-toroidal and inboard-toroidal) to show that the spatial variation of the flow is consistent with incompressibility. Finally, the measured flows are compared with neoclassical predictions (section 4.4) and good agreement is found for the radial electric field (in all the cases studied) and parallel mass flows (in ECRH plasmas without momentum injection).

4.1 Data analysis: flux-surface flows extraction

The general form of the impurity velocity field is (see equation (2.33) and section 2.2)

$$\mathbf{u}_z = E_z(\rho)\frac{\mathbf{B}\times\nabla\rho}{B^2} + (\Lambda_z(\rho) + E_z(\rho)h)\,\mathbf{B}, \tag{4.1}$$

where the perpendicular velocity is given by $\mathbf{E}\times\mathbf{B}$ and diamagnetic contributions, see equations (2.25) and (2.26). The parallel flow in (4.1) is composed of a parallel mass flow, $\Lambda_z\mathbf{B}$, and the

local parallel Pfirsch-Schlüter (PS) flow, $E_z h\mathbf{B}$, see equation (2.29) and figure 2.1 in section 2.2. In order to obtain flux-surface averaged (FSA) flows from poloidal and toroidal CXRS velocity measurements, it is convenient to define dimensionless vectors, which store the variation of the flow within the surface. These are

$$\mathbf{f} = -\frac{\langle B\rangle}{\langle|\nabla\rho|\rangle}\left(\frac{\mathbf{B}\times\nabla\rho}{B^2}+h\mathbf{B}\right), \tag{4.2}$$

$$\mathbf{g} = \frac{\langle B\rangle}{\langle B^2\rangle}\mathbf{B}. \tag{4.3}$$

Note that the vector $\mathbf{f}$ has both perpendicular and parallel components, the latter coming from the PS contribution, $\mathbf{f} \equiv \mathbf{f}_\perp + \mathbf{f}_{\rm PS}$. Poloidal cuts of such dimensionless parallel vector were presented in figure 2.1. Then, impurity flows are expressed as

$$\mathbf{u}_z = \mathbf{f}U_\perp(\rho) + \mathbf{g}U_{\rm b}(\rho). \tag{4.4}$$

Here, the following perpendicular and parallel FSA flows are defined,

$$U_\perp(\rho) \equiv \frac{E_{\rm r}}{\langle B\rangle} - \frac{1}{nZe}\frac{{\rm d}p}{{\rm d}\rho}\frac{\langle|\nabla\rho|\rangle}{\langle B\rangle}, \tag{4.5}$$

$$U_{\rm b}(\rho) \equiv \Lambda_z(\rho)\frac{\langle B^2\rangle}{\langle B\rangle} = \frac{\langle \mathbf{u}_z\cdot\mathbf{B}\rangle}{\langle B\rangle}, \tag{4.6}$$

where the FSA radial electric field is given by $E_{\rm r}(\rho) \equiv -\langle|\nabla\rho|\rangle {\rm d}\Phi/{\rm d}\rho$. In the following, impurity ion *bootstrap flow* refers to the FSA parallel flow, U_b, since it is the contribution of the ion velocity to the bootstrap current. This is done in order to distinguish it from the PS flow, which is also parallel.

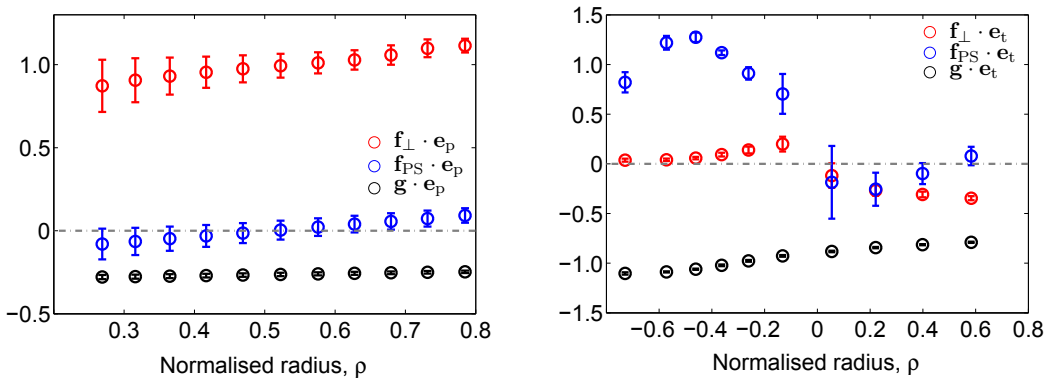

Figure 4.1. Dimensionless factors that store the variation of the flows on the surface for the (left) poloidal-bottom and (right) toroidal fibre arrays. The vector $\mathbf{f}$ has been split into their parallel and perpendicular components ($\mathbf{f}_{\rm PS} = \mathbf{f}\cdot\hat{b}$ and $\mathbf{f}_\perp = (\hat{b}\times\mathbf{f})\times\hat{b}$, respectively).

Finally, taking the projections of the velocity vector $\mathbf{u}_z$ over the poloidal-bottom and toroidal sightlines ($u_{\rm p} = \mathbf{u}_z\cdot\mathbf{e}_{\rm p}$ and $u_{\rm t} = \mathbf{u}_z\cdot\mathbf{e}_{\rm t}$, respectively) the FSA mean velocities are obtained from the measured flows as

$$\begin{pmatrix} U_\perp(\rho) \\ U_{\rm b}(\rho)\end{pmatrix} = \frac{1}{\Delta}\begin{pmatrix} g_{\rm t} & -g_{\rm p} \\ -f_{\rm t} & f_{\rm p}\end{pmatrix}\begin{pmatrix} u_{\rm p} \\ u_{\rm t}\end{pmatrix}. \tag{4.7}$$

Here, $\Delta = g_t f_p - g_p f_t$, and the sub-index (p, t) denote the projection of a vector ($\mathbf{u}_z, \mathbf{g}$ or $\mathbf{f}$) over the poloidal and toroidal lines of sight. Accordingly, the FSA flows can be obtained from two different measurements performed on a surface, but not necessarily at the same location. The results of this procedure are presented in the next section.

The projection of the geometrical vectors, $\mathbf{f}$ or $\mathbf{g}$, over the poloidal-bottom and toroidal sight-lines is displayed in figure 4.1. The vector $\mathbf{f}$ has been split into their parallel and perpendicular components, to illustrate their contributions on the velocity field[1]. As expected, the poloidal velocity is dominated by the perpendicular contribution, although the parallel one (through the $\mathbf{g} \cdot \mathbf{e}_p$ factor) has to be accounted for. The sample volumes located at the outboard plane are close to stagnation points of the PS flow and therefore its contribution to these measurements is modest, unlike in the inboard region where it can become dominant for toroidal velocities. In addition, the mean values and standard deviation of these geometrical quantities have been obtained through the average over the measurement volume for a given fibre, as explained in section 3.3. It can be observed that when moving towards the plasma centre, the dispersion in these factors increases, since the poloidal views become more perpendicular to the surfaces. The errors in the results will consist therefore of the statistical ones, plus those due to the average in the measurement volume.

4.2 Plasma scenarios

In this work, two plasmas scenarios are considered, both being operated in the 100_44_64 magnetic configuration. The first one, heated by ECRH, is characterized by flat electron density ($n_e(0) \approx 0.5 \times 10^{19}$ m^{-3}) and peaked electron temperature profiles ($T_e(0) \approx 0.8$ keV), see figure 4.2. However, ions remain cooler, $T_i(0) \sim 80$ eV ($T_i \approx T_c$ is assumed, see the comparison in figure 3.27), with slightly hollow temperature and impurity density profiles. The data presented here corresponds to TJ-II discharge #25801, which is representative of several similar discharges that are briefly discussed at the end of this chapter.

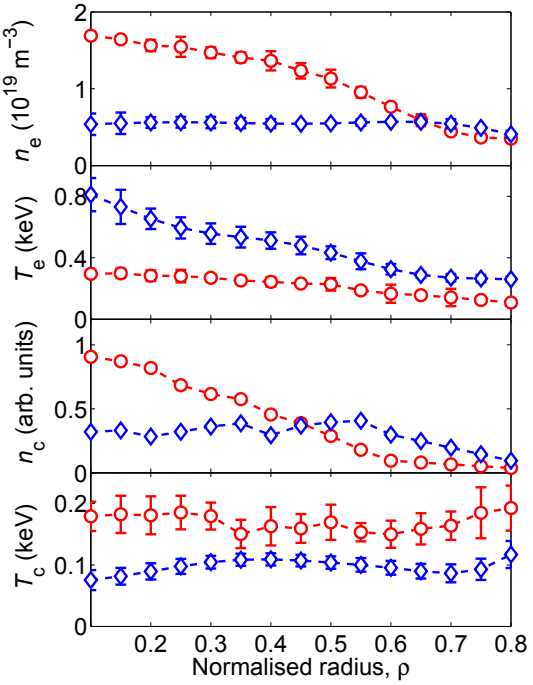

Figure 4.2. Profiles of n_e, T_e, n_c and T_c (from top to bottom) for the ECRH scenario, shot #25801 (blue diamonds); and the NBI case, discharge #28263 (red circles).

In the second scenario, plasmas are heated with a tangential NBI injected in the direction of

[1] The projections of the P-S dimensionless vector, $\mathbf{f}_{PS} \cdot \mathbf{e}_i$, presented in figure 4.1 are consistent with those shown in figure 2.1. Let us consider, e.g. an inboard toroidal view for which $\mathbf{B} \cdot \mathbf{e}_t < 0$ and $\mathbf{f}_{PS} \cdot \mathbf{e}_t > 0$. Then, the Pfirsch-Schlüter factor should be negative, $f_{PS} < 0$. This is consistent with the values presented in figure 2.1 for the poloidal plane $\phi = 75^o$.

the toroidal magnetic field. The resultant density profile is more peaked, with $n_e(0) \approx 1.6 \times 10^{19}$ m^{-3}, whilst the electron temperature decreases to $T_e(0) \sim 300$ eV. In contrast, the ions reache temperatures up to 200 eV. The discharge chosen for this case, #28263, is not representative of fully developed NBI heated plasmas, as it corresponds to the first steps of the NBI phase, where the density grows rapidly. Nevertheless, it is included here to highlight that for these low density plasmas the results are independent of the heating method.

Finally, the measurements presented are restricted to the region $|\rho| \leq 0.8$, because CXRS measurements are not reliable at the edge of TJ-II, due to the poor statistics and the possible presence of suprathermal ions [203].

4.3 Flow incompressibility

The assumption of an incompressible velocity field like the one in equation (4.1) is widely used in present day CXRS data analysis (see, e.g., references [164, 165, 201]). In this subsection this hypothesis is verified by applying the method developed in the previous section, equation (4.7), to the poloidal and toroidal velocities measured in the discharges presented in figure 4.2.

The observed velocity pattern, after correcting for fine structure effects and pseudo-velocities (see sections 3.4.3.1 and 3.4.4), is represented in figure 4.3 for the ECRH and NBI heating scenarios under study. Poloidal top velocity measurements are not shown, since they were already used to correct for fine structure effects, and so do not provide further information about poloidal flow. In this figure, positive velocities corresponds to particles moving away from the observer. In the ECRH plasma, the toroidal rotation is opposite to the magnetic field direction, while the toroidal flow is reversed in the NBI case. In addition, ECRH toroidal measurements exhibit a strong in/out asymmetry that is explained next.

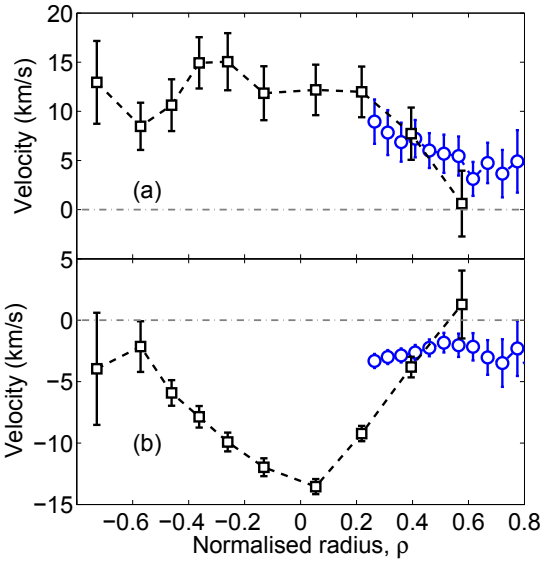

Figure 4.3. Carbon impurity ion flows observed by toroidal (black squares) and poloidal bottom (blue circles) sightlines, for the: (a) ECRH plasma, discharge #25801; and (b) NBI plasma, discharge #28263.

As commented before, CXRS toroidal velocity measurements are performed on both sides of the magnetic axis in TJ-II, see figure 3.8. Therefore, they are suitable for the verification of flow incompressibility, due to its redundancy on several magnetic surfaces. In figure 4.4 the perpendicular, $U_\perp(\rho)$, and parallel, $U_b(\rho)$, FSA flows obtained are plotted. The values that result from inboard toroidal measurements are presented as open circles, whilst the ones deduced from outboard toroidal velocities are squares. In both cases, the poloidal measurements inserted in equation (4.7) come from the outboard region.

The agreement found between inboard and outboard measurements confirms the main hypothesis of the applied method, i.e., that impurity flows are incompressible for the low density plasmas presented here. Indeed, to the authors' knowledge, this is the first time that this fundamental assumption of kinetic theory is checked with independent measurements at different locations of a surface (recent works at TCV and DIII-D [165, 168, 223] extract the poloidal flow from toroidal in/out measurements, but are not compared with direct poloidal measurements, due to difficulties associated with such measurement in these tokamaks).

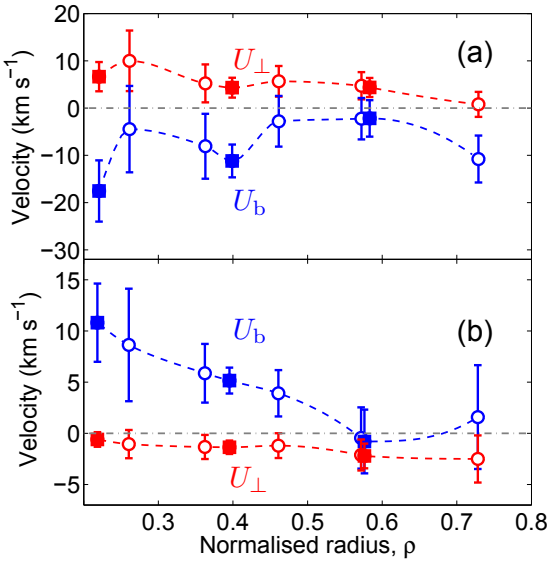

Figure 4.4. Flux-surface averaged flows $U_\perp(\rho)$ and $U_b(\rho)$, for the: (a) ECRH discharge, #25801; and (b) NBI plasma, #28263. The circles correspond to toroidal measurements performed in the inboard region, and the squares to those taken in the outboard one.

The strong asymmetry in the toroidal velocity observed in the ECRH scenario, figure 4.3 (a), is explained by the larger (compared to the NBI case) perpendicular flow, which generates significant variations in the parallel velocity, through the local Pfirsch-Schlüter flow. As expected, there is a change from electron to ion root in the radial electric field with increasing density [45, 87, 107], and therefore, a change of sign in $U_\perp$ (the impurity diamagnetic contribution is negligible[2], except for $\rho \sim 0.7$ in the NBI case, where it reaches ~ 1 km s^{-1}). Finally, a positive parallel velocity is observed in the NBI plasmas, which is compatible with the injection of the beam in the direction of the magnetic field. This will be discussed in the next subsection.

As an indication of the importance of this previous check on the flow spatial variation prior to its comparison with neoclassical estimates, it is noted that in higher density NBI plasmas, which are studied in the next chapter, a *compressible* flow variation is observed in TJ-II. More specifically, the flow is found to be compressible in the sense that the two (inboard and outboard) measured bootstrap velocity components are different. Therefore, this component of the flow does not show and incompressible form like $f(\rho)\mathbf{B}$, as it would be expected. This makes the comparison of parallel velocities with standard neoclassical theory not straightforward. Indeed, impurity density variations within a flux surface have been theoretically predicted in the presence of large ion pressure gradients [100], and recently observed in several tokamak devices (Alcator C-Mod [140] and ASDEX-Upgrade [141]). The asymmetry is related to ion-impurity friction and ultimately to impurity radial fluxes, which makes its comprehension particularly relevant for nuclear fusion. The analysis of such plasmas [209] is presented in chapter 5.

Finally, as an additional benchmark of the method presented in here, the extracted FSA

[2] As explained in section 3.5.2, systematic errors in carbon density measurements were observed and attributed to the lack of absolute calibration of the optical path. However, such uncertainties are not so critical for the plasmas presented in this chapter, as demonstrated in figure 3.28.

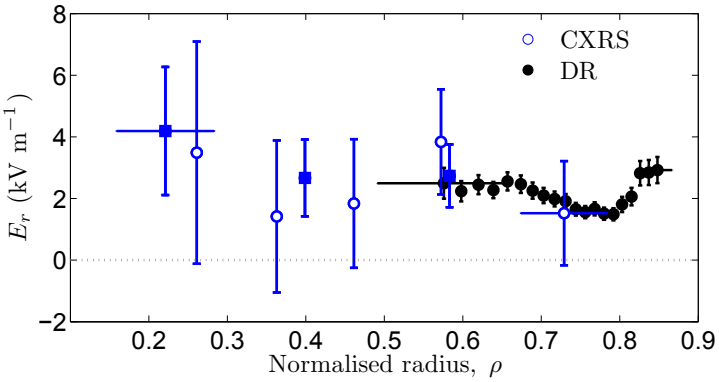

Figure 4.5. Comparison of E_r as measured by CXRS and Doppler Reflectometry for two similar ECRH discharges (shots #32599 and #32598). Typical horizontal error bars are shown.

radial electric field is compared with that measured by Doppler reflectometry (DR) [67], see figure 4.5. The error bars in CXRS measurements are large, due to the small S/N ratio typical from a low density, ECRH heated, lithium coated plasmas. On the other hand, for these steady-state ECRH plasmas in which plasma parameters are almost constant, DR measurements are taken in a wide temporal frame[3], thus allowing for large counting statistics and small vertical error bars. In the latter measurements the phase velocity of turbulent structures is neglected. On the other hand, the impurity diamagnetic contribution has been neglected when determining E_r from CXRS velocity measurements, due to the uncertainties in carbon density measurements explained in section 3.5.2. As aforementioned, such contribution is negligible in TJ-II ECRH plasmas. Furthermore, the good quantitative agreement found in between CXRS and DP gives confidence in the analysis method developed here. It also confirms the hypothesis made in DP data analysis [109].

In the following, a comparison of CXRS flow measurements with NC calculations of the radial electric field and main-ion parallel mass flow is provided.

4.4 Comparison with neoclassical theory

The Drift Kinetic Equation is solved by using the numerical code DKES [95] complemented with momentum correction techniques [117, 224]. DKES calculates the monoenergetic transport coefficients of the magnetic configuration. These coefficients are convoluted with a Maxwellian distribution function which in turn depends on local density and temperature, see e.g. equation (2.63). The inclusion of the thermodynamical forces (gradients of density and temperature and radial electric field) allows the FSA neoclassical fluxes to be estimated. The neoclassical radial electric field itself is found iteratively by imposing ambipolarity on the particle radial fluxes, equation (2.46). Specific details of the bootstrap calculation for TJ-II are found in [44, 45], and references therein. These simulations are consistent with other calculations of the bootstrap current [225, 226].

The inputs for this calculation are the magnetic field equilibrium and TJ-II density and temperature profiles. The former is taken to be the vacuum equilibrium, for the low β plas-

[3] The radial location of the DR system is changed, in this case, each 5 ms, while CXRS measures the whole velocity profile in 5 ms.

mas studied here. The latter require data from the Thomson Scattering, Helium beam probe, Reflectometry, Interferometry (see [55] and references there in) and CXRS diagnostics. The uncertainties in the transport coefficients and in the measured profiles are propagated to the final theoretical estimate, as in [44].

In order to estimate accurately the parallel and poloidal momentum balance, one should make the calculation by including protons, electrons and main impurities present in the plasma. However, for the lithium-coated plasmas studied in this work, the impurity concentration is low [73] and does not modify the ambipolar equation, leaving E_r unchanged. Since the impurity diamagnetic term is small, this completely determines the poloidal impurity rotation. On the other hand, once one ensures momentum conservation in the calculations (by including inter-species friction), the bootstrap flow of the trace impurities is shown to follow that of the bulk ions, which are calculated as in [44]. Finally, one may wonder if values of E_r close to resonances could be found, as in [164]. In such a case, the poloidal $E \times B$ drift and the poloidal component of the thermal motion along the magnetic field cancel out, producing a peaking of the radial fluxes so the local ansatz and the $E \times B$ incompressibility assumption [221], underlying DKES computations, fail. At TJ-II, this occurs for very large values of E_r [227] for the ion temperatures observed in this thesis, i.e. $T_i > 50$ eV. The agreement found in the present comparison supports the hypotheses in our calculation.

Some general considerations can be made, following the results obtained for model plasma profiles [44, 45, 107, 226]. Low density ECRH plasmas in TJ-II are in the electron root: E_r is positive and large, and therefore it partially cancels the large contribution of the T_e gradient to the electron radial transport (see figure 4.2). This large radial electric field drives a large ion parallel flow, especially close to the centre, where the fraction of trapped particles is small and E_r is considerable. On the contrary, NBI plasmas are in the ion root. In order to reduce the ion particle radial transport -driven by the ion temperature gradient- to the electron level, E_r is small and negative. This partial cancellation of the ion channel has consequences in the parallel momentum balance as well, where the negative E_r leads to a small ion bootstrap current.

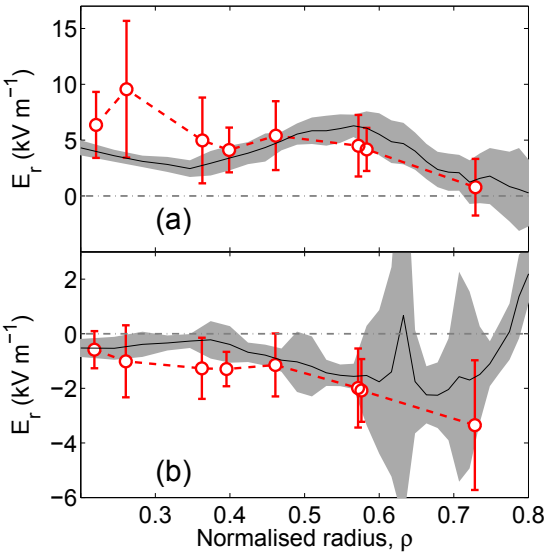

Figure 4.6. Comparison of neoclassical (grey shading) and measured (red circles) E_r, for the: (a) ECRH discharge, #25801; and (b) NBI plasma, #28263.

In the following, the results of a comparison between NC theory and CXRS measurements are presented. Since CXRS active data has been obtained from two different discharges (shot-to-shot technique [46], where main plasma parameters: n_e, T_e, etc., are reproducible within diagnostic error bars), we compare the experimental data with the average of NC outcomes for both plasmas. In figure 4.6, the measured and calculated radial electric field are shown. The

experimental values are in agreement with previous results obtained in similar plasmas with the HIBP diagnostic [66], and agree with the NC predictions within the error bars. Nonetheless, the mean values observed at the core of the ECRH plasma are somewhat larger than that of the neoclassical estimate; however, the error bars are significant. Moreover, the contribution to the experimental E_r from toroidal measurements, $\propto -g_{\|}\hat{b}\cdot\mathbf{e}_p u_t$, equation (4.7), is similar to that of the poloidal flows, $\propto g_{\|}\hat{b}\cdot\mathbf{e}_t u_p$, due to the high toroidal velocities observed in the core region, see figures 4.1 and 4.3 (a). As a result the uncertainties in E_r increase, since toroidal sightlines are almost aligned with the magnetic field lines, and thus, the extraction of its perpendicular contribution is less reliable.

In the NBI plasma, the experimental errors are reduced, see figure 4.6 (b). The inferred radial electric field is in good quantitative agreement with neoclassical calculations. The error bars about the NC estimates in figure 4.6 correspond to the not insignificant uncertainties in the plasma profiles, as in [45]. In particular, for $\rho \geq 0.6$, both electron and ion roots can result, as different values of density and temperature are considered within the error bars of figure 4.2, hence the significant uncertainties. Finally, the agreement found for this discharge in the radial electric field suggests that fast NBI ions do not contribute significantly to the radial ambipolar balance, although they inject parallel momentum, as discussed in the following text.

Figure 4.7 (a) shows calculations of neoclassical bootstrap ion flow during the ECRH phase, together with the C^{6+} parallel flux-surface flow, $\langle \mathbf{u}\cdot\mathbf{B}\rangle/\langle B\rangle$. A strong parallel rotation driven by the radial electric field is observed at the core region, that is well reproduced by the neoclassical predictions. In the higher density unbalanced NBI case, the parallel flow consists of the neoclassical one (bootstrap), plus the rotation induced by the NBI heating neutrals. Indeed, these measurements show that the NBI external momentum input dominates, producing a parallel flow larger in magnitude and opposite in sign to the calculated bootstrap contribution to the flow. Since this is a low density NBI heated plasma, the injected fast neutrals can penetrate to the core. This would explain why the deviation of the parallel flow is maximum towards $\rho \sim 0.2$, whilst measured parallel flow approaches bootstrap calculations for $\rho \geq 0.6$.

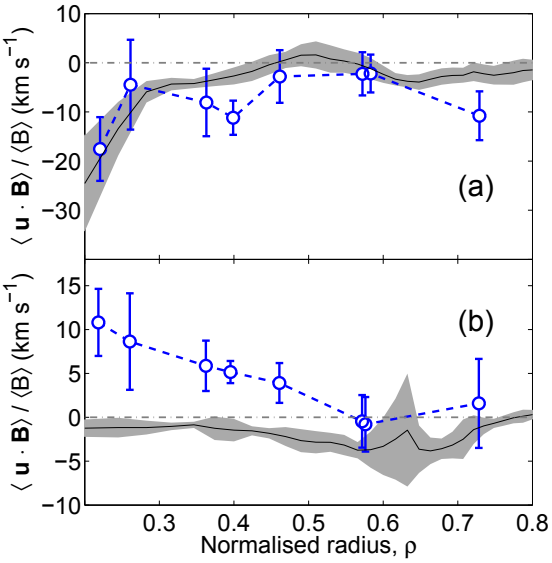

Figure 4.7. Comparison of neoclassical and measured parallel flow, U_b, for the: (a) ECRH discharge, #25801; and (b) NBI plasma, #28263.

In order to highlight the reproducibility of the results in the ECRH scenario, the comparison of the measured radial electric field and bootstrap flow with NC calculations have been depicted in figure 4.8, for a set of similar ECRH discharges. The features observed in figures 4.6 (a) and 4.7 (a) are replicated in these discharges, and the agreement with the NC theory is repeated as well.

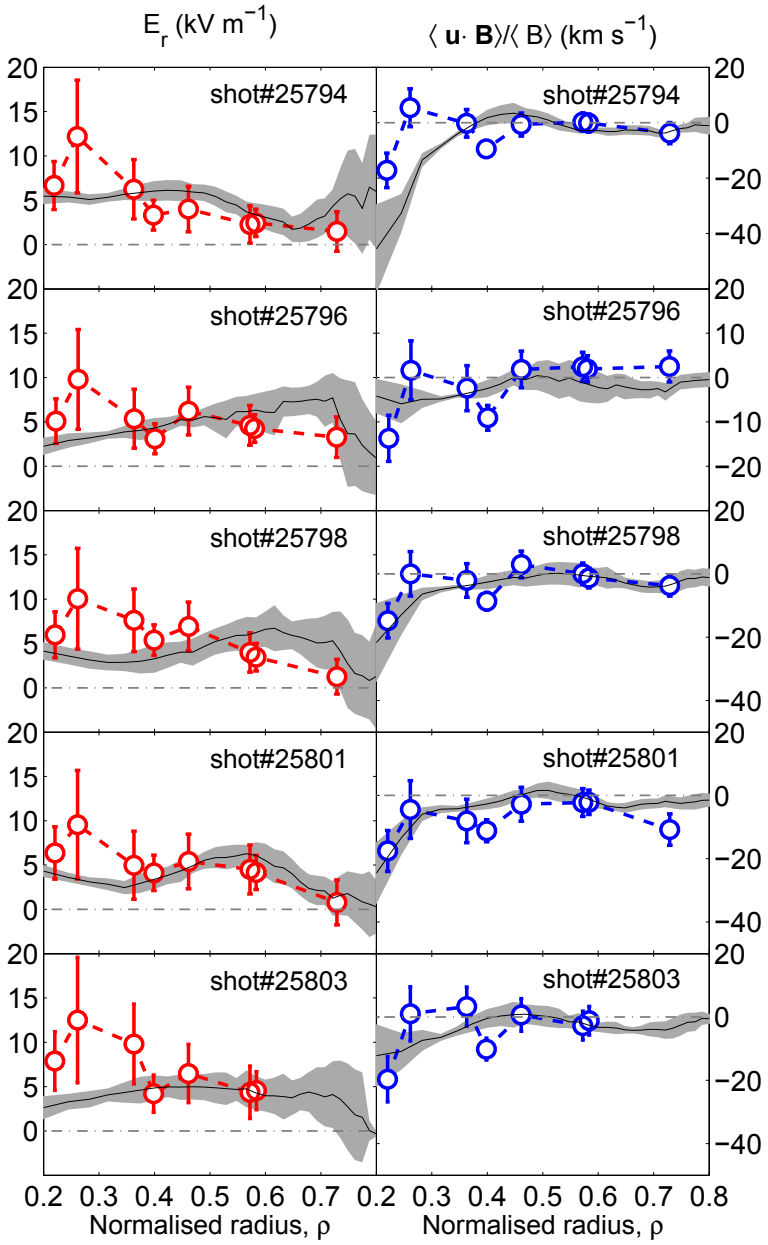

Figure 4.8. Comparison of NC and measured radial electric field and bootstrap flow, for a set of ECRH discharges. Circles correspond to CXRS measurements, and grey shading to NC estimates.

Finally, the recent comparison [228] between NC calculations and CXRS flow measurements in the vicinity of the so-called *low-density transition*, see e.g. [79], is presented in figure 4.9, for the same set of reproducible plasma discharges #32597 – #32599 presented in figure 4.5. For this plasma scenario the electron density, $n_e(0) \approx 0.6 \times 10^{19}$ m^{-3}, is close to the density in which the radial electric field changes from electron- to ion-root. In such a transition, a sheared E_r appears at the edge of the plasma [78, 80], where the density gradient is maximum, and propagates towards the centre as the density is increased, see e.g. [81, 87]. As observed in figure 4.9 the theoretical and experimental E_r profiles are positive. Agreement in the parallel

bootstrap flow is observed within the experimental error bars, although the predicted values are smaller than CXRS parallel mass flow measurements at the core. At $\rho \sim 0.8$, the DR measures a minimum of E_r, with a double-shear layer on both sides of it. It is at this radial position where the reversal of the radial electric field typically starts [81], which means that indeed the plasma in figure 4.9 is very close to the transition. The predicted neoclassical E_r also shows a double-shear-layer, although at a slightly outer radial position. The calculations slightly overestimate E_r in the region $0.5 < \rho < 0.8$. The results are consistent with an underestimation of the ion radial flux: as indicated in [228] if finite-orbit-width effects were included in the calculation, as in reference [229], the theoretical predictions and experimental values would show better agreement. This is currently under investigation.

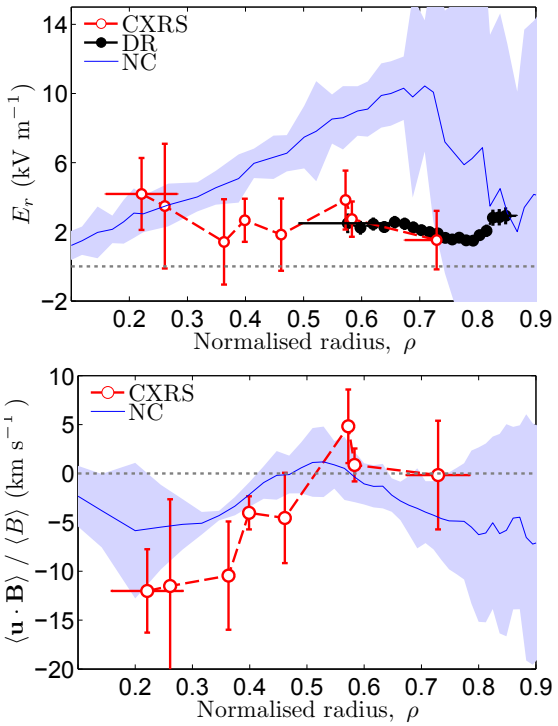

Figure 4.9. Comparison of NC and measured radial electric field (left) and bootstrap flow (right), for a set of reproducible ECRH discharges #32597 − #32599 close to the electron- to ion-root transition.

4.5 Summary

A review on the comparison between CXRS experimental flows and neoclassical calculations has been provided. The attention has been focused first on poloidal tokamak flows, and all velocity components (tangent to the surface) in stellarators. The present work contributes to this systematic comparison in between CXRS experimental flows and neoclassical predictions. Good quantitative agreement has been found between measured and NC radial electric fields for low density ECRH plasmas, far from the electron- to ion-root transition. Furthermore, a comparison of impurity parallel rotation with the NC bootstrap contribution to the parallel flow has been done for the first time in TJ-II, showing consistency with the calculations in these plasmas. In addition, in an unbalanced, not fully developed, NBI discharge with relatively low density good agreement has been found for the radial electric field, while a change in the direction of parallel rotation (with respect to the NC calculations, which do not account for momentum injection) has been observed. This points to a minor role of the fast ion-driven radial current in the ambipolar balance (or poloidal momentum balance) of the TJ-II stellarator.

The quantitative agreement found in the literature –an also in this work– leaves the neoclassical framework as a useful tool for predicting –viscous– forces within the surface and the damping of the flows. However, since standard[4] neoclassical theory assumes an incompressible spatial

[4] i.e., the one surging after imposing ambipolarity on the fluxes, as described in chapter 2, but without a consistent treatment of quasi-neutrality.

pattern of the flows, such hypothesis must be verified in the experiments prior to establishing a comparison with a transport theory. In this chapter, the basic form of the velocity field, i.e. a divergence-free total flow tangent to magnetic surfaces, has been verified. To this end, a general treatment of sightlines and flow geometry has been applied to two pairs of three independent velocity measurements performed at different locations of a flux surface, and consistency with a 2D incompressible flow has been demonstrated.

In this sense, the experimental observations on JET and DIII-D in high-performance plasmas scenarios, which showed a large discrepancy -even in the sign- between the experimental poloidal velocity and the neoclassical prediction, could have been obscured by the development of an impurity density asymmetry within the surface, a plausible hypothesis for the high-pressure gradients present in those plasmas. In that case, a compressible flow should be expected, making the comparison with neoclassical theory not straightforward.

CHAPTER 5

COMPRESSIBLE IMPURITY FLOWS

In chapter 4 fully-ionised carbon impurity flow measurements were undertaken using CXRS in low density, ECRH plasmas of the TJ-II stellarator. The CXRS viewing line geometry was used to verify that the in-surface variation of parallel impurity flow was consistent with an incompressible total flow tangent to flux surfaces. In addition, the measured perpendicular and parallel flows were compared with neoclassical calculations of radial electric field and ion parallel flow, showing good agreement in those low density plasmas. However, as indicated in [105], measurements in-medium density plasmas, $\bar{n}_{\mathrm{e}} \in (1.2 - 2.4) \times 10^{19}$ m^{-3}, reveal a compressible pattern like that described in section 2.4, which must be accompanied by an impurity density variation within the surface. Large uncertainties in carbon density profile measurements arise in TJ-II from the lack of calibration of the optical paths inside the vacuum chamber, see the discussion in section 3.5.2. Therefore, to study whether the density is constant on flux surfaces the approach taken is to examine the spatial variation of the flows, as in references [140, 141]. These observations are detailed here.

The CXRS diagnostic makes use of impurity lines to measure the temperature, density and velocity of an impurity ion (here fully ionised carbon). Now, because of their high collision frequency with main ions, the temperature and parallel flow of impurities are generally taken to be a proxy of the main ion temperature and parallel mass flow. However, such collisional coupling between main ions and medium to high Z impurities can induce impurity density variations within a surface that are comparable with their mean value on the surface, as described in section 2.4. The in-surface density variations cause the impurity parallel flow to deviate from the ion parallel flow as the parallel density gradients drive a return flow. Furthermore, such a return flow needs not preserve an incompressible pattern as particle conservation $\nabla \cdot (n_z \mathbf{u}_z) = 0$ does not reduce to flow incompressibility $\nabla \cdot \mathbf{u}_z = 0$ for non-constant impurity density n_z. Indeed, several tokamak devices have reported on a substantial poloidal variation of low-Z impurity parallel flow on a surface at a tokamak pedestal, see references [140, 143, 144] and [141, 142]. In stellarators, a poloidal variation of C^{6+} density and poloidal velocity was observed in the core region of CHS outwards shifted plasmas [145].

While such behaviour of impurity flows limits the capability of CXRS on fully ionized impurity ions to directly track the bulk flow (arguably its intended purpose), the study of impurity density asymmetries and flow variations provides valuable information on impurity-ion friction, which is expected to be an important mechanism of impurity radial transport (see, e.g. reference [102]). Impurity dynamics, and particularly their radial transport and accumulation in the core of fusion plasmas is of utmost importance for fusion viability, as impurities can produce unacceptable energy losses through radiation as well as diluting the fusion reactants. Nevertheless, the radial transport of impurities displays considerable complexity which often has eluded a theoretical explanation. Classical examples are the impurity screening shown by the High-Density H-mode observed in W7-AS [230] and the impurity hole in LHD plasmas [220]. Therefore, the experimental validation of theoretical models of impurity density redistribution within a flux surface is of considerable importance as it provides some indirect validation of model predictions for impurity radial transport [138]. In addition, from the data interpretation point of view, the parallel return flows associated with a density inhomogeneity might complicate a comparison of CXRS rotation measurements with standard NC theory, particularly in the presence of large main ion gradients [201, 215].

In this chapter CXRS measurements of C^{6+} flows in NBI heated, ion-root plasmas of the TJ-II stellarator are presented. Significant and reproducible deviations in the measured impurity flow from an incompressible pattern are observed as density increases, which points to a redistribution of impurity density within flux surfaces as was observed in [140–142] although it appears in more internal regions of the plasma, as in [145]. We present these flow measurements and compare the observed deviations with the parallel return flow from a modelled impurity density redistribution driven by ion-impurity friction [100]. Such a friction model was adapted to a general stellarator geometry with the bulk ions in the Pfirsch-Schlüter regime of collisionality in reference [102] and is extended here for main ions in the plateau regime, provided the ion temperature gradient is small (a plausible assumption for the plasmas under consideration). The calculated return flow substantially modifies the incompressible velocity pattern, being comparable to the impurity parallel PS flow. However it is shown that the calculated modifications at the precise locations of the CXRS measurements are not in the direction of the measured in-surface variations of impurity parallel flow. The inclusion of inertial and parallel electric field forces in the parallel momentum balance does not provide a better understanding of the experimental observations.

This chapter is organised as follows: in section 5.1, the methodology used to relate the velocity field to the CXRS flow measurements through the appropriate geometric quantities is explained. In section 5.2 the impurity flow measurements and their compressible asymmetries are described. These asymmetries are compared to the outputs of an ion-impurity friction model in section 5.3, where modifications to the impurity flow incompressible pattern caused by an in-surface impurity density variation are detailed. In section 5.4 the validity of the friction model is examined and the impurity parallel force balance is extended to account for inhomogeneities of the electrostatic potential within a magnetic surface. Finally, conclusions are drawn in section 5.5.

5.1 Data analysis

For the medium to high density plasmas under study in this chapter, a systematic deviation of the parallel flows from the form given by equation (2.29) is observed. The deviation is interpreted to be caused by variations of impurity density n_z within flux surfaces, in which case the reduction of the number conservation condition to the incompressibility of total impurity flows no longer holds. This situation is treated by allowing the function Λ_z in (2.29) to have angular dependencies, see section 2.4. To quantify the deviations it is convenient to define an impurity parallel return flow as $\Lambda(\rho,\theta,\phi) = \Lambda_z(\rho,\theta,\phi) - \Lambda_i(\rho)$, which is associated with parallel gradients of the impurity density. With this particular choice, impurity flows are written as the sum of an incompressible flow $\mathbf{u}_{z0}$, see equation (2.81), plus the return flow, $\Lambda\mathbf{B}$, which compensates for the impurity density redistribution, see equation (2.80), i.e. $\mathbf{u}_z = \mathbf{u}_{z0} + \Lambda(\rho,\theta,\phi)\mathbf{B}$. Note that this velocity field is the same as that given by equations (2.25) and (2.29), but with $\Lambda_z(\rho,\theta,\phi) = \Lambda(\rho,\theta,\phi) + \Lambda_i(\rho)$. The case $\Lambda = 0$ reduces to an incompressible flow pattern with the z impurities dragged by the ion parallel flow, i.e. $\Lambda_z = \Lambda_i(\rho)$.

The data analysis employed here, which is an adaptation of that presented in chapter 4, accounts for possible compressible variations of the parallel impurity flow discussed previously. The method makes use of the three independent flow measurements performed at the same flux surface (two of them at the same point on a surface, refer to figure 3.8) to obtain independent measurements of the impurity parallel mass flow Λ_z at two locations of the same flux surface. The logic can be summarised as follows: first, the intersecting poloidal and toroidal outboard sight lines are used to extract the local parallel and perpendicular flows. The perpendicular flow provides a direct estimate of $E_z(\rho)$, which is then used to subtract the PS component from the parallel velocity to get a measurement of Λ_z in the outboard region, i.e. Λ_z^{Out}. Next, the obtained value of $E_z(\rho)$ is used to calculate the projections of the perpendicular and parallel PS flows on the inboard toroidal measurement at the same flux surface. After subtraction of these projections a second value of the impurity parallel mass flow, Λ_z^{In}, is obtained in the inboard region.

To make the above description more explicit the impurity flow given by equation (2.82) is recast as

$$\mathbf{u}_z = \mathbf{f}U_\perp + \Lambda_z\mathbf{B}, \tag{5.1}$$

with the dimensionless geometric vector $\mathbf{f}$ given by (4.2) and the perpendicular flow $U_\perp$ defined in (4.5). This surface-constant $U_\perp(\rho)$ is calculated from the intersecting poloidal and toroidal sight lines at three radial positions in the outboard region ($\rho \sim 0.2, 0.4$ and 0.6, see figure 3.8). These values of $U_\perp$ are used together with the condition $U_\perp(0) = 0$ to interpolate $U_\perp$ at the radial locations of all CXRS toroidal measurement with $|\rho| \leq 0.6$. Note: in order to minimize the uncertainties in the extrapolation of $U_\perp$, the innermost CXRS toroidal measurement position at $\rho = -0.75$, see figure 3.8, is not used in this chapter.

Next, the quantity $\Lambda_z(\rho,\theta,\phi)$ is obtained form toroidal velocity measurements as

$$\Lambda_z = \frac{u_{z,\mathrm{t}} - f_{\mathrm{t}}U_\perp}{B_{\mathrm{t}}}. \tag{5.2}$$

The sub-index t indicates the projection of a vector ($\mathbf{u}_z$, $\mathbf{f}$ and $\mathbf{B}$) in the toroidal viewing direction, $\mathbf{e}_\mathrm{t}$, as in previous chapters. Figure 5.2 shows several examples of these profiles, that are discussed in the next section. Finally, the differences in the parallel mass flow (divided by the local magnetic field strength) are

$$\Delta\Lambda_z = \Delta\left(\frac{u_{z,\mathrm{t}}}{B_\mathrm{t}}\right) - U_\perp \Delta\left(\frac{f_\mathrm{t}}{B_\mathrm{t}}\right), \tag{5.3}$$

where $\Delta(X) \equiv X^{\mathrm{In}} - X^{\mathrm{Out}}$. Note that the differences in the impurity parallel mass flow equal those of the impurity return flow defined in equation (2.82), i.e. $\Delta\Lambda_z = \Delta\Lambda$. Therefore, if flows are incompressible, Λ_z is a flux function proportional to the $U_b(\rho)$ defined in section 4.1. The in-out differences in Λ_z (see figure 5.2 of section 5.2) can then be compared with the symmetry in U_b profiles found in low density density plasmas (figures 4.4, 4.8 and 4.9 of chapter 4).

5.2 Experimental results

In this chapter, two close magnetic configurations are considered: 100_44_64 and 100_40_63. For both configurations, on-axis magnetic field is about 0.95 T. The vacuum rotational transform, ι, covers the range $1.55 \leq \iota \leq 1.65$ and $1.509 \leq \iota \leq 1.608$, and the volumes are 1.098 and 1.043 m^3, respectively. These two configurations have been studied in references [44] and [45] from the neoclassical point of view. For similar plasma profiles and momentum input, no qualitative differences are predicted in the flows within a magnetic surface. The plasmas presented here are heated by one of the two tangential NBIs, either in the direction of the magnetic field (co-injection), or in the opposite direction (counter-injection). The line averaged densities scanned in this chapter cover the range $\bar{n}_e \in (1.2 - 2.4) \times 10^{19}$ m^{-3}.

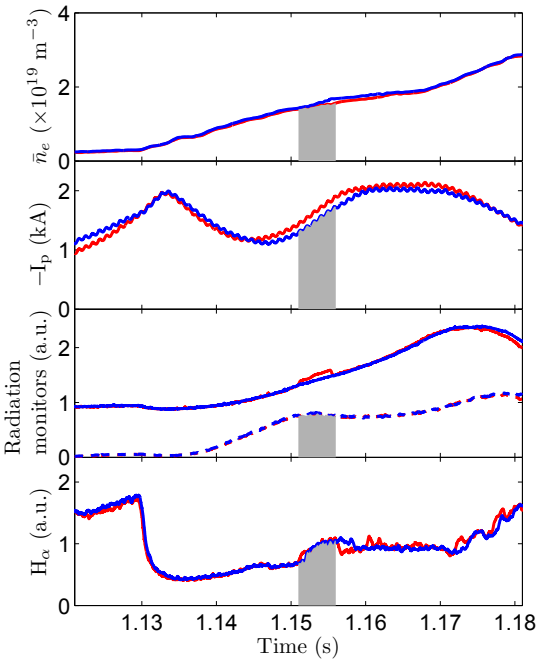

Figure 5.1. Time evolution of two similar plasma discharges. In red, shot#32577 with a DNBI pulse and in blue, shot#32576 without DNBI, used to remove the C^{5+} passive contribution. From top to bottom, time traces of: line averaged electron density, $\bar{n}_e$; plasma current (reversed), $-\mathrm{I_p}$; radiation monitors: bolometer (solid line) and C^{4+} (dashed); H_α monitor, located in sector away from DNBI sector. The DNBI injection is shown in grey.

Time traces of a representative plasma discharge, #32577, in the 100_44_64 configuration are shown in figure 5.1. The evolution of the reference discharge (#32576) used to remove background C^{5+} emission is in blue, whilst the one in which the DNBI was fired, #32577, is in red. The time interval in which the DNBI is injected is plotted as a grey shadow. The NBI heating causes an increase in the line-averaged density and radiation. The radiation monitors in figure 5.1 correspond to a bolometer

signal (whose view-line intersects the DNBI path) and a C^{4+} spectral line monitor, shown as solid and dashed lines, respectively. A small increase is observed in the bolometer signal for discharge #32577, which corresponds to photon excitation induced by the DNBI. Finally, the plasma current, I_p, is negative corresponding to counter-injection (a co-injection reverses the sign of the current). The small oscillation observed in the plasma current is produced by small variations in the current of the external coils. The good reproducibility of the two discharges shown in figure 5.1 is representative of the data set used in this work and allows an accurate subtraction of the background C^{5+} emission from the active DNBI discharge.

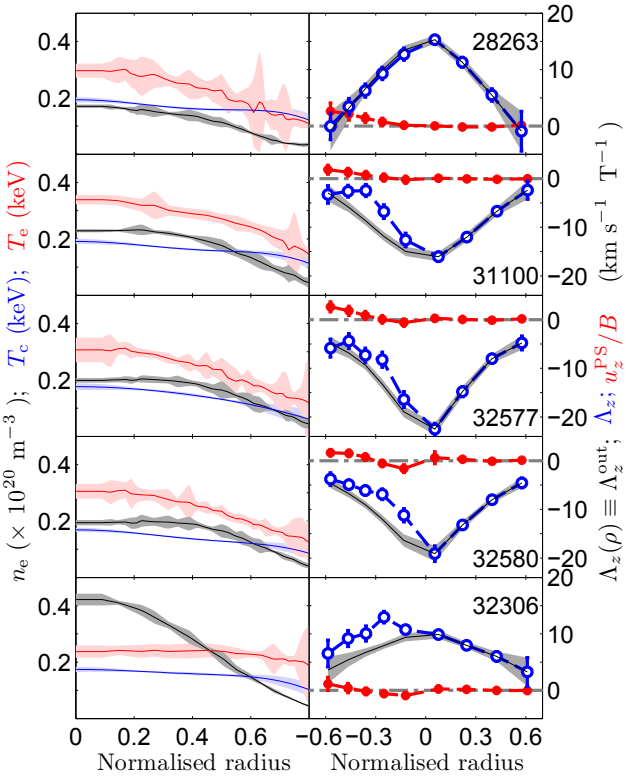

Figure 5.2. Left: profiles of the electron density (n_e, in gray) and temperature (T_e, in red), together with carbon temperature profiles (T_c, in blue). Right: measured profile of Λ_z, in blue, and the incompressible expected values extrapolated from the outboard measurements, in grey. The calculated Pfirsch-Schlüter contribution is displayed in red. The discharge #28263, in which flows were demonstrated to be incompressible [105], is included here as a reference. The discharges #31100, #32577 and #32580, heated with one NBI in counter-injection (consistent with $\Lambda_z < 0$) are presented to highlight the reproducibility of the departure from incompressibility observed in Λ_z. Discharges #31100 and #32306 were performed in the configuration 100_40_63.

Electron density and temperature profiles (n_e and T_e, respectively) are measured by the Thomson scattering diagnostic [55], see figure 5.2. The discharges in the figure were performed in the 100_44_64 magnetic configuration, except discharges #31100 and #32306 (configuration 100_40_63). In all the discharges considered in this chapter, the electron temperature profile is approximately parabolic, with $T_e(0) \approx 300$ eV, whilst the carbon temperature profile is rather flat, with $100 \leq T_c \leq 200$ eV (it is assumed that main ion and impurities are in thermal equilibrium). In the right column of figure 5.2 the C^{6+} parallel mass flow, $\Lambda_z \mathbf{B}$, and PS flow, $\mathbf{u}_z^{PS} = E_z h \mathbf{B}$, contributions to the total parallel velocity, $\mathbf{u}_{z\|} = \mathbf{u}_z^{PS} + \Lambda_z \mathbf{B}$, are shown in blue and red, respectively (see section 5.1 for an explanation of the extraction of these flow components from the experimental measurements). The direction of the bulk toroidal flow is mainly determined by the NBI momentum injection. The incompressible expected value extrapolated from the outboard measurements, i.e. $\Lambda_z = \Lambda_z(\rho) = \Lambda_z^{Out}$, is shown in grey. The discharge #28263 is heated by the co-NBI injector and shows a lower line-averaged density

($\bar{n}_e = 1.2 \times 10^{19}$ m^{-3}). In chapter 4, flows in this low-density NBI discharge were shown to be incompressible [105], see figure 4.4, and are included here as a reference. The measured Λ_z profile departs from the incompressible expectation in the co-NBI discharge #32306 and the counter-NBI discharges #31100, #32577 and #32580. The reproducibility of the Λ_z profile for the counter-NBI discharges, that are similar in terms of n_e, T_e and T_c profiles, but otherwise distant in time and impurity content, reinforces the reproducibility of the observed flow deviations. The general tendency observed in the experimental database, with few exceptions, is that the inboard parallel flow is more positive than the outboard one, and thus, the in-out differences in the parallel mass flow, $\Delta\Lambda_z$ from equation (5.3), are always positive. This observation is nearly independent on the magnetic configuration and the direction of injection of the heating NBIs.

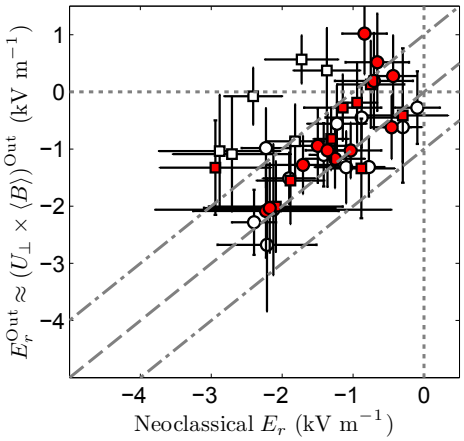

Figure 5.3. Comparison of experimentally measured radial electric fields for the outboard region, E_r^{Out}, with corresponding NC values for several TJ-II discharges. Dashed lines correspond to NC values (diagonal) and the region of confidence $E_r^{\mathrm{Out}} = E_r^{\mathrm{NC}} \pm 1$ kV m^{-1} (upper and lower diagonals), respectively. Here, circles and squares represent data from the 100_44_64 and 100_40_63 magnetic configurations, respectively. Red points indicate NBI in counter-**B** direction (consistent with $\Lambda_z < 0$) while open points indicate co-injection. Note that the impurity diamagnetic term is not included in computing the measured E_r (see text).

As indicated in section 5.1, toroidal and poloidal view lines of the CXRS system intersect at three locations ($\rho \approx 0.2, 0.4$ and 0.6) on the outboard side of the DNBI path. This enables unambiguous determination of the perpendicular and parallel flow components at those locations –assuming a small radial flow component compared to the perpendicular and parallel flows. The perpendicular impurity flow component is expected to be dominated by the $E \times B$ flow because of the $1/Z$ factor of the diamagnetic flow. Figure 5.3 shows a comparison of this experimental approximation to the radial electric field with NC expectations, calculated as in [45]. The database shown here is comprised of 12 discharges. Note that the impurity diamagnetic term is not included in the calculation of the experimental radial electric field, because of the uncertainties in determining the carbon density profile in TJ-II. Nevertheless, a rough estimate of the diamagnetic contribution (obtained from the CXRS signals while ignoring the calibration deficiencies mentioned in section 3.5.2) typically results in absolute values ≤ 1 kV m^{-1} at $\rho = 0.6$, with little or no impact for more internal regions, as expected from the $1/Z$ dependence. This estimation is consistent with the main-ion diamagnetic velocities calculated from experimental data, $|v_{\mathrm{diam},i}| \leq 4$ km s^{-1} for $|\rho| \leq 0.6$.

Despite this uncertainty in the estimated radial electric field, it should be noted that the radial electric field does not enter any of the expressions for impurity flows alone (sections 2.2 and 5.3), but rather in combination with the diamagnetic component as the total perpendicular flow. Such a velocity component is provided by the overlapping CXRS velocity measurements

through geometric factors only and is not subject to such uncertainties. In the following, the measured parallel mass flow deviations in the region $|\rho| \in (0.2, 0.6)$ are studied in light of an impurity density redistribution model, see subsection 2.4.1.

5.3 Friction-driven impurity density redistribution

Impurity temperature and parallel mass flow are generally taken to be a proxy of those of the main ions, as the impurity fluid is typically strongly collisionally coupled to the main ion fluid. For similar temperatures ($T_z \approx T_i$) and a large mass difference ($m_z \gg m_i$), impurity z and ion i normalised collisionalities relate to each other through $\hat{\nu}_{zi} = (m_i/m_z)^{1/2}(q_z/q_i)^2\hat{\nu}_{ii}$, see e.g. [22]. The pre-factor is $(m_i/m_z)^{1/2}(q_z/q_i)^2 \sim 10$ for a hydrogen plasma and C^{6+} impurity which, for the plateau ions characteristic of TJ-II [45], places the impurity ions under study in the Pfirsch-Schlüter collisional regime. This collisional character of medium to high-Z impurities can cause their density variations within a surface to be comparable with the mean value on that surface [100], and thus, the impurity parallel mass flow to differ from that of the main-ions. In order to study the measured parallel mass flow deviations from an incompressible pattern, the continuity equation (2.28) and the impurity parallel force balance

$$T_z \nabla_\parallel n_z = R_{z\parallel}, \tag{5.4}$$

need to be solved for the unknown functions n_z and Λ_z. Here, $R_{z\parallel}$ is the parallel friction on the impurities. The inclusion of other forces in equation (5.4) –namely the impurity inertia and the parallel electric field– is described and evaluated in section 5.4, while the impurity parallel viscosity is neglected against the parallel impurity pressure gradient, $\nabla_\parallel p_z$ [100]. As also shown in reference [100], the strong ion-impurity energy equilibration keeps the impurity temperature close to the ion one and thus $T_z = T_i(\rho)$.

In terms of the Λ function defined in (2.82) and a normalised impurity density $n \equiv n_z/\langle n_z\rangle$ equations (2.28) and (5.4) are written as

$$\mathbf{B}\cdot\nabla(n\Lambda) = -\mathbf{u}_{z0}\cdot\nabla n, \tag{5.5a}$$

$$\mathbf{B}\cdot\nabla \ln n = \gamma_{\mathrm{f}} B^2 \left(A_{\mathrm{i}} h + B_{\mathrm{i}} - \Lambda\right). \tag{5.5b}$$

The solubility condition is $\langle \Lambda B^2\rangle = B_i(\rho)\langle B^2\rangle$, see subsection 2.4.1. The compressible pattern (2.82) has been used to express the continuity equation in its form (5.5a). In addition, a flux-constant friction coefficient $\gamma_{\mathrm{f}}(\rho)$ and thermodynamic forces $A_{\mathrm{i}}(\rho)$ and $B_{\mathrm{i}}(\rho)$ have been defined in (5.5b) as

$$\gamma_{\mathrm{f}} \equiv \frac{m_i Z^2}{T_{\mathrm{i}}\tau_{ii}}, \tag{5.6a}$$

$$A_{\mathrm{i}} \equiv \frac{T_{\mathrm{i}}}{e}\frac{\mathrm{d}\ln n_{\mathrm{i}}}{\mathrm{d}\rho} - \frac{1}{2e}\frac{\mathrm{d}T_{\mathrm{i}}}{\mathrm{d}\rho}, \tag{5.6b}$$

$$B_{\mathrm{i}} \equiv -\frac{3}{5}\frac{\langle \mathbf{q}_{\mathrm{i}}\cdot\mathbf{B}\rangle}{p_{\mathrm{i}}\langle B^2\rangle}, \tag{5.6c}$$

where τ_{ii}, the ion self-collision time, is defined in (2.55) and $\mathbf{q}_{\mathrm{i}}$ is the ion heat flow. In deriving expression (5.5b) trace impurities are considered, i.e. $\sum n_z Z^2 \ll n_i$, and so the parallel friction

on the impurities is approximated by that exerted by main ions, i.e. $R_{z\parallel} \approx R_{zi\parallel} = -R_{iz\parallel}$. The ion-impurity collision operator is modelled with a Lorentz pitch-angle scattering operator plus a term guaranteeing momentum conservation [100]. Finally, no assumption is made on bulk ion collisionality since its distribution function is expanded by Legendre and Laguerre polynomials, as is customary in the so-called moment approach to NC transport [22, 93]. Here, the so-called 13 M approximation [147] is adopted, i.e. contributions from $j>1$ Laguerre components are neglected, see section 2.4.1. Note that in the axisymmetric tokamak case, the impurity continuity equation (2.28) yields an algebraic relationship between the parallel impurity flow and the impurity density, see equation (2.79), whereas such a simplification does not occur in general stellarator geometry [102].

The ion-impurity parallel friction is studied first in the next subsection. The effect of a parallel electric field and impurity inertial forces are considered in section 5.4. It is anticipated here that the parallel momentum balance in (5.5b) is dominated by the friction force and that the general behaviour of the solutions is to display $\Delta\Lambda_z < 0$, in contrast with the measured in-out variation. This can be heuristically understood by noting that the differences in the Pfirsch-Schlüter flow, $A_i hB$ in equation (5.5b), drive the impurity density redistribution. As a consequence of the in-surface density variation, an impurity return flow ΛB is established (equation (5.5a)) which must act to reduce the overall ion-impurity friction so that the density redistribution is not further amplified. Since the term $A_i h$ on the RHS of equation (5.5b) is more negative on the inboard side, the return flow Λ tends to behave similarly.

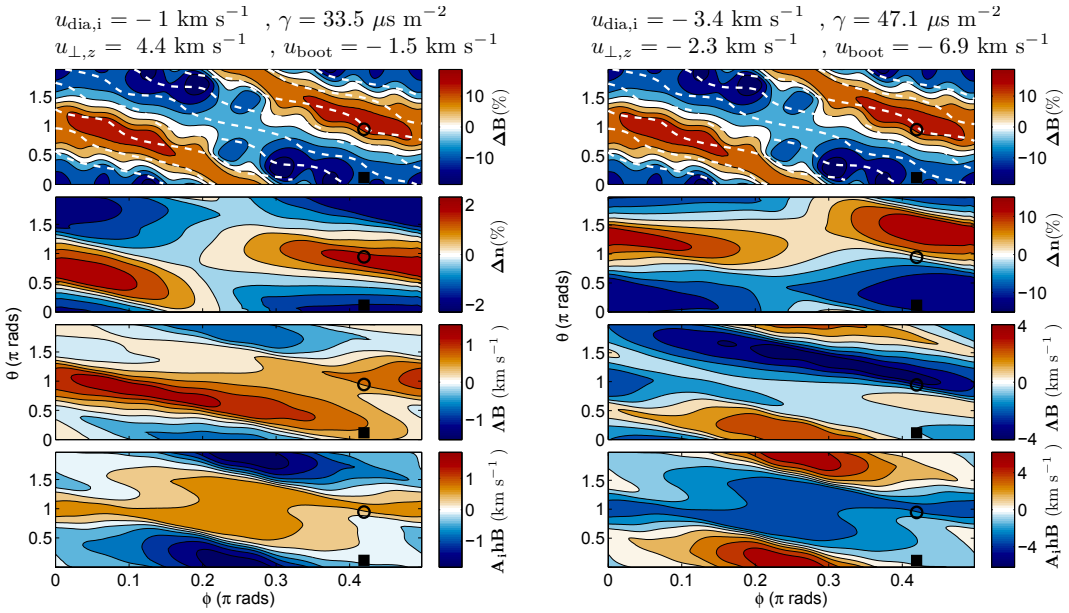

Figure 5.4. C^{6+} impurity density redistribution simulation for discharges #25801 (left) and #32577 (right) on the surface $\rho = 0.6$. From top to bottom: magnetic field strength variation, $\Delta B = B/\langle B\rangle - 1$ (field lines are plotted in white); density variation, $\Delta n = n_z/\langle n_z\rangle - 1$; return parallel flow, ΛB; and the differences in the Pfirsch-Schlüter velocity, $\Delta u_\parallel^{PS} \sim A_i hB$. The inboard/outboard toroidal measurement positions are shown as an open circle and filled square, respectively.

5.3.1 Calculation of the friction-driven impurity redistribution

The two coupled equations (5.5a) and (5.5b) can be recast as a second order partial differential equation for the unknown function $n(\rho, \theta, \phi)$ (see subsection 2.4.1 and the appendix C). The radial coordinate is a parameter in those equations which involve angular derivatives only. The required inputs are the main ion parameters (temperature T_i, density $n_\mathrm{i} \approx n_\mathrm{e}$, parallel mass flow Λ_i and flux-surface averaged parallel heat flow $\langle \mathbf{q}_\mathrm{i} \cdot \mathbf{B} \rangle$) together with the impurity perpendicular flow. The CXRS and Thomson Scattering diagnostics provide measurements of these parameters, except for the ion parallel mass and heat flows. The latter is calculated with DKES [95], complemented with momentum correction techniques [224]. On the other hand, the measured Λ_z in the outboard region is used as a first guess for the ion parallel mass flow when solving the differential equations, i.e. $\Lambda_i^{(0)} = \Lambda_z^{\mathrm{Out}}$, since the external input of momentum is not included in the DKES Λ_i calculations. A new guess for the main ion parallel flow is then obtained upon subtraction of the calculated impurity-ion flow difference, $\Lambda^{(0)}$ in our notation, i.e. $\Lambda_i^{(1)} = \Lambda_z^{\mathrm{Out}} - \Lambda^{(0)}$. Note: throughout this process momentum conservation is imposed, i.e. $\langle \Lambda B^2 \rangle = B_i(\rho) \langle B^2 \rangle$ from equation (5.5b). Finally, further iterations eventually lead to a solution for the impurity flow that matches the outboard CXRS measurement, $\Lambda_z^{(n+1)} \equiv \Lambda_i^{(n+1)} + \Lambda^{(n)} = \Lambda_z^{\mathrm{Out}}$. In practice only one iteration is necessary because the impurity return flow Λ is not very sensitive to the ion parallel flow Λ_i and the outboard measurement locations happen to be close to a stagnation point of the calculated impurity return flow, so that $\Lambda_i = \Lambda_z^{\mathrm{Out}}$ is a good initial guess.

An example of a solution is shown in figure 5.4 for discharge #32577 (presented in figures 5.1 and 5.2) and for the $\rho = 0.6$ magnetic surface. These results correspond to fully ionised carbon C^{6+} impurity that is used for the CXRS measurements. For comparison to the low-density plasmas studied in chapter 4, the same quantities for discharge #25801 are presented, see figure 4.2. The slightly hollow density profiles, typical in ECRH discharges in TJ-II, result in a small and negative

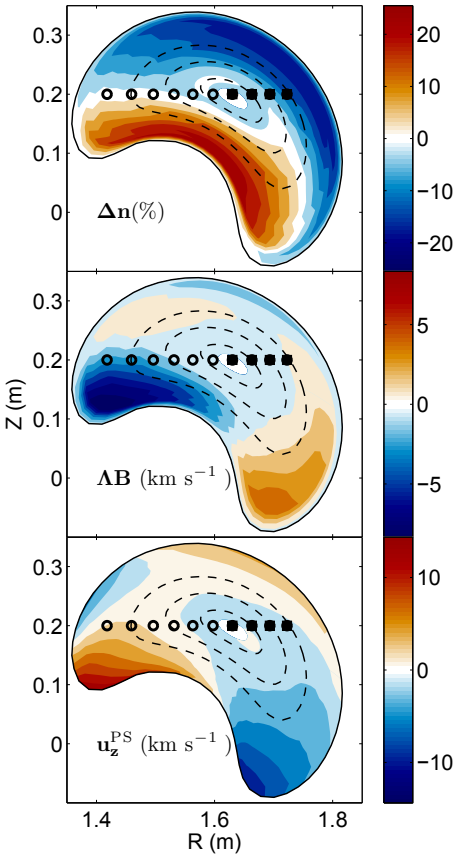

Figure 5.5. Mapping of C^{6+} impurity density redistribution simulation in the CXRS poloidal plane of measurement for discharge #32577. From top to bottom: density variation, $\Delta n = n_z/\langle n_z \rangle - 1$; impurity return flow, ΛB; and the impurity Pfirsch-Schlüter velocity. The inboard and outboard toroidal measurement positions are shown as open circles and filled squares, respectively. The magnetic surfaces in which the inboard/outboard comparison is made, namely $\rho \sim 0.2, 0.4$ and 0.6, are also shown as dashed lines.

thermodynamic force A_i, see equation (5.6a). Correspondingly, both the relative impurity density variations and return flow are small. In particular, it should be recalled that the measured impurity flows were shown to be nearly incompressible for this discharge, see figure 4.4. The results of the calculations of impurity density redistribution for discharge #32577 and for several magnetic surfaces, $\rho \leq 0.8$, are plotted in figure 5.5 for the toroidal section where the CXRS measurements are made, $\phi = 75.5^{\text{o}}$.

Some general comments on the solution can be made in light of the simulation results shown in figures 5.4 and 5.5. For the plasma profiles used in this chapter, $\bar{n}_{\text{e}} \in (1.2-2.4) \times 10^{19}$ m^{-3}, carbon impurities tend to accumulate in the interior region of the bean-shaped plasma poloidal cross section (which is close the region of maximum magnetic field strength in TJ-II due to the proximity of the central coil, see figure 3.8). The resulting return flow is comparable in size to the PS impurity flow. Its angular dependence also shows a dominant $\cos\theta$ component. The difference in sign between the PS and return parallel flows is in line with the overall tendency heuristically described at the beginning of this section: the return flow Λ tends to compensate the $A_i hB$ friction drive in equation (5.5b), for in these ion root plasmas A_i and $\mathrm{d}\Phi/\mathrm{d}\rho$ are of similar magnitude and different signs so that $u_z^{PS} \approx (\mathrm{d}\Phi/\mathrm{d}\rho)hB \sim -A_i hB$. Consequently, the differences in the simulated impurity parallel return flow at the locations of the CXRS measurements, $\Delta\Lambda_z \equiv \Delta\Lambda$ from (2.82), are found to be negative for the high-density shots in our CXRS database.

5.3.2 Comparison with experiment

Figure 5.6 shows radial profiles of the friction-driven simulated (black) and experimental (blue) differences in the impurity parallel mass flow, $\Delta\Lambda_z$, for the 5 discharges presented in figure 5.2. The simulated compressible modifications to the impurity flow are small at the CXRS measurement locations and thus do not account for the observed differences. A comparison of the experimental and simulated values of $\Delta\Lambda_z$ is presented in figure 5.7 for the same database as in figure 5.3. Error bars in figures 5.6 and 5.7 originate from the spread of the simulated velocities in the measurement volumes, see equations (3.7) and (3.8). As discussed in section 5.3.1, the parallel friction term in equation (5.5b) calculated from experimental profiles appears capable of producing a measurable impurity density asymmetry and parallel return flow, even for the internal positions considered in this work (the region of maximum gradient is typically located

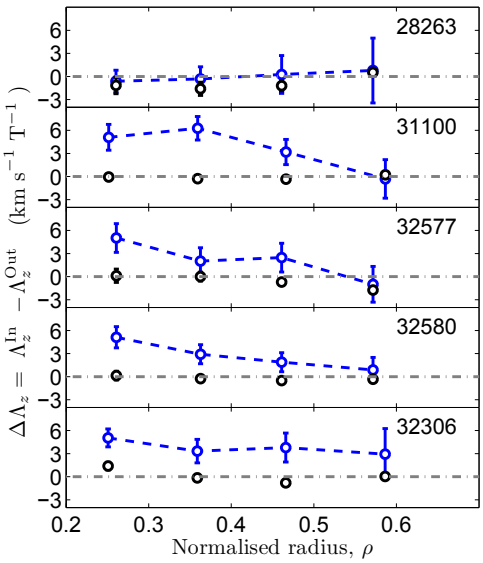

Figure 5.6. Radial profiles of the friction-driven simulated (black) and experimental (blue) differences in the parallel mass flow, $\Delta\Lambda_z$, for the discharges presented in figure 5.2. The error bars in the simulation originate from the spread of the calculated velocities in the measurement volumes.

at $|\rho| \sim 0.7 - 0.8$ in TJ-II plasmas). Values of $\Delta\Lambda_z^{\text{theo}} \sim -2$ km s^{-1} T^{-1}, or larger, are found in the simulation, while the experimental differences can easily reach $\Delta\Lambda_z^{\text{exp}} \sim 6$ km s^{-1} T^{-1}. The overall tendency of the simulated return flows to be more negative on the inboard side is also clear from figure 5.7. Note that at the inboard positions the impurity return flow varies sharply, see figure 5.4, which translates into large error bars.

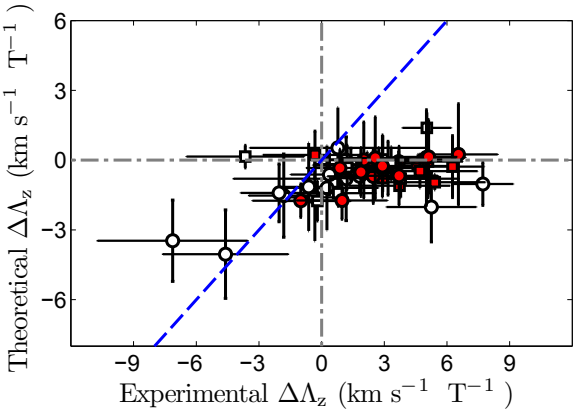

Figure 5.7. Comparison of the experimental and theoretical values of $\Delta\Lambda_z$. It is observed that the simulated and measured values are systematically in disagreement, except for a few cases. The symbols legend is the same as in figure 5.3. The error bars in the simulation come from the spread of the calculated velocities in the measurement volumes.

From the above comparison it is concluded that although impurity-ion parallel friction (in its modelled form in equation (5.5b)) is capable of causing impurity density asymmetries and return flows of the order of magnitude of the observed in-out flow differences, the simulated return flows do not agree with the observed in-surface variation of the impurity parallel mass flow Λ_z at the CXRS measurements locations for most cases. In the following section some of the assumptions made in the model (5.5b) are examined, and the parallel force balance (5.4) is extended to account for impurity inertia and the effect of a parallel electric field.

5.4 Discussion on the validity and extensions of the model

A previous impurity parallel friction model for stellarators [102] considered main ions in the Pfirsch-Schlüter regime of collisionality. This regime is not strictly applicable to the plasmas presented here ($n_{\text{i}} \in (0.5 - 3) \times 10^{19}$ m^{-3}, $T_{\text{i}} \in 100 - 200$ eV) since main ions are in the plateau regime $\hat{\nu}_{ii} \sim 10^{-2} - 10^{-1}$ [45]. As indicated in section 5.3, and explained in subsection 2.4.1, no assumption is made in this work on main ion collisionality, although the ion distribution function is truncated in the Laguerre expansion ($j \leq 1$, see 2.4.1) as in the 13 M approximation to neoclassical theory [22, 147].

In order to quantify the impact of this approximation let main ions be in the Pfirsch-Schlüter regime, as in reference [102]. In this regime of collisionality $\langle \mathbf{q}_i \cdot \mathbf{B} \rangle = 0$ (hence $B_i = 0$ in (5.6c)) and $A_i^{\text{PS}} = (T_i/e) \times (\mathrm{d} \ln n_i / \mathrm{d}\rho)$. Now, if a $j > 1$ truncation is applied to the exact collisional result, the thermodynamic force A_i in (5.5b) becomes

$$A_i^{\text{PS, truncated}} = A_i^{\text{PS}} - 1/(2e) \times (\mathrm{d}T_i/\mathrm{d}\rho),$$

which equals the general result A_i in (5.6c). The resultant impurity redistribution and return flow obtained from the exact and truncated collisional results are displayed in figure 5.8. As

observed, the impurity density in-surface variation reaches values up to $\Delta n \sim \pm 20$ % in the full collisional result while $\Delta n \sim \pm 13$ % when truncating the main ion distribution function. The simulated return velocity, ΛB, is similarly affected by the truncation (values of ± 6 and ± 4 km s^{-1} are obtained in the exact and truncated friction models, respectively). This comparison and the proximity of TJ-II main ion collisionalities to the Pfirsch-Schlüter regime indicate that the inclusion of higher order Legendre components [147] in the modelled friction (5.5b) is unlikely to change the tendencies in the simulated impurity redistribution and return flow presented in section 5.3. On the other hand, the generalization of the parallel friction presented in (5.5b) allows one to directly use the measured main-ion parameters (since no assumption is made on collisionality) and to include the effect of a non-zero parallel heat flow, thus extending the friction model presented in reference [102].

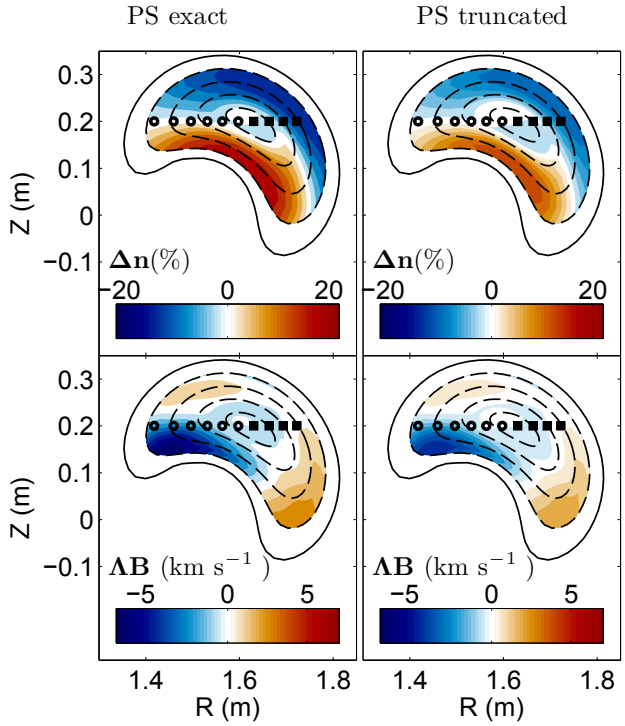

Figure 5.8. Mapping of C^{6+} impurity density redistribution and return flow in the CXRS polodial plane for discharge #32577. On the left, the exact Pfirsch-Schlüter main ion distribution function is used [102]. On the right, a $j > 1$ truncation is applied to the PS result.

Besides the above discussion on the generalization of the ion-impurity parallel friction, the impurity parallel force balance (5.4) can be extended to account for inertial and electrostatic parallel forces as

$$m_z n_z \mathbf{b} \cdot (\mathbf{u}_z \cdot \nabla \mathbf{u}_z) + n_z Z e \nabla_\parallel \Phi + T_z \nabla_\parallel n_z = R_{z\parallel}, \tag{5.7}$$

where the first term on the left hand side is the impurity parallel inertia and the second one is the parallel electric field. The former can be approximated by

$$m_z n_z \mathbf{b} \cdot (\mathbf{u}_z \cdot \nabla \mathbf{u}_z) \approx m_z n_z \Lambda_i^2 \mathbf{B} \cdot \nabla B,$$

since the local PS and return parallel flows are expected to be smaller than the main ion parallel mass flow in internal regions, $|\rho| \leq 0.4$, of TJ-II NBI heated plasmas. This same approximation leads to centrifugal outboard accumulation of high-Z impurities in tokamaks [139]. In order to

examine the impact of inertia on the impurity density redistribution, let the impurity parallel force balance be dominated by the inertia, i.e. $\nabla_\parallel \ln n_z = -\gamma_c^2 \nabla_\parallel b^2$ with $b \equiv B/\langle B \rangle$, $\gamma_c(\rho) \equiv \Lambda_i \langle B \rangle / v_z$ and v_z the impurity thermal velocity. Then the impurity inhomogeneity is $\Delta n = \exp\left\{-\gamma_c^2 (b^2 - 1)\right\}$. Note that although impurity thermal velocities ≤ 50 km s^{-1} are comparable to main ion parallel mass flows ≤ 20 km s^{-1} (i.e. $\gamma_c \leq 0.4$), the small aspect ratio of TJ-II $(b^2 - 1) \sim a/R \sim 0.1$ makes $\Delta n \leq 2$ % across all the plasma minor radius. Such an estimation has been confirmed numerically. Therefore, impurity parallel inertia is neglected henceforth.

Finally, the term containing the electrostatic potential variation on a flux surface, $\tilde{\Phi} = \Phi - \langle \Phi \rangle$, in equation (5.7) is considered. This portion of the full electrostatic potential, Φ, results from imposing quasi-neutrality among the non-equilibrium density parts of the coexistent species. Furthermore the calculation, carried out with the particle-in-cell code EUTERPE [138], considers adiabatic electron response as well as trace impurities. Under these approximations the resulting map of $\tilde{\Phi}$ mirrors that of the main ion density. As an example, $\tilde{\Phi}$ is shown in figure 5.9 for discharge #32577, where values of $\tilde{\Phi} \leq \pm 3$ V are obtained in the simulation for the CXRS plane of measurement.

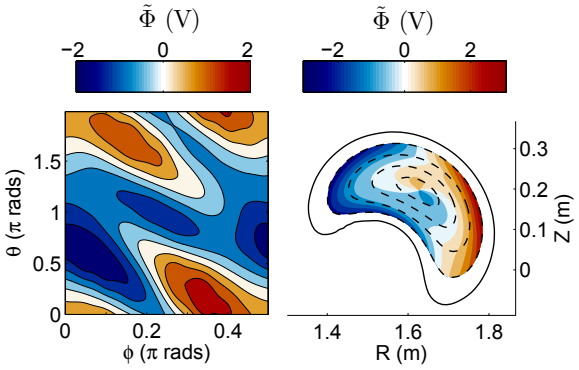

Figure 5.9. Electrostaic potential inhomogeneity, $\tilde{\Phi}$ in Volts, for discharge #32577. (Left) In-surface variations for $\rho = 0.6$. (Right) Mapping in the CXRS poloidal plane for several magnetic surfaces, $|\rho| \leq 0.8$.

Now, if parallel inertia is neglected, the impurity momentum balance (5.7) becomes

$$\mathbf{B} \cdot \nabla \ln n = \gamma_f B^2 \left(A_i h + B_i - \Lambda\right) - \frac{eZ}{T_z} \mathbf{B} \cdot \nabla \Phi, \tag{5.8}$$

see subsection 2.4.1. The parallel momentum balance in its form (5.8), together with particle conservation (5.5a), can be transformed into a second order partial differential equation for the unknown n, as in section (5.3.1). Figure 5.10 displays a mapping of the simulation results for discharge #32577 in the CXRS poloidal plane for magnetic surfaces $|\rho| \leq 0.8$, after considering (left) friction-only and (right) friction plus the $\nabla_\parallel \Phi$ forces in its model form (5.8). As observed, the impurity redistribution and return flow patterns are affected by the inhomogeneity of the potential only at external radial locations $|\rho| > 0.7$. Nevertheless the tendency to display $\Delta\Lambda < 0$ remains unaltered, thus contradicting the experimental observations.

A possibly important omission of the impurity re-distribution model used in this work could be the assumption of trace impurities. For the plasmas considered here values of $Z_{\text{eff}} \sim 1.2 - 1.6$ are obtained from soft X-ray emission, which would give rise to impurity strengths of $n_z Z^2 / n_i \sim 0.2 - 0.6$. For such cases both the inhomogeneity of the electrostatic potential [146] and the collision operator used to model the parallel friction on the impurities [142] would change, thus modifying the impurity redistribution within a magnetic surface. The inclusion of these effects is out of the scope of this thesis and is left for future work.

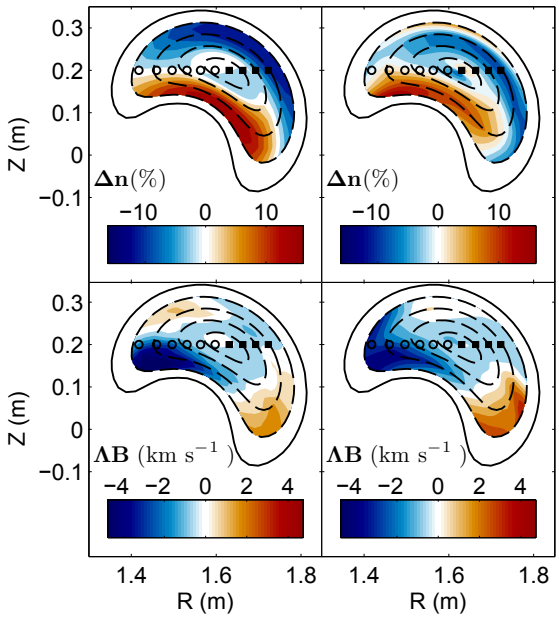

Figure 5.10. Mapping in the CXRS poloidal plane of the simulated C^{6+} density inhomogeneity, Δn, and return flow, $\Lambda\mathbf{B}$, for discharge #32577 and for magnetic surfaces $|\rho| \leq 0.8$, after considering: (left) friction-only and (right) all relevant forces in model (5.8).

5.5 Summary

Fully-ionised carbon impurity perpendicular flows are found to be in reasonable agreement with neoclassical calculations of the radial electric field. The parallel flow of these impurity ions is obtained at two locations on the same flux surface. For this, the calculated Pfirsch-Schlüter parallel velocity is subsequently subtracted. The resultant component of the flow is observed to vary systematically on each flux surface, pointing to a breakdown of impurity flow incompressibility in the medium density plasmas studied. The experimentally observed velocity deviations are compared with parallel return flows calculated using a modelled impurity density redistribution driven by ion-impurity friction. Such a model is extended to account for impurity inertia and inhomogeneities in the electrostatic potential. The simulation results show that the parallel impurity force balance is dominated by parallel friction for the plasmas considered here, and demonstrate that the calculated return flow substantially modifies the incompressible velocity pattern. However, the simulated differences become almost insignificant at the CXRS measurement locations and thus do not explain the in-surface variations of impurity parallel flow. The experimental validation of theoretical models of impurity density redistribution within a flux surface is of considerable importance as it provides an indirect validation of the model predictions for impurity radial transport.

CONCLUSIONS AND OUTLOOK

Experimental set-up. In this thesis the Charge Exchange Recombination Spectroscopy (CXRS) technique has been used in the TJ-II stellarator to measure temperature and velocity profiles of fully-ionized carbon impurity ions, with the purpose of validating the incompressibility condition of light-Z impurity flows. In order to undertake such studies, it has been necessary to upgrade the existing CXRS optical system by installing toroidal viewing sightlines so that the TJ-II now possess the capability of measuring impurity flows at both sides of the magnetic axis. Furthermore, this diagnostic now provides three independent C^{6+} velocity measurements at three specific magnetic surfaces, namely at $\rho \sim 0.2$, 0.4 and 0.6. Such features, together with the high throughput of the instrumentation used, make the CXRS system at TJ-II suitable for studying the spatial structure of impurity flows on a magnetic surface. However, before velocity measurements can be determined several atomic, neutral beam-related and instrument effects in the recorded impurity line emissions need to be identified, quantified and corrected for. In addition, given the criticality of sightline alignment methods have been developed to align these optical light collection systems. Finally, numerical routines have been created to account for possible uncertainties introduced by the averaging in the beam/plasma interaction volume for each sightline.

Incompressibility in low-density plasmas and comparison with neoclassical theory. In order to extract the flux-surface averaged (FSA) flows determining an incompressible flow, a general treatment of sightlines and flow geometry has been developed and applied to two pairs of three independent velocity measurements performed at different locations of the same flux surface. In this way, consistency with a 2D incompressible flow has been demonstrated for low-density, i.e. $\bar{n}_e \leq 1.2 \times 10^{19}$ m^{-3}, plasmas in TJ-II [105]. In addition, good quantitative agreement has been obtained between measured and NC radial electric fields for low density ECRH plasmas, except when approaching the low density transition, where the extracted FSA radial electric field agrees within error bars with that measured by Doppler reflectometry, but is slightly overestimated by NC calculations [228]. On the other hand, a comparison of impurity parallel rotation with NC bootstrap flow has been undertaken for the first time in TJ-II, showing consistency with the calculations for ECRH plasmas [105].

Compressible impurity flow. When the studies of flow incompressibility have been extended to ion-root NBI-heated plasmas in the TJ-II, the measured radial electric field has been observed to be in reasonable agreement with neoclassical calculations; this indicates a minor role of the fast ion-driven radial current in the poloidal momentum balance of the TJ-II stellarator, as the inputs for NC calculations only include density profiles of thermalised species. However, in-surface variations of the impurity parallel mass flow have been observed systematically, except in an unbalanced, not fully developed, NBI heated discharge with relatively low density, i.e. $\bar{n}_e = 1.2{\times}10^{19}$ m^{-3}. Such observations point to a breakdown of impurity flow incompressibility in medium-density, i.e. $\bar{n}_e \in (1.2-2.4){\times}10^{19}$ m^{-3}, plasmas in the TJ-II, that must be accompanied by in-surface variations of impurity particle density.

Impurity density redistribution model. In order to understand the origin of these experimentally observed velocity deviations from an incompressible pattern, a comparison has been made with parallel return flows calculated using a modelled impurity density redistribution driven by ion-impurity friction; such a friction-based model extends the work presented in reference [102] since no restriction on main ion collisionality is imposed. Although the calculated impurity return flow substantially modifies the incompressible velocity pattern, these modifications become insignificant at the CXRS measurement locations and therefore do not explain the observed in-surface variations of impurity parallel mass flow [209].

The above friction model has been extended here to account for inertial and parallel electric field forces. As demonstrated, centrifugal forces are negligible in the plasmas studied due to the large aspect-ratio of TJ-II. On the other hand, small parallel gradients of the electrostatic potential, ~ 3 V m^{-1}, calculated with the particle-in-cell code EUTERPE [138], have been shown to be sufficient to compete with the parallel friction on the impurities and to drive additional impurity inhomogeneities. However, the resultant impurity return flow does not explain the experimental observations.

Impurity transport and parallel lines of research. The experimental validation of theoretical models of impurity density redistribution within a flux surface is important as it provides some indirect validation of the model predictions on impurity radial transport. Indeed, substantial changes in the radial transport of impurities are expected form their density redistribution [102] and in-surface variations of the potential [138]. In this sense, the studies presented in this thesis could help validate the model predictions on impurity radial transport. On the other hand, the observations of compressible impurity flows reported here –and its relation with impurity radial transport– have led to a renewed interest on impurity dynamics in TJ-II. For instance, an adaptation of the friction-driven impurity density redistribution model presented here has been used [231] to help seed light on previously reported measurements of an asymmetry in plasma broadband radiation measured by bolometers [61]. In parallel, the in-surface variations of the potential are being investigated by means of two distant probes [232].

Validity of neoclassical theory when predicting plasma rotation. In addition, from the data interpretation point of view, the parallel return flows associated with an impurity

density inhomogeneity might complicate the comparison of CXRS rotation measurements to standard[1] neoclassical theory, as the latter assumes an incompressible spatial pattern of the flows. In particular, the experimental observations in high-performance plasmas scenarios on JET [214, 215] and DIII-D [201], which exhibited a large discrepancy –even in the sign– between the experimental poloidal velocity and the neoclassical prediction, could have been obscured by the development of an impurity density asymmetry within the surface –a plausible hypothesis for the high pressure gradients present in those plasmas. In this sense, i.e. in the absence of in-surface impurity density variations, the quantitative agreement found in the literature between CXRS rotation measurements and the neoclassical theory [105] leaves such a framework as a useful tool for predicting the equilibrium ionic flows, for situations where considerable ripple exists in the magnetic field strength.

Benchmark of Hamada poloidal inertia and neoclassical viscosities. Finally, it is noted that the experimental observations presented here rely on the calculation of the geometrical part of the Pfirsch-Schlüter flow (i.e., the parallel component of the Hamada poloidal vector). Such a calculation is benchmarked by means of a comparison of the poloidal inertia determined by the modelling procedure developed and by DKES. This numerical verification is important not only for calculation of the equilibrium flow, but also for obtaining the theoretical decay times of flows [87] for comparison with experimental measurements, see e.g. [84]. It should also be noted that the calculations of the viscosity coefficients with DKES have been successfully benchmarked with semi-analytical theories [115], thus reinforcing those works.

Outlook

In view of the results collected in this work, upgrades of the experimental set-up and improvements to the theoretical models are proposed in order to fully exploit the work developed here:

- For instance, an absolute calibration of the throughput of the CXRS optical system from the beam/plasma interaction volume to the CCD detector is required in order to obtain reliable impurity ion density profiles. This problem has been addressed partially by the combination of beam H_α emission and CXRS measurements, see e.g. ref. [233]. For this, light collected with the current optical CXRS system could be divided in the spectrograph by inserting a beam splitter located between its input lens and the bandpass filter. This would require a second transmission grating (centred on the H_α line at 6563 Å) as well as a second CCD camera, but would allow a beam through CCD throughput calibration to be performed.

- The main forces in the impurity parallel force are the friction on the impurities and the parallel gradient of the potential; the former scales with the square of the impurity charge, i.e. Z^2, whilst the latter scales with Z. Therefore, their contributions could be isolated by studying other impurities. For instance, the work presented here could be repeated for fully ionized helium, He^{2+}, since the reactions rates are similar to those for C^{6+}, and

[1] I.e., the one arising after imposing ambipolarity on the FSA radial particle fluxes, but without a consistent treatment of quasi-neutrality.

He could be injected into TJ-II plasmas when required. For this it would be necessary to replace the current transmission grating with one centred on the He II spectral line ($n = 4 \rightarrow 3$) at 4686 Å. An even more attractive experiment would be the combination of CXRS measurements of He II and C VI with beam H_α line emission measurements above.

- An automatic spectrograph calibration system [193] is recommended in order facilitate and ease regular spectral calibration, see the schematic diagram in the figure below. It might involve the robotic insertion and removal of a spectral calibration lamp between the light collection lens and fibre bundle ferrule. The key point for this calibration system lies in the inner surface of the diffusive chamber walls, where light from the calibration lamp is directed towards the fibre optic ferrule. Some trails have been made using a thin white light reflectance coating on a glass test plate of *Coating white reflectance 6080 premix/250*, by Labsphere Inc. However, the coating did not stuck firmly to the surface under trial[2]. Another possibility would be the use of Teflon (polytetrafluoroethylene, PTFE) for the chamber walls, which diffuses a transmitting light nearly perfectly –exhibiting a Lambertian reflectance– and is commonly used in optical radiometry.

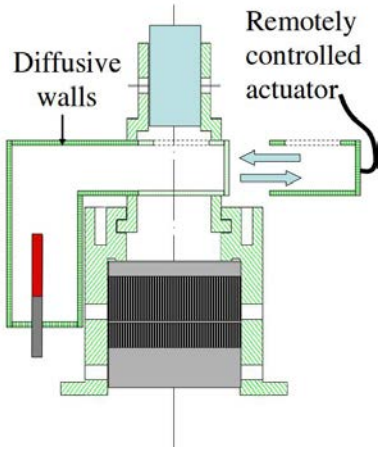

- At present the number of sightlines (36) is limited by the number of spectral regions that can be recorded by the CCD camera without overlapping of signals from these fibres. However, two of the twelve toroidal sightlines cannot view the plasma as they are blocked by the vacuum chamber. In addition, a total of 4 poloidal sightlines observe outside the plasma. Hence, 6 of the 36 positions at the CCD camera do not curretly provide useful information. Therefore, it is recommended that a new 12-way fibre bundle be mounted on the unused inboard poloidal top view port, see figure 3.3, as CXRS measurements at the inboard region will have two benefits: firstly, the deduction of the radial electric field at more positions (currently, when impurity flow compression is observed, the radial electric field can only be determined at three positions of the outboard region); secondly, it could bring new insights to the understanding of impurity flow compression.

[2] We are grateful to the help of the Materials Group in the Laboratorio Nacional de Fusión, CIEMAT.

- A detailed comparison of main ion and carbon impurity ion temperatures is required for TJ-II. After recent upgrades of the TJ-II Neutral Particle Analysers [206, 207] and CXRS [59] diagnostic better agreement between main ion and CXRS ion temperatures was found, although not complete. For instance, as indicated in section 3.5.1, the Toroidal and Poloidal NPAs observe different main-ion temperatures [205]. As the temperature anisotropy caused by NC viscosity is not capable of giving rise to the observed discrepancy, further studies are required regarding this issue. On the other hand, comparisons of temperatures of different ionic species should be addressed. The high collision frequency of impurity species suggests that similar values should be observed due to rapid thermalization. However, in the literature, significant discrepancies are found when comparing heavy ion species (Si, Fe) with bulk ion temperatures in fusion plasmas [234] and in space plasmas. The concepts used here regarding the impurity parallel dynamic might shed light on such studies.

- The main-ion friction on the impurities modelled in section 2.4.1 can be extended to include higher order Laguerre polynomials in the expansion of the $(l=1)$ Legendre component of the main-ion first order distribution function. Indeed, such a component is written as [117]

$$f_{\mathrm{i}1}^{(l=1)} = \frac{m_{\mathrm{i}}}{T_{\mathrm{i}}} v_{\parallel} f_{\mathrm{iM}} \sum_{j=0}^{\infty} u_{\mathrm{i}\parallel,j} L_j^{(3/2)}(x_{\mathrm{i}}^2).$$

  In the work presented here, only the first two Laguerre components are utilized, with $u_{\parallel \mathrm{i}0} = u_{\parallel \mathrm{i}}$ and $u_{\parallel \mathrm{i}1} = -2q_{\parallel \mathrm{i}}/(5p_{\mathrm{i}})$, see equation (2.89). Higher order terms $j \geq 2$

$$u_{\mathrm{i}\parallel,j} = \frac{B}{\langle B^2 \rangle} \langle B u_{\mathrm{i}\parallel,j} \rangle,$$

  can be computed with numerical codes such as DKES complemented with momentum correction techniques, see e.g. [224]. However, since the (θ, ϕ) angular dependence of $f_{\mathrm{i}1}^{(l=1,j\geq 2)}$ is that of the magnetic field strength B, the inclusion of these terms in the parallel friction is unlikely to change the simulation results presented in chapter 5.

  On the other hand, such $j \geq 2$ terms might affect the impurity radial transport in its form (2.99). Indeed, the generalization of (2.99) to include higher order Laguerre polynomials is straightforward and yields

$$\langle \Gamma_z \cdot \nabla \rho \rangle = \frac{T_z \gamma_{\mathrm{f}}}{e_z} \left[A_i \langle n_z (hB)^2 \rangle + \left\langle n_z h B^2 \left\{ \sum_{j \geq 1} C_j \frac{\langle B u_{\mathrm{i}\parallel,j} \rangle}{\langle B^2 \rangle} - \Lambda \right\} \right\rangle \right],$$

  with $C_j = (2j+1)!!/(j!2^j) \approx 1.5, 1.9, 2.2, 2.5, ..., 2(n/\pi)^{1/2}$ for $j = 1, 2, 3, 4, ..., n \gg 1$.

- Finally, the experimental observations of an in-surface C^{6+} density variation reported in the CHS stellarator [145] could be explained by the impurity density redistribution model presented in this work. As indicated in the conclusions of that reference,

  > the inboard/outboard asymmetric poloidal rotation velocity of fully ionized carbon is observed in CHS where the neoclassically predicted Pfirsch-Schlüter-like toroidal flow velocity is damped.

As noted in chapter 2, the Pfirsch-Schlüter equilibrium flow arises in response to the compression of the perpendicular flow component and so is set once the radial electric field is damped to its equilibrium value. Such a "vanishing" of the Pfirsch-Schlüter flow might be understood in terms of the friction model described in 5: the differences between main-ion and impurity Pfirsch-Schlüter flows cause a parallel friction on the impurities that drives an impurity density redistribution. A return impurity flow appears to compensate the density compression and must act to reduce the overall ion-impurity friction so that the density redistribution is not further amplified. Therefore, the sum of the Pfirsch-Schlüter and return impurity flows tends to cancel out, in line with the observations reported in CHS.

Appendices

APPENDIX A

FLOW AND MAGNETIC FIELD RELATED COORDINATES

In this appendix the curvilinear coordinates utilized in this thesis are explained. Most of the content shown in this appendix is collected in chapter 6 of reference [36]. The geometry modulus used to obtain the magnetic topology of the TJ-II stellarator [21] is briefly described in section A.1. In section A.2 the coordinates in which **B**-lines are straight are implemented, and their relation with the PEST-1 coordinates of EUTERPE is explained. Finally, the Hamada coordinates and the connection with the Pfirsch-Schlüter flow in a stellarator are outlined in section A.3.

A.1 Magnetic library "g3d"

All the calculations in this document are performed using the libraries created by J. Guasp for the TJ-II Stellarator [21]. A curvilinear system $(\rho_{\rm g3d}, \phi_{\rm g3d}, \theta_{\rm g3d})$ is defined, with $\rho_{\rm g3d} \equiv \rho$ in equation (1.3), $\phi_{\rm g3d}$ the usual toroidal angle, and $\theta_{\rm g3d}$ a poloidal angle-like coordinate, defined as the arc of curve which results from the intersection of the surfaces $\rho_{\rm g3d}$ and $\phi_{\rm g3d}$ constant, normalized to 2π. The surface label $\rho_{\rm g3d}$ increases monotonically from the magnetic axis towards the last closed magnetic surfaced. The toroidal angle $\phi_{\rm g3d}$ is directed in the counter clockwise direction when viewing the device from the top. The poloidal angle $\theta_{\rm g3d}$ varies in such a way that the triad $(\nabla\rho_{\rm g3d}, \nabla\phi_{\rm g3d}, \nabla\theta_{\rm g3d})$ is right-handed (i.e. $\theta_{\rm g3d}$ increases in the $\mathbf{E}\times\mathbf{B}$ direction for positive radial electric field). In the following, the subindex g3d is dropped.

The transformation between the above curvilinear coordinates (ρ, ϕ, θ) and (machine-like) cylindrical coordinates (R, ϕ, Z) is obtained with the call `g3d_invers`$(\rho, \phi, \theta; \mathtt{R}, \mathtt{Z})$. Here, Z is the coordinate along the axis of the torus; ϕ the toroidal angle –coincident with the toroidal angle in the curvilinear coordinates; and R the horizontal distance between each point $\vec{r}$ and the torus axis. This sub-routine, like many other in the library, utilizes a linear interpolation. Hence, the calculations presented in this thesis report are at most as accurate as this interpolation allows. A simple inspection of the interpolating sub-routine shows that errors of $\sim 3\%$ are expected.

The metric of the curvilinear system is obtained from the subroutine

$$\texttt{g3d\_metr\_fl}(\rho,\phi,\theta;\texttt{J},\texttt{g}_{\texttt{ij}}(\texttt{3x3}),\texttt{g}^{\texttt{ij}}(\texttt{3x3}),\mathbf{e}_\rho,\mathbf{e}_\phi,\mathbf{e}_\theta,\nabla\rho,\nabla\phi,\nabla\theta).$$

Here, $\mathbf{e}_i$ are the tangent vectors to the coordinate curves $u^i=(\rho,\phi,\theta)$, and ∇u^i the gradients of such coordinates, thus perpendicular to the surfaces u^i =constant; J is the Jacobian, $\mathrm{J}^{-1}=g^{-1/2}=\nabla\rho\cdot(\nabla\phi\times\nabla\theta)$; g_{ij} and g^{ij} are the co- and contra-variant components of the metric tensor. The last call returns some of the variables of the metric, but in cartesian coordinates. Thus, they are converted to cylindrical coordinates in the usual way (i.e. $X=R\cos\phi;\ Y=R\sin\phi;\ Z=Z$).

Note that in the triad (ρ,ϕ,θ) utilized in the g3d library the toroidal and poloidal angles have been interchanged with respect to the most common definition (ρ,θ,ϕ). Since most of the equations in the literature are obtained in the latter system, it is useful to define a coordinate system with that order. To this end, the new poloidal coordinate

$$\tilde{\theta}=-\theta, \tag{A.1}$$

allows us to define the (right-handed) triad $(\rho,\tilde{\theta},\phi)$. Any quantity X is resampled in the new coordinate system as $X(\rho,\phi,\theta)=X(\rho,\tilde{\theta},\phi)=X(\rho,2\pi-\theta,\phi)$, since any physical quantity must be single-valued and thus periodic in its angles. The Jacobian of this coordinate system equals the original one, i.e. $[J(\rho,\phi,\theta)]^{-1}=\nabla\rho\cdot\nabla\phi\times\nabla\theta=\nabla\rho\cdot\nabla\tilde{\theta}\times\nabla\phi=[J(\rho,\tilde{\theta},\phi)]^{-1}$. However, the poloidal co- and contra-variant **B**-components reverse its sign, i.e.

$$B^\theta=\mathbf{B}\cdot\nabla\theta=\mathbf{B}\cdot\nabla(-\tilde{\theta})=-B^{\tilde{\theta}}, \tag{A.2a}$$

$$B_\theta=\mathbf{B}\cdot\mathbf{e}_\theta=\sqrt{g}\mathbf{B}\cdot\nabla\rho\times\nabla\phi=-\sqrt{g}\mathbf{B}\cdot\nabla\phi\times\nabla\rho=-\mathbf{B}\cdot\mathbf{e}_{\tilde{\theta}}=-B_{\tilde{\theta}}. \tag{A.2b}$$

As a result, the poloidal magnetic flux variation changes its sign

$$\Psi'_{p,0}=\frac{1}{2\pi}\int_0^{2\pi}\mathrm{d}\theta\int_0^{2\pi}\mathrm{d}\phi\sqrt{g}B^\theta=-\frac{1}{2\pi}\int_0^{2\pi}\mathrm{d}\tilde{\theta}\int_0^{2\pi}\mathrm{d}\phi\sqrt{g}B^{\tilde{\theta}}=-\Psi'_p. \tag{A.3}$$

Here, the prime denotes a derivative respect to ρ and the symbol $\Psi'_{p,0}$ is the poloidal flux variation when considering the original coordinates. Since the toroidal flux variation remains unaltered, the rotational transform becomes positive, i.e. $\iota=\mathrm{d}\Psi_p/\mathrm{d}\Psi_t=-\iota_0$.

Finally, it is noted that all the figures presented in this report are plotted in the original g3d triad (ρ,ϕ,θ), although the calculations are performed in $(\rho,\tilde{\theta},\phi)$.

A.2 Straight B-lines coordinates

The zero divergence of the magnetic field, $\nabla\cdot\mathbf{B}=0$, permits to rewrite **B** in the Glebsch form

$$\mathbf{B}=\nabla\rho\times\nabla\nu. \tag{A.4}$$

From the contravariant representation of the magnetic field, $\mathbf{B}=B^i\mathbf{e}_i$, and the definition of a magnetic surface, $B^\rho=\mathbf{B}\cdot\nabla\rho=0$, the stream function $\nu(\rho,\theta,\phi)$ verifies

$$\frac{\partial\nu}{\partial\theta}=\sqrt{g}B^\phi,\ \frac{\partial\nu}{\partial\phi}=-\sqrt{g}B^\theta. \tag{A.5}$$

With the initial condition $\nu(s,0,0)=0$, the stream function is integrated as

$$\nu(\rho,\theta,\phi)=\left[\int_0^{\theta}\sqrt{g}B^{\phi}d\theta'\right]_{\phi=0}-\int_0^{\phi}\sqrt{g}B^{\theta}d\phi'. \tag{A.6}$$

Since **B** is single valued it must be periodic in its angles, and so, the cross product in (A.4) is periodic in its angles. Therefore, the general expression of ν consist of a periodic part, ν_p, plus terms with a linear dependence on the angles, i.e. $\nu=\nu_p+a(\rho)\theta+b(\rho)\phi$. Otherwise, $\nabla(\nu-\nu_p)$ will be a non-periodic function as it depends on the angles. The flux-constant coefficients a and b are then obtained from (A.5) and the definition of a poloidal and toroidal flux variations, e.g.

$$\Psi_t'\equiv\frac{\mathrm{d}\Psi_t}{\mathrm{d}\rho}=\frac{1}{2\pi}\int_0^{2\pi}\mathrm{d}\theta\int_0^{2\pi}\mathrm{d}\phi\sqrt{g}B^{\phi}=\frac{1}{2\pi}\int_0^{2\pi}\mathrm{d}\theta\int_0^{2\pi}\mathrm{d}\phi\frac{\partial\nu}{\partial\theta}=2\pi a(\rho),$$

where the integration of $\partial\nu_p/\partial\theta$ over θ vanishes because ν_p is periodic in θ. Similarly, $\Psi_p'=-2\pi b(\rho)$, and thus

$$\nu(\rho,\theta,\phi)=\nu_p(\rho,\theta,\phi)+\frac{1}{2\pi}(\Psi_{\mathrm{t}}'\theta-\Psi_{\mathrm{p}}'\phi). \tag{A.7}$$

Note that, from expression (A.4), the equation of a field line lying on a flux surface is ν=constant. Therefore, a new coordinate system $(\rho,\theta_{\mathrm{f}},\phi_{\mathrm{f}})$ can be chosen so that the equation of a magnetic field line is a straight line in the $(\theta_{\mathrm{f}},\phi_{\mathrm{f}})$ plane, i.e. $\nu=\text{constant}=(\Psi_{\mathrm{t}}'\theta_{\mathrm{f}}-\Psi_{\mathrm{p}}'\phi_{\mathrm{f}})/(2\pi)$ and thus

$$\mathbf{B}=\frac{1}{2\pi}\nabla\rho\times\nabla\left(\Psi_{\mathrm{t}}'\theta_{\mathrm{f}}-\Psi_{\mathrm{p}}'\phi_{\mathrm{f}}\right)=\nabla\rho\times\nabla\left(\psi'\theta_{\mathrm{f}}-\chi'\phi_{\mathrm{f}}\right), \tag{A.8}$$

with $\chi'=\Psi_{\mathrm{p}}'/(2\pi)$ and $\psi'=\Psi_{\mathrm{t}}'/(2\pi)$. The contra-variant **B**-components are thus

$$B^{\theta_{\mathrm{f}}}=\frac{\chi'}{\sqrt{g_{\mathbf{f}}}},\quad B^{\phi_{\mathrm{f}}}=\frac{\psi'}{\sqrt{g_{\mathbf{f}}}}. \tag{A.9}$$

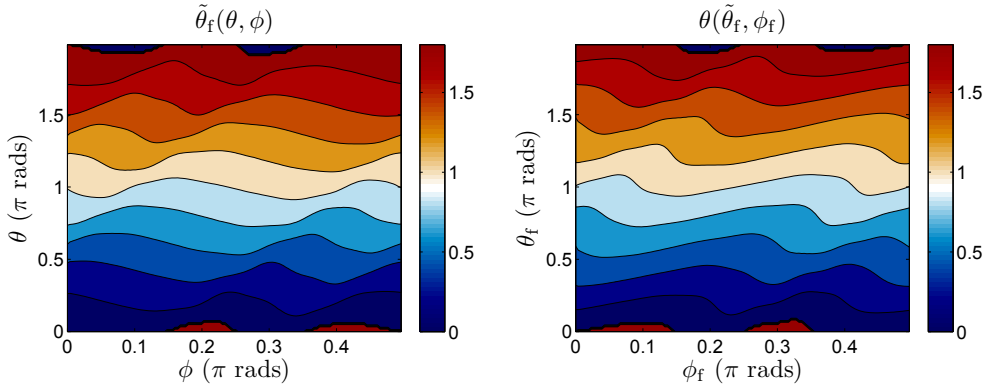

Figure A.1. Poloidal angle in the flux coordinate system, $\theta_{\mathrm{f}}(\theta,\phi)$, at the surface $\rho=0.6$. On the right, the function $\tilde{\theta}_{\mathrm{f}}$ required to resample a quantity in flux coordinates is plotted, see the text.

Coordinates in which **B**-lines are straight lines are called flux coordinates (sometimes, magnetic coordinates). There are many transformations which led to the form (A.8). One possibility is to leave the toroidal angle unaltered, i.e.

$$\theta_{\mathrm{f}}=\theta+\frac{\nu_p}{\psi'};\quad \phi_{\mathrm{f}}=\phi. \tag{A.10}$$

With this particular choice the flux coordinates are sometimes called θ^* coordinates. Note that the poloidal angle in flux coordinates, equation (A.10), might take values outside the interval $[0, 2\pi]$. However, since any physical quantity A must be periodic in the angles, i.e. $A(x + 2\pi n, \phi) = A(x, \phi)\ \forall n \in \mathrm{Z}$, the relation

$$\begin{aligned} A(\theta_\mathrm{f}, \phi_\mathrm{f}) &= A(\theta + \frac{\nu_p}{\psi'}, \phi) = A\left(\left[\theta + \frac{\nu_p}{\psi'}\right] + 2\pi n, \phi\right) \\ &= A\left(\theta + 2\pi n + \frac{\nu_p(\theta + 2\pi n, \phi)}{\psi'}, \phi\right) = A(\theta_\mathrm{f}(\theta + 2\pi n, \phi), \phi_\mathrm{f}), \end{aligned}$$

holds. Hence, the values of $\theta_\mathrm{f} \notin [0, 2\pi]$ can be associated with

$$\tilde{\theta}_\mathrm{f}(\theta, \phi) \equiv \begin{cases} \theta_\mathrm{f} + 2\pi, & \text{if } \theta_\mathrm{f} < 0 \\ \theta_\mathrm{f}, & \text{if } \theta_\mathrm{f} \in [0, 2\pi] \\ \theta_\mathrm{f} - 2\pi, & \text{if } \theta_\mathrm{f} > 2\pi \end{cases} \tag{A.11}$$

The angle $\tilde{\theta}_\mathrm{f}(\theta, \phi)$ is utilized to resample a quantity, originally expressed in flux coordinates, in the curvilinear coordinates. On the other hand, the transformation $\theta(\tilde{\theta}_\mathrm{f}, \phi_\mathrm{f})$ is used to resample a function of (θ, ϕ) in the flux system. These transformations are presented in figure A.1.

Finally, its is noted here that the coordinates PEST-1, utilized e.g. in the particle-in-cell code EUTERPE [138], uses the same transformation (A.10) as the θ^* system, and are hence equivalent. The magnetic field strength resampled in both PEST-1 and θ^* coordinate systems is shown in figure A.2.

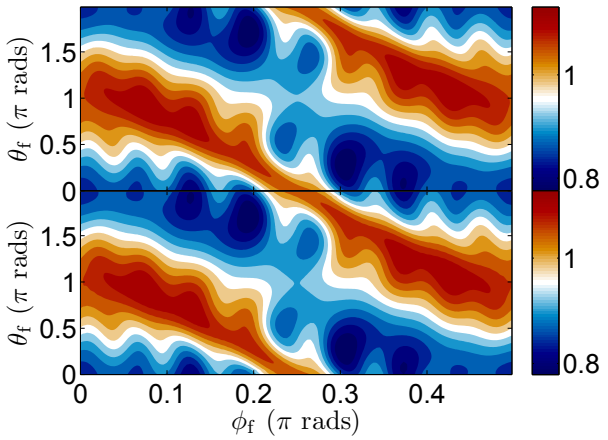

Figure A.2. Magnetic field strength at the surface $\rho = 0.6$ in (top) PEST-1 and (bottom) θ^* flux coordinates.

A.2.1 Glebsch form of an incompressible flow

For a velocity field that is incompressible, i.e $\nabla \cdot \mathbf{u} = 0$ see section 2.2, a Glebsch-form like (A.4) can be obtained as

$$\mathbf{u} = \nabla\rho \times \nabla\omega, \tag{A.12}$$

with $\partial_\theta \omega = \sqrt{g} u^\phi$ and $\partial_\phi \omega = -\sqrt{g} u^\theta$, since $\mathbf{u} \cdot \nabla\rho = 0$. As explained in section (2.2), the incompressible flow is recast as

$$\mathbf{u} = E(\rho)\left(\frac{\mathbf{B} \times \nabla\rho}{B^2} + h\mathbf{B}\right) + \Lambda(\rho)\mathbf{B},$$

see equation (2.33). Then, the contravariant **u**-components are

$$u^\theta = (Eh + \Lambda)\, B^\theta + \frac{E B_\phi}{\sqrt{g} B^2}, \tag{A.13}$$

$$u^\phi = (Eh + \Lambda)\, B^\phi - \frac{E B_\theta}{\sqrt{g} B^2}. \tag{A.14}$$

With the initial condition $\omega(s,0,0)=0$, the stream function is integrated as

$$\omega(\rho,\theta,\phi)=\left[\int_0^{\theta}\sqrt{g}u^{\phi}d\theta'\right]_{\phi=0}-\int_0^{\phi}\sqrt{g}u^{\theta}d\phi'. \tag{A.15}$$

As in section A.2 the stream function is decomposed into a periodic part and a linear combination of the angles, i.e. $\omega=\omega_p+a\theta+b\phi$. The flux-constant coefficients are calculated form the flux-surface averaged of the contravariant **u**-components in (A.13), to yield

$$\omega(\rho,\theta,\phi) \quad = \quad \omega_p(\rho,\theta,\phi)+\frac{\langle u^{\phi}\rangle\theta-\langle u^{\theta}\rangle\phi}{\langle\sqrt{g}^{-1}\rangle}. \tag{A.16}$$

The velocity field lines lying in a constant surface are obtained from the condition ω=constant. It is clear that a proper choice of the angles would make such lines straight, i.e. there are $(\theta_{\rm F},\phi_{\rm F})$ coordinates such that

$$\omega(\rho,\theta_{\rm F},\phi_{\rm F})=\frac{\langle u^{\phi_{\rm F}}\rangle\theta_{\rm F}-\langle u^{\theta_{\rm F}}\rangle\phi_{\rm F}}{\langle\sqrt{g_{\rm F}}^{-1}\rangle}.$$

Then, the flow (A.12) is written as

$$\mathbf{u}=\nabla\rho\times\nabla\omega=\frac{\sqrt{g_{\rm F}}^{-1}}{\langle\sqrt{g_{\rm F}}^{-1}\rangle}\left(\langle u^{\theta_{\rm F}}\rangle\mathbf{e}_{\theta_{\rm F}}+\langle u^{\phi_{\rm F}}\rangle\mathbf{e}_{\phi_{\rm F}}\right). \tag{A.17}$$

The coordinates in which both the magnetic field and the velocity field are straight lines are called Hamada coordinates and are introduced next.

A.3 Hamada coordinates

The Hamada coordinates [110] appear naturally in the context of ideal MHD equlibrium, since a coordinate system in which both the magnetic field and current density lines are straight greatly simplifies the force balance $\nabla p=\mathbf{j}\times\mathbf{B}$. As indicated in section A.2 the transformation (A.10) was somehow arbitrary, since the toroidal angle remained unaltered. Thus, we seek for a further transformation of the angles that leaves the magnetic field lines straight, as in the form (A.8) or the equivalent form (A.9). With

$$\theta_{\rm F}=\theta_{\rm f}+\chi' G, \tag{A.18a}$$

$$\phi_{\rm F}=\phi_{\rm f}+\psi' G, \tag{A.18b}$$

and imposing that the contravariant **B**-components have the from (A.9), a magnetic equation for the stream function G is obtained,

$$\mathbf{B}\cdot\nabla G=\frac{1}{\sqrt{g_{\rm F}}}-\frac{1}{\sqrt{g_{\rm f}}}, \tag{A.19}$$

with the Jacobian $\sqrt{g_{\rm F}}$ still undetermined. Next, the inspection of equation (A.17) suggests the choice

$$\sqrt{g_{\rm F}}=\langle\sqrt{g_{\rm F}}^{-1}\rangle^{-1}=\frac{1}{4\pi^2}\frac{{\rm d}V}{{\rm d}\rho}. \tag{A.20}$$

so that the field velocity $\mathbf{u} = \left(\langle u^{\theta_F}\rangle \mathbf{e}_{\theta_F} + \langle u^{\phi_F}\rangle \mathbf{e}_{\phi_F}\right)$ in (A.17) consist of straight lines. With this flux-constant Jacobian -i.e. only dependent on the radial coordinate-, both the current density -equivalently the flow velocity- and the magnetic field lines are straight lines. Furthermore, their contravariant components are constants on the surface. In the following, the coordinates verifying (A.18) and (A.20) are regarded as the Hamada coordinates, (ρ, ϑ, ζ), with $\sqrt{g}^{-1} = \nabla\rho \cdot \nabla\vartheta \times \nabla\zeta = 4\pi^2/V'$.

An important property of the Hamada coordinates is that the basis vectors, $\mathbf{e}_i$, have a zero divergence, i.e. $\nabla \cdot \mathbf{e}_i = \nabla \cdot \left(\sqrt{g}\nabla x^i \times \nabla\rho\right) = \sqrt{g}\nabla \cdot \left(\nabla x^i \times \nabla\rho\right) = 0$. As a consequence the flux-surface of the operator $\mathbf{e}_i^{\mathrm{H}} \cdot \nabla$, $i \equiv \vartheta, \zeta$, acting on a scalar field is zero

$$\langle \mathbf{e}_{\mathrm{H},i} \cdot \nabla g \rangle = 0, \; \forall \; g(\rho, \vartheta, \zeta). \quad \text{(A.21)}$$

The Hamada stream function G is obtained after solving the magnetic equation (A.19) (see section A.4 for the description of the method). The resultant Hamada stream function, G in (A.18), is presented in figure A.3, as function of the flux coordinates.

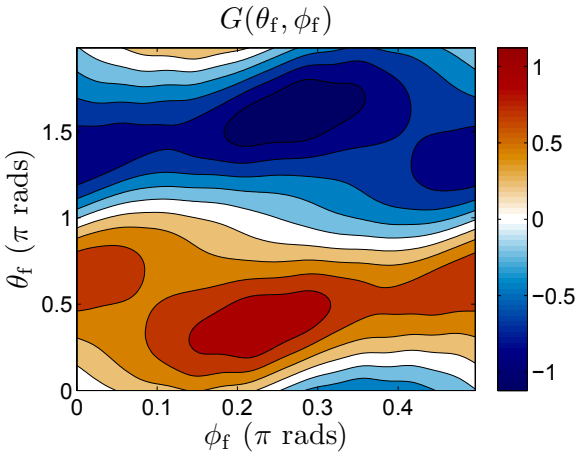

Figure A.3. Stream function to obtain the Hamada coordinates at the surface $\rho = 0.6$.

A.3.1 Relation of the Pfirsch-Schlüter flow and the Hamada poloidal vector

Here, a relationship between the expression of the flow in Hamada coordinates, equation (2.42), and in general coordinates, equation (2.33), is derived. This is equivalent to demonstrating that the relation

$$\mathbf{e}_\vartheta = \frac{\mathbf{B} \times \nabla\psi}{B^2} + \psi' h \mathbf{B},$$

holds. As $\mathbf{e}_\vartheta \times \mathbf{B} = B^\zeta \mathbf{e}_\vartheta \times \mathbf{e}_\zeta = \nabla\psi$, the perpendicular component of the Hamada poloidal vector is

$$\mathbf{e}_{\vartheta\perp} = \mathbf{b} \times (\mathbf{e}_\vartheta \times \mathbf{b}) = \frac{\mathbf{B} \times \nabla\psi}{B^2}.$$

On the other hand, since the Hamada basis vectors are divergence-free the parallel component of the Hamada poloidal vector, $\mathbf{e}_{\vartheta\parallel} = \mathbf{e}_\vartheta \cdot \mathbf{b}$ is obtained from the relation $\nabla \cdot \mathbf{e}_{\vartheta\parallel} = -\nabla \cdot \mathbf{e}_{\vartheta\perp}$ or, equivalently,

$$\mathbf{B} \cdot \nabla \left(\frac{\mathbf{e}_\vartheta \cdot \mathbf{B}}{B^2}\right) = -\mathbf{B} \times \nabla\psi \cdot \nabla \left(\frac{1}{B^2}\right) = \psi' \mathbf{B} \cdot \nabla h.$$

In the latter equality, the magnetic equation (2.30) that defines the PS function h is used. Hence,

$$\mathbf{e}_\vartheta \cdot \mathbf{B} = \psi' h B^2 + \Omega(\psi) B^2.$$

Note that $\langle hB^2 \rangle = 0$, see equation (2.31). Since $\langle \mathbf{e}_\vartheta \cdot \mathbf{B} \rangle \propto I_T = 0$ for a currentless stellarator, the equivalence between equations (2.33) and (2.42) is demonstrated.

A.4 Solution of magnetic equations

Here, the solution of a magnetic equation of the form

$$\mathbf{B}\cdot\nabla A = C$$

is addressed. Note that since $\langle \mathbf{B}\cdot\nabla A\rangle = 0$ for any scalar A, the solubility condition $\langle C\rangle = 0$ must be satisfied.

If the magnetic field is expressed in flux coordinates, see (A.8), the above magnetic equation is recast as

$$(\chi'\partial_{\theta_\mathrm{f}} + \psi'\partial_{\phi_\mathrm{f}})A = S, \tag{A.22}$$

with $S \equiv \sqrt{g}C$ resampled in flux coordinates. In the following the subindex 'f' is dropped. The partial differential equation (A.22) can be transformed into an algebraic equation by expanding the functions A and S in a double Fourier Series in the angles, e.g.

$$\hat{A}(s,k_\theta,k_\phi) = \sum_{m=0}^{N_p-1}\sum_{n=0}^{N_t-1} A(s,\theta_m,\phi_n)\exp\left(-i(k_\theta\theta_m + k_\phi\phi_n)\right), \tag{A.23a}$$

$$A(s,\theta_m,\phi_n) = \frac{1}{N_pN_t}\sum_{k_\theta=0}^{N_p-1}\sum_{k_\phi=0}^{N_t-1} \hat{A}(s,k_\theta,k_\phi)\exp\left(i(k_\theta\theta_m + k_\phi\phi_n)\right), \tag{A.23b}$$

with $\theta_m = 2\pi m/N_p$ and $\phi_n = 2\pi n/N_t$, and $m, n, k_\theta, k\_phi \in \mathrm{Z}$. A similar transformation is applied to the source S. Then equation (A.22) results

$$\hat{A} = \frac{-i}{\chi' k_\theta + \psi' k_\phi}\hat{S}, \tag{A.24}$$

and the solution A is obtained by the inverse Fourier transformation of (A.24).

Care must be taken when $\chi' k_\theta + \psi' k_\phi = 0$. For the mode $k_\theta = k_\phi = 0$, $\hat{S}(0,0)$ must be zero as deduced from the solubility condition

$$0 = \langle \vec{B}\cdot\nabla G\rangle = \langle C\rangle \propto \sum_{m=0}^{N_p-1}\sum_{n=0}^{N_t-1} A(s,\theta_m,\phi_n) = \hat{S}(0,0).$$

In resonant modes, $\iota k_\theta^r = -k_\phi^r$,

$$\begin{aligned}\hat{S}(s,k_\theta^r,k_\phi^r) &= \sum_{m=0}^{N_p-1}\sum_{n=0}^{N_t-1} S(s,\theta_m,\phi_n)\exp(-ik_\theta^r(\theta_m - \iota\phi_n)) \\ &\propto \oint \frac{dl}{B}C = 2\pi\oint dl\frac{\partial G}{\partial l} = 0\end{aligned} \tag{A.25}$$

Here we have used that, along a magnetic field line, $(\theta_m - \iota\phi_n)$ remains constant within a magnetic surface. The integral can be performed along (closed) magnetic field lines, and so the exponential becomes constant. Since the function G is single-valued, the integral in a rational surface is zero.

APPENDIX B

FINE STRUCTURE CALCULATION

Troughout this section we mostly follow the book *Quantum mechanics of one- and two-electron atoms*, by Hans Bethe and Edwin Salpeter [176].

B.1 Energy levels

Neglecting quantum electrodynamic effects (which only contribute to the $l = 0$ level), the energy levels of a hydrogen-like atom within the Pauli approximation are

$$E(nl^2L_J) = -\frac{\mu\alpha^2Z^2}{n^2}\left(1 + \frac{\alpha^2Z^2}{n^2}\left(\frac{n}{j+\frac{1}{2}} - \frac{3}{4}\right)\right). \tag{B.1}$$

Here α is the fine structure constant; $\mu = \frac{m}{1+m/M}$ is the reduced mass, with m and M the electron and atom mass rest; Z is the charge viewed by the outer electron; n is the principal quantum number; $l = n-1, n-2, ..., 0$, the orbital quantum number; and $j = l \pm \frac{1}{2}$. It should be noticed that states with the same j and n are completely degenerate.

B.2 Intensities in the LS approximation

Let us consider an optically allowed transition from a state $\gamma \equiv nl$ to a state $\gamma' \equiv n'l'$. We will use the notation

$$X_{\gamma'\gamma} \quad \text{or} \quad X_{\gamma}^{\gamma'}, \tag{B.2}$$

to denote any magnitude X related with such transition.

In the dipole approximation, the intensity of the emitted light per atom (integrated in all the directions of propagation, $\vec{k}$; and without considering any particular polarization) is

$$I_{\gamma'\gamma} = h\nu_{\gamma'\gamma}A_{\gamma'\gamma} \quad (\mathrm{J}\cdot\mathrm{s}^{-1}), \tag{B.3}$$

where

$$\nu_{\gamma'\gamma} = \frac{E_\gamma - E'_\gamma}{h}, \tag{B.4}$$

the frequency of the transition, and

$$A_{\gamma'\gamma} = \frac{64\pi^4\nu^3_{\gamma'\gamma}}{3hc^3}\frac{l_>}{2l+1}e^2a_0^2\left(R^{\gamma'}_{\gamma}\right)^2, \tag{B.5}$$

the total transition probability (in s^{-1}). Here, h is the Planck constant; c the speed of the light; e the electron charge; and $a_0 = \frac{\hbar}{mc\alpha}$ the Bohr radius. The notation $l_>$ stands for the largest of l and l'. This probability (usually known as the Einstein coefficient) can be expressed in terms of an averaged (*i.e.*, without considering polarization) oscillator strength, $f_{\gamma'\gamma}$, as

$$A^{\gamma'}_{\gamma} = \frac{8\pi^2e^2\nu^2_{\gamma'\gamma}}{mc^3}f^{\gamma'}_{\gamma}, \tag{B.6a}$$

$$f^{\gamma'}_{\gamma} \equiv f^{n'l'}_{nl} = \frac{1}{3}\frac{h\nu_{\gamma'\gamma}}{R_Y}\frac{l_>}{2l+1}\left(R^{n'l'}_{nl}\right)^2. \tag{B.6b}$$

Here, $R_Y = \frac{1}{2}mc^2\alpha^2$ is the Rydberg constant. The radial integral is

$$R^{n'l'}_{nl} = \int_0^\infty drP_{n,l}(r)r^3P_{n',l'}, \tag{B.7}$$

can be expressed in terms of hypergeometric functions

$$\begin{aligned} R^{n'l-1}_{nl} \quad = \quad & \frac{(-1)^{n'-l}}{4(2l-1)!}\sqrt{\frac{(n+l)!(n'+l-1)!}{(n-l-1)!(n'-l)!}}\frac{(4nn')^{l+1}(n-n')^{n+n'-2l-2}}{(n+n')^{n+n'}} \times \\ & \left\{F\left(-n+l+1,-n'+l,2l,-\frac{4nn'}{(n-n')^2}\right) - \right. \\ & \left.\left(\frac{n-n'}{n+n'}\right)^2F\left(-n+l-1,-n'+l,2l,-\frac{4nn'}{(n-n')^2}\right)\right\}/Z. \end{aligned} \tag{B.8}$$

Notice that the dipole moment for transitions with $\Delta l = l - l' = -1$ can be calculated also using eq. B.8, since $R^{n'l+1}_{nl} = R^{nl}_{n'l+1}$.

Recently, D. Hoang-Binh has developed a numerical method to calculate B.8 up to $n \sim 1000$ [202]. It is based on the recurrence relation

$$(a-c)F(a-1) = a(1-x)\left(F(a) - F(a+1)\right) + (a+bx-c)F(a), \tag{B.9}$$

where $F(a) \equiv F(a,b,c,x)$, and:

$$a = -n+l\pm 1; \quad b = -n'+l; \quad c = 2l; \quad x = -4nn'/(n-n')^2.$$

The initial values are $F(0) = 1$ and $F(-1) = 1 - bx/c$. We have benchmarked our results with the examples provided in ref. [202][1] and with the tables given in ref. [176].

[1] In ref. [202], there is an erratum in eq. B.8:

$$\begin{aligned} R^{n'l-1}_{nl} \quad = \quad & \frac{(-\mathbf{1})^{\mathbf{n'-1}}}{4(2l-1)!}\sqrt{\frac{(\mathbf{n+1})!(n'+l-1)!}{(n-l-1)!(n'-l)!}}\frac{(4nn')^{l+1}(n-n')^{n+n'-2l-2}}{(n+n')^{n+n'}} \times \\ & \left\{F\left(-n+l+1,-n'+l,2l,-\frac{4nn'}{(n-n')^2}\right) - \left(\frac{n-n'}{n+n'}\right)^2F\left(-n+l-1,-n'+l,2l,-\frac{4nn'}{(n-n')^2}\right)\right\}/Z \end{aligned}$$

Here, we use the expression B.8, obtained from ref. [176]. With this, we have obtained the same results for $\left(R^{n'l'}_{nl}\right)^2$ and the corresponding transition probabilities than the ones provided in [202].

However some differences have been obtained in the value of the absorption oscillator strength. And this is weird, since we use the same expression to calculate them (eq. B.6b). The result is inputed in eq. B.6a to obtain the transition probability.

Hence, since the radial integrals and transition probabilities agree, we should have introduced some error in B.6b, which is corrected in B.6a.

If the initial states γ are statistically populated, the final intensity in the so called Russel-Sunders approximation are

$$I_{nl}^{n'l'} = 2(2l+1)h\nu_{nl}^{n'l'}A_{nl}^{n'l'}. \tag{B.10}$$

B.3 Intensities of fine structure lines

In case of using the Pauli approximation (j-resolved), for a given initial state $\gamma \equiv nl^2L_J$, there are three possible transitions towards the level $\gamma' \equiv n'l - 1^2L_J$:

$$(a)j = l + \frac{1}{2} \to j' = l - \frac{1}{2}, \quad (b)j = l - \frac{1}{2} \to j' = l - \frac{1}{2}, \quad (c)j = l - \frac{1}{2} \to j' = l - \frac{3}{2}.$$

Their relative intensities are just:

$$a : b : c = [(l+1)(2l-1)] : 1 : [(l-1)(2l+1)]. \tag{B.11}$$

Hence, the intensities in the j-resolved picture can be obtained by evaluating first the l-resolved intensities, eq. B.3, and then by multiplying the result by the relative contributions B.11, and dividing by $\frac{1}{2}(2l+1)(2l-1)$:

$$I_{l+\frac{1}{2}}^{\Delta j=1} = I_{nl}^{n'l-1}\frac{2(l+1)(2l-1)}{(2l+1)(2l-1)}, \tag{B.12a}$$

$$I_{l-\frac{1}{2}}^{\Delta j=0} = I_{nl}^{n'l-1}\frac{2}{(2l+1)(2l-1)}, \tag{B.12b}$$

$$I_{l-\frac{1}{2}}^{\Delta j=1} = I_{nl}^{n'l-1}\frac{2(l-1)(2l+1)}{(2l+1)(2l-1)}. \tag{B.12c}$$

If we further assume a statistical population of the initial levels, eqs. B.12 have to be multiplied by $(2j+1)$.

APPENDIX C

NUMERICAL IMPLEMENTATION OF THE IMPURITY DENSITY REDISTRIBUTION

In this appendix, the numerical implementation of the parabolic partial differential equation (PDE) for the impurity density asymmetry is addressed. Let us consider the equation (2.96)

$$\mathbf{B}\cdot\nabla\left(\mathbf{B}\cdot\nabla n\right)-g\mathbf{B}\cdot\nabla n-\gamma_{\rm f}B^2\mathbf{u}_{z\perp}\cdot\nabla n-fn=0, \tag{C.1}$$

with

$$g = \mathbf{B}\cdot\nabla\ln B^2-\frac{eZ}{T_z}\mathbf{B}\cdot\nabla\Phi+\gamma_{\rm f}B^2\left\{(A_i+E_z)h+B_i+\Lambda_i\right\}, \tag{C.2a}$$

$$f = \gamma_{\rm f}A_i\mathbf{B}\times\nabla\rho\cdot\nabla\ln B^2+\frac{eZ}{T_z}\left(\mathbf{B}\cdot\nabla\ln B^2-\mathbf{B}\cdot\nabla\right)\mathbf{B}\cdot\nabla\Phi. \tag{C.2b}$$

In order to facilitate the algebra flux coordinates, $(\theta_{\rm f},\phi_{\rm f})$, are used, see section A.2 in the appendix A. Note also that the in-surface variation of the potential [138], $\Phi-\langle\Phi\rangle$, and the Pfirsch-Schlüter function h, see equation (2.30), are calculated in the $(\theta_{\rm f},\phi_{\rm f})$ system. Since the magnetic field in flux coordinates is a straight line, see equation (A.8), the spatial derivative parallel to the magnetic field is recast as

$$\sqrt{g_{\rm f}}\mathbf{B}\cdot\nabla=\chi'\partial_{\theta_{\rm f}}+\psi'\partial_{\phi_{\rm f}}:=\partial_b.$$

Using the expression $\left(\sqrt{g_{\rm f}}\right)^2\mathbf{B}\cdot\nabla(\mathbf{B}\cdot\nabla n)=\sqrt{g_{\rm f}}\partial_b\left(\sqrt{g_{\rm f}}^{-1}\partial_b\right)n=\partial_b^2 n-\partial_b n\partial_b\ln(\sqrt{g_{\rm f}})$, the parabolic PDE (C.1) is

$$\left(\chi'\frac{\partial}{\partial\theta_{\rm f}}+\psi'\frac{\partial}{\partial\phi_{\rm f}}\right)^2 n-r\frac{\partial n}{\partial\theta_{\rm f}}-s\frac{\partial n}{\partial\phi_{\rm f}}-fn=0, \tag{C.3}$$

with f given by (C.2b) and

$$r = \chi'\partial_b\ln\left(\sqrt{g_{\rm f}}\right)+\sqrt{g_{\rm f}}\left(\chi' g+\gamma_{\rm f}E_z B_{\phi_{\rm f}}\right), \tag{C.4a}$$

$$s = \psi'\partial_b\ln\left(\sqrt{g_{\rm f}}\right)+\sqrt{g_{\rm f}}\left(\psi' g-\gamma_{\rm f}E_z B_{\theta_{\rm f}}\right). \tag{C.4b}$$

Here, g is given by (C.2a) and the relation $B^2\mathbf{u}_{z\perp}\cdot\nabla=(\sqrt{g_{\rm f}})^{-1}E_z(B_{\phi_{\rm f}}\partial_{\theta_{\rm f}}-B_{\theta_{\rm f}}\partial_{\phi_{\rm f}})$ is used. In the following, the sub-index f indicating flux coordinates is dropped.

Next, a finite differences scheme is adopted, where the functions r, s and f are assumed to be known functions of the angles (θ, ϕ) and the radial coordinate ρ. Since equation (C.3) only involves angular derivatives, the radial coordinate is taken as a parameter and is hence not made explicit in the following. Next, a regular grid (θ_i, ϕ_j) with $i = 1, ..., M$; $j = 1, ..., N$ is considered. The angular derivatives of n at the point (i, j) are taken as the centred finite differences in that position, i.e.

$$\frac{\partial n_{ij}}{\partial \theta_i} = \frac{n_{i+1,j} - n_{i-1,j}}{2\Delta\theta}, \tag{C.5a}$$

$$\frac{\partial n_{ij}}{\partial \phi_j} = \frac{n_{i,j+1} - n_{i,j-1}}{2\Delta\phi}, \tag{C.5b}$$

$$\begin{aligned}\left(\chi' \frac{\partial}{\partial \theta_i} + \psi' \frac{\partial}{\partial \phi_j}\right)^2 n_{ij} = & \left(\frac{\chi'}{\Delta\theta}\right)^2 (n_{i+1,j} - 2n_{i,j} + n_{i-1,j}) + \\ & \left(\frac{\psi'}{\Delta\phi}\right)^2 (n_{i,j+1} - 2n_{i,j} + n_{i,j-1}) + \\ & \frac{\psi'\chi'}{2\Delta\theta\Delta\phi}(n_{i+1,j+1} + n_{i-1,j-1} - n_{i+1,j-1} - n_{i-1,j+1})\end{aligned} \tag{C.5c}$$

Note that with equations (C.5), the equation (C.3) couples the entry n_{ij} with

$$n_{i\pm1,j\pm1}, \quad n_{i\pm1,j}, \quad n_{i,j\pm1}, \quad n_{i\pm1,j\mp1}. \tag{C.6}$$

Thus, if any bi-dimensional function is rearranged in a vector indexed by

$$k(i, j) = i + M(j - 1), \text{ with } (i, j) \in (1...M, 1...N), \tag{C.7}$$

the second order PDE (C.3) is recast as a system of linear algebraic equations of the form $A_{kl}n_l = 0$. Here, the non-zero entries of the coefficient matrix A_{kl} are

$$n_{i\pm1,j\pm1} \rightarrow A_{k,k\pm(M+1)} = \frac{\chi'\psi'}{2\Delta\theta\Delta\phi}, \tag{C.8a}$$

$$n_{i\pm1,j\mp1} \rightarrow A_{k,k\mp(M-1)} = -\frac{\chi'\psi'}{2\Delta\theta\Delta\phi}, \tag{C.8b}$$

$$n_{i\pm1,j} \rightarrow A_{k,k\pm1} = \left(\frac{\chi'}{\Delta\theta}\right)^2 \mp \frac{r_k}{2\Delta\theta}, \tag{C.8c}$$

$$n_{i,j\pm1} \rightarrow A_{k,k\pm M} = \left(\frac{\psi'}{\Delta\phi}\right)^2 \mp \frac{s_k}{2\Delta\phi}, \tag{C.8d}$$

$$n_{i,j} \rightarrow A_{k,k} = -2\left\{\left(\frac{\chi'}{\Delta\theta}\right)^2 + \left(\frac{\psi'}{\Delta\phi}\right)^2\right\} - f_k. \tag{C.8e}$$

In the corners of the domain (i.e. $i = 1, M$ and $j = 1, N$) we might need to evaluate the function out of that domain (*e.g.*, when $i = 1$, $n_{i-1,j}$ is not well defined). The periodicity $n_{M+p,j} = n_{p,j}$ and $n_{i,N+p} = n_{i,p}$ gives us the necessary rules for these points[1], i.e.

[1] Since the functions are periodic in the angles and preserve the $n = 4$ toroidal periodicity of TJ-II, the intervals $\theta \in [0, 2\pi)$ and $\zeta \in [0, \pi/2)$ are covered.

for $j = 1...N$:

if $i = 1$

$$A_{k,k-1} \rightarrow A_{k,k+M-1} = \left(\frac{\dot{\chi}}{\Delta\theta}\right)^2 + \frac{r_k}{2\Delta\theta}$$

if $j = 1$,

$$A_{k,k-(M+1)} \rightarrow A_{k,k+MN-1} = \frac{\dot{\chi}\dot{\psi}}{2\Delta\theta\Delta\zeta}$$

$$A_{k,k+(M-1)} \rightarrow A_{k,k+2M-1} = -\frac{\dot{\chi}\dot{\psi}}{2\Delta\theta\Delta\zeta}$$

$$A_{k,k-M} \rightarrow A_{k,k+M(N-1)} = \left(\frac{\dot{\psi}}{\Delta\zeta}\right)^2 + \frac{s_k}{2\Delta\zeta}$$

$$A_{k,k-(M-1)} \rightarrow A_{k,k+1+M(N-1)} = -\frac{\dot{\chi}\dot{\psi}}{2\Delta\theta\Delta\zeta}$$

if $j = N$,

$$A_{k,k-(M+1)} \rightarrow A_{k,k-1} = \frac{\dot{\chi}\dot{\psi}}{2\Delta\theta\Delta\zeta}$$

$$A_{k,k+(M-1)} \rightarrow A_{k,k-1-M(N-2)} = -\frac{\dot{\chi}\dot{\psi}}{2\Delta\theta\Delta\zeta}$$

$$A_{k,k+M} \rightarrow A_{k,k-M(N-1)} = \left(\frac{\dot{\psi}}{\Delta\zeta}\right)^2 - \frac{s_k}{2\Delta\zeta}$$

$$A_{k,k+(M+1)} \rightarrow A_{k,k+1-M(N-1)} = \frac{\dot{\chi}\dot{\psi}}{2\Delta\theta\Delta\zeta}$$

else,

$$A_{k,k-(M+1)} \rightarrow A_{k,k-1} = \frac{\dot{\chi}\dot{\psi}}{2\Delta\theta\Delta\zeta}$$

$$A_{k,k+(M-1)} \rightarrow A_{k,k+2M-1} = -\frac{\dot{\chi}\dot{\psi}}{2\Delta\theta\Delta\zeta}$$

for $j = 1...N$:

if $i = M$

$$A_{k,k+1} \rightarrow A_{k,k-M+1} = \left(\frac{\dot{\chi}}{\Delta\theta}\right)^2 - \frac{r_k}{2\Delta\theta}$$

if $j = 1$,

$$A_{k,k+(M+1)} \rightarrow A_{k,k+1} = \frac{\dot{\chi}\dot{\psi}}{2\Delta\theta\Delta\zeta}$$

$$A_{k,k-(M-1)} \rightarrow A_{k,k+1+M(N-2)} = -\frac{\dot{\chi}\dot{\psi}}{2\Delta\theta\Delta\zeta}$$

$$A_{k,k-M} \rightarrow A_{k,k+M(N-1)} = \left(\frac{\dot{\psi}}{\Delta\zeta}\right)^2 + \frac{s_k}{2\Delta\zeta}$$

$$A_{k,k-(M+1)} \rightarrow A_{k,k+M(N-1)-1} = \frac{\dot{\chi}\dot{\psi}}{2\Delta\theta\Delta\zeta}$$

if $j = N$,

$$A_{k,k+(M+1)} \rightarrow A_{k,k+1-MN} = \frac{\dot{\chi}\dot{\psi}}{2\Delta\theta\Delta\zeta}$$

$$A_{k,k-(M-1)} \rightarrow A_{k,k+1-2M} = -\frac{\dot{\chi}\dot{\psi}}{2\Delta\theta\Delta\zeta}$$

$$A_{k,k+M} \rightarrow A_{k,k-M(N-1)} = \left(\frac{\dot{\psi}}{\Delta\zeta}\right)^2 - \frac{s_k}{2\Delta\zeta}$$

$$A_{k,k+(M-1)} \rightarrow A_{k,k-1-M(N-1)} = -\frac{\dot{\chi}\dot{\psi}}{2\Delta\theta\Delta\zeta}$$

else,

$$A_{k,k+(M+1)} \rightarrow A_{k,k+1} = \frac{\dot{\chi}\dot{\psi}}{2\Delta\theta\Delta\zeta}$$

$$A_{k,k-(M-1)} \rightarrow A_{k,k+1-2M} = -\frac{\dot{\chi}\dot{\psi}}{2\Delta\theta\Delta\zeta}$$

for $i = 2...M-1$:

if $j = 1$,

$$A_{k,k-(M-1)} \rightarrow A_{k,k+1+M(N-1)} = -\frac{\dot{\chi}\dot{\psi}}{2\Delta\theta\Delta\zeta}$$

$$A_{k,k-M} \rightarrow A_{k,k+M(N-1)} = \left(\frac{\dot{\psi}}{\Delta\zeta}\right)^2 + \frac{s_k}{2\Delta\zeta}$$

$$A_{k,k-(M+1)} \rightarrow A_{k,k+M(N-1)-1} = \frac{\dot{\chi}\dot{\psi}}{2\Delta\theta\Delta\zeta}$$

if $j = N$,

$$A_{k,k+(M+1)} \rightarrow A_{k,k+1-M(N-1)} = \frac{\dot{\chi}\dot{\psi}}{2\Delta\theta\Delta\zeta}$$

$$A_{k,k+M} \rightarrow A_{k,k-M(N-1)} = \left(\frac{\dot{\psi}}{\Delta\zeta}\right)^2 - \frac{s_k}{2\Delta\zeta}$$

$$A_{k,k+(M-1)} \rightarrow A_{k,k-1-M(N-1)} = -\frac{\dot{\chi}\dot{\psi}}{2\Delta\theta\Delta\zeta}$$

Finally, the constrain,

$$1 = \langle n \rangle = \frac{1}{\dot{V}} \int d\theta \int d\zeta \sqrt{g} n = \frac{\Delta\theta \Delta\zeta}{\dot{V}} \sum_i \sum_j (\sqrt{g})_{i,j} n_{i,j}, \tag{C.9}$$

must be built in. It can be done, for instance, by considering the equivalent system:

$$(A + B)_{kl} n_l = c_k \tag{C.10}$$

$$B_{kl} = (\sqrt{g})_l \delta_{k,1} \tag{C.11}$$

$$c_l = \textstyle\sum_j (\sqrt{g})_j \delta_{l,1}. \tag{C.12}$$

The nonzero pattern of the resultant sparse coefficient matrix is displayed in figure C.1, for the case of $N = M = 8$.

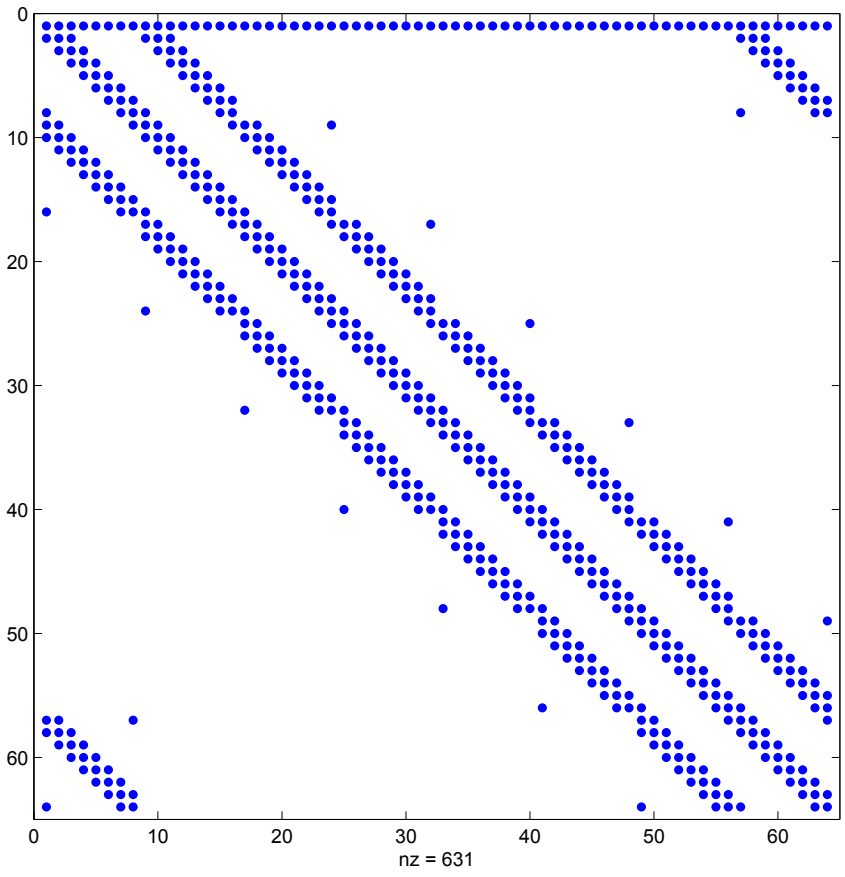

Figure C.1. Nonzero pattern of the coefficient matrix, with $M = N = 8$ poloidal and toroidal points.

BIBLIOGRAPHY

[1] K. Miyamoto, *Controlled Fusion and Plasma Physics*, Taylor&Francis Series on Plasma Physics (2007), ISBN: 1-58488-709-5.

[2] J. Wesson, *Tokamaks*, 2nd Ed., Clarendon Press, Oxford (1997).

[3] M. Wakatani, *Stellarator and Heliotron Devices*, Oxford University Press: International Series of Monographs on Physics, vol. 95 (1998).

[4] International Energy Agency (IEA). Visit `www.iea.org`.

[5] Renewable Global Status report REN21, 2013, available on-line at `http://www.ren21.net/REN21Activities/GlobalStatusReport.aspx`.

[6] J. D. Jackson. Catalysis of nuclear reactions between hydrogen isotopes by μ^- mesons. *Physical Review*, 106:330–339, 1957.

[7] L. Spitzer, *Physics of fully ionized gases,* 2006 Dover Edition of the 1962 second revised edition by John Wiley and Sons, Inc., New York. ISBN: 0-486-44982-3.

[8] R. J. Goldston and P. H. Rutherford, *Introduction to Plasma Physics.* IOP Publishing Ltd (1995). ISBN: 0-7503-0183-X.

[9] A. Hasegawa, H. Daido, M. Fujita, K. Mima, M. Murakami, S. Nakai, K. Nishihara, K. Terai, and C. Yamanaka. Magnetically insulated inertial fusion: A new approach to controlled thermonuclear fusion. *Physical Review Letters*, 56:139–142, 1986.

[10] A. H. Boozer. Physics of magnetically confined plasmas. *Review of Modern Physics*, 76(4):1071, 2005.

[11] J. D. Lawson. Some Criteria for a Power Producing Thermonuclear Reactor. *Proceedings of the Physical Society. Section B*, 70(1):6, 1957.

[12] D. Reiter, G. H. Wolf, and H. Kever. Burn condition, helium particle confinement and exhaust efficiency. *Nuclear Fusion*, 30(10):2141, 1990.

[13] T. J. Dolan. *Fusion Research: Principles, Experiments and Technology.* Pergamon Pr., 1981. ISBN: 0080255655. Available online at `http://www.sunist.org/shareddocuments/FusionResearchCoursebyThomasDolan/`.

[14] Y. Poitevin. The Tritium Breeding Blankets for Fusion Reactors. a key component for sustainability of Fusion Energy. Fusion for Energy (F4E Barcelona). Swiss Nuclear Forum, CRPP/Lausanne, March-23, 2011. Available on-line at `http://www.iter-industry.ch/wp-content/uploads/2010/01/Pr__sentation_Poitevin.pdf`.

[15] M. E. Sawan and M. A. Abdou. Physics and technology conditions for attaining tritium self-sufficiency for the DT fuel cycle. *Fusion Engineering and Design*, 81:1131, 2006.

[16] O. Cabellos, J. Sanz, N. García-Herranz, S. Díaz, S. Reyes, and S. Piedloup. Transmutation analysis of realistic low–activation steels for magnetic fusion reactors and IFMIF. *Journal of Nuclear Materials*, 367-370:1562, 2007.

[17] M. Rubel. Structure materials in fusion reactors: Issues related to tritium, radioactivity and radiation-induced effects. *Fusion Science and Technology*, 53:459, 2008.

[18] Visit `http://www.iter.org/`.

[19] J. P. Freidberg. Ideal magnetohydrodynamic theory of magnetic fusion systems. *Review of Modern Physics*, 54:801–902, 1982.

[20] H. Wobig and J. Kißlinger. On rotation of collisional plasmas in toroidal systems. *Plasma Physics and Controlled Fusion*, 37:893, 1995.

[21] J. Guasp. Módulo de geometría 3D. Technical report, Ciemat. Laboratorio Nacional de Fusión, 2000.

[22] P. Helander and D. J. Sigmar, *Collisional Transport in Magnetized Plasmas*, Cambridge University Press (2002). ISBN: 0-521-80798-0.

[23] L. Spitzer. The stellarator concept. *Physics of Fluids*, 1(4):253–264, 1958.

[24] P. Helander, C. D. Beidler, T. M. Bird, M. Drevlak, Y. Feng, R. Hatzky, F. Jenko, R. Kleiber, J. H. E. Proll, Y. Turkin, and P. Xanthopoulos. Stellarator and tokamak plasmas: a comparison. *Plasma Physics and Controlled Fusion*, 54(12):124009, 2012.

[25] T. E. Evans *et al.* Suppression of Large Edge-Localized Modes in High-Confinement DIII-D Plasmas with a Stochastic Magnetic Boundary. *Physical Review Letters*, 92:235003, 2004.

[26] M. Hirsch *et al.* Major results from the stellarator Wendelstein 7-AS. *Plasma Physics and Controlled Fusion*, 50(5):053001, 2008.

[27] H. Wobig. Theory of advanced stellarators. *Plasma Physics and Controlled Fusion*, 41(3A):A159, 1999.

[28] D. A. Monticello, R. L. Dewar, H. P. Furth, and A. Reiman. Heliac parameter study. *Physics of Fluids*, 27(5):1248–1252, 1984.

[29] A. Reiman and A. H. Boozer. Island formation and destruction of flux surfaces in three-dimensional mhd equilibria. *Physics of Fluids*, 27(10):2446–2454, 1984.

[30] T. C. Hender *et al.* Studies of a flexible heliac configuration. Oak Ridge National Laboratory Report ORNL/TM-10374, 1987. Available on-line at `http://web.ornl.gov/info/reports/1987/3445602635147.pdf`.

[31] B. A. Carreras, J. L. Cantrell, L. A. Charlton, L. García, J. H. Harris, T. C. Hende, H. R. Hicks, J. A. Holmes, J. A. Rome, and V. E. Lynch. MHD Equilibrium and Stability for Stellarator/Torsatron. Proc. 10th Int. Conf. Plasma Physics and Controlled Nuclear Fusion Research, London, Vol. 2, p. 31, International Atomic Energy Agency, 1984. Available on-line at `http://www.osti.gov/bridge/servlets/purl/6401972-JqAliS/6401972.pdf`.

[32] D. A. Gates and L. Delgado-Aparicio. Origin of tokamak density limit scalings. *Physical Review Letters*, 108:165004, 2012.

[33] P. Helander and A. N. Simakov. Intrinsic ambipolarity and rotation in stellarators. *Physical Review Letters*, 101:145003, 2008.

[34] S. P. Gerhardt, J. N. Talmadge, J. M. Canik, and D. T. Anderson. Measurements and modeling of plasma flow damping in the helically symmetric experiment. *Physics of Plasmas*, 12(5):056116, 2005.

[35] M. J. Landreman. *Electric field and transport in optimized stellarators.* PhD thesis, Department of Physics at the Massachusetts Institute of Technology, 2011, available on-line at `http://www.psfc.mit.edu/library1/catalog/reports/2010/11rr/11rr002/11rr002_full.pdf`.

[36] W. D. D'haesleer, W. N. G. Hitchon, J. D. Callen, and J. L. Shohet. *Flux Coordinate and Magnetic Field Structure: A Guide to a Fundamental Tool of Plasma Theroy.* Springer Series in Computational Physics. Springer-Verlag, 1991.

[37] A. H. Boozer. Quasi-helical symmetry in stellarators. *Plasma Physics and Controlled Fusion*, 37(11A):A103, 1995.

[38] D. A. Spong. Generation and damping of neoclassical plasma flows in stellarators. *Physics of Plasmas*, 12(5):056114, 2005.

[39] M. C. Zarnstorff *et al.* Physics of the compact advanced stellarator NCSX. *Plasma Physics and Controlled Fusion*, 43(12A):A237, 2001.

[40] F. Anderson, A. Almagri, D. Anderson, P. Matthews, J. Talmadge, and J. Shohet. The Helically Symmetric Experiment (HSX): goals, design and status. Fusion Technology, 27:273, 1995.

[41] C. Alejaldre *et al.* First plasmas in the TJ-II flexible heliac. *Plasma Physics and Controlled Fusion*, 41(3A):A539, 1999.

[42] V. I. Vargas, D. López-Bruna, J. Herranz, F. Castejón, and the TJ-II Team. Experimental electron heat diffusion in ECH plasmas of the TJ-II stellarator. *Nuclear Fusion*, 47(9):1367, 2007.

[43] F. Tabarés, D. Tafalla, E. Oyarzabal, A. B. Martín-Rojo, M. A. Ochando, E. Ascasíbar, J. A. Ferreira, A. Vertkovv, and V. Balakirev. Studies of plasma-lithium interactions in TJ-II. 24*th* IAEA Fusion Energy Conference, IAEA CN-197, P5, San Diego, CA, USA, 2012.

[44] J. L. Velasco, K. Allmaier, A. López-Fraguas, C. D. Beidler, H. Maassberg, W. Kernbichler, F. Castejón, and J. A. Jiménez. Calculation of the bootstrap current profile for the TJ-II stellarator. *Plasma Physics and Controlled Fusion*, 53:115014, 2011.

[45] J. L. Velasco and F. Castejón. Study of the neoclassical radial electric field of the TJ-II flexible heliac. *Plasma Physics and Controlled Fusion*, 54:015005, 2012.

[46] J. M. Carmona, K. J. McCarthy, R. Balbín, and S. Petrov. Charge-exchange spectroscopic diagnostic for the TJ-II stellarator. *Review of Scientific Instruments*, 77:10F107, 2006.

[47] K. J. McCarthy, R. Balbín, A. López-Fraguas, A. García, J. M. Carmona, J. Sánchez, and A. A. Ivanov. Diagnostic neutral beam injector and associated diagnostic systems for the TJ–II stellarator device. *Review of Scientific Instruments*, 75(10):3499, 2004.

[48] R.C. Isler. An overview of Charge-Exchange Spectroscopy as a plasma diagnostic. *Plasma Physics and Controlled Fusion*, 36:171, 1994.

[49] I. H. Hutchinson. *Principles of Plasma Diagnostics*. Cambridge University Press; 2 edition, 2002.

[50] Visit `http://fusionwiki.ciemat.es/wiki/{TJ-II}#Diagnostics`.

[51] L. Esteban, M. Sánchez, J. A. López, O. Nieto-Taladriz, and J. Sánchez. Continuous plasma density measurement in TJ-II infrared interferometer-advanced signal processing based on FPGAs. *Fusion Engineering and Design*, 85(3-4):328, 2010.

[52] C. J. Barth, F. J. Pijper, H. J. Meiden, J. Herranz, and I. Pastor. High-resolution multiposition thomson scattering for the TJ-II stellarator. *Review of Scientific Instruments*, 70(1):763–767, 1999.

[53] A. Hidalgo, D. Tafalla, B. Brañas, and F. L. Tabarés. Multipulse supersonic helium beam diagnostic in the TJ-II stellarator. *Review of Scientific Instruments*, 75(10):3478–3480, 2004.

[54] T. Estrada, J. Sánchez, B. van Milligen, L. Cupido, A. Silva, M. E. Manso, and V. Zhuravlev. Density profile measurements by AM reflectometry in TJ-II. *Plasma Physics and Controlled Fusion*, 43(11):1535, 2001.

[55] B. Ph. van Milligen, T. Estrada, E. Ascasíbar, D. Tafalla, D. López-Bruna, A. López Fraguas, J. A. Jiménez, I. García-Cortés, A. Dinklage, and R. Fischer. Integrated data analysis at TJ-II: The density profile. *Review of Scientific Instruments*, 82(7):073503, 2011.

[56] D. Baião, F. Medina, M. Ochando, K. McCarthy, F. Tabarés, I. Pastor, and C. Varandas. Central electron temperature estimations of TJ-II neutral beam injection heated plasmas based on the soft x ray multi-foil technique. *Review of Scientific Instruments*, 83(5):053501, 2012.

[57] D. Baião, F. Medina, M. A. Ochando, C. Varandas, A. Molinero, and J. Chércoles. Implementation of multifilter based twin-prototypes for core electron temperature measurements in the TJ-II stellarator. *Review of Scientific Instruments*, 81(10):10D711, 2010.

[58] J. M. Fontdecaba, I. Pastor, J. Arévalo, J. Herranz, K. J. McCarthy, and G. Sáchez Burillo. Comparisons of the electron temperature and density, and ion temperature profiles in the TJ-II stellarator. *Plasma and Fusion Research*, 5:S2085, 2010.

[59] J. Arévalo, K. J. McCarthy, J. M. Carmona, and J. M. Fontdecaba. Impurity temperature correction factors for the transmission grating spectrometer in the TJ-II stellarator. *Review of Scientific Instruments*, 81(10):10D705, 2010.

[60] E. Ascasíbar *et al.* Energy content and magnetic configuration scan in TJ-II plasmas. In proceedings of the 12*th* International Stellarator Workshop (1999).

[61] M. A. Ochando *et al.* Up-down and in-out asymmetry monitoring based on broadband radiation detectors. *Fusion Science and Technology*, 50(2), 2006.

[62] K. J. McCarthy, M. A. Ochando, F. Medina, B. Zurro, C. Hidalgo, M. A. Pedrosa, I. Pastor, J. A. Herranz, and A. Baciero. A first study of impurity behavior during externally induced radial electric fields in the TJ-II stellarator. *Fusion Science and Technology*, 46(1), 2003.

[63] D. Tafalla *et al.* Monitores de H_α para TJ-II. Informe Técnico Ciemat 850. Madrid (1998).

[64] A. Baciero, B. Zurro, K. J. McCarthy, C. Burgos, and V. Tribaldos. A multi-channel spectroscopic system for measuring impurity ion temperatures and poloidal rotation velocities in TJ-II. *Review of Scientific Instruments*, 72(1):971–974, 2001.

[65] D. Rapisarda, B. Zurro, A. Baciero, and V. Tribaldos. Novel passive spectroscopy system for absolutely referenced plasma rotation measurements in clean plasmas. *Review of Scientific Instruments*, 77(3):033506, 2006.

[66] A. Chmyga *et al. Proc. 29th EPS Conf. (Montreux)* vol 26B (ECA), p O1.09, 2002.

[67] T. Happel, T. Estrada, E. Blanco, V. Tribaldos, A. Cappa, and A. Bustos. Doppler reflectometer system in the stellarator TJ-II. *Review of Scientific Instruments*, 80(7):073502, 2009.

[68] F. Tabarés, D. Tafalla, B. Brañas, E. de la Cal, and the TJ-II Team. Plasma-wall interaction in the Spanish stellarator TJ-II. diagnostics and first results. J. Nucl. Mater., 266-269: 1273, 1999.

[69] F. Tabarés, D. Tafalla, R. Balbín, B. Brañas, T. Estrada, I. García-Cortés, F. Medina, and M. A. Ochando. Impact of wall conditioning and gas fuelling on the enhanced confinement modes in TJ-II. J. Nucl. Mater., 313-316: 839, 2003.

[70] F. L. Tabarés *et al.* Plasma performance and confinement in the TJ-II stellarator with lithium-coated walls. *Plasma Physics and Controlled Fusion*, 50(12):124051, 2008.

[71] J. Sánchez *et al.* Confinement transitions in the TJ-II under Li-coated wall conditions. *Nuclear Fusion*, 49:104018, 2009.

[72] T. Estrada *et al.* Sheared flows and transition to improved confinement regime in the TJ-II stellarator. *Plasma Physics and Controlled Fusion*, 51(12):124015, 2009.

[73] J. Sánchez *et al.* Overview of TJ-II experiments. *Nuclear Fusion*, 51(9):094022, 2011.

[74] J. Sánchez *et al.* Dynamics of flows and confinement in the TJ-II stellarator. *Nuclear Fusion*, 53:104016, 2013.

[75] F.L. Tabarés, M. Ochando, D. Tafalla, F. Medina, K. McCarthy, J. M. Fontdecaba, M. Liniers, J. Guasp, E. Ascasíbar, T. Estrada, I. Pastor, and TJ-II Team. Energy and particle balance studies under full boron and lithium-coated walls in TJ-II. *Contributions to Plasma Physics*, 50(6-7):610–615, 2010.

[76] M. A. Ochando, T. Tabarés, D. Tafalla, F. Medina, I. Pastor, D. Baião, M. Liniers, E. Ascasíbar, T. Estrada, D. López-Bruna, and TJ-II Team. Nitrogen-injection effects on NBI heated TJ-II plasma profiles under Li wall conditions: impurity screening and role of rational surfaces. Poster in the $37th$ European Conference on Plasma Physics, Dublin, Ireland. Available online at http://ocs.ciemat.es/EPS2010PAP/pdf/P1.1075.pdf, 2010.

[77] M. A. Ochando, F. Castejon, and A. P. Navarro. An interpretation of low radiation collapses in stellarator plasmas. *Nuclear Fusion*, 37(2):225, 1997.

[78] C. Hidalgo, M. A. Pedrosa, L. García, and A. Ware. Experimental evidence of coupling between sheared-flow development and an increase in the level of turbulence in the TJ-II stellarator. *Physical Review E*, 70:067402, 2004.

[79] B. Ph. van Milligen, M. A. Pedrosa, C. Hidalgo, B. A. Carreras, T. Estrada, J. A. Alonso, J. L. de Pablos, A. Melnikov, L. Krupnik, L. G. Eliseev, and S. V. Perfilov. The dynamics of the formation of the edge particle transport barrier at TJ-II. *Nuclear Fusion*, 51(11):113002.

[80] M. A. Pedrosa, C. Hidalgo, E. Calderón, T. Estrada, A. Fernández, J. Herranz, I. Pastor, and the TJ-II team. Threshold for sheared flow and turbulence development in the TJ-II stellarator. *Plasma Physics and Controlled Fusion*, 47(6):777, 2005.

[81] T. Happel, T. Estrada, and C. Hidalgo. First experimental observation of a two-step process in the development of the edge velocity shear layer in a fusion plasma. *Europhysics Letters*, 84(6):65001, 2008.

[82] M. A. Pedrosa, C. Silva, C. Hidalgo, B. A. Carreras, R. O. Orozco, and D. Carralero. Evidence of long-distance correlation of fluctuations during edge transitions to improved-confinement regimes in the TJ-II stellarator. *Physical Review Letters*, 100:215003, 2008.

[83] C. Hidalgo, M. A. Pedrosa, C. Silva, D. Carralero, E. Ascasíbar, B. A. Carreras, T. Estrada, F. Tabarés, D. Tafalla, J. Guasp, M. Liniers, A. López-Fraguas, B. van Milligen, and M. A. Ochando. Multi-scale physics mechanisms and spontaneous edge transport bifurcations in fusion plasmas. *Europhysics Letters*, 87(5):55002, 2009.

[84] J. A. Alonso, J. L.Velasco, J. Arévalo, C. Hidalgo, M. A. Pedrosa, B. Ph. Van Milligen, and D. Carralero. Dynamics of zonal flow-like structures in the edge of the TJ-II stellarator. *Plasma Physics and Controlled Fusion*, 55:014001, 2013.

[85] T. Estrada, C. Hidalgo, T. Happel, and P. H. Diamond. Spatiotemporal Structure of the Interaction between Turbulence and Flows at the L-H Transition in a Toroidal Plasma. *Physical Review Letters*, 107:245004, 2011.

[86] C. Hidalgo, C. Silva, B. A. Carreras, B. van Milligen, H. Figueiredo, L. García, M. A. Pedrosa, B. Gonçalves, and A. Alonso. Dynamical coupling between gradients and transport in fusion plasmas. *Physical Review Letters*, 108:065001, 2012.

[87] J. L. Velasco, J. A. Alonso, I. Calvo, and J. Arévalo. Vanishing neoclassical viscosity and physics of the shear layer in stellarators. *Physical Review Letters*, 109:135003, 2012.

[88] P. W. Terry. Suppression of turbulence and transport by sheared flow. *Review of Modern Physics*, 72:109–165, 2000.

[89] E. J. Doyle *et al.* Progress in the ITER Physics Basis Chapter 2: Plasma confinement and transport. *Nuclear Fusion*, 47:S18, 2007.

[90] F. L. Hinton and R. D. Hazeltine. Theory of plasma transport in toroidal confinement systems. *Review of Modern Physics*, 48(2):239, 1976.

[91] A. Dinklage *et al.* Inter-machine validation study of neoclassical transport modelling in medium- to high-density stellarator-heliotron plasmas. *Nuclear Fusion*, 53(6):063022, 2013.

[92] S. P. Hirshman and D. J. Sigmar. Neoclassical transport of impurities in tokamak plasmas. *Nuclear Fusion*, 21(9):1079, 1981.

[93] H. Sugama and S. Nishimura. How to calculate the neoclassical viscosity, diffusion, and current coefficients in general toroidal plasmas. *Physics of Plasmas*, 9(11):4637–4653, 2002.

[94] R. D. Hazeltine. Recursive derivation of drift-kinetic equation. *Plasma Physics*, 15(1):77, 1973.

[95] S. P. Hirshman, K. C. Shaing, W. I. van Rij, C. O. Beasley, and E. C. Crume. Plasma transport coefficients for nonsymmetric toroidal confinement systems. *Physics of Fluids*, 29(9):2951–2959, 1986.

[96] J. L. Velasco, J. Arévalo, and J. A. Alonso. Configuration dependence of the the neoclassical viscosity at TJ-II. Poster in 14*th* European Fusion Theory Conference. Frascati, Italy, 2011. Available on-line at `http://www.fusione.enea.it/EVENTS/eventifiles/EFTC14-2011/Posters/PRESENTAZIONIPOSTER/velasco.pdf`.

[97] K. C. Shaing and J. D. Callen. Neoclassical flows and transport in nonaxisymmetric toroidal plasmas. *Physics of Fluids*, 26:3315, 1983.

[98] M. Coronado and H. Wobig. Parallel and toroidal viscosity for nonaxisymmetric toroidal plasmas in the plateau regime. *Physics of Fluids*, 29(2):527–530, 1986.

[99] K. C. Shaing, S. P. Hirshman, and J. D. Callen. Neoclassical transport fluxes in the plateau regime in nonaxisymmetric toroidal plasmas. *Physics of Fluids*, 29:521, 1986.

[100] P. Helander. Bifurcated neoclassical particle transport. *Physics of Plasmas*, 5(11):3999–4004, 1998.

[101] A. J. H. Donné *et al.* *Nuclear Fusion*, 47:S337, 2007.

[102] S. Braun and P. Helander. Pfirsch–Schlüter impurity transport in stellarator edge plasmas with large radial gradients. *Journal of Physics: Conference Series*, 260(1):012004, 2010.

[103] D. Rapisarda, B. Zurro, A. Baciero, V. Tribaldos, E. Ascasíbar, and the TJ-II Team. An investigation of the relationship between toroidal rotation and bootstrap current in the TJ-II stellarator. In *European Pysical Society Conf. on Plasma Physics, Tarragona (Spain).*, 2005.

[104] B. Zurro, A. Baciero, D. Rapisarda, V. Tribaldos, and the TJ-II Team. Comparison of impurity poloidal rotation in ECRH and NBI discharges of the TJ-II HELIAC. *Fusion Science and Technology*, 50(3):419, 2006.

[105] J. Arévalo, J. A. Alonso, K. J. McCarthy, and J. L. Velasco. Incompressibility of impurity flows in low density TJ-II plasmas and comparison with neoclassical theory. *Nuclear Fusion*, 53(2):023003, 2013.

[106] A. N. Simakov and P. Helander. Neoclassical momentum transport in a collisional stellarator and a rippled tokamak. *Physics of Plasmas*, 16(4):042503, 2009.

[107] V. Tribaldos. Monte carlo estimation of neoclassical transport for the TJ-II stellarator. *Physics of Plasmas*, 8(4):1229–1239, 2001.

[108] Y. Turkin, C. D. Beidler, H. Maaßberg, S. Murakami, V. Tribaldos, and A. Wakasa. Neoclassical transport simulations for stellarators. *Physics of Plasmas*, 18(2):022505, 2011.

[109] T. Happel. *Doppler Reflectometry in the TJ-II Stellarator: Design of an Optimized Doppler Reflectometer and its Application to Turbulence and Radial Electric Field Studies*. PhD thesis, Universidad Carlos III de Madrid, Departamento de Físicas, 2010.

[110] S. Hamada. Hydromagnetic equilibria and their proper coordinates. *Nuclear Fusion*, 2(1-2):23, 1962.

[111] M. Coronado and J. N. Talmadge. Evolution of the plasma rotation and the radial electric field for a toroidal plasma in the Pfirsch-Schlüter and plateau regimes subject to a biased electrode. *Physics of Plasmas*, 5(4):1200–1212, 1993.

[112] P. J. Catto and A. N. Simakov. A drift ordered short mean free path description for magnetized plasma allowing strong spatial anisotropy. *Physics of Plasmas*, 11(1):90–102, 2004.

[113] H. Wobig and J. Kißlinger. Viscous damping of rotation in Wendelstein 7-AS. *Plasma Physics and Contol Fusion*, 42:823, 2000.

[114] S. P. Gerhardt, D. T. Anderson, and J. N. Talmadge. Calculations of neoclassical viscous damping on flux surfaces near magnetic islands in the helically symmetric experiment. *Physics of Plasmas*, 12(1):012504, 2005.

[115] J. L. Velasco, J. Arévalo, and J. A. Alonso. Configuration dependence of the the neoclassical viscosity at TJ-II. Poster in the 18*th* International Stellarator/Heliotron Workshop, Australia. Available online at `http://www-fusion.ciemat.es/Jose_Luis_Velasco/presentations/velasco_etal_visco_ISHW2012.pdf`, 2012.

[116] J. L. Velasco, J. A. Alonso, J. Arévalo, and A. López-Fraguas. Extended calculations of neoclassical viscosity for TJ-II. Poster in the 39*th* European Conference on Plasma Physics, Stockholm, Sweden, 2012. Available on-line at `http://ocs.ciemat.es/epsicpp2012pap/pdf/P4.014.pdf`.

[117] H. Sugama and S. Nishimura. Moment-equation methods for calculating neoclassical transport coefficients in general toroidal plasmas. *Physics of Plasmas*, 15(4):042502, 2008.

[118] H. Sugama and W. Horton. Entropy production and onsager symmetry in neoclassical transport processes of toroidal plasmas. *Physics of Plasmas*, 3(1):304–322, 1996.

[119] K. C. Shaing and D. A. Spong. Extending the collisional fluid equations into the long mean-free-path regime in toroidal plasmas. i. plasma viscosity. *Physics of Fluids B: Plasma Physics*, 2(6):1190–1194, 1990.

[120] K. C. Shaing. Poloidal and parallel plasma viscosities in tokamak geometry. *Physics of Fluids B: Plasma Physics*, 2(11):2847–2849, 1990.

[121] K. C. Shaing. Test of tokamak low-mode–high-mode transition theory in stellarators. *Physics of Fluids B: Plasma Physics*, 5(11):3841–3843, 1993.

[122] K. C. Shaing and E. C. Crume. Bifurcation theory of poloidal rotation in tokamaks: A model for L - H transition. *Physical Review Letters*, 63:2369–2372, 1989.

[123] K. C. Shaing. Theory of high-mode phenomena for stellarators. *Physical Review Letters*, 76:4364–4367, 1996.

[124] S. Satake, H. Takahashi, M. Yokoyama, T. Ido, A. Shimizu, S. Matsuoka, H. Sugama, R. Kanno and S. Kitajima. Simulation study on neoclassical poloidal viscosity in the Large Helical Device. *Submitted to Physics of Plasmas*, 2013.

[125] C. T. Hsu, K. C. Shaing, and R. Gormley. Time dependent parallel viscosity and relaxation rate of poloidal rotation in the banana regime. *Physics of Plasmas*, 1(1):132–138, 1994.

[126] K. C. Shaing. Time-dependent plasma viscosity in asymmetric toroidal plasmas. *Physics of Plasmas*, 13(5):052505, 2006.

[127] J. A. Alonso and J. L. Velasco. Equilibrium Flows and Neoclassical Viscosity in a Magnetically Confined Toroidal Plasma. Basic Theory and a Experimental Proposal for TJ-II. *Physics Meetings in TJ-II*, 2010. Available on-line at `http://www-fusion.ciemat.es/fileshare/grupo_de_fisica/Reuniones_grupo_Fisica/2010/09_27/ViscosityMeasure-GrupoFisica.pdf`.

[128] M. A. Pedrosa, B. A. Carreras, C. Hidalgo, C. Silva, M. Hron, L. García, J. A. Alonso, I. Calvo, J. L. de Pablos, and J. Stöckel. Sheared flows and turbulence in fusion plasmas. *Plasma Physics and Controlled Fusion*, 49(12B):B303, 2007.

[129] J. N. Talmadge and S. P. Gerhardt. Numerical calculation of the Hamada basis vectors for three-dimensional toroidal magnetic configurations. *Physics of Plasmas*, 12(7):072513, 2005.

[130] S. P. Gerhardt, J. M. Canik, D. T. Anderson, and L. Owen. H_α detector system for the Helically Symmetric Experiment. *Review of Scientific Instruments*, 75(9):2981–2984, 2004.

[131] T. W. Versloot *et al.* Momentum losses by charge exchange with neutral particles in H-mode discharges at JET. *Plasma Physics and Controlled Fusion*, 53(6):065017, 2011.

[132] IAEA Databases on Atomic and Molecular Data for Fusion, ALADDIN at `http://www-amdis.iaea.org/ALADDIN/collision.html`.

[133] J. M. Fontdecaba, F. Castejón, R. Balbín, D. López-Bruna, S.Y. Petrov, F. Albajar, G. Cortés, J. Dies, J. García, J. Izquierdo, and J. Fontanet. Energy-resolved neutral particle fluxes in TJ-II ECRH plasmas. *Fusion Science and Technology*, 46(2):271, 2004.

[134] J. Guasp, EIRENE code calculations for the CX spectra in the TJ-II Stellarator, Ciemat (2007). Available on-line at `http://www.eirene.de/html/recent_reports.html`.

[135] A. Bustos, J. M. Fontdecaba, F. Castejón, J. L. Velasco, M. Tereshchenko, and J. Arévalo. Studies of the fast ion energy spectra in TJ-II. *Physics of Plasmas*, 20(2):022507, 2013.

[136] E. de la Cal, J. Guasp, A. Salas, D. Reiter, P. Börner, J. A. Alonso, R. Balbín, D. Carralero, C. Hidalgo, J. L. de Pablos, F. L. Tabarés, D. Tafalla, and the TJ-II Team. Spatially resolved H_α-emission simulation with EIRENE in TJ-II to study hydrogen atomic and molecular physics in low density, high temperature fusion edge plasmas. *Nuclear Fusion*, 48(9):095005, 2008.

[137] C. D. Beidler and H. Maaßberg. Implications of the quasi-neutrality condition for neoclassical transport in stellarators. 15th International Stellarator Workshop, Madrid, 2005.

[138] J. M. García-Regaña, R. Kleiber, C. D. Beidler, Y. Turkin, H. Maaßberg, and P. Helander. On neoclassical impurity transport in stellarator geometry. *Plasma Physics and Controlled Fusion*, 55(7):074008, 2013.

[139] M. L. Reinke, I. H. Hutchinson, J. E. Rice, N. T. Howard, A. Bader, S. Wukitch, Y. Lin, D. C. Pace, A. Hubbard, J. W. Hughes, and Y. Podpaly. Poloidal variation of high–Z impurity density due to hydrogen minority ion cyclotron resonance heating on Alcator C-Mod. *Plasma Physics and Controlled Fusion*, 54(4):045004, 2012.

[140] K. D. Marr, B. Lipschultz, P. J. Catto, R. M. McDermott, M. L. Reinke, and A. N. Simakov. Comparison of neoclassical predictions with measured flows and evaluation of a poloidal impurity density asymmetry. *Plasma Physics and Controlled Fusion*, 52(5):055010, 2010.

[141] T. Pütterich, E. Viezzer, R. Dux, R.M. McDermott, and the ASDEX Upgrade Team. Poloidal asymmetry of parallel rotation measured in ASDEX Upgrade. *Nuclear Fusion*, 52(8):083013, 2012.

[142] E. Viezzer, T. Pütterich, E. Fable, A. Bergmann, R Dux, R. M. McDermott, R. M. Churchill, M. G. Dunne, and the ASDEX Upgrade Team. Rotation and density asymmetries in the presence of large poloidal impurity flows in the edge pedestal. *EPS Conf. on Plasma Phys., Helsinki (Finland)*, 2013. Available on-line at `http://ocs.ciemat.es/EPS2013ABS/pdf/I4.112.pdf`.

[143] R. M. Churchill, B. Lipschultz, C. Theiler, J. W. Hughes, and the Alcator C-Mod team. Poloidal flows and in-out impurity density asymmetries in the pedestal region. Oral contribution in the APS Conf. on Plasma Physics, 2012. Available on-line at `https://www.psfc.mit.edu/research/alcator/pubs/APS/APS2012/Churchill_APS2012_cont-oral.pdf`.

[144] R. M. Churchill, B. Lipschultz, C. Theiler, J. W. Hughes, and the Alcator C-Mod team. Poloidal flows and in-out impurity density asymmetries in the pedestal region. Poster presented in the US-EU Transport Task force Workshop, Santa Rosa, California, 2013. Available on-line at `http://www.psfc.mit.edu/research/alcator/pubs/TTF/pdf2013/Churchill_TTF2013_poster.pdf`.

[145] S. Nishimura, K. Ida, M. Osakabe, T. Minami, K. Tanaka, and the CHS Group. Inboard/outboard asymmetry of poloidal flow observed in the Compact Helical System. *Physics of Plasmas*, 7(2):437–440, 2000.

[146] M. Landreman, T. Fülöp, and D. Guszejnov. Impurity flows and plateau-regime poloidal density variation in a tokamak pedestal. *Physics of Plasmas*, 18(9):092507, 2011.

[147] S. Nishimura, H. Sugama, H. Maaßberg, C. D. Beidler, S. Murakami, Y. Nakamura, and S. Hirooka. Erratum: "A convergence study for the Laguerre expansion in the moment equation method for neoclassical transport in general toroidal plasmas" [Phys. Plasmas [bold 17], 082510 (2010)]. *Physics of Plasmas*, 18(6):069901, 2011.

[148] S. Braun and P. Helander. Pfirsch–schl[u-umlaut]ter impurity transport in stellarators. *Physics of Plasmas*, 17(7):072514, 2010.

[149] N. J. Peacock, D. C. Robinson, M. J. Forrest, P. D. Wilcock, and V. V. Sannikov. Measurement of the electron temperature by Thomson Scattering in tokamak T3. *Nature*, 224:488–490, 1969.

[150] R. C. Isler. Observation of the reaction $H^0 + O^{8+} \rightarrow H^+ + O^{7+}$ during Neutral-Beam Injection into ORMAK. *Physical Review Letters*, 38:1359–1362, 1977.

[151] R. C. Isler, L. E. Murray, S. Kasai, J. L. Dunlap, S. C. Bates, P. H. Edmonds, E. A. Lazarus, C. H. Ma, and M. Murakami. Charge-exchange excitation and recombination of oxygen in the ISX-B tokamak. *Physical Review A*, 24(5):2701, 1981.

[152] R. J. Fonck, R. J. Goldston, and D. E. Post. Plasma ion temperature measurements via charge exchange recombination radiation. *Applied Physical Letter*, 42(3):239, 1983.

[153] R. J. Fonck, D. S. Darrow, and K. P. Jaehnig. Determination of plasma-ion velocity distribution via charge-exchange recombination spectroscopy. *Physical Review A*, 29(6), 1984.

[154] http://www.efda.org/glossary/charge-exchange-recombination-spectroscopy-cxrs.

[155] R. E. Bell and E. J. Synakowski. New understanding of poloidal rotation measurements in a tokamak plasma. *AIP Conference Proceedings*, 547(1):39–52, 2000.

[156] M. von Hellermann, P. Breger, J. Frieling, R. König, W. Mandl, A. Maas, and H.P. Summers. Analytical approximation of cross-section effects on charge exchange spectra observed in hot fusion plasmas. *Plasma Physics and Controlled Fusion*, 37:71, 1995.

[157] D. D. Ryutov. Erratum: "Simple theory of the line emission profile for the charge-exchange recombination spectroscopy method" [Phys. Plasmas [bold 7], 1315 (2000)]. *Physics of Plasmas*, 11(3):1244–1244, 2004.

[158] D. M. Thomas. Beams, brightness, and background: Using active spectroscopy techniques for precision measurements in fusion plasma research. *Physics of Plasmas*, 19(5):056118, 2012.

[159] J. M. Carmona. *Caracterización y Análisis de Iones en Plasmas de TJ-II mediante Espectroscopía Activa de Recombinación por Intercambio de Carga*. PhD thesis, Universidad Complutense de Madrid, Facultad de Ciencias Físicas, 2008.

[160] K. Crombé, Y. Andrew, C. Giroud, N. C. Hawkes, A. Murari, M. Valisa, G. Van Oost, K. D. Zastrow, and JET-EDFA Contributors. Calibration of the charge exchange recombination spectroscopy diagnostic for core poloidal rotation velocity measurements on JET. *Review of Scientific Instruments*, 75(10):3452, 2004.

[161] W. M. Solomon, K. H. Burrell, R. Feder, A. Nagy, P. Gohil, and R. J. Groebner. Characterization of cross-section correction to charge exchange recombination spectroscopy rotation measurements using co- and counter-neutral-beam views. *Review of Scientific Instruments*, 79(10):10F531, 2008.

[162] E. Viezzer, T. Pütterich, R. Dux, R. M. McDermott, and the ASDEX Upgrade Team. High-resolution charge exchange measurements at ASDEX Upgrade. *Review of Scientific Instruments*, 83(10):103501, 2012.

[163] I. O. Bespamyatnov, W. L. Rowan, and R. S. Granetz. Compact, accurate description of diagnostic neutral beam propagation and attenuation in a high temperature plasma for charge exchange recombination spectroscopy analysis. *Review of Scientific Instruments*, 79(10):10F315, 2008.

[164] A. Briesemeister, K. Zhai, D. T. Anderson, F. S. B. Anderson, and J. N. Talmadge. Comparison of the flows and radial electric field in the HSX stellarator to neoclassical calculations. *Plasma Physics and Controlled Fusion*, 55(1):014002, 2013.

[165] A. Bortolon, Y. Camenen, A. N. Karpushov, B. P. Duval, Y. Andrebe, L. Federspiel, O. Sauter, and the TCV Team. Indirect measurement of poloidal rotation using inboard−outboard asymmetry of toroidal rotation and comparison with neoclassical predictions. *Nuclear Fusion*, 53(2):023002, 2013.

[166] R. E. Bell and R. Feder. Measurement of poloidal velocity on the national spherical torus experiment. *Review of Scientific Instruments*, 81(10):10D724, 2010.

[167] T. Pütterich, E. Viezzer, R. Dux, R.M. McDermott, and the ASDEX Upgrade Team. Poloidal asymmetry of parallel rotation measured in asdex upgrade. *Nuclear Fusion*, 52(8):083013, 2012.

[168] C. Chrystal, K. H. Burrell, B. A. Grierson, R. J. Groebner, and D. H. Kaplan. Calculation of impurity poloidal rotation from measured poloidal asymmetries in the toroidal rotation of a tokamak plasma. *Review of Scientific Instruments*, 83(10):10D501, 2012.

[169] R. E. Bell. Exploiting a transmission grating spectrometer. *Review of Scientific Instruments*, 75(10):4158, 2004.

[170] R. E. Bell, L. E. Dudek, B. Grek, D. W. Johnson, and R. W. Palladino. Tokamak fusion test reactor poloidal rotation diagnostic. *Review of Scientific Instruments*, 70(1):821, 1999.

[171] W. L. Rowan, I. O. Bespamyatnov, and R. S. Granetz. Wide-view charge exchange recombination spectroscopy diagnostic for Alcator C-Mod. *Review of Scientific Instruments*, 79(10):10F529, 2008.

[172] A. Varias, C. Alejaldre, A.L. Fraguas, L. Garcia, B.A. Carreras, N. Dominguez, and V.E. Lynch. Ideal Mercier stability for the TJ-II flexible Heliac. *Nuclear Fusion*, 30(12):2597, 1990.

[173] H. P. Summers. Atomic data and analysis structure. Technical Report 06, JET, 1994.

[174] A. A. Ivanov, V. I. Davydenko, P. P. Deichuli, A. Kreter, V. V. Mishagin, A. A. Podminogin, I. V. Shikhovtsev, B. Schweer, and R. Uhlemann. Radio frequency ion source for plasma diagnostics in magnetic fusion experiments. *Review of Scientific Instruments*, 71(10):3728–3735, 2000.

[175] B. H. Bransden and C. J. Joachain, *Physics of atoms and molecules*, Longman Scientific & Technical (1990), ISBN: 0-582-44401-2.

[176] H. A. Bethe and E. E. Salpeter, *Quantum Mechanics of one- and two-electron atoms*, Dover Publications (2013), ISBN:0-486-46667-1.

[177] D. Rapisarda. *Estudio de la dinámica de iones por métodos espectroscópicos en el TJ-II*. PhD thesis, Universidad Complutense de Madrid, Facultad de Ciencias Físicas, 2006.

[178] R. P. Schorn, E. Wolfrum, F. Aumayr, E. Hintz, D. Rusbüldt, and H. Winter. Radial temperature distribution of C^{6+} ions in the TEXTOR edge plasma measured with lithium beam activated charge exchange spectroscopy. *Nuclear Fusion*, 32(3):351, 1992.

[179] A. Blom and C. Jupén. Parametrization of the Zeeman effect for hydrogen-like spectra in high-temperature plasmas. *Plasma Physics and Controlled Fusion*, 44(7):1229, 2002.

[180] P. G. Carolan, M. J. Forrest, N. J. Peacock, and D. L. Trotman. Observation of Zeeman spliting of spectral lines from the JET plasma. *Plasma Physics and Controlled Fusion*, 27(10):1101, 1985.

[181] R. E. Bell, R. Andre, S. M. Kaye, R. A. Kolesnikov, B. P. LeBlanc, G. Rewoldt, W. X. Wang, and S. A. Sabbagh. Comparison of poloidal velocity measurements to neoclassical theory on the national spherical torus experiment. *Physics of Plasmas*, 17(8):082507, 2010.

[182] NIST Atomic Spectra Databases at http://www.nist.gov.

[183] http://www.mathworks.es/es/help/matlab/ref/conv.html.

[184] I. O. Bespamyatnov. *Impurity Transport Studies on Alcator C-Mod Tokamak Using Charge Exchange Recombination Spectroscopy*. PhD thesis, Univeristy of Texas at Austin, 2008.

[185] J. M. Carmona, K. J. McCarthy, V. Tribaldos, and R. Balbín. Density dependece of ion temperature measured by active charge-exchange spectroscopy in ECRH plasmas of the TJ-II stellarator. *Fusion Science and Technology*, 54:962, 2008.

[186] R. M. Pengelly and M. J.Seaton. Recombination spectra: II. collisional transitions between states of degenerate energy levels. *Monthly Notices of the Royal Astronomical Society*, 127:165, 1964.

[187] J. Spence and H. P. Summers. The recombination and level populations of ions: III. the role of charge exchange from neutral hydrogen. *Journal of Physics B: Atomic and Molecular Physics*, 19:3749, 1986.

[188] D. H. Sampson. On statistical equilibrium among the sublevels of hydrogenic atoms and ions. *Journal of Physics B: Atomic and Molecular Physics*, 10(4), 1977.

[189] D. Hoang-Binh. A program to compute exact hydrogenic radial integrals, oscillator strengths, and Einstein coefficients, for principal quantum numbers up to n≈1000. *Computer Physics Communications*, 166, 2005.

[190] K. P. Birch and M. J. Downs. An updated Edlén equation for the refractive index of air. *Metrologia*, 30, 1993.

[191] K. P. Birch and M. J. Downs. Correction to the updated Edlén equation for the refractive index of air. *Metrologia*, 31(4):315, 1994.

[192] J. A. García and J. E. Mack. Energy level and line tables for one-electron atomic spectra. *Journal of the Optical Society of America*, 55(6):654, 1965.

[193] P. Gohil, K. H. Burrell, R. J. Groebner, K. Holtrop, D. H. Kaplan, and P. Monier-Garbet. Wavelength calibration of the charge exchange recombination spectroscopy system on the DIII-D tokamak. *Review of Scientific Instruments*, 70(1):878, 1999.

[194] K. Ida, S. Kado, and Y. Liang. Measurements of poloidal rotation velocity using charge exchange spectroscopy in a large helical device. *Review of Scienctific Instruments*, 71(6), 2000.

[195] J. W. Coenen, B. Schweer, M. Cleverand, S. Freutel, O. Schmitz, H. Stoschus, U. Samm, and B. Unterberg. Charge exchange recombination spectroscopy on a diagnostic hydrogen beam measuring impurity rotation and radial electric field at the tokamak Textor. *Journal of Physics B: Atomic, Molecular and Optical Physics*, 43(14):144015, 2010.

[196] B. J. Ding, Y. Sakamoto, and Y. Miura. Modification to poloidal charge exchange recombination spectroscopy measurement in JT-60U tokamak. *Chinese Physics*, 16(11):3434, 2007.

[197] W. M. Solomon, K. H. Burrell, P. Gohil, R. J. Groebner, and L. R. Baylor. Extraction of poloidal velocity from charge exchange recombination spectroscopy measurements. *Review of Scientific Instruments*, 75(10):3481–3486, 2004.

[198] B. J. Ding, Y. Sakamoto, and Y. Miura. Simulated correction to poloidal charge-exchange recombination spectroscopy measurement in a tokamak. *Plasma Physics and Controlled Fusion*, 47(6):789, 2005.

[199] A. R. Field, G. Fussmann, and J. V. Hofmann. Measurement of the radial electric field in the ASDEX tokamak. *Nuclear Fusion*, 32(7):1191, 1992.

[200] J. Fu, Y. Shi, Y. Li, F. Wang, S. Liu, Ji. Zhang, J. Li, Y. Huang, Y. Xie, Z. Liu, C. Hu, B. Wan, and DNB Team. Spectroscopic determination of the species fractions and the power profiles of the diagnostic neutral beam on the HT-7 tokamak. *J. Korean Phys. Soc.*, 58:1141, 2011.

[201] W. M. Solomon, K. H. Burrell, R. Andre, L. R. Baylor, R. Budny, P. Gohil, R. J. Groebner, C. T. Holcomb, W. A. Houlberg, and M. R. Wade. Experimental test of the neoclassical theory of impurity poloidal rotation in tokamaks. *Physics of Plasmas*, 13(1):056116, 2006.

[202] D. Hoang-Binh. A program to compute exact hydrogenic radial integrals, oscillator strengths, and einstein coefficients, for principal quantum numbers up to n $\approx$ 1000. *Computer Physics Comunications*, 166:191, 2005.

[203] D. Rapisarda, B. Zurro, V. Tribaldos, and A. Baciero. The role of fast ion component on the heating of the plasma bulk. *Plasma Physics and Controlled Fusion*, 49(3):309, 2007.

[204] F. Wagner. Neutral particle diagnostics for ohmically and auxiliary heated tokamaks. *Journal of Vacuum Science and Technology*, 20(4):1211, 1982.

[205] J. Arévalo, K. McCarthy, J. M. Fontdecaba, and B. Van Milligen. The ion energy distribution function in anistropic plasmas as viewed by charge-exchange based diagnostics in the TJ-II stellarator. In *European Pysical Society Conf. on Plasma Physics, Dublin (Ireland)*, 2010. Available on-line at `http://ocs.ciemat.es/EPS2010PAP/pdf/P5.196.pdf`.

[206] J. Arévalo. Comparison between main ion and impurity temperatures in the TJ-II stellarator. Master Thesis Essay presented in Universidad Carlos III de Madrid, 2010.

[207] Fontdecaba J. M., Petrov S., and Montreal P. Using the Double code to improve ion temperature calculations for the TJ-II stellarator. In *European Pysical Society Conf. on Plasma Physics, Stockholm (Sweden)*, 2012. Available on-line at `http://labfus.ciemat.es/AR/2012/CAP2/npa_1.pdf`.

[208] J. Herranz, F. Castejón, I. Pastor, and K. J. McCarthy. The spectrometer of the high-resolution multiposition Thomson Scattering diagnostic for the TJ-II. *Fusion Engineering and Design*, 65(4):525, 2003.

[209] J. Arévalo, J. A. Alonso, K. J. McCarthy, J. L. Velasco, J. M. Regaña, and M. Landreman. Compressible impurity flow in the TJ-II stellarator. *Nuclear Fusion*, Accepted.

[210] R. E. Bell, F. M. Levinton, S. H. Batha, E. J. Synakowski, and M. C. Zarnstorff. Poloidal rotation in TFTR reversed shear plasmas. *Physical Review Letters*, 81:1429–1432, 1998.

[211] A. R. Field, J. McCone, N. J. Conway, M. Dunstan, S. Newton, and M. Wisse. Comparison of measured poloidal rotation in MAST spherical tokamak plasmas with neo-classical predictions. *Plasma Physics and Controlled Fusion*, 51:105002, 2009.

[212] G. Kagan, K. D. Marr, P. J. Catto, M. Landerman, B. Lipschultz, and R. McDermott. The effect of the radial electric field on neoclassical flows in a tokamak pedestal. *Plasma Physics and Controlled Fusion*, 53:025008, 2011.

[213] E. Viezzer, T. Pütterich, C. Angioni, A. Bergmann, G. D. Conway, R. Dux, E. Fable, T. Happel, R. M. McDermott, W. Suttrop, E. Wolfrum, and the ASDEX Upgrade Team. Investigations on the edge radial electric field at ASDEX Upgrade. *EPS Conf. on Plasma Phys., Stockholm (Sweden)*, 2012. Available on-line at `http://ocs.ciemat.es/epsicpp2012pap/pdf/O5.118.pdf`.

[214] K. Crombé, Y. Andrew, M. Brix, C. Giroud, S. Hacquin, N. C. Hawkes, A. Murari, M. F. F. Nave, J. Onega, V. Parail, G. Van Oost, I. Voitsekhovitch, and K. D. Zastrow. Poloidal rotation dynamics, radial electric field, and neoclassical theory in the JET Internal-Transport-Barrier region. *Physcial Review Letters*, 95(15):155003, 2005.

[215] T. Tala *et al.* Toroidal and poloidal momentum transport studies in JET. *Nuclear Fusion*, 47(8):1012, 2007.

[216] C. Fenzi, X. Garbet, E. Trier, P. Hennequin, C. Bourdelle, T. Aniel, G. Colledani, P. Devynck, C. Gil, Ö. Gürcan, L. Manenc, M. Schneider, J.-L. Segui, and the Tore Supra team. On plasma rotation with toroidal magnetic field ripple and no external momentum input. *Nuclear Fusion*, 51(10):103038, 2011.

[217] K. Ida, H. Yamada, H. Iguchi, S. Hidekuma, H. Sanuki, K. Yamazaki, and the CHS Group. Electric field profile of a Compact Helical System Heliotron/Torsatron plasma with tangential neutral beam injection. *Physics of Fluids B: Plasma Physics*, 3(3):515–518, 1991.

[218] K. Ida *et al.* Reduction of ion thermal diffusivity associated with the transition of the radial electric field in neutral-beam-heated plasmas in the Large Helical Device. *Physical Review Letters*, 86:5297–5300, 2001.

[219] K. Ida and N. Nakajima. Comparison of toroidal viscosity with neoclassical theory. *Physics of Plasmas*, 4(2):310–314, 1997.

[220] M. Yoshinuma, K. Ida, M. Yokoyama, K. Nagaoka, M. Osakabe, and the LHD Experimental Group. Observations of spontaneous toroidal flow in the LHD. *Nuclear Fusion*, 49(7):075036, 2009.

[221] C. G. Beidler, M. Y. Isaev, S. V. Kasilov, W. Kernbichler, H. Maaßberg, S. Murakami, V. V. Nemov, D. A. Spong, and V. Tribaldos. ICNTS - impact of incompressible ExB flow in estimating mono-energetic transport coefficients. In *17*-th *International Toki Conference and 16*-th *International Stellarator/Heliotron Workshop, Toki, Japan*, 2007.

[222] A. Dinklage *et al.* Inter-machine validation study of neoclassical transport modelling in medium- to high-density stellarator-heliotron plasmas. *Nuclear Fusion*, 53(6):063022, 2013.

[223] Y. Camenen, A. Bortolon, A. N. Karpushov, B.P. Andrebe, Y. Duval, L. Federspiel, and O. Sauter. Accurate poloidal rotation measurement in TCV: an indirect method based on the inboard-outboard difference of toroidal rotation. European Pysical Society Conf. on Plasma Physics, Stockholm (Sweden), 2012. Avalable on-line at `http://ocs.ciemat.es/epsicpp2012pap/pdf/O5.117.pdf`.

[224] H. Maaßberg, C. D. Beidler, and Y. Turkin. Momentum correction techniques for neoclassical transport in stellarators. *Physics of Plasmas*, 16(7):072504, 2009.

[225] J. M. Reynolds Barredo. *Simulación de plasmas mediante las ecuaciones cinéticas de deriva en geometrías complejas*. PhD thesis, Universidad de Zaragoza, Facultad de Ciencias Físicas, 2009.

[226] V. Tribaldos, C. D. Beidler, Y. Turkin, and H. Maassberg. Extended estimations of neoclassical transport for the TJ-II stellarator: The bootstrap current. *Physics of Plasmas*, 18(10):102507, 2011.

[227] J. Guasp and M. Liniers. Loss cone structure for ions in the TJ-II helical axis stellarator. part II: Radial electric field effects. *Nuclear Fusion*, 40(3):411, 2000.

[228] J. L. Velasco, J. A. Alonso, I. Calvo, J. Arévalo, E. Sánchez, S. Perfilov, T. Estrada, A. López-Fraguas, C. Hidalgo, and the TJ-II team. Damping of radial electric field fluctuations in the TJ-II stellarator. Invited oral in the 40*th* EPS Conf. on Plasma Phys., Espoo (Finland).

[229] N. Nakajima H. Sugama S. Satake, M. Okamoto and M. Yokoyama. Non-local simulation of the formation of neoclassical ambipolar electric field in non-axisymmetric configurations. Plasma Fusion Research 1:002, 2006.

[230] K. McCormick *et al.* New advanced operational regime on the W7-AS stellarator. *Physical Review Letters*, 89:015001, 2002.

[231] J. A. Alonso, J. Arévalo, J. L. Velasco, I. Calvo, M. Ochando, J. M. García Regaña, and M. Landreman. Impurity density asymmetries in TJ-II model and first comparisons. Poster in the 19*th* International Stellarator/Heliotron Workshop, Padova., 2013.

[232] M. A. Pedrosa, C. Hidalgo, M. Ochando, and L. Bing. Experimental evidence of asymmetries in edge plasma potential in the TJ-II stellarator. Oral contribution in the 19*th* International Stellarator/Heliotron Workshop, Padova., 2013.

[233] A. Kappatou, R. J. E. Jaspers, E. Delabie, O. Marchuk, W. Biel, and M. A. Jakobs. Method to obtain absolute impurity density profiles combining charge exchange and beam emission spectroscopy without absolute intensity calibration. *Review of Scientific Instruments*, 83(10):10D519, 2012.

[234] K. J. McCarthy, B. Zurro, R. Balbín, A. Baciero, J. Herranz, and I. Pastor. Results of an experiment relating apparent Doppler ion temperatures with non-thermal velocities in hot-fusion plasmas. *Europhysics Letters*, 63(1):49, 2003.

AGRADECIMIENTOS

En primer lugar me gustaría agradecer a mis directores de tesis, Kieran y Arturo, la paciencia y dedicación que han mostrado estos años. Con mucho esfuerzo han conseguido moldear mi –en demasiadas ocasiones– fuerte personalidad, y a ellos debo gran parte de lo que he aprendido en estos años. De verdad, muchas gracias. Del mismo modo, estoy en deuda con José María Fontdecaba y José Luis Velasco por su colaboración estrecha, en muchas ocasiones cercana a una co-dirección. Es un privilegio haber podido trabajar con todos vosotros.

El papel de guía de Carlos Hidalgo ha sido, aunque desde un segundo plano, principal. Su presencia y saber hacer han suavizado y reconducido varios momentos difíciles de mi tesis. Igualmente, guardaré siempre un cariño especial a Marian Ochando que, en palabras suyas, es "esa tía lejana que te reprende cuando te hace falta, Juan". Vuestra combinación de excelencia científica y cercanía humana es un ejemplo a seguir.

Las colaboraciones con Mat Landreman, José Manuel Gracía-Regaña y Andrés de Bustos han sido claves para sacar adelante este trabajo, muchas gracias chicos. Y antes de acabar con la relación, digamos "académica" por ponerle nombre, que he tenido en este periodo, debo recordar las muchas conversaciones con Bernardo Zurro, Antonio López-Fraguas, Paco Medina, Alexis Breisemeister, Mordechai, Jesús Romero, Paco Castejón, Pepe Guasp, Daniel López-Bruna, José Ramón Martín Solís, Teresa Estrada ... y todos a los que en algún momento os he importunado con mis preguntas, ¡que sois muchos!

Para mí, como supongo les habrá pasado a otros antes, lo importante después de una tesis es la gente con la que has estado, las vivencias que has compartido. En este sentido, puedo decir que he tenido la suerte de estar cerca de Marcos Parro, con el que he vivido y compartido incontables historias estos últimos años. Igualmente, Daniel Iglesias y Paz García de Acilu han tirado de mí cuando hacía falta, ya sea arrastrándome a los bares -y escenarios-, o sacándome de ellos.

El grupo de "Carlis" (la auténtica *group maker*) es, quizá, el grupo de amigos con mayor categoría humana que he tenido la suerte de conocer: Kino, la propia Carla, Ángela, el Abuelo, Alvarito y Lore, el Primo y Sese y Atila, Marcos y Elena, Idoia, Laura y Adrien (¡y su bodorrio!), Álex, Santi ... Habéis sido una "constante universal" en mi vida en estos últimos años.

La gente de mi tierra, Valladolid, ha sido también de gran ayuda; recuerdo ahora las largas charlas con los amigos de la facultad: Bea, Julián, Bulba, Cris, Juan's, etc. Por otro lado, volver como el hijo pródigo al núcleo duro vallisoletano fue sin duda un gran acierto, y poder disfrutar de gente de la talla de Pirata y Carmen, Bravo, Carazo, Lucas, Quique, Busti, Kino, Diego,

Jorge y tantos otros. Ahora sois ya medio madrileños, así que os puedo tener mucho más cerca. Y hablando de Madrid –qué gran cuidad, ¡madre mía!– tengo que recordar a toda la gente con la que he tenido la suerte de compartir piso: mis *brothers* Óscar y Lucas, María y Andrelo, Lou, Paez, el Majouni, Montesakas, Tapper, etc.

Mención especial en mi mundo "Ciematero" merece el grupo de "los ingenieros": Bellatrix, Dani Alegre, Iole, Lalia, Natalia, Kikín, Regi, Bárbara, Iván, Geriardo, Oriol, Pablo, Luis Ríos, Elena, Avelinux, Rapi, Cristina, Carlos y Carmona. Igualmente recordaré siempre con cariño a la gente del 20 y aledaños: Begoña, Diana, Álvaro Cappa, Diana Bachiller, Daniel Carralero, José Ferriera, Tim, Rubén, Emilio, Joseh, Fran, Sun, Yuppi... Sin olvidar las divertidísimas escapadas con Luiz, Labor, Rossno y Rudols. ¡Ahora toca repetir en Las Vegas!

También me gustaría agradacer a mi familia el apoyo en estos años. Nadie como mi padre ha sufrido conmigo cuando me hundía y lo mandaba todo al carajo, ni se ha alegrado tanto cuando las cosas han empezado a ir bien. Y agradacer también la sordera extrema que han desarrollado mis hermanos y cuñados a nada que tenga que ver con la Física: Paco, Antonio e Isa, José y Cris y Espe y José Ignacio. Quién nos iba a decir cuando empecé la tesis que seríamos los que somos ahora. Es increíble.

Finalmente, si bien todas las personas que he nombrado me han ayudado un poco o un mucho a hacer esta tesis, sin Ana Mengs simplemente no podría haberla acabado. Parafraseando al gran Sabina, eres "mi escondite, mi clave de sol, mi reloj de pulsera". Física –la puta que me enamora, la fruta que es indigesta– es perecedera, ¡tú eres eterna!

PUBLICATIONS AND CONFERENCE CONTRIBUTIONS

The research papers and conference contributions produced during the elaboration of this thesis are listed below.

PUBLICATIONS:

- J Arévalo, J A Alonso, K J McCarthy, J L Velasco, J M Regaña and M Landreman. *Compressible impurity flow in the TJ-II stellarator.* Nuclear Fusion, accepted (2013).
- J L Velasco, J A Alonso, I Calvo, J Arévalo, E Sánchez and the TJ-II Team. *Damping of radial electric field fluctuations in the TJ-II stellarator.* Plasma Phys. Control. Fusion, accepted (2013).
- J Arévalo, J A Alonso, K J McCarthy and J L Velasco. *Incompressibility of Impurity Flows in Low Density TJ-II Plasmas and Comparison with Neoclassical Theory.* Nuclear Fusion **53**, 023003 (2013).
- A Bustos, J M Fontdecaba, F Castejón, J.L.Velasco, M Tereschenko and J Arévalo. *Studies of the Fast Ion Energy Spectra in TJ-II.* Phys. Plasmas **20**, 022507 (2013).
- J A Alonso, J L Velasco, J Arévalo, C Hidalgo, M A Pedrosa, B Ph Van Milligen and D Carralero. *Dynamics of zonal flow-like structures in the edge of the TJ-II stellarator.* Plasma Phys. Control. Fusion **55**, 014001 (2013).
- J L Velasco, J A Alonso, I Calvo and J Arévalo. *Vanishing neoclassical viscosity and physics of the shear layer in stellarators.* Phys. Rev. Lett. **109**, 135003 (2012).
- J M Fontdecaba, I Pastor, J Arévalo, J Herranz, K J McCarthy and G Sánchez Burillo. *Comparisons of electron temperature and density, and ion*

temperature profiles in the TJ–II stellarator. Plasma and Fusion Res. **5**, S2085 (2010).

- J Arévalo, K J McCarthy, J M Carmona and J M Fontdecaba. *Impurity Temperature Correction Factors for the Transmission Grating Spectrometer in the TJ-II stellarator.* Rev. Sci. Instrum. **81**, 1 (2010).

Other Publications:

- A Dinklage et al. *Inter-Machine Validation Study of Neoclassical Transport Modelling in Medium- to High-Density Stellarator-Heliotron Plasmas.* Nuclear Fusion **53**, 063022 (2013).
- J Sánchez and TJ-II team. *Dynamics of flows and confinement in the TJ-II stellarator.* Nuclear Fusion **53**, 104016 (2013).
- J Sánchez et al. *Overview of TJ-II experiments.* Nuclear Fusion **51**, 094022 (2011).
- K J McCarthy, V Tribaldos, J Arévalo and M Liniers. *The detection of fast oxygen ions in neutral beam heated plasmas in the TJ-II stellarator using spectroscopy methods.* J. Phys. B: Atomic, Molecular and Optical Physics **43**, 144020 (2010).

Conferences Contributions:

Invited Oral:

- J L Velasco, J A Alonso, I Calvo, J Arévalo, E Sńchez and the TJ-II Team. *Vanishing neoclassical viscosity and physics of the shear layer in stellarators.* 40*th* European Phys. Soc. Conf. on Plasma Phys. 2013, Espoo (Finland).
- J L Velasco, J A Alonso, I Calvo, J Arévalo, E Sńchez and the TJ-II Team. *Neoclassical viscosity and rotation in stellarators.* 40*th* European Fusion Theory Conf. (2013), Oxford (U.K.).
- J A Alonso, J Arévalo, D Carralero, C Hidalgo, B Van Milligen, M A Pedrosa, C Silva, J L Velasco and the TJ-II Team. *Dynamic transport regulation by zonal flow-like structures in the TJ-II stellarator.* 18*th* International Stellarator/Heliotron Workshop 2012, Canberra (Australia).
- J A Alonso, D Carralero, J Arévalo, J L Velasco and the TJ-II group. *Rotation in fusion plasmas.* Interdisciplinary Workshop on Plasma Phys. 2011, Escuela Estadística UCM, Madrid (Spain).

Selected Contributed Oral:

- J Arévalo, J A Alonso, K J McCarthy, J L Velasco, J M Gracía-Regaña, M Landreman, M Ochando and C Hidalgo. *Compressible impurity flows in the TJ-II stellarator.* 40*th* European Phys. Soc. Conf. on Plasma Phys. 2013, Espoo (Finland).
- J Arévalo, J A Alonso, K J McCarthy, J L Velasco, J M Gracía-Regaña and M Landreman. *Compressible flows in the TJ-II stellarator.* 11*th* Coordinated Working Group Meeting 2013, Madrid (Spain).

Selected Posters:

- J A Alonso, J Arévalo, J L Velasco, I Calvo, M Ochando, J M García Regaña and M Landreman. *Impurity density asymmetries in TJ-II: model and first comparisons.* 19*th* International Stellarator/Heliotron Workshop 2013, Padova (Italy).
- J L Velasco, J Arévalo and J A Alonso. *Configuration dependence of the the neoclassical viscosity at TJ-II.* 37*th* European Phys. Soc. Conf. on Plasma Phys. 2011, Frascatti (Italy).
- J Arévalo, K J McCarthy, J M Fontdecaba and B Van Milligen. *The ion energy distribution function as viewed by charge-exchange based diagnostics in the TJ-II stellarator.* 36*th* European Phys. Soc. Conf. on Plasma Phys. 2010, Dublin (Ireland).
- J Arévalo, K J McCarthy, J M Carmona and J M Fontdecaba. *Impurity Temperature Correction Factors for the Transmission Grating Spectrometer in the TJ-II stellarator.* 18*th* Topical Conf. on High Temperature Plasma Diagnostics 2010, New Jersey (USA).
- J Arévalo, K J McCarthy, J M Carmona and J M Fontdecaba. *Perfiles de Temperatura de Impurezas en Plasmas del TJ-II stellarator.* 32*th* Biennial on Physics 2009, Ciudad Real (Spain).